Dissertation

Submitted to the
Combined Faculty of Natural Sciences and Mathematics
Heidelberg Universität, Germany
for the Degree of
Doctor of Natural Sciences (Dr. rer. nat.)

Presented by

MSc. Carlos Antonio Angeles De La Torre

From Nezahualcóyotl, México

Date of examination: 18.07.2025

Theme:

Zircon Petrochronology and Thermochemical Modeling of Quaternary Magmatic Systems in Western North America (The Geysers, Eastern Snake River Plain, Blackfoot)

MSc. Carlos Antonio Angeles De La Torre

Examination committee:

Prof. Dr. Axel K. Schmitt, PhD supervisor (reviewer and examiner)

Prof. Dr. Mario Trieloff (reviewer and examiner)

Prof. Dr. Yamirka Rojas Agramonte (additional examiner)

Prof. Dr. Lucie Tajcmanova (additional examiner)

Theme:

Zircon Petrochronology and Thermochemical Modeling of Quaternary Magmatic Systems in Western North America (The Geysers, Eastern Snake River Plain, Blackfoot)

MSc. Carlos Antonio Angeles De La Torre

Supervisor:

Prof. Dr. Axel K. Schmitt

Declaration

This thesis is submitted to the Combined Faculty of Natural Sciences and for Mathematics of the Heidelberg University for the degree of Doctorate of Natural Sciences.

I, the undersigned, declare that this thesis is my own work and has not been submitted in any form from another degree, diploma or study at any university or other institution of tertiary education. Information derived from the published or unpublished work of others has been acknowledged in the text and a list of references is given.

M.Sc. Carlos Antonio Angeles De La Torre

Heidelberg June 6, 2025

Contents

Abstract

Zircon ($ZrSiO_4$) is an accessory mineral commonly present in a wide range of igneous, metamorphic, and sedimentary rocks. When crystallized in-situ, it is a powerful tool for reconstructing chemical and thermal processes in the Earth's crust at high fidelity and with fine temporal resolution. In this dissertation, zircon from a range of mafic to silicic volcanic fields in the western United States was investigated by combining U-Th-Pb geochronology, trace element geochemistry, and $\delta^{18}O$ and εHf isotopic data. This integrated petrochronological approach of studying zircon age and composition in combination with textural constraints yielded new insights into magma origins, evolution, and geothermal potential associated with Quaternary volcanism.

The first part of this study investigates zircon crystallization in the Eastern Snake River Plain (ESRP) and the adjacent Craters of the Moon volcanic field (COM) in southern Idaho. While the ESRP is dominated by voluminous olivine tholeiite lava flows with subordinate trachyandesite and rhyolite lavas, the COM field comprises mainly Fe-rich trachybasalts and rare evolved basaltic trachyandesites. In both settings, zircon is present in intermediate–silicic host rocks. High-resolution U-Pb and U-Th dating and trace element analysis confirm that zircon in these magmas formed autocrystically during protracted fractional crystallization, rather than being inherited from interstitial melts in a crystal mush. Equivalent evolutionary trends in zircon and whole-rock chemistry support this conclusion. Ultimately, zircon saturation in these systems was facilitated by strong enrichment of Zr via fractional crystallization. In the resulting high-Zr, compositionally intermediate ESRP and COM melts, zircon became saturated at unusually high temperatures and in comparatively primitive magma compositions. Since ESRP and COM zircon formed demonstrably in situ, zircon $\delta^{18}O$ and εHf isotopic compositions are also reliable source indicators. These data suggest that ESRP and COM magmas originated from a similar mantle source, but subsequently evolved along different pathways. In the case of the ESRP, magma assimilated hydrothermally altered low-$\delta^{18}O$ felsic rocks in the upper crust, whereas for the COM magmas, two sequential stages of assimilation occurred involving Archean lower crust and normal-$\delta^{18}O$ upper crustal rocks, respectively. These findings underscore the importance of detailed petrochronological analyses of zircon and demonstrate that its presence in magmatic systems dominated by mafic melts has petrogenetic significance.

Building on this framework, the second paper shifts focus to the Geysers Plutonic Complex (GPC) in California, where a rare combination of deep plutonic and cogenetic volcanic rocks is accessible due to extensive geothermal drilling. The GPC and its volcanic equivalents represent a compositionally evolved intrusive complex emplaced between ~700 and nearly 4000 m depth, based on geothermal drill well penetration. Zircon in these rocks records a history of magma evolution marked by early formation of highly fractionated microgranite porphyry, followed by emplacement of larger volumes of less evolved granite and granodiorite. Trace element and isotopic data ($\delta^{18}O$ and εHf) from zircon reveal multiple magma types with different degrees of crustal assimilation. Using previously reported zircon age distributions, a thermal model was developed to reconstruct the magmatic history of the GPC. The model relates zircon saturation to magma temperature and successfully reproduces the observed zircon age distributions for the GPC. In the best-fit model scenario, the main volume of the GPC intruded during a brief, intense flare-up phase lasting for c. 50,000 years. This magma pulse was embedded into a longer interval of low-flux magmatism which lasted for at least c. 900,000 years. The agreement between the modeled volume of the intrusion and the extrapolated GPC volume validates the potential of zircon-based thermal modeling for reconstructing upper crustal magma reservoirs and their thermal histories.

The final case study returns to southern Idaho and evaluates the geothermal potential of the Blackfoot Volcanic Field (BVF), a Pleistocene bimodal volcanic field located ~60 km southeast of the Snake River Plain-Yellowstone hotspot track. Despite hosting some of the youngest topaz rhyolites globally, the geothermal significance of this field remained uncertain. Zircon geochronology and geochemistry were used to constrain its eruptive and magmatic history. U-Pb and U-Th dating revealed two distinct eruptive phases: an early (1,006–785 ka) episode forming mainly the northern domes and a late (63–55 ka) pulse during which the southern domes erupted. Corresponding isotopic data for the BVF indicate a strong Archean crustal component in the parental magmas, consistent with their off-axis position relative to the hotspot. A thermal model for a 120 km^3 magma reservoir emplaced 95,000 years ago and at 6 km depth successfully reproduces the timing of zircon crystallization and magma volumes for the southern domes and their subvolcanic equivalents. It also predicts that temperatures at ~4 km depth still exceed 300 °C today. The lack of surface geothermal manifestations within the BVF is attributed to a structurally complex hydrologic system that dilutes and diverts geothermal fluids.

Collectively, these three case studies illustrate the broad applicability of zircon petrochronology in characterizing the temporal, thermal, and compositional evolution of magmatic systems underneath Quaternary volcanic fields. Zircon saturation can occur in intermediate magma compositions associated with voluminous basaltic magmas, extending the potential of zircon petrochronology for refining models of magma generation, evolution, and emplacement to systems beyond those conventionally investigated. When paired with thermal modeling, zircon data can provide insights into the thermal state of crustal magmatic systems, including those with geothermal energy potential. This thesis demonstrates the integrative power of zircon as a tool for decoding crustal magmatism and guiding geothermal exploration.

Zusammenfassung

Zirkon ($ZrSiO_4$) ist ein akzessorisches Mineral, das in einer Vielzahl magmatischer, metamorpher und sedimentärer Gesteine vorkommt. In-situ gebildeter Zirkon erlaubt es, chemische und thermische Prozesse in der Erdkruste zeitlich hochauflösend zu rekonstruieren. In dieser Dissertation wurde Zirkon aus mehreren Vulkanfeldern im Westen der USA, in denen mafisch bis felsische Magmen gefördert wurden, mittels U-Th-Pb-Geochronologie und Spurenelementgeochemie sowie isotopenanalytisch ($\delta^{18}O$ und εHf) untersucht. Dieser petrochronologische Ansatz, der die kombinierte Analyse von Alter, Zusammensetzung und Gefüge für akzessorische Minerale wie Zirkon integriert, ermöglicht neue Einblicke in die Herkunft, Entwicklung sowie das geothermische Potenzial quartärer magmatischer Systeme.

Der erste Teil dieser Arbeit widmet sich der Zirkonkristallisation in den Eastern Snake River Plain (ESRP) und angrenzenden Craters of the Moon (COM) Vulkanfeldern im Süden Idahos. Während das ESRP Vulkanfeld hauptsächlich aus voluminösen Olivin-Tholeiit-Lavaströmen mit untergeordneten Trachyandesit- und Rhyolith-Laven gebildet wird, kommen im COM hauptsächlich eisenreiche Trachybasalte und, untergeordnet, differenzierte basaltische Trachyandesite vor. In beiden Regionen findet sich Zirkon in intermediären bis silikatischen Wirtsgesteinen. Hochauflösende U-Pb- und U-Th-Datierungen sowie Spurenelementanalysen belegen, dass Zirkon in diesen Magmen originär im Zuge lang andauernder fraktionierter Kristallisation entstand und nicht aus Restschmelzen eines Kristallbreis stammt. Übereinstimmende Entwicklungstrends in der Zirkon- und Gesamtgesteinschemie stützen diese Interpretation. Die Zirkonsättigung wurde in diesen Magmensystemen durch starke Anreicherung von Zr infolge fraktionierter Kristallisation erreicht. In den daraus resultierenden Zr-reichen, intermediären Magmen der ESRP und COM Vulkanfelder kristallisierte Zirkon bei ungewöhnlich hohen Temperaturen und aus vergleichsweise primitiven Magmenzusammensetzungen. Da Zirkon in den ESRP und COM Magmen nachweislich in situ entstand, liefern $\delta^{18}O$- und εHf-Isotopenzusammensetzungen verlässliche Informationen zur Magmenquelle. Diese Daten deuten auf einen gemeinsamen mantelbasierten Ursprung der Schmelzen hin, die jedoch anschließend unterschiedlichen Entwicklungspfaden folgten: Im ESRP Vulkanfeld assimilierte das Magma hydrothermal veränderte, an $\delta^{18}O$-verarmte felsische Oberkruste, während die COM-Magmen zwei aufeinanderfolgende Assimilationsphasen durchliefen. Dabei wurden zunächst Gesteine der

archaischen Unterkruste und später der Oberkruste assimiliert, die eine normale δ^{18}O-Zusammensetzung aufweisen. Diese Ergebnisse unterstreichen die Bedeutung des petrochronologischen Ansatzes in der Untersuchung von Zirkon, auch für magmatische Systeme die von mafischen Schmelzen dominiert werden.

Aufbauend auf diesen Erkenntnissen liegt der Fokus der zweiten Fallstudie auf dem Geysers Plutonic Complex (GPC) in Kalifornien, wo aufgrund umfassender geothermischer Bohrungen ein seltener Einblick in plutonische Gesteine und ihre vulkanischen Äquivalente möglich ist. Der GPC stellt einen chemisch differenzierten Intrusionskörper dar, der sich zwischen etwa 700 und knapp 4000 m Tiefe gebildet hat. Zirkonanalysen belegen eine frühe magmatische Phase, bei der hochdifferenzierte Mikrogranit-Porphyre gebildet wurden. Darauf folgte die Platznahme einiger entwickelter Granite und Granodiorite, die den Hauptteil des GPC ausmachen und in vulkanischen Gesteinen an der Oberfläche ihre Entsprechung haben. Spurenelement- und Isotopenanalysen (δ^{18}O und εHf) an Zirkon dieser Gesteine belegen mehrere Magmentypen, die sich durch variable Anteile krustaler Assimilation unterscheiden. Aufbauend auf bestehenden Altersverteilungen von Zirkon wurde ein thermisches Modell entwickelt, das die magmatische Geschichte des GPC anhand der mit der Abkühlung einhergehenden Zirkonsättigung rekonstruiert. Dieses Modell bildet sowohl die Altersverteilung als auch die Temperaturentwicklung der Magmen ab. Dabei kam es während eines intensiven Magmenpulses, der nur über ca. 50.000 Jahre anhielt, zu einem verstärkten Anwachsen des GPC Magmenkörpers. Dieser Puls war wiederum Teil eines über ~900.000 Jahre andauernden Zeitraums, während dessen nur geringe Magmenmengen zugeführt wurden. Die Übereinstimmung zwischen modelliertem und geologisch extrapoliertem Intrusionsvolumen bestätigt die Aussagekraft zirkonbasierter thermischer Modelle zur Rekonstruktion oberkrustaler Magmenreservoire.

Die dritte Fallstudie ist wiederum im südlichen Idaho angesiedelt und untersucht das geothermische Potenzial des Blackfoot-Vulkanfelds (BVF), eines pleistozänen, bimodalen Vulkanfelds rund 60 km südöstlich des Yellowstone-Hotspot-Tracks. Trotz des Vorkommens rhyolitischer Vulkane, die zu den jüngsten Topas-Rhyolithen weltweit zählen, blieb das geothermische Potenzial des BVF lange unklar. Mithilfe von Zirkongeochronologie und -geochemie wurde die eruptive und magmatische Entwicklung des Vulkanfeldes untersucht. U-Pb- und U-Th-Datierungen von Zirkon belegen zwei eruptive Phasen, während derer mehrere Lavadome gebildet wurden: eine frühe

(1.006–785 ka) hauptsächlich im nördlichen Teil des Vulkanfelds und eine späte (63–55 ka) im Süden. Isotopendaten zeigen eine starke archaische Krustenkomponente in den Magmen an, was mit der randständigen Lage des Vulkanfeldes relativ zum Hotspot einhergeht. Die beobachteten Zirkonkristallisationsdauern und Magmenvolumina im südlichen BVF (einschließlich einer oberflächennahen subvulkanischen Intrusion) werden modellhaft durch die Abkühlung eines ursprünglich 120 km³ umfassenden Magmenreservoirs, welches sich vor 95,000 Jahren in 6 km Tiefe bildete, erklärt. Ebenso lässt die thermische Modellierung erwarten, dass Temperaturen von über 300 °C in ~4 km Tiefe bis heute vorherrschen. Das Fehlen geothermischer Anzeichen an der Oberfläche lässt sich auf ein strukturell komplexes hydrologisches System zurückführen, in dem durch den ehemaligen Magmenkörper aufgeheizte Fluide verdünnt und abgelenkt werden.

Zusammenfassend belegen diese drei Studien die vielseitige Anwendbarkeit der Zirkon-Petrochronologie zur Charakterisierung der zeitlichen, thermischen und chemischen Entwicklung magmatischer Systeme, aus denen sich Eruptionen in quartären Vulkanfeldern speisen. Die Sättigung von Zirkon kann in intermediären Schmelzen auch in basaltisch dominierten Umgebungen auftreten, wodurch sich das Anwendungsspektrum der Zirkon-Petrochronologie auf magmatische Systeme jenseits der häufig untersuchten felsischen Gesteinszusammensetzungen erweitert. In Kombination mit thermischen Modellen liefert Zirkon wichtige Einblicke in den thermischen Zustand der Kruste – auch im Hinblick auf deren geothermisches Potenzial. Diese Dissertation zeigt die weitreichenden Möglichkeiten, die das Mineral Zirkon zur Entschlüsselung magmatischer Prozesse in der Kruste bietet und wie dies die Erkundung geothermischer Vorkommen unterstützen kann.

1. Introduction

Geothermal energy presents a promising solution to supplement the growing global energy demand in a sustainable and environmentally responsible way. When evaluated across key performance metrics—including annual energy generation, greenhouse gas emissions, energy return, and production costs—geothermal ranks just behind nuclear energy as one of the most effective power generation technologies (Dincer & Acar, 2015). Volcanic regions with Quaternary-aged activity often host favorable geothermal conditions, where mid-crustal magma intrusions provide long-lived heat sources (e.g. Elders et al., 1984; Wohletz and Heiken, 1992; Dalrymple et al., 1999). In particular, volcanic fields, where episodic eruptions of intermediate to silicic magmas in addition to basalts occur, are of significant interest because every volume unit of evolved magma erupting represents an even larger volume of less evolved magma at depth. These settings host major geothermal systems worldwide, including "The Geysers" in California, the largest developed geothermal complex on Earth (e.g. Dalrymple et al., 1999; Peacock et al., 2020).

In the United States, California has long been recognized for its geothermal electric potential (Williams et al., 2008). However, Idaho also contains some of the most promising undeveloped geothermal resources, especially in its southern region. There, the migration of the Yellowstone hotspot has produced a track of caldera complexes and basaltic plains (Fig. 1), forming the volcanic province of the Snake River Plain, which is a classic example of a bimodal volcanic system dominated by mafic and felsic magmas with relative few intermediate compositions erupting (Armstrong *et al.,* 1975; Pierce & Morgan, 1992; Smith & Braile, 1994; Ellis et al., 2013; Drew *et al*., 2013; Anders *et al*., 2019, Colón *et al*., 2018, Henry *et al*., 2017). Additionally, post-hotspot Quaternary volcanism has produced isolated rhyolite domes within the eastern Snake River Plain (ESRP). Similarly, the extensive Craters of the Moon (COM) lava field contains Holocene mafic–intermediate scoria cones and lava flows, whereas to the south of the ESRP, the Late Pleistocene Blackfoot Volcanic Field (BVF) with volumetrically dominant basaltic lava flows and several rhyolite domes is one of the youngest recognized bimodal volcanic systems worldwide (Fig. 1).

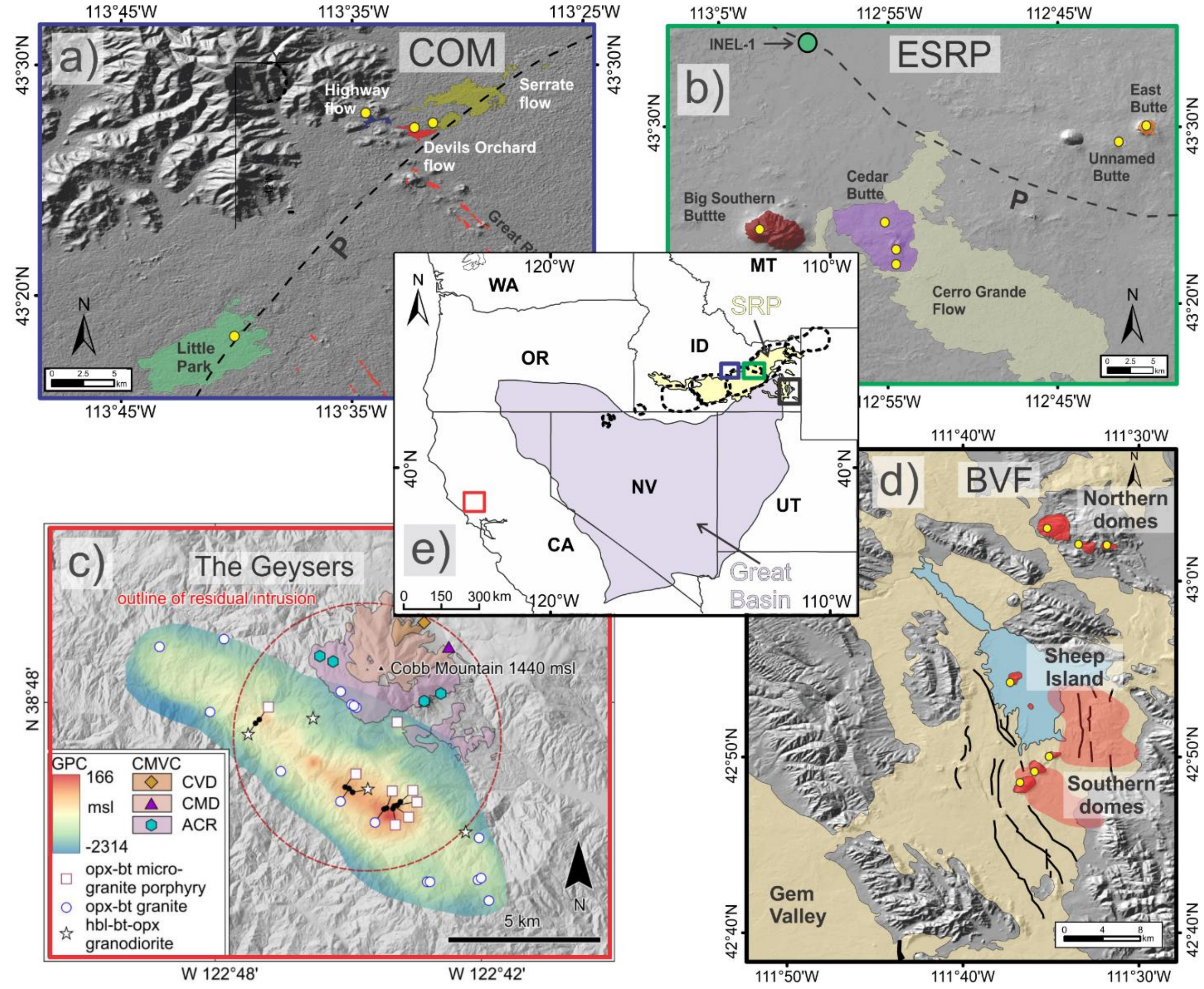

Fig. 1. *Locations of the four study areas presented in this dissertation. (a) Craters of the Moon (COM) volcanic field and the sampled lava flows, some of which are partially contained within the Miocene Picabo Caldera (P). (b) depicts the sampled rhyolite domes within the Eastern Snake River Plain (ESRP). (c) extent of The Geysers Plutonic Complex (GPC) and the cogenetic Cobb Mountain Volcanic Complex (CMVC). (d) geological sketch map of the Blackfoot Volcanic Field (BVF), with Quaternary rhyolite domes marked in red. All sampling locations in the COM, ESRP, and BVF are indicated by yellow dots, while different symbols denote drill core and volcanic units in The Geysers system. Dashed lines in the central map (e) outline the time-transgressive caldera fields associated with the Mid-Miocene to Quaternary Yellowstone hotspot track. The yellow shaded field indicates the full extent of the Snake River Plain (SRP).*

The genesis of rhyolites, either in systems which are dominated by intermediate compositions such as The Geysers or in bimodal volcanic systems like the Snake River Plain –Yellowstone province, remains a subject of debate, with two endmember models proposed (Fig. 2). One model suggests that rhyolites form through extensive fractional crystallization of mantle-derived basaltic magmas during their ascent and storage in the crust, where the evolving melt consequently becomes enriched in silica (e.g., McCurry & Rodgers, 2009; Ellis et al., 2013). The alternative endmember hypothesis proposes that silicic magmas result from partial melting of lower- to mid-crustal rocks, triggered by the intrusion of basaltic magmas (e.g., Shervais et al., 2006; Bonnichsen et al., 2007; Bindeman & Simakin, 2014). In addition, hybridization of mantle derived magmas with crustal rocks via assimilation and simultaneous fractional crystallization (AFC) can explain some of the compositional characteristics of rhyolites. These mechanisms can often be further distinguished by their geochemical and isotopic fingerprints where crustally derived melts would tend to inherit enriched isotopic signatures, whereas fractionated basaltic melts typically would retain more primitive isotopic characteristics.

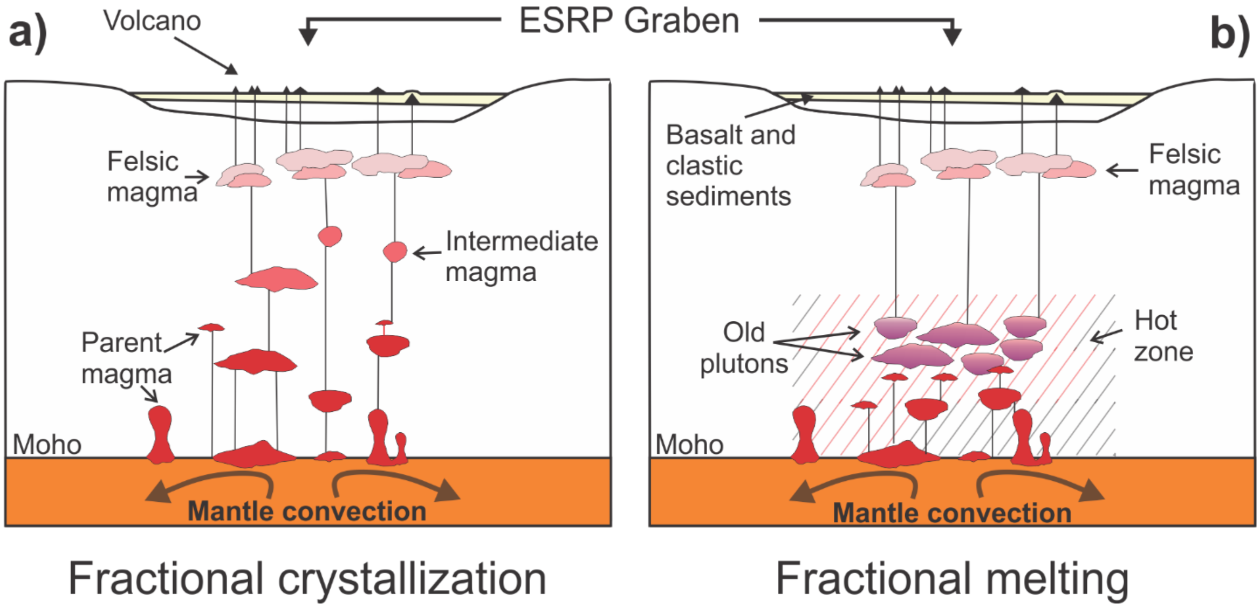

Fig. 2. *Proposed petrogenetic models for the generation of rhyolites and basalts in the ESRP. In the left scenario (a), mantle-derived magmas undergo differentiation via fractional crystallization upon ascent and storage at different crustal depths. The right scenario (b) invokes partial melting of lower crustal rocks at elevated geothermal gradients driven by repeated magma injections, which remobilize and partially melt older plutons emplaced during the passage over the Yellowstone hotspot.*

Identifying geothermal resources and developing new geothermal power plants will be essential for a successful transition to low-carbon energy. Achieving this requires a better understanding of the genesis and volumes associated with magmatism which is critical for assessing the geothermal potential of Quaternary volcanic fields. In this context, zircon petrochronology offers a powerful tool to probe the thermal and chemical evolution of magma systems by extracting the combined information on the timing of magma evolution and its compositional maturation.

Zircon ($ZrSiO_4$), although universally an accessory phase in magmatic rocks, plays an important petrological role due to its ability to retain geochemical and isotopic information over geological timescales. Zircon incorporates uranium and thorium during crystallization, making it ideal for high-precision U–Th–Pb dating (Hanchar & Hoskin, 2003; Schmitt, 2011). Its crystallization is sensitive to magma temperature and composition (Fig. 3; e.g. Watson & Harrison, 1983; Boehnke et al., 2013; Borisov & Aranovich, 2019; Crisp & Berry, 2022), and thus zircon act as a robust recorder of the magmatic thermal history. Furthermore, zircon trace element and isotopic compositions (e.g., $\delta^{18}O$, εHf) provide insights into magmatic processes such as fractional crystallization, crustal assimilation, and recharge events (Cherniak & Watson, 2003; Valley et al., 2005; Kemp et al., 2007; Bindeman, 2008). Although most zircon studies are on evolved rocks, there are also reports of zircon in mafic lavas, where it is unexpected because such melts are characteristically undersaturated in zircon (e.g. Carley *et al*., 2014; Grimes *et al*., 2007; 2011; Bea *et al.*, 2022; Rojas-Agramonte et al., 2022). It is therefore important to better constrain the origins of zircon in magma systems which are dominated by mafic magma compositions.

Recent studies have also demonstrated that zircon age distributions can be used to reconstruct long-term magmatic fluxes and volumes which are otherwise difficult to constrain for hidden magma intrusions. Through numerical modeling of thermal conduction, advective heat transport with intruding magma, and release of the latent heat of crystallization, zircon age spectra are calculated using the experimentally established relationship between temperature and zircon saturation (e.g., Watson and Harrison, 1983). By exploring different model scenarios varying recharge rates durations, volumes, and reservoir thermal environment, different zircon crystallization histories are predicted which can be compared to observed zircon age spectra (e.g., Caricchi et al., 2014, 2016; Tierney et al., 2016; Lukács et al., 2018; Ratschbacher et al., 2018; Weber *et al.*, 2020; Liu et al., 2021; Melnik et al., 2021; Friedrichs et al., 2021; Schmitt et al., 2023).

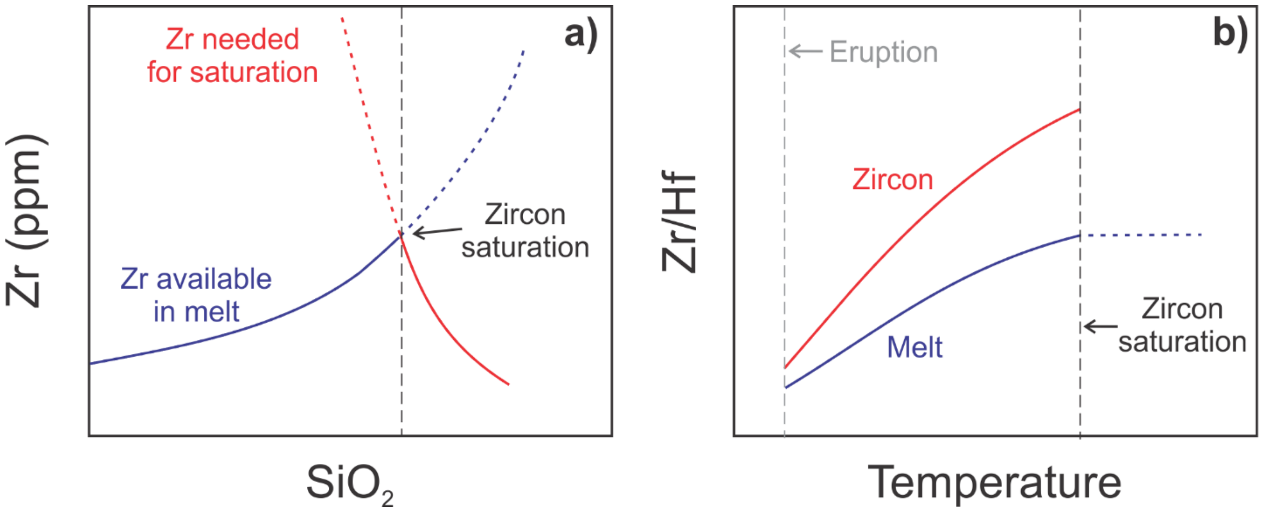

Fig. 3. *Zirconium evolution in magmatic systems. (a) For a given magma composition, fractional crystallization progressively enriches the melt in Zr, eventually reaching zircon saturation. (b) Variation trends of Zr/Hf in melt and zircon during progressive crystallization. Note the direct correlation with decreasing temperature (modified after Aranovich et al., 2018).*

This cumulative dissertation comprises three scientific papers, two published and one submitted to international peer-reviewed journals. All studies center on zircon petrochronology, applying it to a range of magmatic settings to investigate petrological processes and, in two cases, to assess geothermal potential in Quaternary volcanic provinces. The first paper (I) investigates zircon saturation in a dominantly mafic volcanic field, the Craters of the Moon (COM), Idaho. It examines the genesis of zircon in intermediate COM lavas, and compares zircon formation at COM with that in rhyolite melts from the Eastern Snake River Plain (ESRP). The second paper (II) explores the petrogenetic origins of The Geysers geothermal reservoir by integrating zircon data from drilled plutonic rocks and associated eruptive units, which uniquely allows a comparison between plutonic and volcanic counterparts of the same system, thus calibrating thermochemical models for zircon crystallization in open-system magma reservoirs. The third paper (III), under review during writing of this chapter, evaluates the zircon record of the Blackfoot Volcanic Field (BVF) in comparison to the ESRP, and applies a similar modeling approach as in paper II to assess the region’s geothermal potential. Full versions of all three papers are included in the appendix of this thesis, along with their associated supplementary materials in an electronic appendix.

2. Objectives

This research employs zircon petrochronology to investigate volcanic and plutonic rocks associated with geothermal and volcanic systems in the western United States of America, which includes magma compositions ranging from trachyandesite to rhyolite. The study aims to address the following objectives:

- Quantify the ages of pre-eruptive magma crystallization and crystal residence from a zircon perspective using Quaternary volcanic rocks from the ESRP, COM and BVF.
- Assess the conditions enabling zircon saturation in mafic dominated systems, with a particular emphasis on the compositionally intermediate lava flows from COM.
- Reevaluate the petrogenesis of post-Yellowstone hotspot volcanism for the ESRP and COM.
- Apply isotope and trace elements geochemistry in zircon to determine the evolution of silicic magma at The Geysers, and estimate magma volumes and recharge rates responsible for the development of The Geysers geothermal system.
- Constrain the genesis of topaz-bearing rhyolites in the BVF and apply thermochemical modeling to address the potential of a hidden geothermal system underneath the BVF bimodal volcanic field.

3. Methodology

3.1 Sampling and sample preparation

Kilogram-sized samples were collected from selected lava flows and domes across the different volcanic systems, with the exception of The Geysers, for which previously dated zircon grains extracted from geothermal well cuttings and surface sample of lava were utilized (Schmitt et al., 2003a, 2003b). Sampling for the Eastern Snake River Plain (ESRP) included four rhyolitic domes and two intermediate lava flows. At Craters of the Moon (COM), three intermediate lava flows within the National Monument area were sampled, along with a xenolith fragment from a primitive flow, which was obtained from the Idaho State University collection. Finally, in the Blackfoot Volcanic Field (BVF), seven topaz rhyolite domes were sampled. Locations of all samples are displayed in Figure 1.

Samples were initially fragmented using a hammer or a hydraulic press, and the material was sieved to isolate grains smaller than 250 µm. Heavy mineral separates were obtained by hydrodynamic density separation. For COM samples, additional separation using a Frantz magnetic separator was employed to remove magnetic phases and concentrate non-magnetic minerals such as zircon. Zircon grains were handpicked under a binocular microscope (Fig. 4a-b) and embedded in epoxy resin alongside with zircon reference materials AS3 (Paces & Miller, 1993), 91500 (Wiedenbeck et al., 2004), and Temora 2 (Black et al., 2004). The mount surfaces were abraded with silicon carbide paper and polished with 1 µm diamond paste to expose crystal interiors on a flat surface (Fig. 4c).

To assess internal textures and zoning, zircon mounts were imaged using a Zeiss EVO MA 15 scanning electron microscope (SEM) at Heidelberg University. Backscattered electron (BSE) images were acquired using a high-definition detector under accelerating voltages of 18 keV and beam currents between 0.5–4.0 nA. Cathodoluminescence imaging (CL) was conducted in low-vacuum mode using a variable pressure secondary electron (SE) detector at 10 keV and 10 nA (Fig. 4d-f). An ~20 nm gold coating was applied for imaging and subsequently removed prior to further processing. To prepare for secondary ion mass spectrometry (SIMS) analysis, the mounts were rinsed multiple times with deionized water and methanol, and then recoated with an ~50 nm thick layer of gold to ensure proper surface conductivity (Fig. 4c). After SIMS analysis, ion microprobe crater dimensions were determined for selected spots using a KEYENCE VK-X200 laser microscope.

3.2 U-Th and U-Pb zircon crystallization dating

Zircon geochronology was performed using the CAMECA ims 1300-HR^3 secondary ion mass spectrometer (SIMS) housed at the John de Laeter Centre, Curtin University, Australia (Fig. 5a-c). U-Th disequilibrium dating employed a $^{16}O^-$ primary ion beam (~40 nA) operated in Gaussian mode, focused to a ~25 µm spot diameter and a resulting crater depth of ~6 µm. Secondary ions were extracted at 10 kV and analyzed at a mass resolving $m/\Delta m$ of ~5000. Simultaneous measurements were conducted for 244.03 (background), $^{230}Th^{16}O$ (via electron multipliers), and $^{232}Th^{16}O$ and $^{238}U^{16}O$ signals (via Faraday cups). A total of 20 cycles were collected for each analysis, the data was later corrected for detector dead time and Faraday cup baselines using the ZIPS v3.1.1 reduction software. Analytical accuracy for the (^{230}Th)/(^{238}U) activity was verified against the AS3 (in secular equilibrium) zircon reference material.

For U-Pb dating, a $^{16}O^-$ primary beam of 12–18 nA was used, focused to a spot size of ~20 µm, resulting in a ~6 µm deep crater (Fig. 5a-c). Secondary ions were passed through 400 µm contrast and 3000 µm field apertures, with an energy bandpass of 50 eV and a vertical distortion introduced by the rectangular mode applied to lenses in the coupling section of the mass spectrometer to enhance mass resolution. Isotopes of Zr, Pb, Th, and U were sequentially analyzed in peak-hopping mode over 10 cycles, following a 20-second pre-sputtering step. Relative sensitivity factors (RSFs) for U-Pb, U-Th, and U-Zr were calibrated using the AS3 and 91500 zircon references. Corrections for common Pb were applied using measured ^{207}Pb (for Quaternary ages) and ^{204}Pb (for pre-Quaternary ages in xenocrysts or xenoliths). For Quaternary ages, the $^{206}Pb/^{238}U$ ages were also corrected for initial ^{230}Th disequilibrium based on Th/U ratios derived from whole-rock compositions from the corresponding study areas.

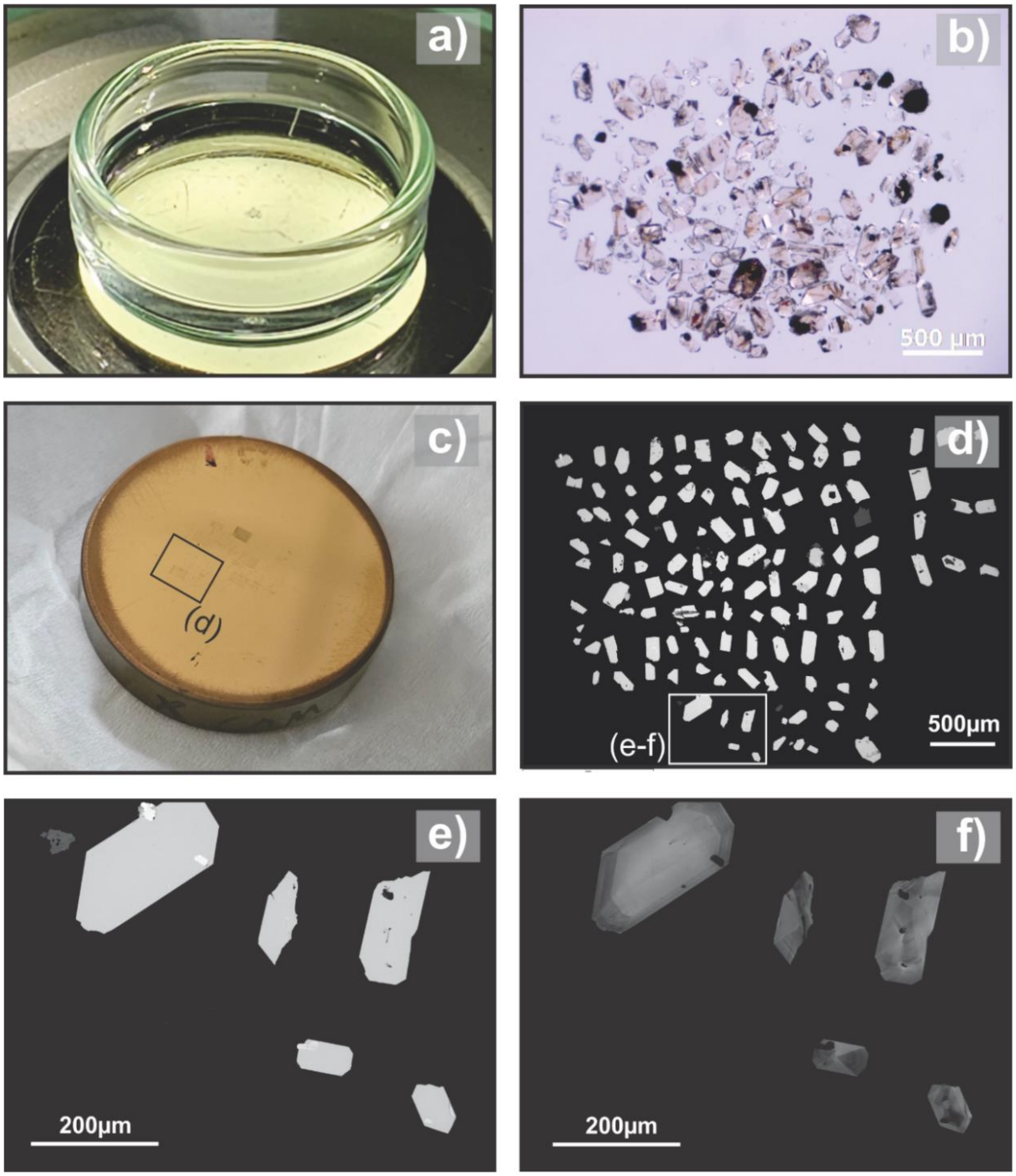

Fig. 4. *Zircon selection and preparation process for SIMS analysis. Zircon crystals were handpicked from the heavy mineral fraction under a binocular polarizing microscope (a–b). Crystals were then mounted in epoxy resin and polished to expose their interiors (c). An overview map of the exposed zircon crystals was produced using backscattered electron (BSE) imaging (d). Higher-resolution BSE and cathodoluminescence (CL) images were subsequently acquired to assess internal zoning and guide analytical spot placement (e–f). All samples shown are from the East Butte rhyolite dome in the Eastern Snake River Plain (ESRP). Petri dish in (a) and epoxy mount in (c) are 3 and 2.5 mm in diameter respectively.*

3.3 Trace element in zircon determination and modelling

Trace element concentrations in zircon were measured using the CAMECA ims 1300-HR³ SIMS at the John de Laeter Centre, following protocols adapted from Schmitt et al. (2017) (Fig. 5a-c). A ~15 nA $^{16}O^{-}$ primary ion beam in Gaussian mode was used to target the same analytical spots previously employed for U-Th-Pb geochronology. For zircon trace element quantification, RSF values were obtained from NIST SRM 610 glass (Pearce et al., 1997), and the accuracy of the measurements was verified through repeated analyses of the 91500 zircon reference material (Wiedenbeck et al., 2004). Analytical data were rigorously evaluated to exclude results affected by beam overlap onto inclusions of non-zircon phases such as oxides or glass.

Titanium concentrations in zircon (TiZr) were used as a geothermometer to estimate crystallization temperatures, employing the calibration proposed by Ferry and Watson (2007), which relates Ti content in zircon Ti_{zrn} to temperature under assumptions of specific silica and titania activity a conditions:

$$\log(Ti_{zrn}) = (5.711 \pm 0.072) - \frac{(4800 \pm 86)}{T\ (k)} - loga_{SiO_2} + loga_{TiO_2}$$

Silica activity was constrained by petrologic observations, whereas titania activity was calculated from Fe-Ti exchange in coexisting magnetite-ilmenite pairs (Ghiorso and Evans, 2008).

To explore the magmatic evolution and trace the crystallization behavior of coexisting minerals, fractional crystallization modeling was applied. The model tracked changes in trace element concentrations in the melt and zircon as crystallization proceeded, based on a mass balance equation that incorporates the initial element concentration:

$$C_m = C_{m0} \times F^{D-1}$$

where C stands for the concentration of the element in the residual melt m and the initial magma concentration $m0$, F for the fraction of the remaining melt ranging 1 to 0, and D for the bulk partition coefficient of the element. Partition coefficients for relevant elements were sourced from the literature, including those compiled in the GERM database (http://www.earthref.org/GERM/). Modelled zircon trace element concentrations are then obtained from the melt composition using zircon-specific partitioning coefficients.

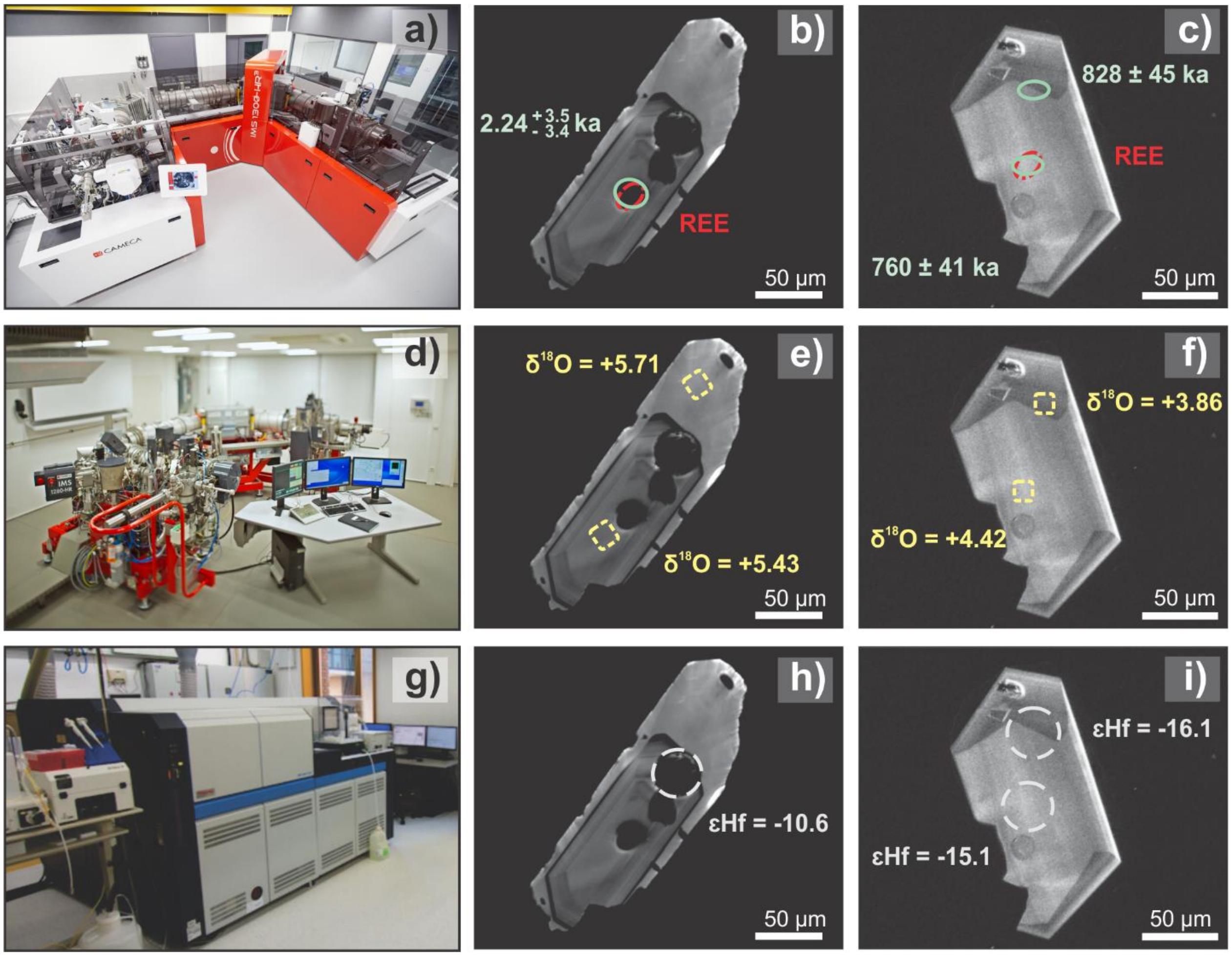

Fig. 5. *Analytical setup and spot dimensions for SIMS and MC-ICP-MS zircon analyses. U-Th and U-Pb geochronology and trace element data were obtained using a CAMECA ims 1300-HR^3 SIMS at the John de Laeter Centre, Curtin University, Australia (a–c). Oxygen isotope analyses were conducted with a CAMECA ims 1280-HR SIMS at Heidelberg University (d–f). Hafnium isotopic compositions were measured using a ThermoScientific NEPTUNE Plus MC-ICP-MS at the FIERCE Laboratory, Goethe University Frankfurt (g–i). Zircon crystals HF-14 (b, e, h) and SI-5 (c, f, i), analyzed in this study, are from Craters of the Moon and the Blackfoot Volcanic Field, respectively. Instrument images (a, d) were provided by Janet Harvey; image (g) was provided by Axel Gerdes.*

3.4 Oxygen and hafnium isotopes in zircon determination and modelling

Oxygen isotope ($^{18}O/^{16}O$) analyses were carried out using the CAMECA ims 1280-HR at the Heidelberg Ion Probe Laboratory (Fig. 5d-f). A Cs^+ primary beam (1.0–1.6 nA, 10 µm raster) was employed to sputter negative secondary ions of ^{16}O and ^{18}O using a normal-incidence electron gun for charge compensation. Oxygen ions were simultaneously measured in multicollection mode, resulting in a ~10 × 10 µm wide and ~0.5 µm deep crater. Results are expressed in $\delta^{18}O$ notation relative to the Vienna Standard Mean Ocean Water (V-SMOW; Baertschi, 1976):

$$\delta^{18}\mathrm{O} = \left[\frac{\left(\frac{^{18}O}{^{16}O}\right)_{sample}}{\left(\frac{^{18}O}{^{16}O}\right)_{VSMOW}} - 1\right] \times 1000$$

Instrumental mass fractionation and drift were corrected using the zircon reference materials AS3 ($\delta^{18}O$ = +5.34 ‰; Trail et al., 2007) and 91500 ($\delta^{18}O$ = +9.86 ‰; Wiedenbeck et al., 2004), with analyses of 10–15 unknowns bracketed by standards. Analytical uncertainties were propagated by combining internal errors and the standard deviation of the bracketing reference zircon in quadrature.

Hafnium isotope ($^{176}Hf/^{177}Hf$) measurements in zircon were conducted at the FIERCE Laboratory, Goethe University Frankfurt, using a ThermoScientific NEPTUNE Plus MC-ICP-MS coupled to a RESOlution 193 nm ArF Excimer laser system equipped with an S155 two-volume ablation cell (Fig. 5g-i). Analytical protocols followed Gerdes and Zeh (2006, 2009). Ablation was performed with a 33 µm spot size, fluence of 3.5 J cm^{-2}, repetition rate of 5.2 Hz, and total ablation depth of ~23 µm. Instrumental mass bias was corrected using an exponential law with $^{179}Hf/^{177}Hf = 0.7325$, and Yb interference was corrected with a daily βHf/βYb factor of 1.080 (Gerdes & Zeh, 2009), which has remained stable over two decades. Data were normalized to the JMC475 Hf standard ($^{176}Hf/^{177}Hf$ = 0.282160), and uncertainties reflect both within-run precision and the long-term reproducibility of JMC475 (0.0028% 2σ, n = 8). Results are reported as εHf values using CHUR parameters of $^{176}Lu/^{177}Hf = 0.0336$ and $^{176}Hf/^{177}Hf = 0.282785$ (Bouvier et al., 2008):

$$\varepsilon\mathrm{Hf} = \left[\frac{\left(\frac{^{176}Hf}{^{177}Hf}\right)_{sample}}{\left(\frac{^{176}Hf}{^{177}Hf}\right)_{CHUR}} - 1\right] \times 1000$$

Initial ^{176}Hf/^{177}Hf and εHf values were calculated using SIMS-derived zircon ages from U-Th and U-Pb dating (see Section 3.2). Secondary zircon references GJ-1 (^{176}Yb/^{177}Hf < 0.008) and Temora 2 (^{176}Yb/^{177}Hf = 0.02–0.07) analyzed alongside unknowns showed repeatability of 0.6 and 0.8 εHf units (2σ) and were consistent with published values.

To interpret zircon isotopic data, δ^{18}O and εHf values were compared to compositional trends resulting from combined assimilation–fractional crystallization (AFC) models, applying the equations of DePaolo (1981):

$$\epsilon_m = \frac{\left(\frac{r}{r-1}\right)\frac{C_i^a}{z}\left(1-F^{-z}\right)\epsilon_a + C_i^{om}F^{-z}\,\epsilon_m^o}{\left(\frac{r}{r-1}\right)\frac{C_i^a}{z}\left(1-F^{-z}\right) + C_i^{om}F^{-z}}$$

Where ϵ_m is the isotopic composition of the magma, ϵ_m^o and ϵ_a are the initial isotopic compositions in the magma and in the wall rock respectively, C_i^{om} is the original concentration for a given element or oxide *i* in the magma and C_i^a for the assimilant, *F* is the melt fraction following a AFC interval, *r* is the ratio of the mass rate of assimilation to the mass rate of crystallization, and finally, the parameter *z* is calculated using the equation: $z = (r + D_i - 1)/(r - 1)$, where D_i refers to the bulk distribution coefficient of *i* between liquid and crystalline phases. Partition coefficients were also taken from the literature. Hafnium isotopic compositions in the magma are reasonably assumed to be identical to those in zircon because of the negligible mass difference in Hf isotopes. However, oxygen isotope zircon-melt equilibrium fractionation differs from unity, and therefore a compositionally based fractionation factor was applied (Trail et al., 2009).

3.5 Thermal-chemical modelling of zircon saturation in melt reservoirs open for recharge

The thermochemical modeling employed in this study is adapted from the methodology of Tierney et al. (2016), which simulates zircon age distributions in volcanic and plutonic systems by varying magma input rates over defined recharge intervals and durations. This approach is grounded in the recharge–assimilation–fractional crystallization framework of Spera and Bohrson (2001), and tracks magma and host rock temperatures within a 20 × 60 km (depth × width) crustal section at a 0.1 × 0.1 km grid resolution. A constant heat flux is applied at both the surface and base of the model domain. In the model, magma is injected into the central region of an ellipsoidal intrusion at a specified recharge rate while maintaining a fixed aspect ratio (height-to-width). As each injection occurs, the model tracks temperature changes in both the host rock and the magma, identifying cells that fall within the zircon crystallization window where the magma remains above the solidus, and zircon saturation is feasible.

Zircon crystallization is calculated within the grid zones and integrated over time, but only those cells retaining melt at supersolidus temperatures (>700 °C) are considered in the context of volcanic zircon records. Each simulation incorporates predefined initial parameters, including intrusion depth, recharge temperature, injection rate, and duration of the run. Resulting zircon crystallization ages are compiled and visualized as cumulative probability density functions (CPDFs), which are then compared to measured zircon age distributions for qualitative assessment (Fig. 6). These CPDFs offer insights into zircon crystallization histories and magma recharge dynamics. Additionally, the model estimates average eruption temperatures and melt volumes for each scenario. These outputs, alongside percentile-based age offsets, are used to further constrain and refine the modeling results.

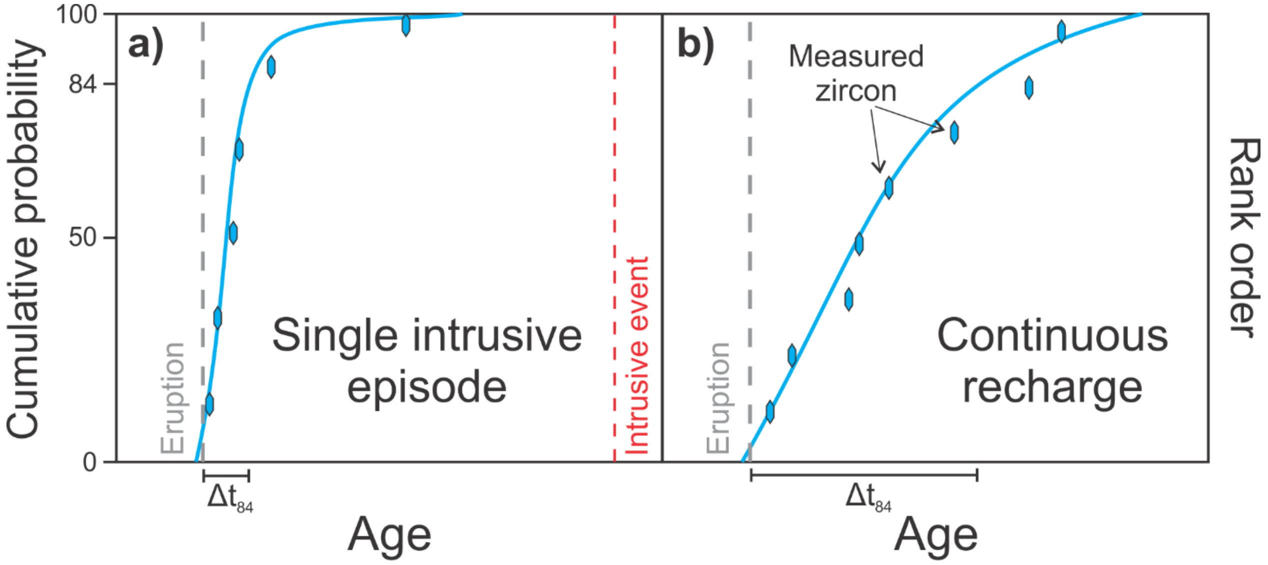

Fig. 6. *Schematic illustration of observed (zircon symbols) and modelled (solid lines) zircon crystallization age distributions for different magmatic scenarios: (a) A single, short-lived intrusive event yields a narrow zircon age distribution, as reflected by a brief offset between the 84th percentile age and the eruption age (Δt_{84}). (b) Prolonged zircon crystallization driven by recurrent melt injections causing sustained thermal conditions above the solidus. This results in broader Δt_{84}. age distributions than in scenario (a). Zircon age modelling thus provides unique insights into the longevity and recharge history of silicic magma reservoirs.*

4. Main results and discussions

Article 1 (Appendix I): Linking zircon crystallization to magmatic processes in basalt dominated lava fields: The Eastern Snake River Plain – Craters of the Moon testbed

The genesis and evolution of post Yellowstone hotspot track volcanism was explored using zircon from three of the most evolved Craters of the Moon (COM) basaltic trachyandesite lava flows and Quaternary rhyolite domes from the Eastern Snake River Plain (ESRP) in Idaho (USA). In particular, the occurrence of zircon in these COM intermediate flows has required an explanation, because zircon saturation in mafic magma dominated systems is unexpected. Hence, zircon crystals in mafic rocks are often interpreted as being xenocrystic, and therefore ignored as relevant indicators for the petrogenesis of the magmas that host them. Additionally, this study resolved to what extent crustal assimilation and fractional crystallization modified the isotopic and trace element signatures of erupted intermediate to silicic magmas which ultimately achieved zircon crystallization in the COM and ESRP volcanic fields. Petrogenesis of zircon in this area accurately recorded how assimilation and fractional crystallization processes operated differently within these two volcanic settings which share a genetic link to the same mafic parental magmas. Differences in zircon composition between these systems are attributed to magma evolution in a heterogeneous lithospheric architecture shaped by passage of the Yellowstone hotspot.

The autocrystic origin of COM zircon is being supported by a $6.2^{+2.6}_{-2.5}\ ka$ (MSWD = 1.30; n = 23) U-Th model age which is in good agreement with a Holocene 2.26 ± 0.58 ka eruption age. The lack of age differences between zircon rim and cores also suggest rapid growth prior to eruption. Only a small xenocrystic fraction was found within the lavas, which isotopically correspond to Archean zircon ages for a xenolith located within the COM lava field dated at 3,239 ± 15 Ma by U-Pb methods. U-Pb zircon ages obtained for the ESRP rhyolite domes range between 1,534 ± 22 ka and 335 ± 5 ka. These crystallization ages closely agree with literature K-Ar and $^{40}Ar/^{39}Ar$ eruption ages.

Zircon from COM lavas record a complex magmatic evolution, which is reflected in the εHf and $\delta^{18}O$ isotopic compositions. The AFC modeling suggests that COM magmas generated near the ESRP margin, where Archean crust persists, interacted with at least two distinct crustal components during ascent and storage. Zircon isotopic compositions require an early assimilation of lower crustal Archean rocks and a later magmatic overprinting by interaction with mid-crustal felsic wallrocks.

ESRP zircon trace element and isotope data consistently record crystallization in residual evolved melts. This aligns with existing models proposing differentiation in relatively isolated magma reservoirs developed along the Yellowstone hotspot track (e.g., McCurry et al., 2008). The close agreement between zircon trace element ratios (Eu/Eu*, Zr/Hf) and modeled fractionation paths supports an extensive closed-system fractional crystallization history. Furthermore, the low and invariant εHf and δ^{18}O values within each dome suggest that assimilation of altered, hydrothermally reworked crustal material occurred early in the magmatic evolution and was limited in scope. In contrast to magma evolution in the COM volcanic field, the ESRP rhyolite parents avoided interaction with Archean rocks, likely due to extensive reworking of the crust by the hotspot (Fig. 7).

The AFC modeling starts out with the same mantle derived mafic parent for both ESRP and COM magmatic systems, as proposed in the literature. These parental magmas then followed different crustal assimilation paths governed by the local crustal architecture (Fig. 7). Although zircon records crustal assimilation processes in both ESRP and COM fields, it is important to recall that the isotopic composition was already established prior to zircon saturation. Zircon petrochronology thus only presents snapshots of the final stages of the magmatic evolution, but with the capability to reveal important petrogenetic insights into the magmatic conditions prior to zircon saturation. This decoupling is particularly evident in the ESRP, where isotopic trends suggest early crustal interaction with low δ^{18}O rocks, yet zircon remains isotopically uniform within each dome, suggesting that crustal assimilation had ended by the time zircon became saturated in the magma.

Zircon saturation in both systems was ultimately possible only after extensive fractional crystallization which progressively increased the Zr concentrations in the magma. Zircon trace element concentrations support fractional crystallization with zircon forming at different F (remaining melt fraction) values in the COM and ESRP systems. COM zircon mostly crystallized in high-temperature, comparatively unevolved melts ($F > 0.5$), whereas ESRP zircon largely record crystallization in low-temperature, highly evolved melts (up to $F \approx 0.25$).

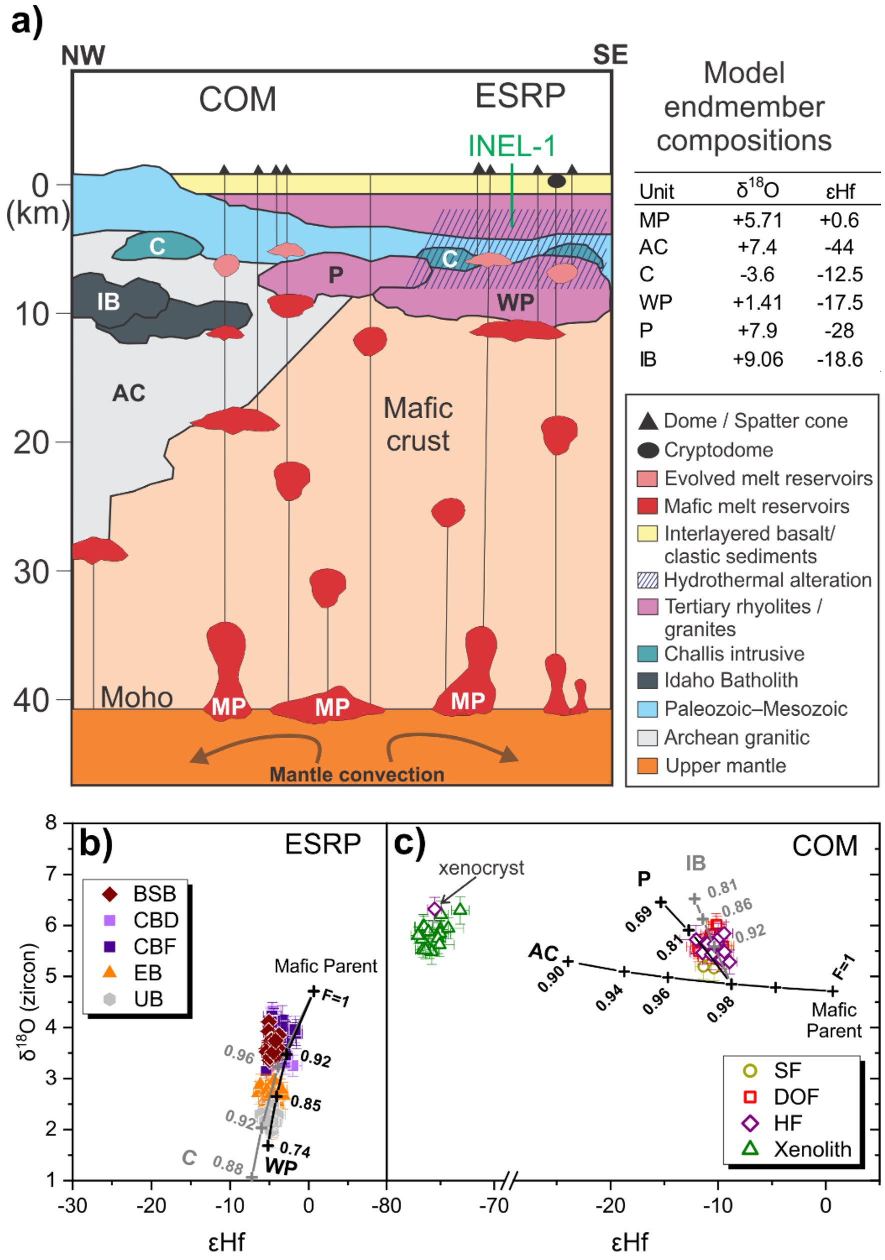

Model endmember compositions

Unit	$\delta^{18}O$	εHf
MP	+5.71	+0.6
AC	+7.4	-44
C	-3.6	-12.5
WP	+1.41	-17.5
P	+7.9	-28
IB	+9.06	-18.6

Fig. 7. *Petrogenetic model of the ESRP and COM magma systems. (a) Simplified conceptual model modified after McCurry et al. (2008) where mantel-derived magmas (MP) experienced extensive fractional crystallization and subsequently followed different crustal assimilation paths. (b-c). (b) Assimilation and fractional crystallization (AFC) models for ESRP Big Southern Butte (BSB), Cedar Butte Dome (CBD), Cedar Butte flows (CBF), East Butte (EB), and Unnamed Butte (UB). (c) AFC trends for COM Serrate, Devils Orchard (DOF) and Highway (HF) intermediate flows with an Archean xenolith from COM lava as representing a crustal endmember. Numbers along curves indicate the fraction of remaining melt (F).*

The anomalously high Zr concentrations in COM lavas compared to a global compilation of magma composition for large igneous provinces promoted zircon saturation at unusually high temperatures (~900 °C). The high Zr concentration levels were the result of multiple extensive fractional crystallization episodes involving mantle derive magmas which abnormally enriched the system in Zr. Although local saturation of zircon is also evident in COM lavas (where zircon is associated with olivine, clinopyroxene, ilmenite, and pyrite), it is also present in the matrix, demonstrating that in high Zr-melts, zircon saturation is feasible. Thus, not all zircon in such rocks is xenocrystic, and its presence is petrogenetically meaningful.

This study has demonstrated that integration of zircon petrochronology and whole-rock geochemistry across both the COM and ESRP volcanic fields provided a coherent picture of magma generation, evolution, and storage within two distinct but geodynamically linked settings. The key distinction between the COM and ESRP systems lies in the relative degrees and types of country rock assimilation, as well as the contrasting thermal and compositional evolution paths recorded by their zircon cargo.

Article 2 (Appendix II): A common magma source for plutonic and volcanic rocks of The Geysers geothermal field, California: volume and intrusive history derived from zircon

Zircon populations in volcanic and plutonic rocks can provide critical constraints on the thermal and chemical evolution of magmatic systems, yet the extent to which zircon can record a common magmatic history of cogenetic intrusive and extrusive rocks remains insufficiently resolved. In the Geysers-Cobb Mountain system (California, USA), the rare juxtaposition of a drilled subvolcanic pluton (the Geysers Plutonic Complex, GPC) and its overlying volcanic units (Cobb Mountain Volcanic Center, CMVC) offers a unique opportunity to investigate this link directly. Previous studies have suggested a genetic connection between GPC and CMVC magmas based on spatial association and overlapping zircon crystallization ages (e.g. Schmitt et al., 2003a, 2003b). However, key uncertainties persisted regarding the comparability of zircon age spectra with its geochemical signatures, the timing and extent of crystal recycling, and the dynamics of magma accumulation and differentiation within the shared magma reservoir. This study addressed these gaps by comparing trace element, εHf, and $\delta^{18}O$ isotopic compositions in zircon from volcanic and plutonic samples. Results were integrated with existing geochronological constraints to quantify crustal assimilation as well as the thermal evolution and recharge history of the GPC-CMVC magmatic system.

Zircon trace element and isotopic data presented in this study revealed that only zircon from two units of the GPC (classified as granite and granodiorite) match the compositional and isotopic signatures of volcanic zircons from CMVC units. Notably, zircon from another GPC intrusive unit, called the microgranite porphyry, displays distinct trace element and isotopic signatures. Although the younger granite and granodiorite units are genetically related to the earlier microgranite porphyry, there is limited antecrystic recycling potential. Similarly, zircon recycling from the microgranite porphyry was also undetected in younger volcanic rocks. The identification of two isotopically distinct zircon populations further refines concepts about the magma plumbing structure and indicates that significant heterogeneity existed even within individual intrusive units.

The progressive compositional evolution of zircon across CMVC and GPC units advocates fractional crystallization coupled with assimilation of crustal rocks as an important process governing magma composition. AFC modeling results provide new zircon-based evidence showing that early-stage magmas evolved at lower to mid-crustal depths via assimilation of the Franciscan greywacke complex, followed by upper crustal storage and episodic reheating. Zircon trace element abundances and low TiZr temperatures for the microgranite porphyry indicate that it originated from a highly differentiated melt, which represents an early, cooler stage of the upper crustal system that lacked sufficient thermal energy for significant crustal assimilation. In contrast, more evolved CMVC lavas contain highly crustally influenced zircon crystals which also match in composition those from the coeval granite and granodiorite plutons. This indicates late recharge events that efficiently remobilized thermally matured portions of the system (Fig. 8).

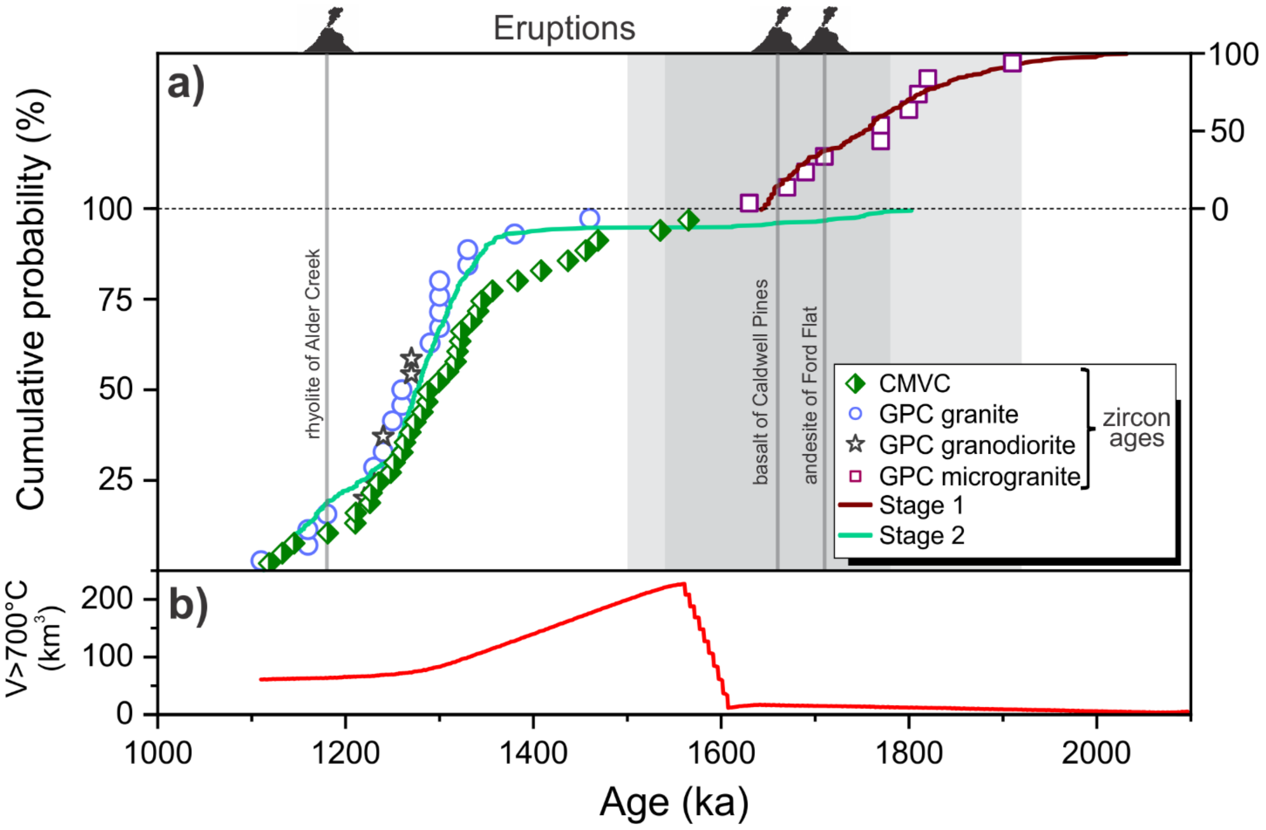

Fig. 8. *Age distributions for GPC and CMVC zircon (symbols) in comparison to predicted crystallization ages from a two-stage thermochemical model (solid lines) of the underlying magma intrusion. Gray lines and fields indicate regional eruption ages and uncertainties, respectively. a) Cumulative probability density function for zircon ages related to stage 1 of the model reproducing the microgranite porphyry zircon ages at low, steady-state magma recharge. Stage 2 involves rapid magma accumulation and subsequent cooling, which matches the zircon age distribution in cogenetic plutonic and volcanic rocks of the GCP and CMVC, respectively. b) Volume of magma above 700 °C during the GPC evolution indicating the rapid growth of the pluton at c. 1,600 ka.*

Zircon saturation thermal modeling supports the presence of a ~300 km³ intrusive body emplaced between 2 to 1.1 Ma, which was formed through a combination of steady-state and punctuated high-flux magma input (Fig. 8, 9). Additionally, the model indicates that the GPC is the upper crustal expression of a deeper, long-lived magmatic system at ~6 km. The model also suggests that GPC magma dominantly accumulated during a single high-flux episode at c. 1.6 Ma, which added up to 200 km^3 within ~50 ka to the intrusion. This high-flux event is consistent with the incorporation of significant amounts of country rock as indicated by a subpopulation of GPC-GMVC zircon crystallized with distinctly elevated $\delta^{18}O$ and more negative εHf values. Although the model geometry is conservative in terms of heat loss and volumetric estimates, it successfully reproduces the zircon age spectrum and compositional diversity found across both GPC and CMVC units. Furthermore, the model suggests that melt could have been preserved in deeper crustal regions for extended periods, allowing for zircon crystallization well beyond the emplacement and cooling timescale of the GPC itself. This persistent magmatic environment was facilitated by episodic small rejuvenation events (~0.1 km^3/a), some of which produced the late-stage volcanic activity observed in the CMVC. Ultimately, continued emplacement of small magma increments could also be responsible for the current geothermal anomaly at The Geysers. Our results also demonstrate that short-lived, high-flux episodes can be key drivers in the construction of large felsic magma bodies, consistent with time-transgressive volcanic activity observed in other Coast Range fields.

This study highlights the power of combining zircon geochemical and isotopic data with forward thermal modeling to reconstruct magmatic histories, including volume accumulation and recharge dynamics. Outstandingly, the Geysers-Cobb Mountain system provides a rare opportunity to test this integrative approach using both volcanic and plutonic samples, validating such models across different expressions of a magmatic system involving surface volcanic and subsurface plutonic rocks. The strong agreement between observed zircon data and model outputs demonstrates that this method can effectively constrain the longevity, flux variability, and architecture of magma reservoirs. Given that most studies rely solely on surface volcanic rocks, the validation of this model framework using both plutonic and volcanic endmembers of the magmatic spectrum offers a methodology for reconstructing subsurface magmatic processes in less accessible systems worldwide.

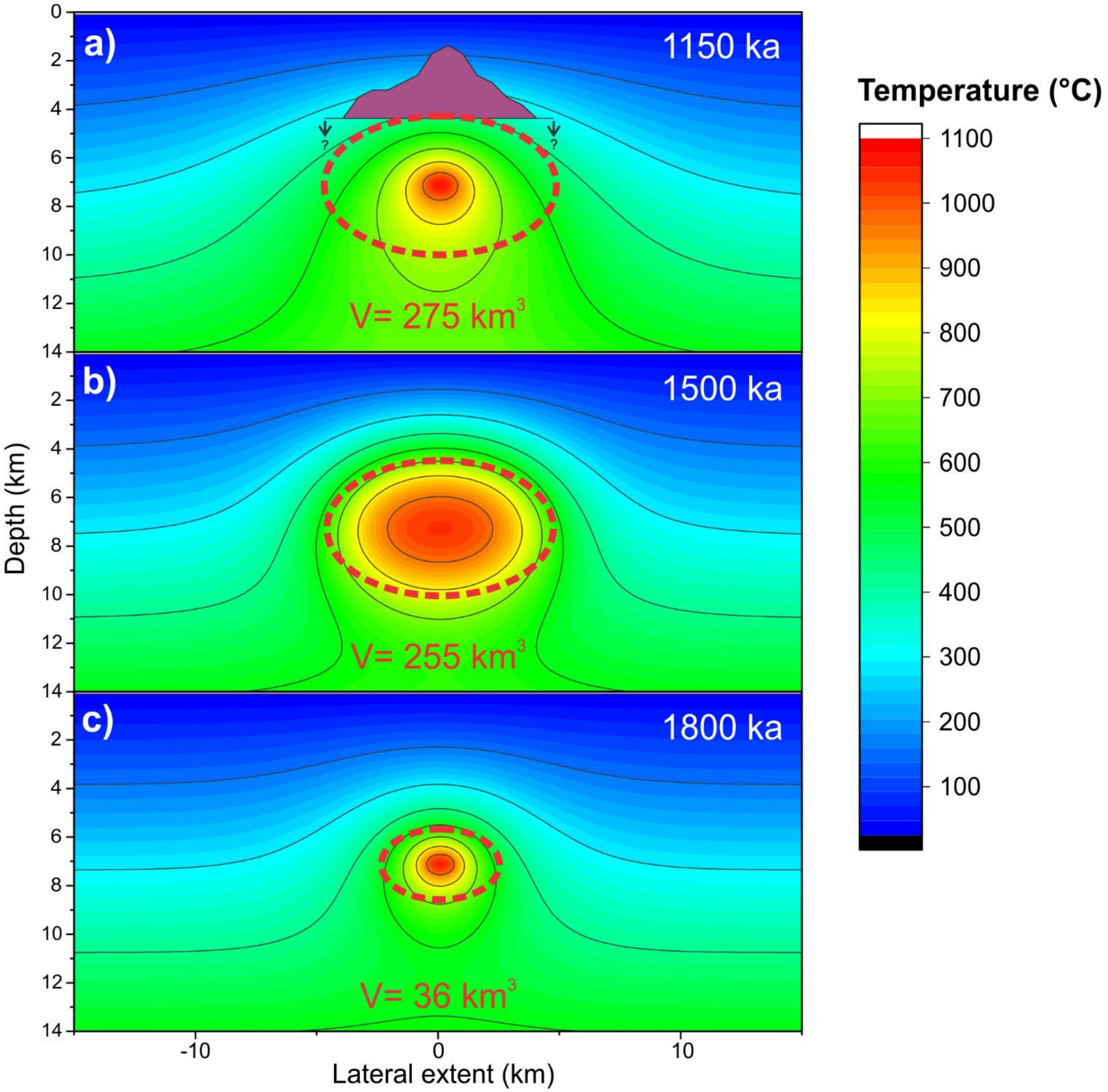

Fig. 9. *Modelled thermal evolution of the magma feeding the GPC-CMVC system at 1,150 (a), 1,500 (b) and 1,800 ka (c). Dashed lines represent the total intruded volume into the system at different times. Outline of the GPC in cross section as explored by geothermal drilling is shown for comparison in (a).*

Article 3 (Appendix III): Provenance and thermal evolution of rhyolite magma in the Blackfoot volcanic field

The Yellowstone-Snake River Plain bimodal magmatic province represents one of North America's most promising geothermal regions due to its high subsurface heat flow and association with young volcanism. Among these volcanic centers, the Blackfoot Volcanic Field (BVF) stands out as one of the youngest systems in the area, comprising Late Pleistocene eruptions of domes with an unusual composition referred to as topaz rhyolite (Ford, 2005). Moreover, two volumetric subsurface silicic intrusions have been recently inferred for the BVF based on gravity anomalies (Hastings et al., 2021). Despite its volcanic youth and magmatic activity, surface geothermal manifestations within the BVF are minimal, and drilling efforts have yet to encounter high-temperature geothermal fluids, raising critical questions about the viability of its geothermal resources. This study addressed this conundrum by applying zircon petrochronology using U-Th and U-Pb dating, trace element analysis, and isotopic compositions (O and Hf) to better constrain the thermal and temporal evolution of the magmatic system. The results were then used to generate a zircon saturation-based thermochemical model for the BVF that helps to reconcile the apparent lack of geothermal surface indicators with the evidence for persistent subsurface heat associated with magmatism.

The geochemical and isotopic compositions of BVF zircon suggest a mantle derived mafic parent. This is primarily reflected by $\delta^{18}O$ compositions similar to those found in mantle zircon. By contrast, zircon εHf compositions require significant assimilation of Archean country rocks by the parental magmas for the BVF rhyolites. Zircon $\delta^{18}O$ and εHf compositions clearly distinguish BVF rhyolites from other Yellowstone-Snake River Plain rhyolite magmas. Isotopic differences provide evidence that the BVF rhyolites are not simple derivatives of Yellowstone-Snake River Plain-like melts, but rather evolved independently through localized crustal processing. This agrees with literature data indicating that mafic to intermediate lavas in both regions exhibit isotopic variability reflecting different degrees of Archean crustal assimilation. This demonstrates that isotopic differences in these systems are the consequence of magma interaction with deep crustal rocks. The BVF rhyolites also inherited this variable Archean crustal influence on their parental magmas. This is consistent with homogeneous zircon isotopic signatures within each BVF dome revealing crustal assimilation prior to shallow differentiation to a zircon-saturated rhyolite magma.

Zircon trace element modeling further reveals that the rhyolite magmas underwent extreme, near-eutectic fractional crystallization in a dominantly closed system. This process occurred after the isotopic composition was established. The absence of antecrysts together with the isotopic compositions advocate at least two different magmatic systems where the fractionation occurred before eruptive mobilization. Compared to zircon data for rhyolites from the Yellowstone-Snake River Plain and Tertiary-Quaternary topaz rhyolites within the Great Basin, the BVF zircon population is distinguished by different evolutionary trends in elements like Zr, Hf, Th, U and REEs indicating also highly fractionated melt compositions. Some mismatches with the fractional crystallization trends are attributed to model simplifications, where only apatite, zircon and thorite were considered as minor and accessory phases. These simplifications were unavoidable because of the absence of published partitioning coefficients for other accessory minerals which potentially influence REE fractionation such as clinofergusonite-(Y) identified in heavy mineral separates.

Fractional crystallization modeling also indicates extensive fractional crystallization where F (remaining melt fraction) values as low as 0.02 are required to reproduce the trace element compositions of zircon in BVF domes. This extreme fractional crystallization has also been documented for Yellowstone zircon, where trace element patterns indicate up to 99.9% crystallization (e.g., Troch et al., 2018). A key implication of these models is that zircon crystallized in an almost completely solidified magma. Although this is consistent with inclusion-rich, CL-dark textures found in BVF zircon, it is on first sight difficult to reconcile with the crystal-poor nature of the erupted BVF rhyolite domes. The presence of mafic enclaves within the domes, however, supports a preeruptive rejuvenation of this nearly completely solidified intrusive body causing magmatic reheating, which facilitated the subsequent eruption.

Thermochemical modeling of a magma reservoir as constrained by zircon crystallization ages, indicates that 120 km^3 of trachyandesite magma was emplaced at 6 km depth around 95 ka (Fig. 10). This scenario reasonably reproduces both the measured zircon age offset, and magma crystallization temperature as estimated by the Ti-in-zircon geothermometer (Ferry and Watson, 2007). Additionally, the model reservoir retains sufficient eruptible magma at the time of eruption to produce the total erupted volume alongside the inferred silicic intrusion. The best-fit thermal model also predicts a significant modern-day thermal anomaly extending to accessible drilling depths (0–4 km), with temperatures exceeding 300 °C at 4 km depth directly above the former magma reservoir (Fig. 11). However, this potential geothermal signature is absent at the surface, and in the Hubbard-25-1 exploration well nearby, which yielded only relatively low-temperature (~96 °C) fluids. This suggests that modern geothermal gradients may be obscured by regional hydrological conditions, including groundwater circulation, heat advection along regional fault structures, and thermal insulation from thick basaltic cover sequences.

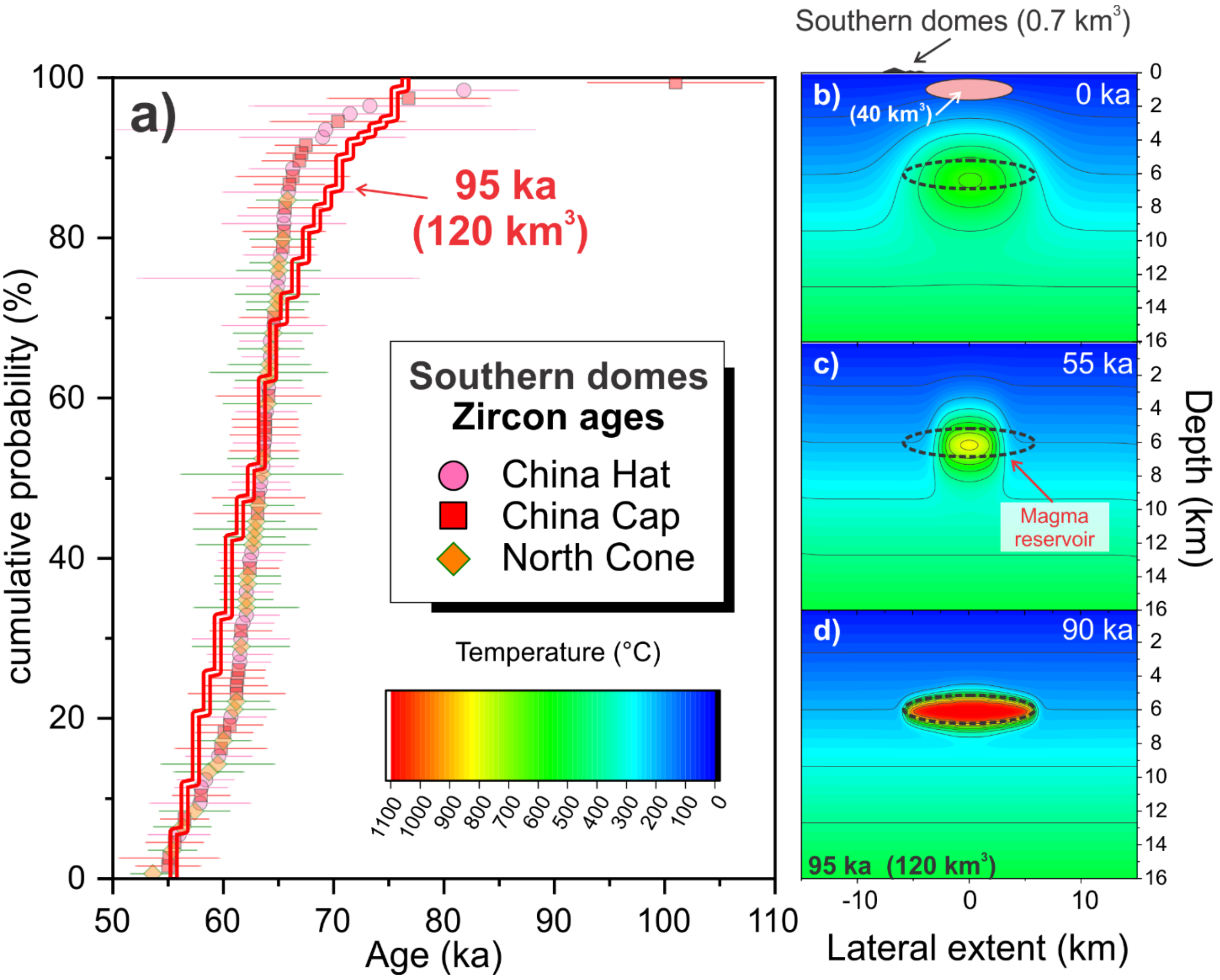

Fig. 10. *Thermochemical model design for the BVF geothermal system. (a) Zircon age distribution for the BVF southern domes (symbols) and cumulative probability of modeled ages from the best-fit model (solid line). The preferred model prescribes a single recharge event of 120 km*^{3} *of melt at 6 km depth. Thermal conditions of the magma reservoir and the surrounding country rock at present-day (b), at 55 ka prior to eruption (c) and immediately after magma reservoir filling (d).*

Overall, integrated zircon geochemistry and thermochemical modeling paint a picture of a still thermally potent, but likely inactive magma system beneath the southern BVF. Although the magma reservoir appears to have fully crystallized, its thermal legacy could still influence the crustal heat budget. However, the muted surface expression of geothermal activity emphasizes the importance of regional structural and hydrogeologic controls in determining whether deep-seated magmatic heat translates into viable geothermal resources at drillable depths.

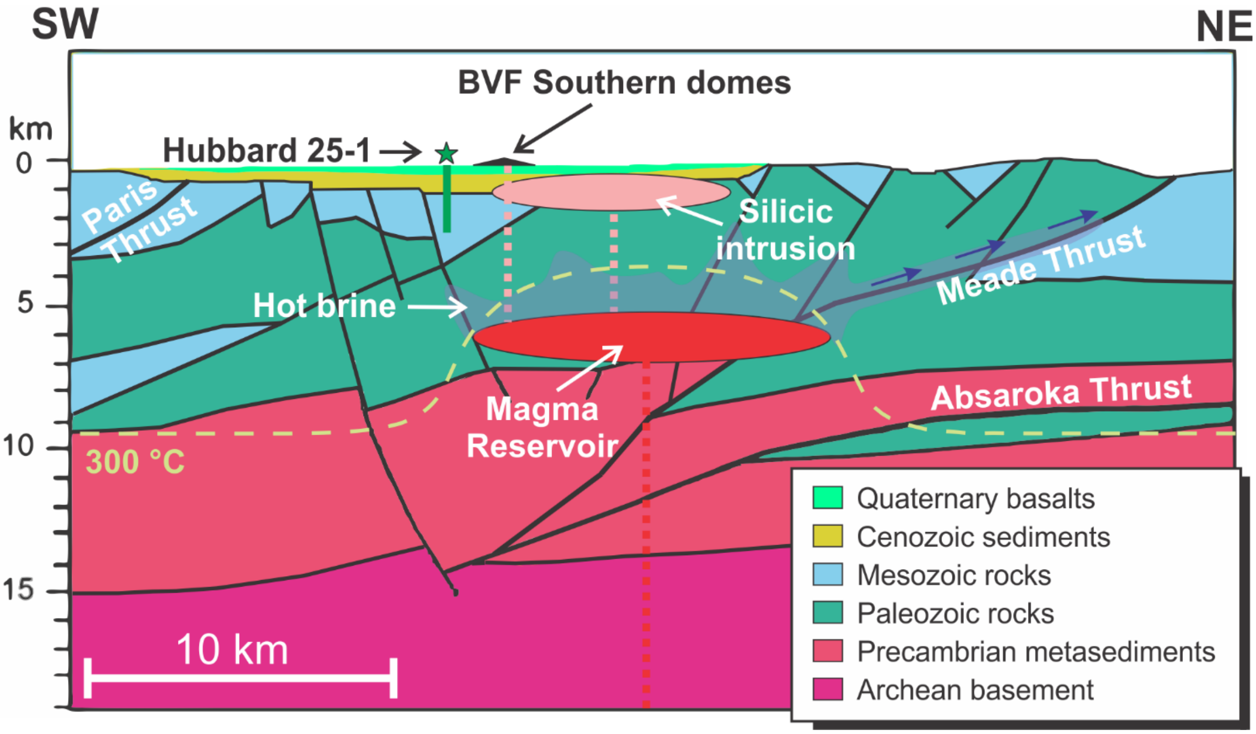

Fig. 11. *Conceptual model of the modern geothermal system within the BVF (after Welhan et al., 2014). An ~120 km^3 upper crustal magma reservoir emplaced at ~6 km depth is inferred to have supplied magma for an ~40 km^3 silicic intrusion (Hastings et al., 2021) and the eruption of three rhyolite domes at 55 ka. Ongoing heat loss from the former magma reservoir generates an elevated geothermal gradient predicted to exceed 300 °C at ~4 km depth (isotherm overlain from the conductive heat transport model shown in Fig. 10b). Blue arrows indicate the circulation of hot geothermal brines above the cooling reservoir. Fluids are possibly diluted and laterally diverted northeastward along structurally controlled permeable zones within overthrusted basement rocks. Vertical dashed lines symbolize magma ascent pathways interconnecting deeper and shallower magmatic systems as well as near-surface intrusions and the rhyolite domes. Geothermal exploration well Hubbard 25-1 is shown for comparison.*

5. Conclusions

This cumulative dissertation demonstrates the critical role of zircon petrochronology when studying the temporal and thermal evolution of intermediate to silicic magmatic systems. Zircon geochronology also has important implications for quantifying igneous processes and for applied geothermal exploration. Across these three case studies, zircon age spectra, $\delta^{18}O$ and εHf isotopic compositions, as well as trace element data have shown their importance for constraining the timescales of magma storage, differentiation, and eruption. These data also refined the previous concepts about the architecture and longevity of upper crustal magma reservoirs. Through a combination of high-temporal resolution geochronology in a petrological context and thermochemical modeling, zircon emerges not merely as a chronological tool but as a multi-dimensional proxy for understanding subvolcanic processes.

Although zircon is typically associated with evolved, silica-rich magmas, results from this study demonstrate that under specific geochemical conditions, particularly were Zr becomes enriched in the melt through extensive differentiation, zircon can achieve saturation in magmatic environments dominated by mafic melts. The occurrence of zircon in such settings, as shown for the basaltic trachyandesitic magmas investigated from the Craters of the Moon volcanic field, highlights the importance of considering zircon in basaltic and intermediate rocks as potentially autocrystic. Hence, their presence can provide valuable insights into the thermal and compositional evolution of magma, should be systematically evaluated in geochronological and petrogenetic interpretations, even in low-SiO_2 magmatic environments.

The exceptional geological context of active geothermal fields like The Geysers, where both deep drill core and surficial volcanic rocks are accessible, has provided unique opportunities to link geochemical models with direct observations on zircon geochemistry and ages. The second article highlights the need to harness this context for calibrating and validating zircon-saturation thermochronological modeling as a tool to investigate the magmatic evolution and heat transport of volcanic systems. Such sites serve as natural laboratories for testing the fidelity of zircon-based reconstructions of reservoir histories and long-term magmatic behavior.

Furthermore, zircon records from the three investigated volcanic systems show that magmas evolve over different timescales, with zircon crystallization preceding eruption by thousands to hundreds of thousands of years. The temporal decoupling between zircon growth and eruptive activity reveals differences in the longevity of subvolcanic magma bodies, where crystallization histories are shaped by episodic recharge, thermal insulation, and storage at near-solidus conditions. Such insights are key in redefining the understanding of active magmatic systems, particularly those without historic eruptions but with zircon records suggesting sustained magmatic activity.

These findings have also a direct relevance for geothermal exploration. When measured zircon age offsets (Δt values) are integrated with thermochemical models, important inferences can result regarding the longevity, size, and thermal state of magma reservoirs at the time of eruption and, by extension, the present-day thermal structure of the crust. In the case of the BVF, for instance, the best-fit model that reproduces zircon age distributions also predicts relatively elevated crustal temperatures at geothermal drilling depths, suggesting residual thermal anomalies even in the absence of obvious surface manifestations. This highlights the potential of zircon petrochronology as a geothermal exploration tool, which is unique in recording magmatic crystallization conditions. This not only reveals when magmas became emplaced, but also whether magma was sufficiently voluminous, hot, and shallow to influence the modern geothermal gradient. These attributes are particularly valuable in hidden geothermal systems where traditional geophysical or fluid-gas geochemical indicators are ambiguous or absent.

Zircon petrochronology is a cornerstone in modern volcanological and geothermal studies. By linking geochronology, petrology, and thermal modeling, it offers a robust framework for characterizing magmatic systems with implications far beyond eruptive histories. Together, this information ultimately helps in the identification of geothermal targets that might otherwise remain undetected and assessing their potential with greater confidence. As such, zircon serves not only as a recorder of magmatic histories, but as a predictive tool for geothermal exploration.

6. References

Anders, M. H., DiVenere, V. J., Hemming, S. R. & Gombiner, J. (2019). ^{40}Ar/^{39}Ar and paleomagnetic constraints on the age and areal extent of the Picabo volcanic field: Implications for the Yellowstone hotspot. *Geosphere* **15**, 716-735.

Armstrong, R. L., Leeman, W. P. & Malde, H. E. (1975). K--Ar dating quaternary and Neogene volcanic rocks of the Snake River Plain, Idaho. *Am. J. Sci.;(United States)* **275**.

Baertschi, P. (1976). Absolute ^{18}O content of standard mean ocean water. *Earth and Planetary Science Letters* **31(3)**, 341-344.

Bea, F., Bortnikov, N., Cambeses, A., Chakraborty, S., Molina, J., Montero, P., Morales, I., Silantiev, S. & Zinger, T. (2022). Zircon crystallization in low-Zr mafic magmas: Possible or impossible? *Chemical Geology* **602**, 120898.

Bindeman, I. (2008). Oxygen isotopes in mantle and crustal magmas as revealed by single crystal analysis. *Reviews in Mineralogy and Geochemistry*, **69(1)**, 445-478.

Bindeman, I. & Simakin, A. (2014). Rhyolites—Hard to produce, but easy to recycle and sequester: Integrating microgeochemical observations and numerical models. *Geosphere* **10**, 930-957.

Black, L. P., Kamo, S. L., Allen, C. M., Davis, D. W., Aleinikoff, J. N., Valley, J. W., Mundil, R., Campbell, I. H., Korsch, R. J. & Williams, I. S. (2004). Improved ^{206}Pb/^{238}U microprobe geochronology by the monitoring of a trace-element-related matrix effect; SHRIMP, ID–TIMS, ELA–ICP–MS and oxygen isotope documentation for a series of zircon standards. *Chemical Geology* **205**, 115-140.

Boehnke, P., Watson, E. B., Trail, D., Harrison, T. M. & Schmitt, A. K. (2013). Zircon saturation re-revisited. *Chemical Geology* **351**, 324-334.

Bonnichsen, B., Leeman, W. P., Honjo, N., McIntosh, W. C. & Godchaux, M. M. (2008). Miocene silicic volcanism in southwestern Idaho: geochronology, geochemistry, and evolution of the central Snake River Plain. *Bulletin of Volcanology* **70**, 315-342.

Borisov, A. & Aranovich, L. (2019). Zircon solubility in silicate melts: New experiments and probability of zircon crystallization in deeply evolved basic melts. *Chemical Geology* **510**, 103-112.

Bouvier, A., Vervoort, J. D. & Patchett, P. J. (2008). The Lu–Hf and Sm–Nd isotopic composition of CHUR: constraints from unequilibrated chondrites and implications for the bulk composition of terrestrial planets. *Earth and Planetary Science Letters* **273**, 48-57.

Carley, T. L., Miller, C. F., Wooden, J. L., Padilla, A. J., Schmitt, A. K., Economos, R. C., Bindeman, I. N. & Jordan, B. T. (2014). Iceland is not a magmatic analog for the Hadean: Evidence from the zircon record. *Earth and Planetary Science Letters*, **405**, 85-97.

Caricchi, L., Simpson, G. & Schaltegger, U. (2014). Zircons reveal magma fluxes in the Earth's crust. *Nature* **511**, 457-461.

Caricchi, L., Simpson, G. & Schaltegger, U. (2016). Estimates of volume and magma input in crustal magmatic systems from zircon geochronology: the effect of modeling assumptions and system variables. *Frontiers in Earth Science* **4**, 48.

Colón, D. P., Bindeman, I. N., Wotzlaw, J.-F., Christiansen, E. H. & Stern, R. A. (2018). Origins and evolution of rhyolitic magmas in the central Snake River Plain: insights from coupled high-precision geochronology, oxygen isotope, and hafnium isotope analyses of zircon. *Contributions to Mineralogy and Petrology* **173**, 1-18

Cherniak, D. J. & Watson, E. B. (2003). Diffusion in zircon. *Reviews in Mineralogy and Geochemistry* **53**, 113-143

Crisp, L. J. & Berry, A. J. (2022). A new model for zircon saturation in silicate melts. *Contributions to Mineralogy and Petrology* **177**, 71, https://doi.org/10.1007/s00410-022-01925-6.

Dalrymple, G.B., Grove, M., Lovera, O.M., Harrison, T.M., Hulen, J.B. and Lanphere, M.A. (1999) Age and thermal history of the Geysers plutonic complex (felsite unit), Geysers geothermal field, California: a ^{40}Ar/^{39}Ar and U–Pb study. *Earth and Planetary Science Letters* **173**, 285-298.

Dincer, I., & Acar, C. (2015). A review on clean energy solutions for better sustainability. *International journal of energy research*, **39(5)**, 585-606.

Drew, D. L., Bindeman, I. N., Watts, K. E., Schmitt, A. K., Fu, B. & McCurry, M. (2013). Crustal-scale recycling in caldera complexes and rift zones along the Yellowstone hotspot track: O and Hf isotopic evidence in diverse zircons from voluminous rhyolites of the Picabo volcanic field, Idaho. *Earth and Planetary Science Letters* **381**, 63-77.

Elders, W. A., Bird, D. K., Williams, A. E., & Schiffman, P. (1984). Hydrothermal flow regime and magmatic heat source of the Cerro Prieto geothermal system, Baja California, Mexico. *Geothermics*, **13(1-2)**, 27-47.

Ellis, B., Wolff, J., Boroughs, S., Mark, D., Starkel, W. & Bonnichsen, B. (2013). Rhyolitic volcanism of the central Snake River Plain: a review. *Bulletin of Volcanology* **75**, 1-19.

Ferry, J. & Watson, E. (2007). New thermodynamic models and revised calibrations for the Ti-in-zircon and Zr-in-rutile thermometers. *Contributions to Mineralogy and Petrology* **154**, 429-437.

Ford, M. T. (2005). The petrogenesis of quaternary rhyolite domes in the bimodal Blackfoot volcanic field, Southeastern Idaho. MSc thesis Idaho State University. 133 p.

Friedrichs, B., Schmitt, A. K., Lovera, O. M. & Atıcı, G. (2021). Zircon as a recorder of contrasting magma recharge and eruptive recurrence patterns. *Earth and Planetary Science Letters* **571**, 117104.

Gerdes, A. & Zeh, A. (2006). Combined U–Pb and Hf isotope LA-(MC-) ICP-MS analyses of detrital zircons: comparison with SHRIMP and new constraints for the provenance and age of an Armorican metasediment in Central Germany. *Earth and Planetary Science Letters* **249**, 47-61.

Gerdes, A. & Zeh, A. (2009). Zircon formation versus zircon alteration—new insights from combined U–Pb and Lu–Hf in-situ LA-ICP-MS analyses, and consequences for the interpretation of Archean zircon from the Central Zone of the Limpopo Belt. *Chemical Geology* **261**, 230-243.

Ghiorso, M. S. & Evans, B. W. (2008). Thermodynamics of rhombohedral oxide solid solutions and a revision of the Fe-Ti two-oxide geothermometer and oxygen-barometer. *American Journal of science* **308**, 957-1039.

Grimes, C. B., John, B. E., Kelemen, P., Mazdab, F., Wooden, J., Cheadle, M. J., Hanghøj, K. & Schwartz, J. (2007). Trace element chemistry of zircons from oceanic crust: A method for distinguishing detrital zircon provenance. *Geology* **35**, 643-646.

Grimes, C. B., Ushikubo, T., John, B. E. & Valley, J. W. (2011). Uniformly mantle-like $\delta^{18}O$ in zircons from oceanic plagiogranites and gabbros. *Contributions to Mineralogy and Petrology* **161**, 13-33.

Hanchar, J. M., & Hoskin, P. W. (2003). Zircon: Reviews in mineralogy and geochemistry. *Mineralogical Society of America*, **53**, 500.

Hastings, M. S., Connor, C., Wetmore, P., Malservisi, R., Connor, L., Rodgers, M. & La Femina, P. C. (2021). Large-Volume and Shallow Magma Intrusions in the Blackfoot Reservoir Volcanic Field (Idaho, USA). *Journal of Geophysical Research: Solid Earth* **126**, e2021JB022507.

Henry, C. D., Castor, S. B., Starkel, W. A., Ellis, B. S., Wolff, J. A., Laravie, J. A., McIntosh, W. C. & Heizler, M. T. (2017). Geology and evolution of the McDermitt caldera, northern Nevada and southeastern Oregon, western USA. *Geosphere* **13**, 1066-1112.

Kemp, A.I.S., Hawkesworth, C.J., Foster, G.L., Paterson, B.A., Woodhead, J.D., Hergt, J.M., Gray, C.M. and Whitehouse, M.J. (2007) Magmatic and crustal differentiation history of granitic rocks from Hf-O isotopes in zircon. Science, 315(5814), 980-983.

Liu, P.-P., Caricchi, L., Chung, S.-L., Li, X.-H., Li, Q.-L., Zhou, M.-F., Lai, Y.-M., Ghani, A. A., Sihotang, T. & Sheldrake, T. E. (2021). Growth and thermal maturation of the Toba magma reservoir. *Proceedings of the National Academy of Sciences* **118**, e2101695118.

Lukács, R., Harangi, S., Guillong, M., Bachmann, O., Fodor, L., Buret, Y., Dunkl, I., Sliwinski, J., von Quadt, A. & Peytcheva, I. (2018). Early to Mid-Miocene syn-extensional massive silicic volcanism in the Pannonian Basin (East-Central Europe): Eruption chronology, correlation potential and geodynamic implications. *Earth-science reviews* **179**, 1-19.

McCurry, M., Hayden, K. P., Morse, L. H. & Mertzman, S. (2008). Genesis of post-hotspot, A-type rhyolite of the Eastern Snake River Plain volcanic field by extreme fractional crystallization of olivine tholeiite. *Bulletin of Volcanology* **70**, 361-383.

McCurry, M. & Rodgers, D. W. (2009). Mass transfer along the Yellowstone hotspot track I: Petrologic constraints on the volume of mantle-derived magma. *Journal of Volcanology and Geothermal Research* **188**, 86-98.

Melnik, O. E., Utkin, I. S. & Bindeman, I. N. (2021). Magma chamber formation by dike accretion and crustal melting: 2D thermo-compositional model with emphasis on eruptions and implication for zircon records. *Journal of Geophysical Research: Solid Earth* **126**, e2021JB023008.

Peacock, J.R., Earney, T.E., Mangan, M.T., Schermerhorn, W.D., Glen, J.M., Walters, M. and Hartline, C. (2020) Geophysical characterization of the Northwest Geysers geothermal field, California. *Journal of Volcanology and Geothermal Research* **399**, 106882.

Pearce, N. J., Perkins, W. T., Westgate, J. A., Gorton, M. P., Jackson, S. E., Neal, C. R. & Chenery, S. P. (1997). A compilation of new and published major and trace element data for NIST SRM 610 and NIST SRM 612 glass reference materials. *Geostandards newsletter* **21**, 115-144.

Pierce, K. L. & Morgan, L. A. (1992). The track of the Yellowstone hot spot: Volcanism, faulting, and uplift. In: Link, P.K., Kuntz, M.A. & Platt, L. (eds.) Regional Geology of Eastern Idaho and Western Wyoming, *Geological Society of America Memoir* **179**, 1-53.

Ratschbacher, B. C., Keller, C. B., Schoene, B., Paterson, S. R., Anderson, J. L., Okaya, D., Putirka, K. & Lippoldt, R. (2018). A new workflow to assess emplacement duration and melt residence time of compositionally diverse magmas emplaced in a sub-volcanic reservoir. *Journal of Petrology* **59**, 1787-1809.

Rojas-Agramonte, Y., Kaus, B. J., Piccolo, A., Williams, I. S., Gerdes, A., Wong, J., Xie, H., Buhre, S., Toukkeridis, T., Montero, P. & Garcia-Casco, A. (2022). Zircon dates long-lived plume dynamics in oceanic islands. *Geochemistry, Geophysics, Geosystems*, **23(11)**, e2022GC010485.

Schmitt, A.K., Grove, M., Harrison, T.M., Lovera, O., Hulen, J. and Walters, M. (2003a) The Geysers-Cobb Mountain Magma System, California (Part 1): U-Pb zircon ages of volcanic rocks, conditions of zircon crystallization and magma residence times. *Geochimica et Cosmochimica Acta* **67**, 3423-3442.

Schmitt, A.K., Grove, M., Harrison, T.M., Lovera, O., Hulen, J. and Walters, M. (2003b) The Geysers-Cobb Mountain Magma System, California (Part 2): Timescales of pluton emplacement and implications for its thermal history. *Geochimica et Cosmochimica Acta* **67**, 3443-3458.

Schmitt, A. K. (2011). Uranium series accessory crystal dating of magmatic processes. *Annual Review of Earth and Planetary Sciences* **39**, 321-349.

Schmitt, A. K., Klitzke, M., Gerdes, A. & Schäfer, C. (2017). Zircon hafnium–oxygen isotope and trace element petrochronology of intraplate volcanic rocks from the Eifel (Germany) and implications for mantle versus crustal origins of zircon megacrysts. *Journal of Petrology* **58**, 1841-1870.

Schmitt, A. K., Sliwinski, J., Caricchi, L., Bachmann, O., Riel, N., Kaus, B. J. P., Cisneros de Léon, A., Cornet, J., Friedrichs, B. & Lovera, O. (2023). Zircon age spectra to quantify magma evolution. *Geosphere* **19**, 1006-1031.

Shervais, J. W., Branney, M. J., Geist, D. J., Hanan, B. B., Hughes, S., Prokopenko, A. A. & Williams, D. F. (2006). HOTSPOT: the Snake River scientific drilling project–Tracking the Yellowstone Hotspot through space and time. *Scientific Drilling* **3**, 56-57.

Smith, R. B. & Braile, L. W. (1994). The yellowstone hotspot. *Journal of Volcanology and Geothermal Research* **61**, 121-187.

Spera, F. J. & Bohrson, W. A. (2001). Energy-constrained open-system magmatic processes I: General model and energy-constrained assimilation and fractional crystallization (EC-AFC) formulation. *Journal of Petrology* **42**, 999-1018.

Tierney, C. R., Schmitt, A. K., Lovera, O. M. & de Silva, S. L. (2016). Voluminous plutonism during volcanic quiescence revealed by thermochemical modeling of zircon. *Geology* **44**, 683-686.

Trail, D., Bindeman, I. N., Watson, E. B., & Schmitt, A. K. (2009). Experimental calibration of oxygen isotope fractionation between quartz and zircon. *Geochimica et Cosmochimica Acta*, **73(23)**, 7110-7126.

Troch, J., Ellis, B. S., Schmitt, A. K., Bouvier, A.-S. & Bachmann, O. (2018). The dark side of zircon: textural, age, oxygen isotopic and trace element evidence of fluid saturation in the subvolcanic reservoir of the Island Park-Mount Jackson Rhyolite, Yellowstone (USA). *Contributions to Mineralogy and Petrology* **173**, 1-17.

Valley, J. W., Bindeman, I. N., & Peck, W. H. (2003). Empirical calibration of oxygen isotope fractionation in zircon. *Geochimica et Cosmochimica Acta*, **67(17)**, 3257-3266.

Valley, J., Lackey, J., Cavosie, A., Clechenko, C., Spicuzza, M., Basei, M. A. S., Bindeman, I., Ferreira, V., Sial, A. N. & King, E. (2005). 4.4 billion years of crustal maturation: oxygen isotope ratios of magmatic zircon. *Contributions to Mineralogy and Petrology* **150**, 561-580.

Watson, E. B. & Harrison, T. M. (1983). Zircon saturation revisited: temperature and composition effects in a variety of crustal magma types. *Earth and Planetary Science Letters* **64**, 295-304.

Wiedenbeck, M., Alle, P., Corfu, F., Griffin, W. L., Meier, M., Oberli, F. v., Quadt, A. v., Roddick, J. & Spiegel, W. (1995). Three natural zircon standards for U-Th-Pb, Lu-Hf, trace element and REE analyses. *Geostandards newsletter* **19**, 1-23.

Wiedenbeck, M., Hanchar, J. M., Peck, W. H., Sylvester, P., Valley, J., Whitehouse, M., Kronz, A., Morishita, Y., Nasdala, L. & Fiebig, J. (2004). Further characterisation of the 91500 zircon crystal. *Geostandards and Geoanalytical Research* **28**, 9-39.

Williams, C. F., Reed, M. J., Mariner, R. H., DeAngelo, J. & Galanis, S. P. (2008). Assessment of moderate-and high-temperature geothermal resources of the United States. *U.S. Geological Survey.* **2008-3082** 4 p.

Wohletz, K., & Heiken, G. (1992). Volcanology and geothermal energy (Vol. 432). Berkeley: University of California Press.

Financial support

This thesis was financially supported by the Deutsche Forschungsgemeinschaft (DFG) - Project number 429859409

Declaration of generative AI and AI-assisted technologies in the writing process.

During the preparation of this work, ChatGPT (by OpenAI) was used to improve readability and check for grammar and language issues within the text.

Appendix

Formblatt Kumulative Dissertation Stand 14.02.2023

1. **Publikation/*Publication*:**

   Vollständige bibliographische Referenz/*Complete bibliographic reference:*

   Angeles-De La Torre, C. A., Schmitt, A. K., Lovera, O. M., Gassert, H., Gerdes, A. & Harvey, J. C. (2023). A common magma source for plutonic and volcanic rocks of the Geysers geothermal field, California: Volume and intrusive history derived from zircon. Chemical Geology 624, 121414

2. Erst- oder gleichberechtigte Autorenschaft/*First or equal authorship:* Ja/*Yes* ☑ Nein/*No* ☐

3. Veröffentlicht/*Published* ☑ Zur Veröffentlichung akzeptiert/*Accepted* ☐

   *Q1/Q2**: Ja/*Yes* ☑ Nein/*No* ☐

   **SCImago Journal Rank (SJR) indicator*

   Im Erscheinungsjahr oder im letzten verfügbaren Vorjahr/*In the year of publication or the last prior year available:* 2023

   Eingereicht/*Submitted* ☐ Noch nicht eingereicht/*Not yet submitted* ☐

4. **Beteiligungen/*Contributions*****

Contributor Role	Doktorand/in/ *Doctoral student*	Co-Autor/in 1/ *Co-author 1*	Co-Autor/in 2/ *Co-author 2*
Name, first name	Angeles De La Torre Carlos A.	Schmitt Axel K.	Harvey Janet
Methodology	☑	☐	☐
Software	☐	☐	☑
Validation	☑	☑	☐
Formal analysis	☑	☑	☐
Investigation	☑	☐	☐
Resources	☐	☑	☐
Data Curation	☑	☑	☐
Writing-Original Draft	☑	☐	☐
Writing-Review&Editing	☑	☑	☑
Visualization	☑	☐	☑
Supervision	☐	☑	☐
Project administration	☐	☑	☐
Funding acquisition	☐	☑	☐

*****Kategorien des CRediT (Contributor Roles Taxonomy, https://credit.niso.org/)***

Hiermit bestätige ich, dass alle obigen Angaben korrekt sind/*I confirm that all declarations made above are correct.*

Unterschrift/*Signature* ________________ A. K. ________________ Janet Harvey ________________

Doktorand/in/*Doctoral student* Co-Autor/in 1/*Co-author 1* Co-Autor/in 2/*Co-author 2*

Betreuungsperson/*Supervisor:*

Hiermit bestätige ich, dass alle obigen Angaben korrekt sind und dass die selbstständigen Arbeitsanteile des/der Doktoranden/in an der aufgeführten Publikation hinreichend und signifikant sind/*I confirm that all declarations made above are correct and that the doctoral student's independent contribution to this publication is significant and sufficient to be considered for the cumulative dissertation.*

Prof. Dr. Axel K. Schmitt A. K. 29/05/2025

Name/*Name* Unterschrift/*Signature* Datum/*Date*

Appendix I

A common magma source for plutonic and volcanic rocks of The Geysers geothermal field, California: volume and intrusive history derived from zircon

Authors

Carlos A. Angeles-De La Torre, Axel K. Schmitt, Oscar M. Lovera, Henja Gassert, Axel Gerdes, & Janet C. Harvey.

Abstract

The Geysers Plutonic Complex (GPC) in the California Coast Ranges underlies one of the world's premier geothermal resources. The GPC consists of three major intrusive phases, orthopyroxene-biotite microgranite porphyry, orthopyroxene-biotite granite, and hornblende-biotite-orthopyroxene granodiorite (in sequence of emplacement). These are nearly coeval and compositionally equivalent to lavas of the overlying Cobb Mountain Volcanic Center which includes (from older to younger) rhyolite of Alder Creek, dacite of Cobb Mountain, and dacite of Cobb Valley. Zircon from GPC plutonic and associated volcanic rocks were analyzed at high spatial resolution for their trace element abundances along with oxygen and hafnium isotopic compositions. Pronounced negative Eu anomalies and high incompatible trace element (e.g., Y, Hf, and U) abundances in zircon along with low Ti-in-zircon temperatures reveal that the GPC microgranite porphyry magma was more evolved than GPC granite and granodiorite. Isotopically, GPC microgranite porphyry, granite, and granodiorite zircon crystals closely overlap ($\delta^{18}O$ = +4.76 to +9.18; εHf = +1.4 to +10.7), but a subpopulation with elevated $\delta^{18}O$ (~8.05) and lower εHf (~4.4) is only present in GPC granite and granodiorite. Zircon from coeval volcanic units share this dichotomy, with a dominant population at ($\delta^{18}O$ = +4.92 to +9.38; εHf = +3.4 to +11.3) and a generally minor population with elevated $\delta^{18}O$ and low εHf, which is particularly prominent in dacite of Cobb Valley. Anticorrelated $\delta^{18}O$ and εHf values indicate progressive assimilation of Franciscan Complex basement rocks, but fractional crystallization was decoupled from crustal assimilation. Together with published U-Th-Pb geochronology, these data reveal distinct degrees of crust-mantle interaction and constrain the thermochemical conditions during different stages in the evolution of a composite intrusive body that fed the GPC and contemporaneous volcanoes. A thermal model for such a body emplaced at ~7 km depth quantitatively matches the GPC zircon age distribution when magma accumulation started at low recharge rates (0.1 km^3/ka), intermittently peaked during a brief flare-up (4 km^3/ka for 50 ka), and then returned to a low recharge flux (0.1 km^3/ka). This model also qualitatively explains the initial presence of small-volume, highly evolved melts forming the microgranite porphyry, followed by massive emplacement of less evolved magmas forming the GPC granite-granodiorite complex. During this second stage, crustal assimilation locally intensified due to prior thermal priming of the country rock. The total injected magma volume into the upper-crustal reservoir between c. 2.1 and 1.1 Ma amounts to ~300 km^3, which is about three to four times the known volume from geothermal well

penetration into the GPC. The accumulation of large volumes of silicic magma along the western North American continental margin in the wake of the northward migrating Gorda slab edge thus appears limited to a brief (c. 50 ka) pulse of high magma influx from the mantle that was pre- and post-dated by protracted low-flux magmatism.

1. Introduction

1.1. Crystals and the volcanic-plutonic connection

Complex crystal origins are increasingly recognized for magmatic rocks, and therefore polygenetic crystal populations can track the thermal and chemical evolution of magmas over a significant part of their lifetime, in some cases from magmatic sources to emplacement at the surface (e.g., Barth and Wooden, 2010). Accessory mineral geochronology is particularly important to identify crystals that can be unequivocally linked to processes such as magma emplacement, cooling, and differentiation (e.g., Chelle-Michou et al., 2014). U-Th-Pb zircon ages in intermediate to evolved subalkaline volcanic rocks nearly universally reveal protracted crystallization prior to eruption (e.g., Simon et al., 2005), but surprisingly, truly xenocrystic zircon is often scarce (e.g., Kern et al., 2016). This suggests that evolved melts had precursors that were originally zircon undersaturated, a condition which facilitates resorption of xenocrystic zircon during the early stages of magmatic differentiation. Crystal recycling from different parts of an evolving plutonic complex has been recognized in volcanic zircon crystals based on a comparison with cogenetic plutonic enclaves in pyroclastic deposits (Schmitt et al., 2010; Barboni et al., 2014). Although plausible, it is difficult to demonstrate a correlation between volcanic and plutonic crystals in general, because either the subvolcanic plutons are concealed, or the volcanic counterparts have been eroded. Moreover, cogenetic plutonic enclaves in volcanic rocks remain ambiguous as a probe into the underlying intrusive complex because these are dislodged from their original location, and their exact provenance is thus uncertain.

The Geysers-Cobb Mountain system in the California Coast Ranges is a rare example of cogenetic volcanic and plutonic rocks that are accessible for direct comparison due to shallow emplacement of a pluton underneath a volcanic field, with the entirely subsurface pluton being drilled by numerous geothermal wells (Fig. 1). Wells up to nearly 4 km deep have penetrated a shallow composite pluton termed the Geysers Plutonic Complex (GPC), informally known as the “felsite”, which encompasses subintrusions of orthopyroxene-biotite microgranite porphyry, orthopyroxene-biotite granite, and hornblende-biotite-orthopyroxene granodiorite. The geothermal reservoir (“The Geysers”) hosted by the GPC and its caprock is one of the world’s most productive, with an installed capacity of ~1.5 GW (Bertani, 2012). Its heat source has been attributed to unidentified intrusions within or below the known GPC (Dalrymple et al., 1999; Donnelly-Nolan and Hearn, 1981; Hulen et al., 1997; Kennedy and Truesdell, 1996; Peacock et al., 2020; Schmitt et al., 2003a; Schriener Jr and Suemnicht, 1980; Stimac et al., 2001). Volcanic rocks exposed nearby in the Cobb Mountain Volcanic Center (CMVC) comprise rhyolite of Alder Creek (ACR), rhyodacite of Cobb Mountain (CMD), and dacite of Cobb Valley (CVD). ACR yielded a widely used Quaternary reference sanidine for ^{40}Ar/^{39}Ar geochronology, where the dominant population of single-crystal sanidine ages defines an eruption age of 1.1864 Ma (Jicha et al., 2016; Rivera et al., 2013). However, a tail of older sanidine crystals was detected in several studies and interpreted as recycling from plutonic rocks (Rivera et al., 2013). Zircon defines an even wider-ranging spectrum of ages, with the youngest U-Th-Pb zircon ages overlapping with the ^{40}Ar/^{39}Ar sanidine eruption age, but many zircon crystals are also significantly older, and these have also been interpreted as inherited from older intrusions in the magma source region (Rivera et al., 2013; Schmitt et al., 2003a, b).

While earlier studies emphasized a strong link between GPC rocks and the CMVC, they did not resolve (1) whether zircon ages and compositional trends correspond between volcanic and plutonic rocks, or if they evolved distinctly, (2) how fractional crystallization and assimilation progressed in different parts of a potentially common magma source, and (3) how the reservoir from which GPC and CMVC magmas were extracted waxed and waned in time and space. Zircon is particularly useful to provide new perspectives for answering these questions because it is chemically and physical resilient with negligible diffusion of most components even at magmatic temperatures (Cherniak and Watson, 2003; Page et al., 2007; Peck et al., 2003) or in agressive hydrothermal environments (e.g., Wilson et al., 2008; Milicich et al., 2013). Hence, it records the thermal and chemical evolution of magma with absolute time information, and it contains abundant O and Hf where isotopic compositions are clear indicators for different mantle vs. crustal contributions (e.g., Kemp et al., 2007; Payne et al., 2016; Scherer et al., 2007, and references therein). Furthermore, recent studies have laid out the potential of zircon thermal models to quantify extensive parameters such as rates and durations of magma inputs by matching observed age distributions and temperatures of zircon from volcanic or plutonic rocks with the cooling timescales predicted for magma reservoirs undergoing episodic recharge (Caricchi et al., 2014; Friedrichs et al., 2021; Lukács et al., 2021; Tierney et al., 2016; Weber et al., 2020).

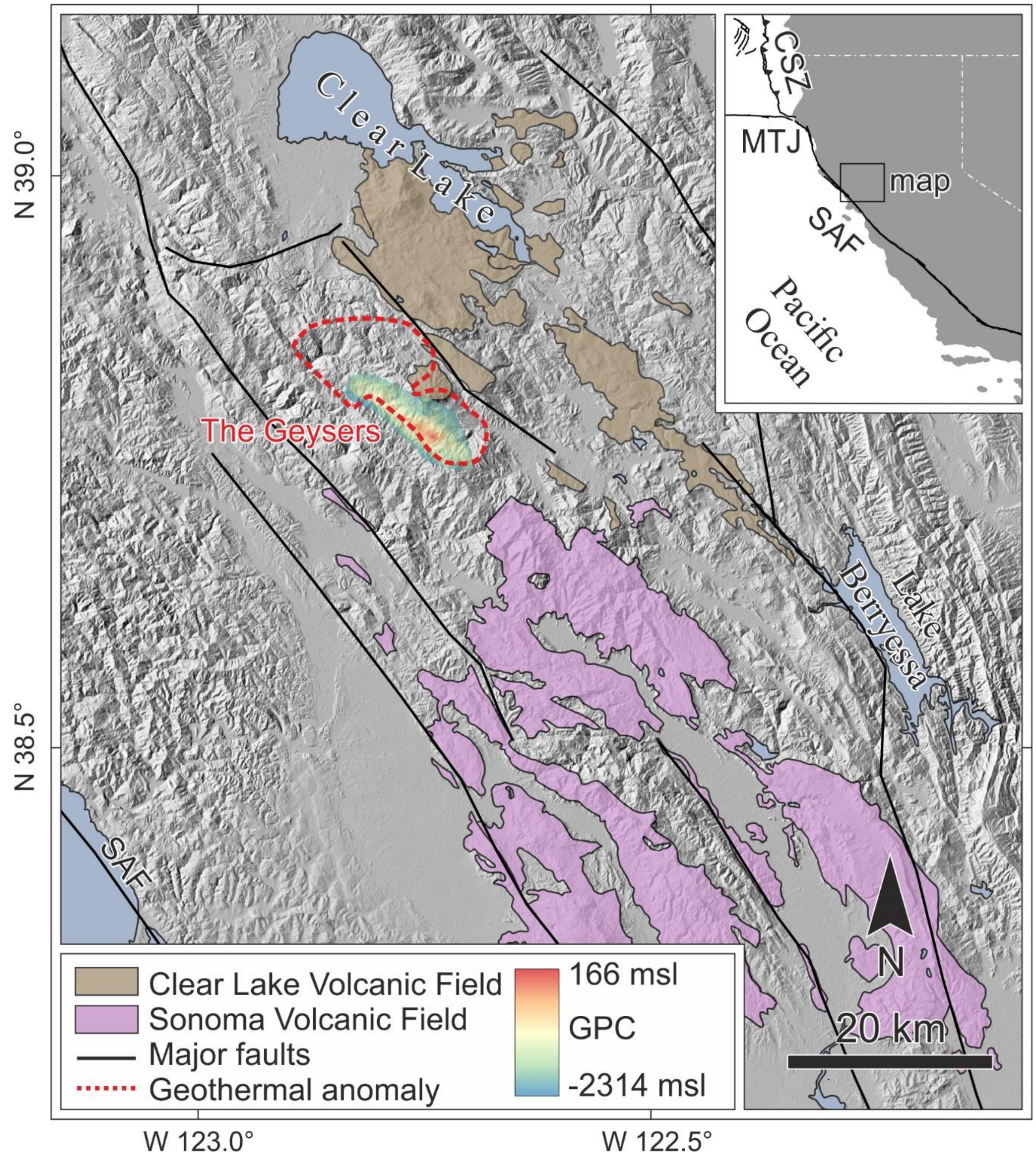

Fig. 1. *Simplified geologic map showing extent of the Clear Lake volcanic field, the Sonoma volcanic field, and the outline of "The Geysers" geothermal anomaly with the subsurface Geysers Plutonic Complex (GPC). Surface of the GPC is stated in meters relative to sea level (msl). Abbreviations: MTJ = Mendocino Triple Junction; CSZ = Cascadia Subduction Zone; SAF = San Andreas Fault. Hillshade derived from SRTM 3 arcsecond DEM. (NASA JPL, 2018); geology after Jennings et al. (2010).*

This study compares trace element, $\delta^{18}O$, and εHf data for zircon from volcanic and plutonic samples of the GPC-CMVC complex using crystals previously dated in Schmitt et al. (2003a, b). We confirm that volcanic and plutonic zircon formed under similar conditions in a common source magma. This magma evolved via crustal assimilation and fractional crystallization, which however, were largely decoupled, and only crystals from the younger and more voluminous GPC granite-granodiorite stage became subsequently recycled during volcanic eruptions. Modelling of magma fluxes into the source system over the duration recorded by zircon between c. 2.1 and 1.1 Ma reveals a progression from slow-paced and gradual magma build up to a brief interval of peak accumulation, and subsequent return to incremental addition at low recharge rate.

1.2. Geological setting and previous geochronology

Covering an area of ~400 km^2, the Clear Lake volcanic field is considered the youngest and northernmost of a series of volcanic centers in the eastern Coast Ranges of California (Fig. 1; Donnelly-Nolan and Hearn, 1981; Fox et al., 1985). The Coast Ranges crust mainly consists of a heterogeneous assemblage of the Franciscan Complex comprising igneous rocks, metamorphosed graywacke, serpentinite, as well as sedimentary rocks, mostly turbiditic metasandstone and argillite (Aalto, 2014; Ernst, 2015; McLaughlin, 1981; Wakabayashi, 2015). Seismic studies indicate crustal thicknesses of 24–30 km for the immediate Clear Lake area of which 12–18 km belong to the Franciscan Complex overlying gabbroic rocks (Castillo and Ellsworth, 1993; Mooney and Weaver, 1989). Magmatism in the Clear Lake area began at about 2.1 Ma and progressively became younger to the north as consequence of the northward migration of the Mendocino triple junction (Dickinson and Snyder, 1979; Donnelly-Nolan and Hearn, 1981; Hearn Jr et al., 1981; Johnson and O'Neil, 1984). A transcrustal complex of magma bodies was emplaced underneath the entire Clear Lake volcanic field based on thermobarometry from metamorphic xenoliths indicating magma ponding at 780–900°C and 400–600 MPa (12–18 km depth; Stimac et al., 2001). The deeper parts of these magma systems were dominated by mafic intrusions where crustal contamination occurred, and from which hybridized, silicic magma subsequently migrated to shallower levels (Hammersley and DePaolo, 2006; Stimac and Pearce, 1992). Intermediate to evolved magmas originated from hybridized mantle-crustal rocks based on their mixed stable ($^{18}O/^{16}O$) and radiogenic ($^{87}Sr/^{86}Sr$, $^{143}Nd/^{144}Nd$, $^{206}Pb/^{204}Pb$) isotopic inventory. Magma hybridization and subsequent melt evolution occurred in multiple stages involving early assimilation and fractional crystallization (AFC) at depth, followed by shallow fractional crystallization (Hammersley and DePaolo, 2006; Johnson and O'Neil, 1984; Schmitt et al., 2006).

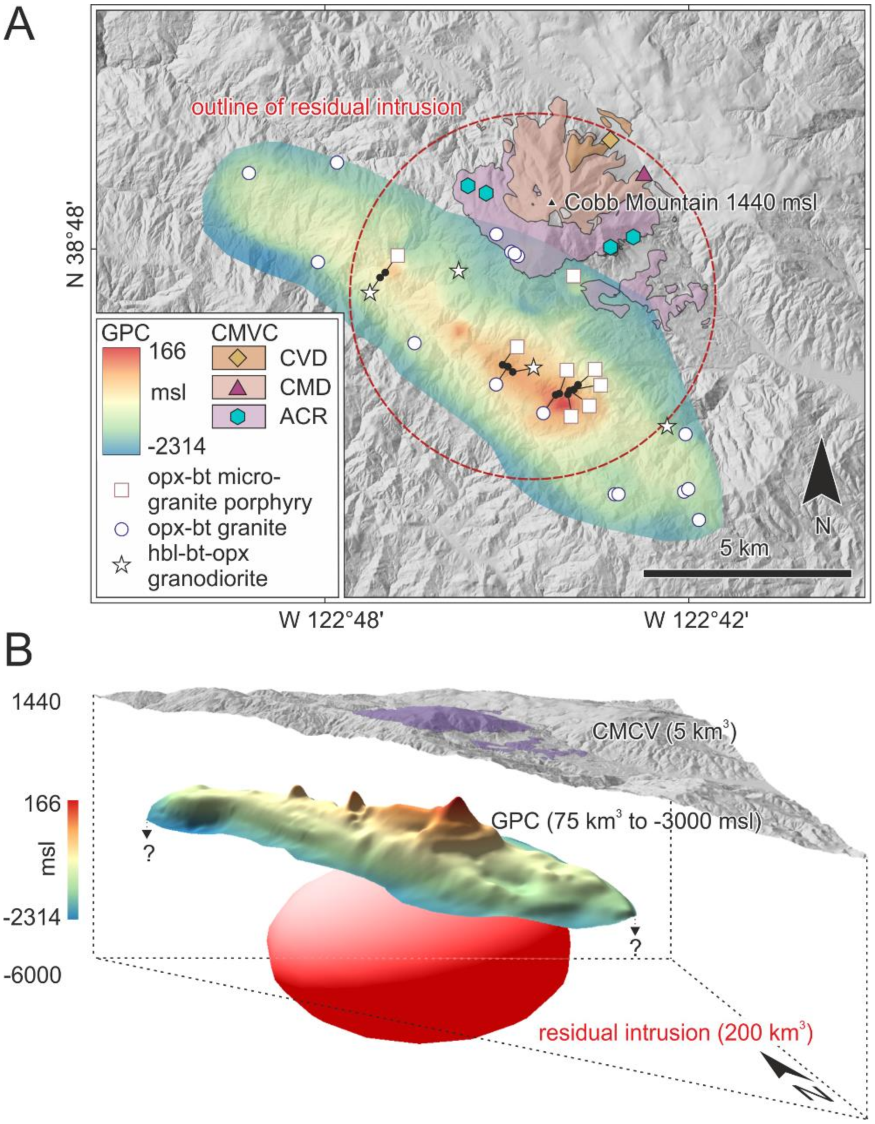

***Fig. 2**. A) Overview map of the Cobb Mountain Volcanic Complex and the underlying Geysers Plutonic Complex. Sample locations (surface for the CMVC and geothermal wells for GPC; Schmitt et al., 2003a, b) are indicated. Outline of the modelled residual intrusive system representing the common magma source after extraction of the GPC and volcanic units based on zircon age modelling is plotted for comparison (see text). B) Surface topography, top of the GPC and the underlying modelled intrusive ellipsoid in a 3D perspective view. Illumination from the NW. Hillshade derived from U.S. Geological survey 1/3 arc second DEM (U.S. Geological Survey 2017). Depth to top of GPC interpolated from points provided by CALPINE (pers. comm.).*

The southwestern zone of the Clear Lake volcanic field includes "The Geysers", one of the most productive geothermal fields worldwide. It is underlain by the GPC (Fig. 2) which, based on geothermal drill well penetration, mainly consists of three petrologically distinct units that also differ in age (from old to young; Fig. 3): a shallow (~0.2–1.2 km depth below the surface) orthopyroxene-biotite microgranite porphyry with an U-Th-Pb zircon average age of 1.75 ± 0.01 Ma, and a deeper (~1.1–2.8 km) complex of orthopyroxene-biotite granite (1.27 ± 0.01 Ma), and hornblende-biotite-orthopyroxene granodiorite (1.24 ± 0.01 Ma; Hulen and Nielson, 1993; Norton and Hulen, 2001; Schmitt et al., 2003b). Assuming that the complex extends to a depth of -3000 m relative to sea level (msl) yields a conservative volume estimate of ~75 km^3 for the GPC (this study, based on interpolation of depth to the GPC provided by CALPINE, pers. comm.). Closely associated with the GPC are Quaternary volcanic rocks that cover the full compositional range from basalt to rhyolite. The oldest units within the area of the steam field comprise andesite of Ford Flat and basalt of Caldwell Pines with reported whole-rock K–Ar ages of 1.71 ± 0.21 and 1.66 ± 0.12 Ma, respectively (Donnelly-Nolan and Hearn, 1981). Lavas and minor pyroclastic deposits of intermediate–rhyolitic composition of the CMVC totaling ~ 5 km^3 are exposed above the eastern margin of the steam field (Fig. 2). The CMVC was active at 1.1850 ± 0.0016 Ma (ACR; Rivera et al., 2013), 1.10 ± 0.02 Ma (CMD), and 1.00 ± 0.05 Ma (CVD; Schmitt et al., 2003a), with zircon crystallization ages generally predating the respective eruption ages by up to several hundreds of ka (Fig. 3; Rivera et al., 2013). Older and younger volcanic rocks are mapped as rhyolite of Pine Mountain ($^{40}Ar/^{39}Ar$ sanidine age = 2.17 ± 0.02 Ma) and dacite of Tyler Valley ($^{40}Ar/^{39}Ar$ sanidine age = 0.67 ± 0.01 Ma) towards the southeast and northwest of the GPC, respectively (Schmitt et al., 2003a). Only the Hachimantai geothermal area, Japan, with the subsurface Kakkonda pluton, is comparable to the GPC-CMVC in providing access to a Quaternary pluton with cogenetic volcanic rocks preserved at the surface (e.g., Ito et al., 2013).

The recent Geysers steam field is a vapor-dominated hydrothermal system with temperatures varying from ~240 °C in the southeast and increasing with depth up to ~340°C towards the northwest. Heat flow in the steam field peaks at values of up to 500 mW/m^2 which even exceeds the already elevated heat flow of the Clear Lake volcanic field by a factor of three (Walters and Combs, 1992). Based on K-feldspar $^{40}Ar/^{39}Ar$ incremental-heating ages, the GPC had cooled to <350 °C by c. 0.9 Ma (Dalrymple et al., 1999) when a fluid-dominated hydrothermal system became established (Hulen et al., 1997; Hulen and Nielson, 1995; Moore et al., 2000; Moore and

Gunderson, 1995). As indicated by vein adularia ^{40}Ar/^{39}Ar ages combined with fluid inclusion data, temperatures cooled down to <300 °C at c. 0.26 Ma, when the shallow hydrothermal system became vapor-dominated (Hulen et al., 1997). Elevated ^{3}He/^{4}He (6.8–8.3 times relative to atmosphere) and Cl abundances in modern geothermal fluids indicate a young magmatic intrusion that provides the heat for the current steam field (Beall and Wright, 2010; Donnelly-Nolan and Hearn, 1981; Kennedy and Truesdell, 1996; Stimac et al., 2001). Because the highest temperatures in the modern geothermal system are encountered in the NW Geysers area, a recent intrusion along with a putative partial melt zone at >7 km extending in a NE direction towards the Clear Lake volcanic field has been proposed (Peacock et al., 2020), although plutonic rocks of such young age have yet to be drilled.

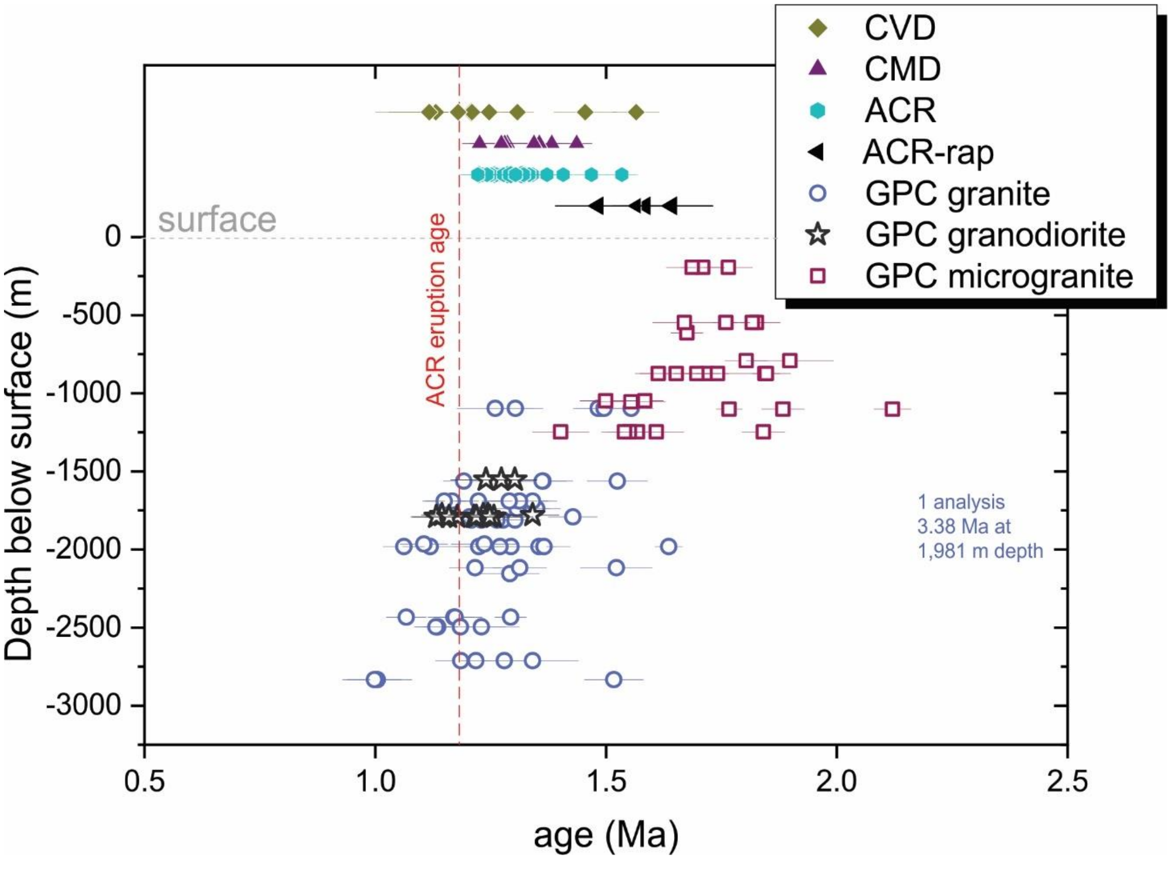

Fig. 3. *SIMS U-Th-Pb zircon ages (from Schmitt et al., 2003 a, b) for the GPC against depth below surface (open symbols), and for the CMVC (filled symbols) in chronostratigraphic order. Data were screened for >85% radiogenic* ^{206}*Pb.*

2. Material and methods

2.1. Sample origins and processing

All zircon crystals were previously dated using U-Th-Pb geochronology (Schmitt et al., 2003a, b). New U-Th-Pb zircon ages for a thin pyroclastic deposit on the SE flank of Cobb Mountain (sample CM-04-01 from the Anderson Flat area) that underlies ACR lava and was mapped as unit "rap" in Hearn et al. (1995) are included in Fig. 3 and the supplementary data (Table S1). Lava was collected as kg-sized specimens at surface outcrops, crushed, and sieved. For the pyroclastic sample CM-04-01, a composite sample of several cm-sized lapilli was processed similar to the lava samples. Most plutonic samples originated as ~10–100 g of mm-sized air drill cuttings which were gently crushed on a steel plate (Schmitt et al., 2003a, b). Zircon crystals were separated from sieved material <250 µm using conventional density and magnetic enrichment, followed by hand-picking and mounting for optical and cathodoluminescence imaging and high spatial resolution (secondary ionization mass spectrometry, SIMS, and laser ablation inductively coupled plasma mass spectrometry, LA-ICP-MS) analysis. Surfaces were gently reground and polished between analyses.

2.2. SIMS and LA-ICP-MS analysis of zircon

Zircon U-Th-Pb analyses were carried out at University of California Los Angeles on a CAMECA ims1270 as outlined in Schmitt et al. (2003a). Trace element and oxygen isotope analysis of zircon was performed using the CAMECA ims 1280-HR at the Heidelberg Ion Probe (HIP) laboratory following methods described in Schmitt et al. (2017) with cathodoluminescence (CL) imaging carried out using a Gatan MiniCL on a Leo 440 scanning electron microscope. For trace element analysis, a ~15 nA $^{16}O^-$ primary beam was focused into a ~20 µm Köhler-illuminated spot on the re-polished zircon surface, targeting the same domains previously analyzed for U-Th-Pb (often CL-dark interiors in the interiors). Using energy filtering (-100 eV), secondary ions were detected at low (m/Δm = 2000) mass resolution. Molecular interferences of light rare earth element (LREE) oxides on atomic ion species of the middle and heavy rare earth elements (MREE, HREE) were subtracted for $^{156}Gd^+$ ($^{140}CeO^+$), $^{158}Gd^+$ ($^{142}CeO^+$, $^{142}NdO^+$), $^{159}Tb^+$ ($^{143}NdO^+$), $^{165}Ho^+$ ($^{149}SmO^+$), $^{169}Tm+$ ($^{153}EuO^+$), $^{172}Yb^+$ ($^{156}GdO^+$), and $^{175}Lu^+$ ($^{159}TbO^+$) using correction factors for oxide and hydride species determined on doped glasses. Relative sensitivity factors were calibrated on NIST SRM 610 (Pearce et al., 1997), and accuracy was monitored by analyzing 91500 reference zircon

(Wiedenbeck et al., 2004). All data on unknowns were screened for anomalies in the light rare earth element index (LREE-I = Dy/Nd + Dy/Sm) and La abundances, discarding all values >30 and >0.1, respectively (Bell et al., 2019), which are interpreted as indicating overlap onto non-zircon phases (e.g., apatite, glass, or oxide inclusions); the full data set, including values for the secondary zircon reference, is presented in the supplement (Fig. S1, Table S2). Temperatures for zircon crystallization based on Ti abundances in zircon (TiZr) were obtained following the equation in Ferry and Watson (2007) for quartz-saturated, but rutile-absent melt using activities of $\alpha_{SiO2} = 1$ and $\alpha_{TiO2} = 0.55$, consistent with Rivera et al. (2013) in their trace element study of ACR zircon. Analytical uncertainties translate into temperature uncertainties of <10 °C based on the external reproducibility of Ti analysis of 91500 zircon reference (4.7 ± 0.3 ppm; 1 SD; n = 9). For oxygen isotope (^{16}O and ^{18}O) analysis, a ~2 nA Cs^+ beam in critical illumination was rastered over a 10×10 μm^2 area on zircon. Intensities of $^{16}O^-$, $^{16}OH^-$, and $^{18}O^-$ were simultaneously monitored in three Faraday detectors and corrected for detector yield and average backgrounds recorded prior to each analysis. Reference zircon AS3 ($\delta^{18}O$ = +5.34 ‰; Trail et al., 2009; all values reported on the VSMOW scale) was intermittently analyzed to determine instrumental mass fractionation factors that were applied to unknowns. Reproducibility of the sliding average of multiple AS3 analyses per analysis day was between 0.14 and 0.22 ‰ (1SD). Because targeted zircon domains are typically much larger than the ~5 µm thick surface layer lost due to re-surfacing after SIMS analysis, age, trace element, and oxygen isotope results can be reliably correlated.

For Hf isotope measurements, a ThermoScientific NEPTUNE Plus multicollector (MC)-ICP-MS system at FIERCE, Goethe University Frankfurt coupled to a RESOlution S155 193nm ArF Excimer (Resonetics) laser system was used as described in Gerdes and Zeh (2006, 2009). Laser spots with lateral dimension of ~35 µm in diameter were set on top of SIMS analysis pits. Each grain was ablated for 38 s using a fluence of 4 J cm^{-2} and a frequency of 8 Hz, which resulted in an ablation rate of 0.65 µm s^{-1}, or ~25 µm total depth. An exponential law with $^{179}Hf/^{177}Hf$ value of 0.7325 was used for instrumental mass bias corrections. For Yb isotopes, instrumental mass bias was corrected using the Hf mass bias of the individual integration step multiplied by a daily $\beta Hf/\beta Yb$ offset factor (Gerdes and Zeh, 2009). All data were adjusted relative to the JMC475 $^{176}Hf/^{177}Hf$ ratio = 0.282160 and quoted uncertainties are quadratic additions of the within-run precision of each analysis and the reproducibility of JMC475 (2SD = 0.0028%, n = 8). Secondary zircon references Temora and GJ-1 analyzed in the same analytical session agree with published values (see full data in supplement).

2.3. Numerical modelling

Zircon crystallization in a magmatic reservoir open for recharge was modelled modifying the approach of Tierney et al. (2016) to accommodate multiple magma extraction events. This model is based on the equations for recharge-assimilation-fractional crystallization (Spera and Bohrson, 2001) and has a grid resolution of 0.1 × 0.1 km over a 20 × 60 km (width × depth) rectangle representing a block of upper–middle crust. Constant heat flow through the base and surface is maintained during the model run. Magma recharge occurs every 5000 years into the center of an ellipsoidal magma chamber, which retains its originally defined aspect ratio (here: height to width ratio = 0.6). The temperature of the cells as they are displaced outward from the center of the intrusion is monitored continuously with each recharge step, along with zircon production in cells that are in a temperature range where zircon saturation is reasonably expected for subalkaline melt compositions and where the magma is above the solidus (i.e. 800–700 °C; Tierney et al., 2016). The relative amounts of zircon crystallized in these cells are integrated for the time of magma extraction. Intrusion depths and temperatures of the recharge magma and the country rock are prescribed, along with a small, generally insignificant initial intrusion volume (5 km^3). Magma input rates and timing are then varied to compute a zircon age distribution that is to be matched to that detected in volcanic or plutonic samples. Model results are evaluated against observations using cumulative probability density functions and the age difference (Δt) between the 16–84 % percentiles of the model and data distributions.

As the depth of intrusion, we adopted 7 km in all models as this is intermediate between the lower limit of the known GPC depth (~3 km) and the top of the inferred mid-lower crustal mafic magma storage zone (~12 km; Stimac and Pearce, 1992). A similar depth was previously proposed for the magma reservoir of nearby Mt. Hannah volcano (Isherwood, 1981; McLaughlin, 1981), and corresponds to the low-resistivity domain detected underneath the Northwest Geysers steam field and adjacent parts of the Clear Lake volcanic field (Peacock et al., 2020). Recharge temperatures of 1000, 1100, and 1200 °C were explored. The lower bound represents the maximum temperature for silicic magmas in the Coast Ranges, whereas a maximum corresponds to regional mafic magmas typically estimated at 1150–1170 °C (Stimac et al., 2001). Geothermal gradients for the pre-intrusion crust are between 30 and 40 °C/km, similar to those previously used in thermal models for the region (Norton and Hulen, 2001; Schmitt et al., 2006). Modeled zircon age distributions were then compared to average zircon ages previously determined in Schmitt et al. (2003b).

3. Results

3.1. Trace elements

All zircon crystals from the GPC and related volcanic units exhibit pronounced negative Eu and positive Ce anomalies. Overall higher HREE abundances and lower Eu/Eu* set apart the microgranite porphyry from the other plutonic and volcanic units (Fig. 4). Microgranite porphyry zircon on average displays very low Eu/Eu* = 0.0045, whereas zircon from the GPC granite and granodiorite as well as those from the volcanic units have Eu/Eu* mostly between 0.01 and 0.1 (Fig. 5 A). Moreover, Eu/Eu* negatively correlates with Hf and positively with Ti abundances in zircon (Fig. 5 A, B). This relation holds for the overall zircon population, in which the microgranite stands out as having the highest Hf and lowest Ti abundances, but also for individual subgroups (e.g., GPC granite), indicating a fractional crystallization trend involving feldspar prior to and during zircon crystallization (e.g., Claiborne et al., 2010). The plot of U against Yb abundances discriminates among different petrogenetic origins of zircon (Grimes et al., 2007), with all zircon from the GPC and CMVC lavas having U/Yb >0.1 indicative of continental crustal sources (Fig. S2). Zircon crystals from the microgranite porphyry display the highest abundances in U (up to 17,400 ppm), whereas zircon from all other units contains U at <7,000 ppm (Fig. S3). The exceptions are zircon crystals from the pre-ACR pyroclastic deposit that feature high U abundances similar to GPC microgranite porphyry zircons. On average, TiZr thermometry ranges between ~670 °C for the microgranite porphyry and ~720 °C for the GPC granite and granodiorite. Calculated temperatures for CMVC zircon are generally >680 °C; ACR and CMD yielded indistinguishable TiZr averages of ~725 °C, whereas CVD displays the highest average of ~735 °C (Fig. 5 B).

When plotting zircon differentiation indices (e.g., U, Th, Hf abundances or Eu/Eu*) against the age of zircon (Fig. S3), a trend is recognized from the older (c. 1.5–2.1 Ma), shallower, and significantly more evolved microgranite porphyry to the younger, deeper, and less evolved GPC granite-granodiorite as well as the overlying CMVC (c. 1.1–1.5 Ma). Zircon data from ACR reported by Rivera et al. (2013) mimic a similar trend, however, over a briefer timescale between c. 1.15 and

1.33 Ma. GPC granite zircon analyses only rarely overlap in age and composition with those of the shallower microgranite zircon, suggesting very limited zircon carry over from older to younger parts of the intrusion. Even for the few crystals in the GPC granite for which a microgranite origin can be inferred, we caution that this could be due to contamination of the drill cuttings from the deeper GPC rocks by the overlying microgranite porphyry.

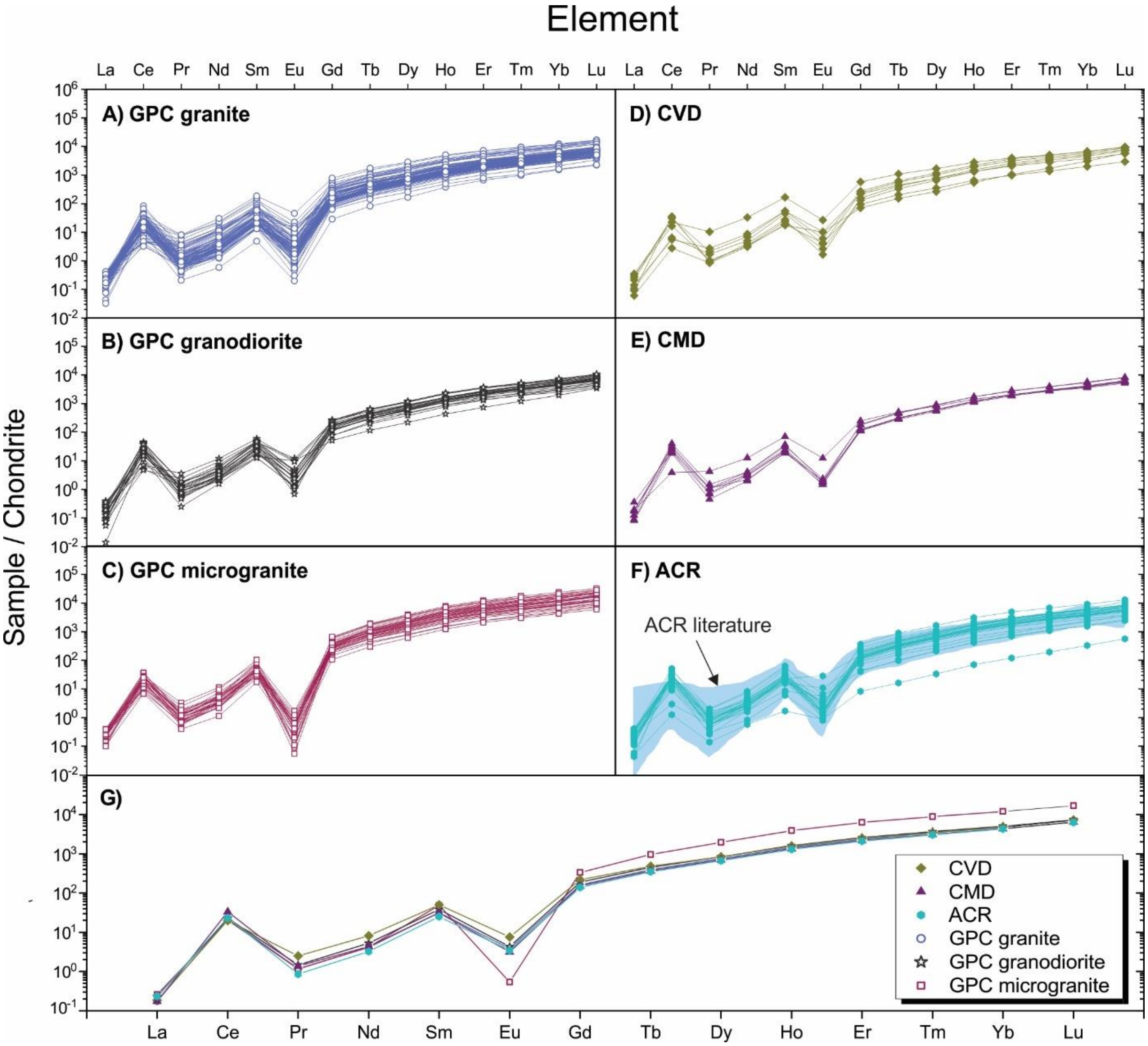

Fig. 4. *Chondrite normalized REE abundances in zircon for the GPC (A to C), CMVC (D to F) and average compositions (G) determined by SIMS. LA-ICP-MS data for ACR (blue field) from Rivera et al. (2013) are shown for comparison. All data on unknowns with the exception of the literature field were screened for contamination by non-zircon phases using the LREE-I and La filters (see text).*

3.2. O- and Hf-isotopes

Zircon $\delta^{18}O$ values of all samples vary between +4.8 and +9.4, with most data above values for zircon crystallized in purely mantle-derived melts (~+5.3; Valley et al., 1998). When accounting for $^{18}O/^{16}O$ fractionation between melt and zircon by adding~1 ‰ to the zircon values (Trail et al., 2009), this range largely overlaps with inferred magma compositions for volcanic rocks from the California Coast Ranges ($\delta^{18}O$ = +8.4 to 10.5 for dacites-rhyolites from Clear Lake) that have been interpreted to be strongly affected by crustal anatexis and assimilation by mantle-derived mafic melts where regional country rock compositions of the Franciscan Complex have $\delta^{18}O$ values of +10 to +16 (Johnson and O'Neil, 1984; Lambert and Epstein, 1992). Essentially the full range in $\delta^{18}O$ is covered by zircon from the GPC granite which displays a bimodal distribution with peaks at +6.4 and +8.6, whereas GPC microgranite zircon $\delta^{18}O$ is unimodal, and has a narrower range between +5.5 and +7.6 (Fig. 6). Volcanic units ACR and CMD mostly overlap with the lower $\delta^{18}O$ cluster in the GPC granite that also encompasses the data for the GPC microgranite and granodiorite, whereas CVD zircons with one exception match the higher $\delta^{18}O$ cluster (Fig. 6). Overall, the $\delta^{18}O$ and εHf compositions negatively correlate, with again two clusters most prominently displayed in the GPC granite population (peak values at +3.5 and +7.5 and an overall range from +1.4 to +10.7), and a distribution of the other units that corresponds to that displayed by the $\delta^{18}O$ data (Fig. 6). Although published data for εHf from potential mantle and crustal end-members in the California Coast Ranges are lacking, the negative correlation displayed by zircon in $\delta^{18}O$ and εHf is consistent with mixing or AFC trends frequently observed in continental magmatic settings (e.g., Kemp et al., 2007). For illustration, εHf was calculated from published εNd data and plotted against $\delta^{18}O$ for mixing and AFC between basaltic and crustal end-members (Fig. 6). While such a model can explain the isotopic composition of the source magmas that produced the majority of the GPC and CMVC zircons, a simple single-stage AFC model (where Hf is incompatible with a bulk partition coefficient D_{Hf} = 0.2) would miss the more crustally contaminated zircon population. This suggests that melt evolution occurred in multiple stages, with Hf becoming compatible in evolved melts upon zircon saturation (second-stage AFC curve with a bulk partition coefficient D_{Hf} = 1.8; Fig. 6).

For $\delta^{18}O$ vs. Eu/Eu*, two clusters in $\delta^{18}O$ are evident, but even the zircon crystals from the microgranite porphyry with the lowest Eu/Eu* display inconspicuously low $\delta^{18}O$ (Fig. 7A). In the εHf vs. Hf abundance plot for zircon, the data are broadly correlated, which is, however, opposite to the expected AFC trend where Hf in zircon would increase with increasing fractionation, and εHf would decrease with increasing crustal contamination (Fig. 7A). Hence, isotopic composition and trace element indices for magma differentiation (Eu/Eu*, Hf abundance in zircon) lack the systematic co-variation that is characteristic for AFC (Fig. 7A, B), similar to findings for the bulk composition of evolved rocks in the Clear Lake volcanic field (Hammersley and DePaolo, 2006; Johnson and O'Neil, 1984; Schmitt et al., 2006).

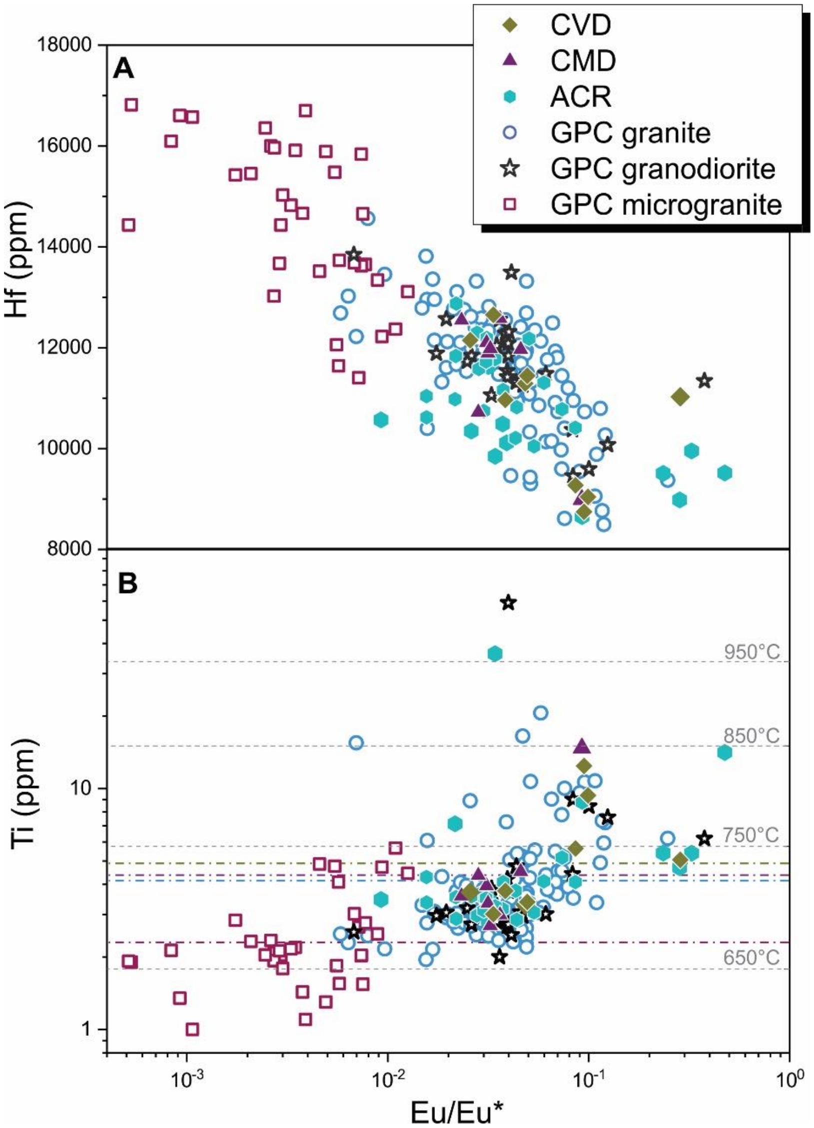

***Fig. 5**. Trace element Hf abundances against Eu/Eu* (A) and Ti abundances against Eu/Eu* (B) for GPC and CMVC zircon determined by SIMS. Right axis in (B) indicates Ti-in-zircon temperatures calculated for a(SiO_2) = 1 and a(TiO_2) = 0.55 (see text), average temperatures of individual units are shown by dashed-dot lines.*

3.3. Thermal models

Initial models explored a steady recharge history for a c. 900 ka interval of evolved magma presence that is constrained by average zircon ages for each well sample between c. 2.0 and 1.1 Ma (Schmitt et al. 2003b;) at uniform recharge rates of 0.1, 0.3, and 1 km^3/ka. A recharge rate <0.1 km^3/ka will produce an intrusion with a volume smaller than the known extent of the GPC and would therefore be unrealistic. Time-invariant recharge results in steady zircon crystallization after an initial incubation period, but contrasts with the observed hiatus in the zircon ages between c. 1.5 and 1.6 Ma (Fig. S4). Moreover, the resulting Δt (which decreases with increasing recharge rate from c. 374 to 281 ka; Table 1) is less than the observed age spread. Consequently, models with a uniform recharge rate (single-stage) were abandoned in favor of two-stage models that reflect the evolution of the GPC where emplacement of the shallow microgranite predated the subsequent intrusion of the granite and granodiorite. The conspicuous absence of zircon recycling from the microgranite by the subsequently intruded granite and granodiorite (and as well in the CMVC lavas) places important constraints on two-stage models: if the volume of the initially intruded magma system up to the time of magma extraction that formed the microgranite was too high, a large amount of zircon would be produced. These zircons would inevitably become recycled during subsequent extraction of the GPC granite and granodiorite magmas because a large intrusion would remain hot, and the magma including its zircon cargo would be mobile. This recycling is, however, not observed, indicating that within the magma reservoir feeding the GPC, zircon crystallizing from a large-volume second pulse must grossly outweigh zircon generated during the first stage, when a comparatively small and cool intrusion was formed that only produced insignificant amounts of zircon compared to the later growth stage of the magma system (Fig. 8).

Trying to match separate, quasi-continuous zircon age distributions for both populations, zircon from the GPC microgranite and the granite-granodiorite, two distinct, but invariable recharge rates were explored over the 900 ka model run-time. For modeling zircon in the microgranite (Fig. S5A), recharge rates >0.1 km^3/ka result in a model intrusion that is too hot to produce zircon during the early stages, whereas recharge at the minimum rate of 0.1 km^3/ka matches the actual distribution in Δt. A good fit between model and data is obtained when the magma system initiated at 2.110 Ma. The observed Δt in zircon from the GPC granite and granodiorite (195 ka) is slightly longer than that of the microgranite (181 ka; Table 1). This, and the absence of recycled older zircon, can be modeled by a brief pulse of elevated recharge between 1.61 and 1.56 Ma, resulting in a 50 ka high-flux event that approximates the timing of the observed zircon age hiatus. Whereas a modelled intrusion formed at 2 km^3/ka would cool too rapidly (within c. 57 ka) to match Δt for zircon from the GPC granite-granodiorite, a magma body emplaced at 4 km^3/ka would crystallize zircon close to the observed Δt (Table 1; Fig. S5B). At recharge rates of 6 and 8 km^3/ka, Δt increases, but more importantly the magma system would remain too hot to crystallize significant zircon by the time zircon saturation was already recorded in the GPC granite-granodiorite (Table 1; Fig. S5B). Therefore, a peak recharge rate of 4 km^3/ka is adopted as the best-fit value. Lastly, we explored recharge temperatures at 1000 and 1200 °C (covering the range of temperatures for potential parental mafic magmas, as represented by andesite of Ford Flat or basalt of Caldwell Pines) as well as different initial geothermal gradients (30 and 40 °C), and only found minor effects for magma cooling during the second, high-flux, phase (Table 1; Fig. S6). For the initial phase, better fits are observed for higher magma temperatures or geothermal gradients, but given the small contribution of this phase to the overall magma volume, these parameters are of second-order importance. In the preferred model (Table 1; Fig. 9), a slightly better fit is obtained when (1) stage 1 starts at 2.11 Ma with 0.1 km^3/ka for 500 ka, and (2) stage 2 initiates with a high flux event at 1.61 Ma, followed by an intermittent shut-down at 1.56 Ma, and then resuming recharge at a low recharge rate of 0.1 km^3/Ma that is maintained between 1.31 and 1.11 Ma. This model scenario is consistent with the timing of volcanism in the CMVC, and thus geologically more reasonable than a complete shut-down of magma recharge after 1.56 Ma.

Model results can also be qualitatively compared to the thermochemical indices recorded by GPC zircon crystals. The modelled thermal evolution of the intrusive complex from which GPC and CMVC magmas were extracted shows protracted thermal stability during stage 1, followed by a thermal excursion and then a gradual temperature decline. This is consistent with the low but constant temperatures in zircon from the GPC microgranite, whereas higher and more heterogeneous temperatures are observed for GPC granite and granodiorite zircon (Fig. S7). Similarly, the more diverse and crustally influenced isotopic compositions of zircon from GPC granite and granodiorite compared to microgranite zircon agree with the expected thermal maturation of the crust following the high-flux event. With this preferred model, a total volume of the intrusive system underlying the GPC approaching ~300 km^3 is predicted (Figs. 8 and 9). Whereas magma volumes (defined by the volume of the intrusion >700 °C) are generally low (<10 km^3) during stage 1 (microgranite porphyry intrusion), a more considerable amount of magma (~50 km^3) has accumulated by the time of the youngest zircon crystallization recorded within the GPC granite-granodiorite and CMVC units (Fig. 9, S8).

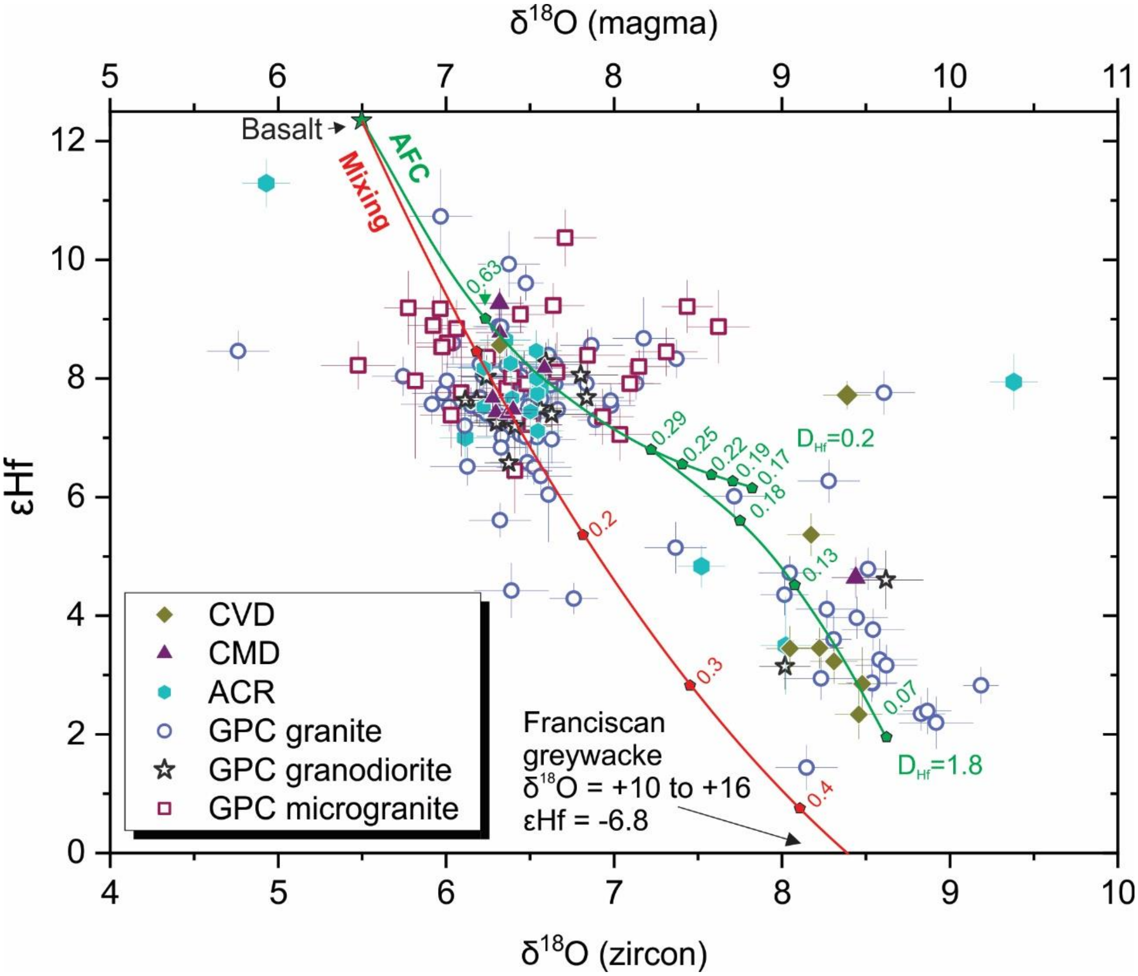

Fig 6. *Covariation diagram of Hf isotopes vs. O isotopes of GPC and CMVC zircon. Lower axis is for zircon values, and upper axis is for magma values based on whole rock data; axes are shifted to accommodate a -1 ‰ fractionation between zircon and melt (Trail et al., 2009). Curves illustrate mixing and AFC trends between potential mantle (basalt of Caldwell Pines) and crustal (Franciscan Complex graywacke) end-members with numbers indicating fraction of crustal contaminant (mixing) and fraction of melt remaining (AFC). End-member compositions from Johnson and O'Neil (1984) and Schmitt et al. (2006), with εNd values recalculated as εHf according to the global arrays in Chauvel et al. (2008) for the basaltic end-member and Vervoort et al. (2011) for metasediments. Abundances of Hf (estimated from whole rock Zr data assuming chondritic Zr/Hf), and r value (ratio of assimilation to fractionation = 0.2) were adapted from Schmitt et al. (2006). Incompatible behavior of Hf was assumed for fractional crystallization prior*

to zircon saturation (bulk mineral-melt partitioning coefficient D_{Hf} = 0.2), which corresponds to the initial mafic-intermediate melt evolution, and D_{Hf} = 1.8 after onset of zircon saturation in evolved melts. Bulk D_{Hf} values were adapted from Kemp et al. (2007) for either a zircon-free mineral assemblage, or zircon being present at 0.05%, acknowledging that a constant amount of zircon and the resulting D_{Hf} value are simplifying assumptions as both are expected to vary during magma evolution.

4. Discussion

4.1. Revising the volcanic-plutonic links between CMVC and GPC from a zircon perspective

Previous studies have linked individual volcanic and plutonic units based on broad geochronological equivalence as well as mineralogical and whole rock geochemical similarities (Hulen et al., 1997; Rivera et al., 2013; Schmitt et al., 2003b). For ACR zircon, the presence of two populations with distinct ages and compositions has been interpreted by Rivera et al. (2013) to result from partial remelting of older, evolved intrusions (1.38–1.24 Ma) by more primitive magma recharge that produced a dominant antecrystic population; this was followed by crystallization of a less abundant zircon population between 1.23 and 1.18 Ma, immediately before eruption of ACR. Our new trace element and O-Hf-isotopic results generally agree with this model of antecrystic recycling and late-stage reheating, but we also emphasize that recycling excluded older and highly evolved zircon from the shallow microgranite porphyry: only zircon from the GPC granite and granodiorite matches the trace elemental and isotopic range of ACR zircon (Fig. 6). This also holds for zircon from CMD and CVD, for which such data were previously lacking. Isotopic data also reveal two distinct populations among GPC and CMVC zircons that have not been previously described. Both populations are present in the younger GPC granite and granodiorite, as well as in all CMVC units, whereas only one population (showing less crustal influence) was detected in the microgranite porphyry. Collectively, these observations indicate that the microgranite porphyry itself was too cold for remelting and recycling of zircon, and/or too small to have delivered any significant amount of zircon antecrysts during the main CMVC stage. The exception may be the pre-ACR explosive eruption (sample CM-04-01) preserved in limited outcrops underneath ACR lavas (unit "rap" in Hearn et al., 1995). In comparison to ACR zircon, U abundances in this sample are elevated, and U-Th-Pb ages overlap with those of microgranite porphyry (Fig. S3). Although the eruption age of this unit remains unconstrained, its zircon crystallization age would be consistent with it being a small-volume eruptive equivalent of the microgranite porphyry.

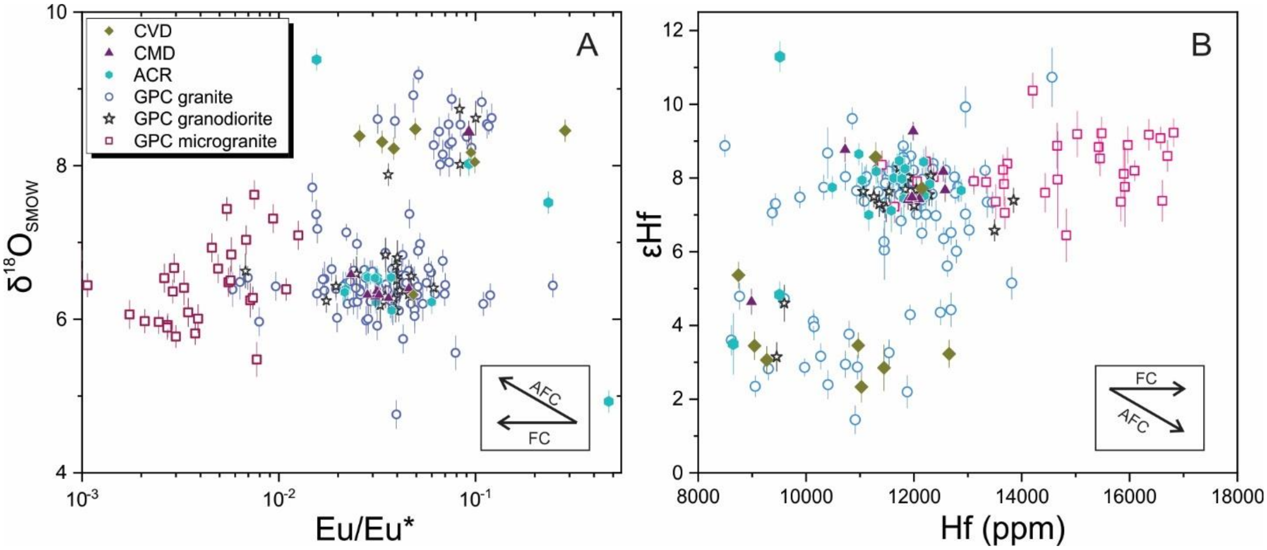

***Fig.** 7. Zircon O isotopes vs. Eu/Eu* (A), and zircon Hf isotopes vs. Hf (B) for GPC and CMVC units. Note that Eu/Eu* and Hf are indices of fractionation, with Eu/Eu* decreasing and Hf increasing with higher degrees of fractionation. Arrows indicate schematic trends for fractional crystallization (FC) and assimilation coupled with fractional crystallization (AFC).*

4.2. Significance of fractional crystallization vs. assimilation and implications for the GPC magma system

The increasing thermal and compositional complexity of zircon in the GPC granite-granodiorite and CMVC units compared to the microgranite porphyry implies a maturation of the magma system where fractional crystallization and assimilation progressed at different rates. In general, magmas tapped by volcanoes in the Coast Ranges of northern California evolved via coupled fractional crystallization and crustal assimilation that has been quantified in different AFC scenarios (Dickinson, 1997; Hammersley and DePaolo, 2006; Johnson and O'Neil, 1984; Schmitt et al., 2006). Multiple stages of assimilation are evident, with basaltic to basaltic andesites acquiring hybrid isotopic signatures through efficient lower-middle crustal assimilation (Hammersley and DePaolo, 2006; Schmitt et al., 2006). Xenoliths in mafic lavas support that most crustal assimilation occurred primarily at lower to mid-crustal depths (Hearn Jr et al., 1981; Stanley and Blakely, 1995;

Stimac, 1993). This was typically followed by a second stage where dacitic to rhyolitic magmas evolved via upper crustal fractional crystallization where assimilation became only significant when high temperatures prevailed (Hammersley and DePaolo, 2006; Schmitt et al., 2006). Magma differentiation at shallow levels also involved remelting of previous intrusions due to renewed magma input (Rivera et al., 2013; Schmitt et al., 2006).

The thermochemical and isotopic variability of GPC-CMVC zircon indicates that magmatic heterogeneity existed in evolved melts that were zircon saturated during storage in an upper crustal magma reservoir, as suggested by the AFC model curve for Hf being compatible (Fig. 6). This heterogeneity implies thermal maturation of a long-lived magma system undergoing frequent recharge of more primitive, hot magma (basaltic to andesitic in composition) where country rocks eventually became sufficiently heated to facilitate their assimilation even at shallow crustal depths. Interestingly, the chemically least evolved CVD lava contains a comparatively large percentage of highly crustally influenced zircon, suggesting that magma recharge efficiently remobilized part of intrusive system that had previously assimilated country rock. This hints at a magma reservoir open for episodic recharge below the depth of the GPC, because the GPC itself was emplaced into cold country rock where assimilation would be negligible. Such a scenario is supported by the rapid cooling of the GPC as indicated by K-feldspar thermochronology, revealing that the GPC was magmatically short-lived, although the underlying magma system from which the GPC was fed had a more protracted lifespan (Dalrymple et al., 1999). The absence of shallow GPC rocks underneath the CMVC also favors that the source for these magmas was below the known GPC.

Microgranite porphyry zircons are isotopically uniform and equivalent to the dominant zircon population in GPC granite-granodiorite and CMVC rocks, but nonetheless they crystallized from unusually highly evolved melts as indicated by their extremely low Eu/Eu*, high incompatible trace element abundances (e.g., Y, Hf, and U), and low TiZr temperatures. Decoupling of fractional crystallization and assimilation implies magma residence at upper crustal levels where additional crustal input beyond the first stage of mid-lower crustal assimilation (sensu Hammersley and DePaolo, 2006) was largely precluded, at least during the early evolutionary stages of the system. Therefore, it is concluded that the upper crustal magma reservoir was initially small and comparatively cold during the formation of the microgranite porphyry, and only subsequently waxed into a larger system capable of producing a wider range of melt compositions along with locally elevated crustal inputs. This growth spurt of the magma system postdates the emplacement of the microgranite porphyry at c. 1.6 Ma, which is consistent with the c. 1.66 Ma age of basalt of Caldwell Pines, where mafic magma seemingly ascended to the surface without becoming trapped in the subsurface by a large, partially molten and therefore low-density magma reservoir (Fig. 9). Other regional volcanic events during the lifespan of the GPC-CMVC system comprise the early, c. 2.2 Ma and 1.7 Ma extrusions of rhyolite of Pine Mountain and andesite of Ford Flat, respectively, both to the southeast of the GPC-CMVC. Although these centers may not be directly related to the GPC, their ages agree with the inferred onset of GPC emplacement as well as a potential high-flux episode at c. 1.6 Ma as developed in the model, respectively. Dacite of Tyler Valley with an eruption age of c. 0.67 Ma, by contrast, is significantly younger than the GPC, and due to the lack of zircon of such young age in GPC-CMVC rocks, the model is unconstrained after c. 1.1 Ma. The eruption of dacite of Tyler Valley just outside the northwestern margin of the steam field, however, is consistent with higher temperatures purportedly associated with young intrusive activity in the geothermal reservoir in this direction (Peacock et al., 2020).

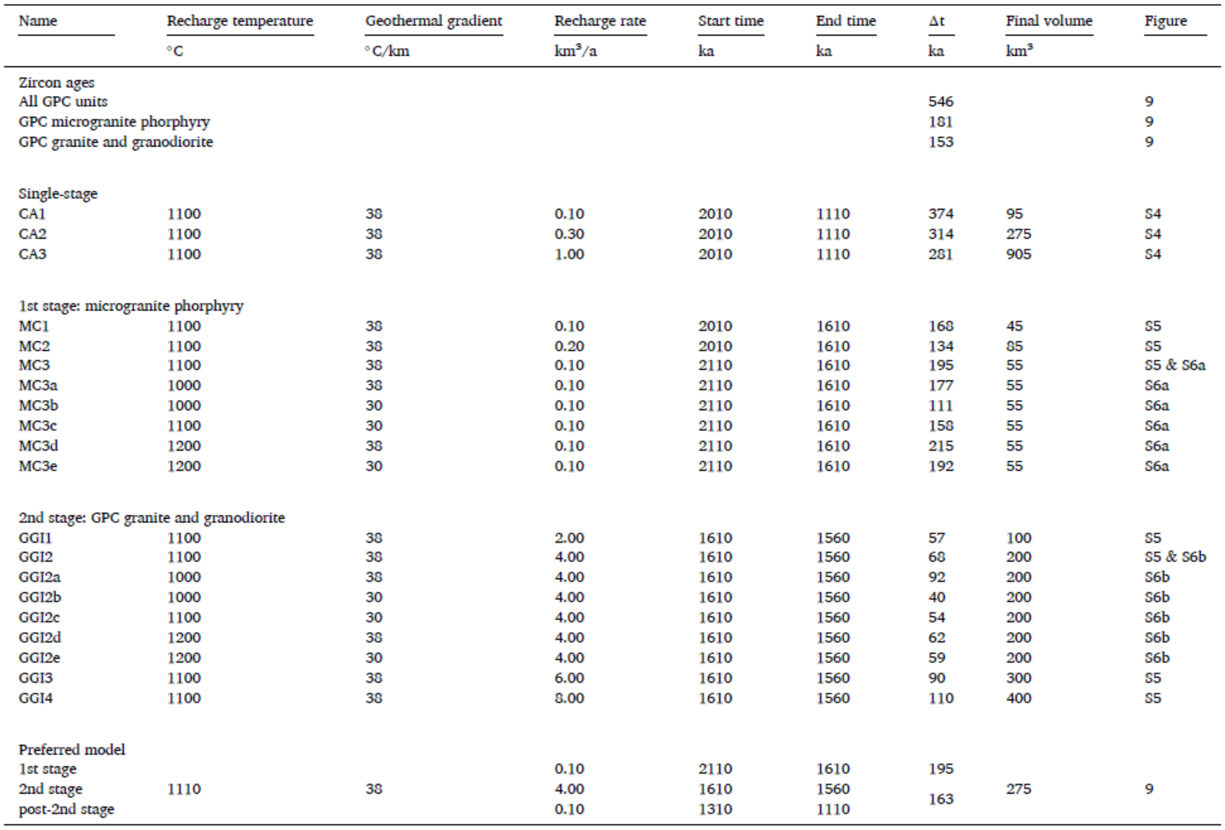

Name	Recharge temperature	Geothermal gradient	Recharge rate	Start time	End time	Δt	Final volume	Figure
	°C	°C/km	km³/a	ka	ka	ka	km³	
Zircon ages								
All GPC units						546		9
GPC microgranite phorphyry						181		9
GPC granite and granodiorite						153		9
Single-stage								
CA1	1100	38	0.10	2010	1110	374	95	S4
CA2	1100	38	0.30	2010	1110	314	275	S4
CA3	1100	38	1.00	2010	1110	281	905	S4
1st stage: microgranite phorphyry								
MC1	1100	38	0.10	2010	1610	168	45	S5
MC2	1100	38	0.20	2010	1610	134	85	S5
MC3	1100	38	0.10	2110	1610	195	55	S5 & S6a
MC3a	1000	38	0.10	2110	1610	177	55	S6a
MC3b	1000	30	0.10	2110	1610	111	55	S6a
MC3c	1100	30	0.10	2110	1610	158	55	S6a
MC3d	1200	38	0.10	2110	1610	215	55	S6a
MC3e	1200	30	0.10	2110	1610	192	55	S6a
2nd stage: GPC granite and granodiorite								
GGI1	1100	38	2.00	1610	1560	57	100	S5
GGI2	1100	38	4.00	1610	1560	68	200	S5 & S6b
GGI2a	1000	38	4.00	1610	1560	92	200	S6b
GGI2b	1000	30	4.00	1610	1560	40	200	S6b
GGI2c	1100	30	4.00	1610	1560	54	200	S6b
GGI2d	1200	38	4.00	1610	1560	62	200	S6b
GGI2e	1200	30	4.00	1610	1560	59	200	S6b
GGI3	1100	38	6.00	1610	1560	90	300	S5
GGI4	1100	38	8.00	1610	1560	110	400	S5
Preferred model								
1st stage			0.10	2110	1610	195		
2nd stage	1110	38	4.00	1610	1560	163	275	9
post-2nd stage			0.10	1310	1110			

***Table 1**: Compilation of observational and model parameters along with zircon age distributions quantified as the age difference between the 16% and 84% percentiles* (Δt). *Model solutions are also displayed in figures as referenced in the last column.*

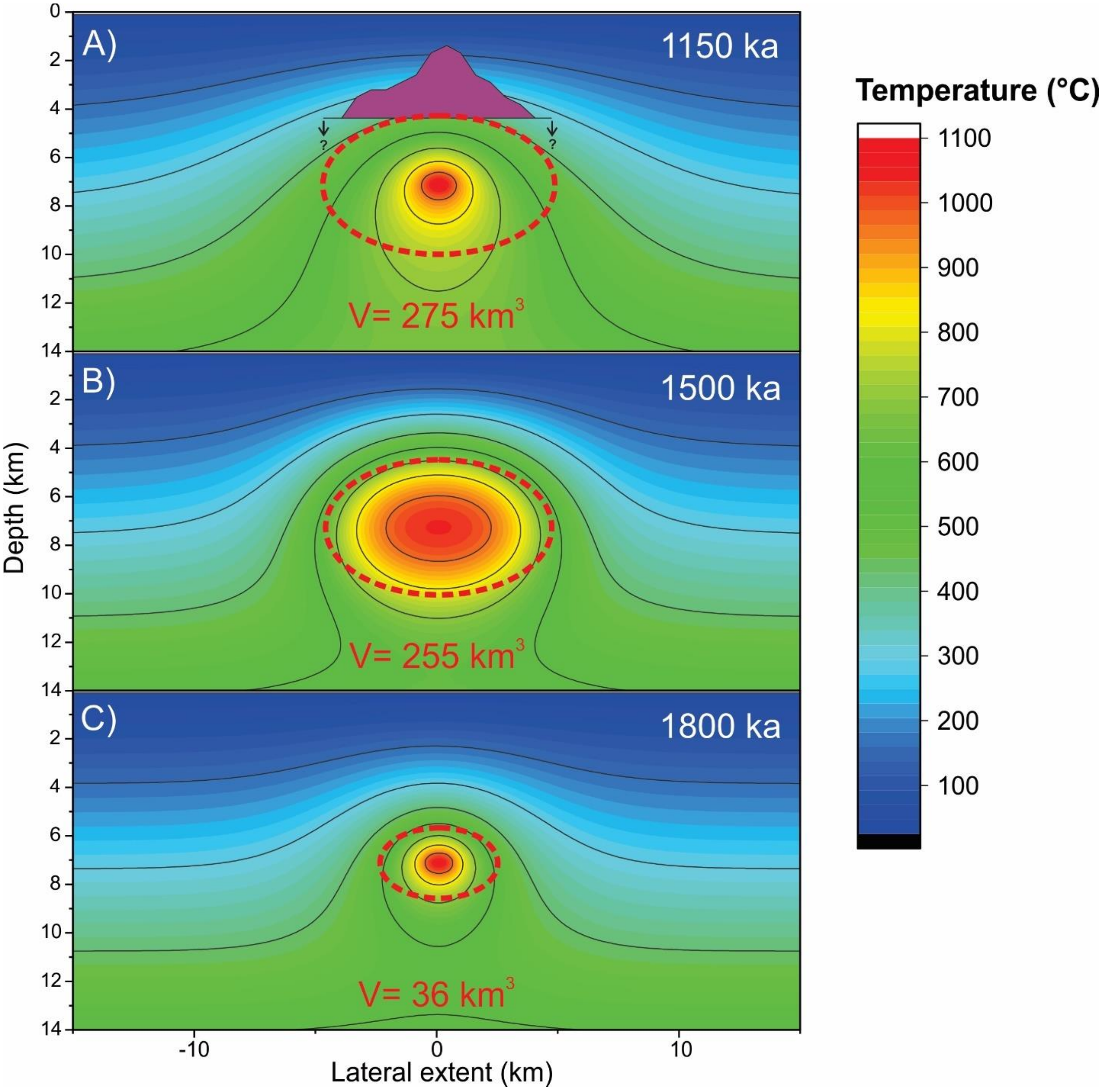

***Fig. 8**. Time slices for the modelled thermal evolution of the magma feeding the GPC-CMVC system at 1800, 1500 and 1150 ka (panels A to C in younging upward sequence). Panels plot central cross-sections through an ellipsoidal magma reservoir with radial symmetry where magma intrusion occurs in the center (0 km lateral extent, 7 km depth). Outlines of the total intruded volumes are indicated by dashed lines; panel A) also compares the outline of the GPC in a N-S profile with the final dimensions of the underlaying intrusion at the end of the model run. Note that the actual model dimensions (lateral extent = 60 km; depth = 20 km) are larger than the plotted range.*

4.3. Geological implications from thermal models of the GPC magma system

Models seeking to explain the thermal anomaly of The Geysers invoked a long-lived magma chamber emplaced at mid crustal depths (e.g., Dalrymple et al., 1999; Isherwood, 1981). Although emplacement of a single, large plutonic body at shallow depth would generate a highly elevated geothermal gradient satisfying the conditions within the modern steam field, this thermal anomaly would be transient over timescales that are much shorter than indicated by radiometric ages for the GPC (Dalrymple et al., 1999; Norton and Hulen, 2001; Schmitt et al., 2003b). Repeated injections of magma would extend the duration of a thermal anomaly, and even though multiple phases of emplacement have been recognized based on mineralogical, geochemical, and geochronological differences within the GPC (Dalrymple et al., 1999; McLaughlin, 1981; Schmitt et al., 2003b; Stanley et al., 1998; Stimac et al., 2001), their collective ages are still too old to maintain current conditions of elevated heat flow. The notion that the GPC itself is too shallow and too small for protracted release of magmatic heat is also supported by K-feldspar thermochronometry indicating that the GPC had already cooled to <350 °C within a few 100 ka after its emplacement (Dalrymple et al., 1999). Rapid cooling of the GPC also supports that zircon with a comparatively large age span (>200 ka for the GPC granite-granodiorite and ACR volcanics as independently indicated by SIMS and TIMS data, respectively; Rivera et al., 2013; Schmitt et al., 2003b) could not have formed in-situ, but rather crystallized in a long-lived magmatic environment, where melts were sufficiently evolved to become zircon saturated and thermal conditions were conducive for the extended presence of melt.

Our model results imply that an intrusive body of nearly 300 km^3 had accumulated by 1.1 Ma, (Figs. 8 and 9), the youngest U-Th-Pb zircon age for the GPC encountered in a shallow dike (Schmitt et al., 2003b). This intrusive body represents the common magma source for the GPC and CMVC. Volume estimates for this body are conservative because of the selected model parameters where (1) new magma recharge is always emplaced in the central, and therefore hottest, part of the magma system, minimizing heat loss to the surroundings, and (2) the intrusion has an ellipsoidal shape and thus a comparatively low surface to volume ratio, (3) the model is only constrained to the youngest zircon ages in GPC-CMVC rocks of c. 1.1 Ma; subsequent intrusions such as the likely rejuvenation of the magma system that led to the eruption of the ACR, CMD, and CVD units (~5 km^3) happened at the end of the modelled interval and were thus not recorded by the accessible zircon populations. Assumptions (1) and (2) translate into slower cooling of the intrusion compared to other geometries, e.g., where a magma body is formed by stacking sills displacing country rock downward and thus always exposing the newest recharge to colder, shallower rocks (Annen et al., 2001). Thin sills also have high surface to volume ratios, so that they solidify quickly. Although our model geometry is schematic, the results broadly match geological constraints: the extent of the residual intrusive ellipsoid after extraction of ~75 km^3 of magma forming the GPC and ~5 km^3 of CMVC lava is ~200 km^3, broadly encompassing the area covered by the GPC and the CMVC when projected towards the surface (Fig. 2). Alternative geometries for the model intrusion are conceivable, for example by trying to match the NW-SE extension of the GPC which is likely controlled by transtension between regional faults (Stanley et al., 1998). However, in the absence of firm constraints on the geometry of the GPC beyond its drilled extent, we deem such efforts premature.

Previous estimates of GPC volumes beyond its known extent from drill well penetration were derived from extrapolating the known geometry to greater depths (e.g., 4.4 km, yielding an estimate of ~300 km^3; Norton and Hulen, 2001), about three times the total erupted volume of the Clear Lake volcanic field (>100 km^3; Donnelly-Nolan and Hearn, 1981). Magma recharge rates for the Clear Lake area have been estimated at 2–3 km^3/ka (Hammersley and DePaolo, 2006) or 10 km^3/ka mantle input (Shaw, 1985), with a fraction of this corresponding to the production of felsic magma (~10%; Shaw, 1985). Our modelled time-integrated recharge rate of 0.1 km^3/ka is consistent with these estimates, but we emphasize that zircon age distributions and compositional diversity were only matched by varying this rate substantially with time. Our best-fit model implies a brief interval of high magma flux (4 km^3/ka for 50 ka) that was preceded and followed by intrusive accumulation at low flux (0.1 km^3/ka). Because our model is only concerned with the duration of known zircon crystallization in GPC-CMVC rocks, we cannot add any new direct insights relating to the question of the heat source for the modern geothermal system, but continuous low-flux activity over the past 1 Ma would be consistent with the notion that high heat flux was maintained or rejuvenated by multiple, smaller (possibly mafic) intrusions at depths below the GPC (e.g., Dalrymple et al., 1999).

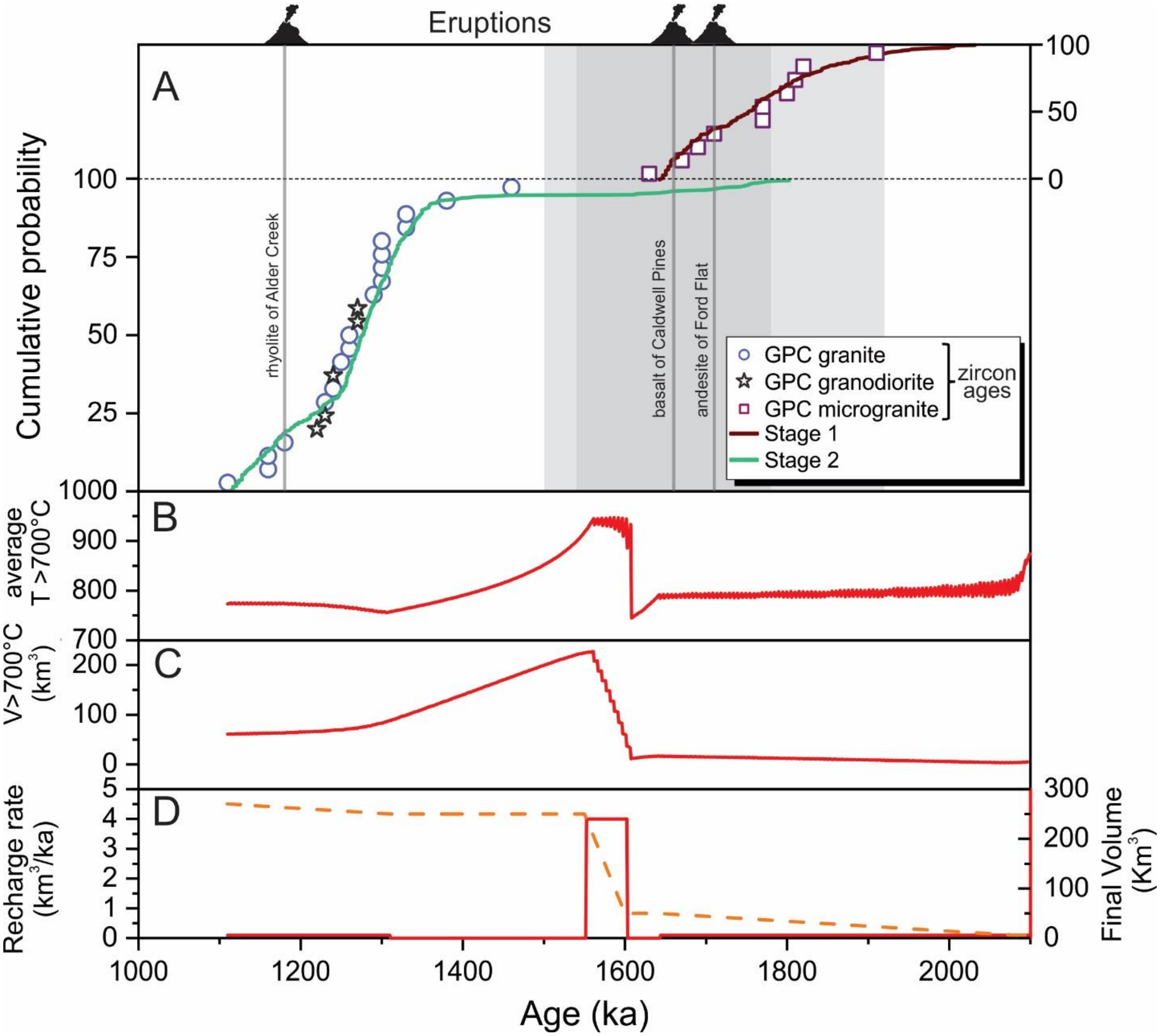

Fig. 9. *Two-stage thermal model reproducing the age distribution for GPC zircon. A) cumulative probability density functions for stage 1 and 2 of the model versus the GPC zircon age averages in ranked order separated according to microgranite and granite-granodiorite units, respectively (data from Schmitt et al., 2003b). Panels below show the temporal evolution of B) average magma temperature (>700 °C), C) volume of magma above the solidus (>700 °C), and D) prescribed magma recharge rate (red solid line) with the resulting cumulative volume of the intrusion (orange dashed line). The preferred model (see text) starts with steady recharge of 0.1 km^3/ka at 2110 ka for 500 ka and is followed by higher recharge of 4 km^3/ka for 50 ka. After an episode of zero recharge dominated by magma cooling, the model returns to a steady recharge of 0.1 km^3/ka after 1310 ka. Critical eruptions within the GPC-CMVC area are indicated by vertical bars and volcano symbols on top.*

Time-transgressive volcanism and elevated crustal heat flow following the northward migration of the Mendocino triple junction has long been recognized as a hallmark of volcanism in the California Coast Ranges (Dickinson and Snyder, 1979; Johnson and O'Neil, 1984; Lachenbruch and Sass, 1980). Oblique convergence of the Pacific-Farallon ridge-transform plate boundary system opened a slab window underneath the western margin of North America (Furlong and Schwartz, 2004) where influx of hot asthenosphere from the former mantle wedge in the wake of northward migration of the subducting Gorda slab heated the overlying continental margin and triggered volcanism (Furlong and Schwartz, 2004). Coast Range volcanism thus forms an array of progressively younger fields that track the northward migrating Mendocino triple junction (e.g., Sweetkind et al., 2011; Fig. 1). Although reconstruction of the timing of volcanic activity within individual fields is complicated by their dissection along the San Andreas fault system, the onset of volcanism appears to be delayed by approximately 3 Ma after passage of the triple junction, corresponding to a 90–110 km distance between the volcanic focus and the southern edge of the slab (Furlong and Schwartz, 2004; Sweetkind et al., 2011). During this time span, the influx of asthenosphere-derived mafic melts, characteristically with an arc signature due to prior modification of the mantle wedge, produced transcrustal magma systems, where parental magmas evolved through processes of fractional crystallization coupled with crustal assimilation as described above (Hammersley and DePaolo, 2006; Schmitt et al., 2006). Within the best preserved and least dissected volcanic outcrops of the California Coast Ranges, comprising the <12 Ma Tolay, Sonoma, and Clear Lake volcanic fields, volcanic activity lasted for c. 2–4 Ma at each location (e.g., Fox et al., 1985; Sweetkind et al., 2011; Wagner et al., 2011). The time-volume relations for individual fields, however, remain poorly constrained, but our modelling results hint at an important role of short-lived magmatic flare-ups in the evolution of these fields. In the case of the Clear Lake volcanic field, a brief high-flux event may have formed the main body of the GPC and the coeval CMVC, with most of the magmatic input retained in an intrusive complex underlying the GPC. We speculate that the older fields display a similar pattern of brief high-flux episodes within a much longer interval of volcanic background activity. Intriguingly, three widespread tephras erupted from calderas within the Eastern Sonoma volcanic field, with deposits of the voluminous Lawlor Tuff recorded in basins as far as the lower Colorado River (Harvey, 2014). These caldera-forming eruptions occurred within a comparatively brief interval (Lawlor Tuff: 4.84 Ma, Huichica tuff: 4.76 Ma, and tuff of Napa: 4.70 Ma; Sarna-Wojcicki et al., 2011) relative to the overall lifespan of the Eastern Sonoma volcanic field (c. 5.4–2.8 Ma; Sweetkind et al., 2011). This corroborates our suspicion that the crustal thermal evolution above the expanding slab window opened only a brief window of opportunity for the accumulation of voluminous (>100 km^3) silicic magma bodies that were capable of feeding sizable shallow intrusions (as for the GPC), or large-volume eruptions (as for the Eastern Sonoma calderas).

5. Conclusions

Zircon trace elements and isotopes for GPC and CMVC show considerable overlap, implying that they share a common magmatic source. This source magma system evolved by fractional crystallization independent of its degree of assimilation, which is typical for an intrusion surrounded by comparatively cold country rock. Highly negative Eu anomalies that systematically co-vary with elevated incompatible trace element (e.g., Y, Hf, and U) abundances in zircon and low TiZr temperatures indicate that the oldest unit, GPC microgranite, originated from a highly differentiated melt. Conversely, a distinct zircon population with elevated δ^{18}O and low εHf is exclusively present in the younger population of GPC and CMVC units, implying that assimilation of Franciscan Complex country rock by evolved, zircon-crystallizing magmas only became possible after the magma system achieved thermal maturity. Thermochemical modeling based on GPC zircon crystallization age distributions suggests a final volume of ~300 km^3 for the source magma system, which dominantly accumulated during a single high-flux episode at c. 1.6 Ma, when recharge rates peaked at 4 km^3/ka for 50 ka. Following this event, crustal assimilation increased in parts of the magma system where a subpopulation of younger zircon crystallized with distinctly elevated δ^{18}O and more crustally influenced εHf values. The absence of zircon carried over from the microgranite porphyry into younger GPC granite and granodiorite as well as CMVC lavas implies that the source magma system was still comparatively small during the microgranite porphyry stage. During this early stage, mafic magma recharge at 0.1 km^3/ka maintained conditions in a deeper magma reservoir suitable for low-temperature zircon crystallization in evolved melts for c. 500 ka that later would ascend to form the shallow cap of the GPC. Another upward migration of magma, this time after the reservoir increased massively in volume at c. 1.6 Ma, was then responsible for intrusion of the GPC granite and granodiorite units. Finally, the system returned to a background magma influx, where emplacement of small intrusions could be responsible for the modern geothermal anomaly (e.g., Peacock et al., 2020). Peak magma production rates in the

California Coast Ranges, however, appear to be limited to a time interval much briefer than the longevity of individual volcanic fields established above a migrating slab window.

Acknowledgments

We thank CALPINE corporation (Stephen DeOreo, Craig Hartline) for sharing data for the top of the GPC, and give credit to former CALPINE geologist Mark Walters, who passed away in July 2020, for his contributions. We also thank journal reviewers Seth Burgess and Calvin Miller for supportive comments. This is FIERCE contribution No. 123.

References

Aalto, K. (2014) Examples of Franciscan Complex mélanges in the northernmost California Coast Ranges, a retrospective. International Geology Review 56, 555-570.

Annen, C., Lénat, J.-F. and Provost, A. (2001) The long-term growth of volcanic edifices: numerical modelling of the role of dyke intrusion and lava-flow emplacement. Journal of Volcanology and Geothermal Research 105, 263-289.

Barboni, M., Boehnke, P., Schmitt, A.K., Harrison, T.M., Shane, P., Bouvier, A.S. and Baumgartner, L. (2016) Warm storage for arc magmas. Proceedings of the National Academy of Sciences, 113(49), 13959-13964.

Barth, A.P. and Wooden, J.L. (2010) Coupled elemental and isotopic analyses of polygenetic zircons from granitic rocks by ion microprobe, with implications for melt evolution and the sources of granitic magmas. Chemical Geology, 277(1-2), 149-159.

Beall, J. and Wright, M. (2010) Southern extent of The Geysers high temperature reservoir based on seismic and geochemical evidence. Geothermal Resources Council Transactions 34, 1199-1202.

Bell, E.A., Boehnke, P., Barboni, M. and Harrison, T.M. (2019). Tracking chemical alteration in magmatic zircon using rare earth element abundances. Chemical Geology, 510, 56-71.

Bertani, R. (2012) Geothermal power generation in the world 2005–2010 update report. geothermics 41, 1-29.

Caricchi, L., Simpson, G. and Schaltegger, U. (2014). Zircons reveal magma fluxes in the Earth's crust. Nature 511, 457-461.

Castillo, D.A. and Ellsworth, W.L. (1993) Seismotectonics of the San Andreas fault system between Point Arena and Cape Mendocino in northern California: Implications for the development and evolution of a young transform. Journal of Geophysical Research: Solid Earth 98, 6543-6560.

Chauvel, C., Lewin, E., Carpentier, M., Arndt, N.T. and Marini, J. C. (2008) Role of recycled oceanic basalt and sediment in generating the Hf–Nd mantle array. Nature Geoscience, 1(1), 64-67.

Chelle-Michou, C., Chiaradia, M., Ovtcharova, M., Ulianov, A. and Wotzlaw, J.F. (2014) Zircon petrochronology reveals the temporal link between porphyry systems and the magmatic evolution of their hidden plutonic roots (the Eocene Coroccohuayco deposit, Peru). Lithos, 198, 129-140.

Cherniak, D.J. and Watson, E.B. (2003) Diffusion in zircon. Reviews in mineralogy and geochemistry 53, 113-143.

Claiborne, L.L., Miller, C.F. and Wooden, J.L. (2010) Trace element composition of igneous zircon: a thermal and compositional record of the accumulation and evolution of a large silicic batholith, Spirit Mountain, Nevada. Contributions to Mineralogy and Petrology 160, 511-531.

Dalrymple, G.B., Grove, M., Lovera, O.M., Harrison, T.M., Hulen, J.B. and Lanphere, M.A. (1999) Age and thermal history of the Geysers plutonic complex (felsite unit), Geysers geothermal field, California: a ^{40}Ar/^{39}Ar and U–Pb study. Earth and Planetary Science Letters 173, 285-298.

Dickinson, W.R. (1997) Tectonic implications of Cenozoic volcanism in coastal California. Geological Society of America Bulletin 109, 936-954.

Dickinson, W.R. and Snyder, W.S. (1979) Geometry of triple junctions related to San Andreas transform. Journal of Geophysical Research: Solid Earth 84, 561-572.

Donnelly, J.M., Hearn Jr, B.C., Curtis, G.H. and Drake, R.E. (1981) Geochronology and evolution of the Clear Lake Volcanics, California. Geological Survey professional paper 1141, 47-60.

Ernst, W. (2015) Franciscan geologic history constrained by tectonic/olistostromal high-grade metamafic blocks in the iconic California Mesozoic-Cenozoic accretionary complex. American Mineralogist 100, 6-13.

Ferry, J. and Watson, E. (2007) New thermodynamic models and revised calibrations for the Ti-in-zircon and Zr-in-rutile thermometers. Contributions to Mineralogy and Petrology 154, 429-437.

Fox, K.F., Fleck, R.J., Curtis, G.H. and Meyer, C.E. (1985) Implications of the northwestwardly younger age of the volcanic rocks of west-central California. Geological Society of America Bulletin 96, 647-654.

Friedrichs, B., Schmitt, A.K., Lovera, O.M. and Atıcı, G. (2021) Zircon as a recorder of contrasting magma recharge and eruptive recurrence patterns. Earth and Planetary Science Letters 571, 117104.

Furlong, K.P. and Schwartz, S.Y. (2004) Influence of the Mendocino triple junction on the tectonics of coastal California. Annu. Rev. Earth Planet. Sci. 32, 403-433.

Gerdes, A. and Zeh, A. (2006) Combined U–Pb and Hf isotope LA-(MC-) ICP-MS analyses of detrital zircons: comparison with SHRIMP and new constraints for the provenance and age of an Armorican metasediment in Central Germany. Earth and Planetary Science Letters 249, 47-61.

Gerdes, A. and Zeh, A. (2009) Zircon formation versus zircon alteration—new insights from combined U–Pb and Lu–Hf in-situ LA-ICP-MS analyses, and consequences for the interpretation of Archean zircon from the Central Zone of the Limpopo Belt. Chemical geology 261, 230-243.

Grimes, C.B., John, B.E., Kelemen, P., Mazdab, F., Wooden, J., Cheadle, M.J., Hanghøj, K. and Schwartz, J. (2007) Trace element chemistry of zircons from oceanic crust: A method for distinguishing detrital zircon provenance. Geology 35, 643-646.

Hammersley, L. and DePaolo, D. (2006) Isotopic and geophysical constraints on the structure and evolution of the Clear Lake volcanic system. Journal of Volcanology and Geothermal Research 153, 331-356.

Harvey, J.C. (2014) Zircon age and oxygen isotopic correlations between Bouse Formation tephra and the Lawlor Tuff. Geosphere, 10, 221-232.

Hearn, B., Donnelly-Nolan, J. and Goff, F. (1995) Geologic map and structure sections of the Clear Lake volcanics, northern California.

Hearn Jr, B.C., Donnelly-Nolan, J. and Goff, F.E. (1981) The Clear Lake volcanics: Tectonic setting and magma sources, Research in the Geysers-Clear Lake Geothermal Area, Northern California. US Government Printing Office, pp. 25-45.

Hulen, J.B., Heizler, M.T., Stimac, J.A., Moore, J.N. and Quick, J.C. (1997) New constraints on the timing of magmatism, volcanism, and the onset of vapor-dominated conditions at The Geysers steam field, California, Proceedings of the 22nd Workshop on Geothermal Reservoir Engineering, pp. 75-81.

Hulen, J.B. and Nielson, D.L. (1993) Interim report on geology of The Geysers felsite, northwestern California, The 1993 Annual Meeting on Utilities and Geothermal: An Emerging Partnership, Burlingame, CA, USA, 10/10-13/93, pp. 249-259.

Hulen, J.B. and Nielson, D.L. (1995) Hydrothermal factors in porosity evolution and caprock formation at the Geysers steam field, California--insight from the Geysers Coring Project. Earth Sciences and Resources Institute, University of Utah, Salt Lake City, UT.

Isherwood, W.F. (1981) Geophysical overview of the Geysers, Research in the Geysers-Clear Lake geothermal area, northern California, pp. 83-95.

Ito, H., Tamura, A., Morishita, T., Arai, S., Arai, F. and Kato, O. (2013) Quaternary plutonic magma activities in the southern Hachimantai geothermal area (Japan) inferred from zircon LA-ICP-MS U–Th–Pb dating method. Journal of Volcanology and Geothermal Research, 265, 1-8.

Jicha, B.R., Singer, B.S. and Sobol, P. (2016) Re-evaluation of the ages of ^{40}Ar/^{39}Ar sanidine standards and supereruptions in the western US using a Noblesse multi-collector mass spectrometer. Chemical Geology 431, 54-66.

Johnson, C.M. and O'Neil, J.R. (1984) Triple junction magmatism: a geochemical study of Neogene volcanic rocks in western California. Earth and Planetary Science Letters 71, 241-262.

Jennings, C.W., with modifications by Gutierrez, C., Bryant, W., Saucedo, G., and Wills, C. (2010) Geologic map of California: California Geological Survey, Geologic Data Map No. 2, scale 1:750,000.

Kemp, A.I.S., Hawkesworth, C.J., Foster, G.L., Paterson, B.A., Woodhead, J.D., Hergt, J.M., Gray, C.M. and Whitehouse, M.J. (2007) Magmatic and crustal differentiation history of granitic rocks from Hf-O isotopes in zircon. Science, 315(5814), 980-983.

Kennedy, B.M. and Truesdell, A.H. (1996) The Northwest Geysers high-temperature reservoir: Evidence for active magmatic degassing and implications for the origin of the Geysers geothermal field. Geothermics 25, 365-387.

Kern, J.M., de Silva, S.L., Schmitt, A.K., Kaiser, J.F., Iriarte, A.R. and Economos, R. (2016) Geochronological imaging of an episodically constructed subvolcanic batholith: U-Pb in zircon chronochemistry of the Altiplano-Puna Volcanic Complex of the Central Andes. Geosphere, 12(4), 1054-1077.

Lachenbruch, A.H. and Sass, J. (1980) Heat flow and energetics of the San Andreas fault zone. Journal of Geophysical Research: Solid Earth 85, 6185-6222.

Lambert, S.J. and Epstein, S. (1992) Stable-isotope studies of rocks and secondary minerals in a vapor-dominated hydrothermal system at The Geysers, Sonoma County, California. Journal of volcanology and geothermal research, 53(1-4), 199-226.

Lukács, R., Caricchi, L., Schmitt, A.K., Bachmann, O., Karakas, O., Guillong, M., Molnár, K., Seghedi, I. and Harangi, S. (2021) Zircon geochronology suggests a long-living and active magmatic system beneath the Ciomadul volcanic dome field (eastern-central Europe). Earth and Planetary Science Letters 565, 116965.

McLaughlin, R.J. (1981) Tectonic setting of pre-Tertiary rocks and its relation to geothermal resources in The Geysers-Clear Lake area. Research in The Geysers-Clear Lake Geothermal Area, Northern California 1141, 3-23.

Milicich, S.D., Wilson, C.J.N., Bignall, G., Pezaro, B., Charlier, B.L.A., Wooden, J.L. and Ireland, T.R. (2013). U–Pb dating of zircon in hydrothermally altered rocks of the Kawerau Geothermal Field, Taupo Volcanic Zone, New Zealand. Journal of Volcanology and Geothermal Research, 253, 97-113.

Mooney, W.D. and Weaver, C.S. (1989) Regional crustal structure and tectonics of the Pacific coastal states; California, Oregon, and Washington. Geophysical framework of the continental United States 172, 129-161.

Moore, J.N., Adams, M.C. and Anderson, A.J. (2000) The fluid inclusion and mineralogic record of the transition from liquid-to vapor-dominated conditions in the Geysers geothermal system, California. Economic Geology 95, 1719-1737.

Moore, J.N. and Gunderson, R.P. (1995) Fluid inclusion and isotopic systematics of an evolving magmatic-hydrothermal system. Geochimica et Cosmochimica Acta 59, 3887-3907.

NASA JPL. NASA Shuttle Radar Topography Mission Global 3 arc second. 2018, distributed by USGS EarthExplorer https://doi.org/10.5066/F7F76B1X. Accessed 2022-11-27

Norton, D.L. and Hulen, J.B. (2001) Preliminary numerical analysis of the magma-hydrothermal history of The Geysers geothermal system, California, USA. Geothermics 30, 211-234.

Page, F.Z., Ushikubo, T., Kita, N.T., Riciputi, L. and Valley, J.W. (2007) High-precision oxygen isotope analysis of picogram samples reveals 2 μm gradients and slow diffusion in zircon. American Mineralogist 92, 1772-1775.

Payne, J.L., McInerney, D.J., Barovich, K.M., Kirkland, C.L., Pearson, N.J. and Hand, M. (2016) Strengths and limitations of zircon Lu-Hf and O isotopes in modelling crustal growth. Lithos 248, 175-192.

Peacock, J.R., Earney, T.E., Mangan, M.T., Schermerhorn, W.D., Glen, J.M., Walters, M. and Hartline, C. (2020) Geophysical characterization of the Northwest Geysers geothermal field, California. Journal of Volcanology and Geothermal Research 399, 106882.

Pearce, N.J., Perkins, W.T., Westgate, J.A., Gorton, M.P., Jackson, S.E., Neal, C.R. and Chenery, S.P. (1997) A compilation of new and published major and trace element data for NIST SRM 610 and NIST SRM 612 glass reference materials. Geostandards newsletter 21, 115-144.

Peck, W.H., Valley, J.W. and Graham, C.M. (2003) Slow oxygen diffusion rates in igneous zircons from metamorphic rocks. American Mineralogist 88, 1003-1014.

Rivera, T.A., Storey, M., Schmitz, M.D. and Crowley, J.L. (2013) Age intercalibration of 40Ar/39Ar sanidine and chemically distinct U/Pb zircon populations from the Alder Creek Rhyolite Quaternary geochronology standard. Chemical Geology 345, 87-98.

Sarna-Wojcicki, A.M., Deino, A.L., Fleck, R.J., McLaughlin, R.J., Wagner, D., Wan, E., Wahl, D., Hillhouse, J.W. and Perkins, M. (2011) Age, composition, and areal distribution of the Pliocene Lawlor Tuff, and three younger Pliocene tuffs, California and Nevada. Geosphere 7, 599-628.

Scherer, E.E., Whitehouse, M.J. and Munker, C. (2007) Zircon as a monitor of crustal growth. Elements 3, 19-24.

Schmitt, A.K., Grove, M., Harrison, T.M., Lovera, O., Hulen, J. and Walters, M. (2003a) The Geysers-Cobb Mountain Magma System, California (Part 1): U-Pb zircon ages of volcanic rocks, conditions of zircon crystallization and magma residence times. Geochimica et Cosmochimica Acta 67, 3423-3442.

Schmitt, A.K., Grove, M., Harrison, T.M., Lovera, O., Hulen, J. and Walters, M. (2003b) The Geysers-Cobb Mountain Magma System, California (Part 2): Timescales of pluton emplacement and implications for its thermal history. Geochimica et Cosmochimica Acta 67, 3443-3458.

Schmitt, A.K., Klitzke, M., Gerdes, A. and Schäfer, C. (2017) Zircon Hafnium–Oxygen isotope and trace element petrochronology of intraplate volcanic rocks from the Eifel (Germany) and implications for mantle versus crustal origins of zircon megacrysts. Journal of Petrology 58, 1841-1870.

Schmitt, A.K., Romer, R.L. and Stimac, J.A. (2006) Geochemistry of volcanic rocks from the Geysers geothermal area, California Coast Ranges. Lithos 87, 80-103.

Schmitt, A.K., Stockli, D.F., Lindsay, J.M., Robertson, R., Lovera, O.M. and Kislitsyn, R. (2010) Episodic growth and homogenization of plutonic roots in arc volcanoes from combined U–Th and (U–Th)/He zircon dating. Earth and Planetary Science Letters, 295(1-2), 91-103.

Schriener Jr, A. and Suemnicht, G. (1980) Subsurface intrusive rocks at The Geysers geothermal area, California. Geol. Soc. Am., Abstr. Programs;(United States) 12.

Shaw, H.R. (1985) Links between magma-tectonic rate balances, plutonism, and volcanism. Journal of Geophysical Research: Solid Earth 90, 11275-11288.

Simon, J., Reid, M. and Young, E. (2005) New isotopic measurements of zircon and feldspar constrain the magmatic evolution at Long Valley Caldera. Geochimica et Cosmochimica Acta Supplement 69, A234.

Spera, F.J. and Bohrson, W.A. (2001) Energy-constrained open-system magmatic processes I: General model and energy-constrained assimilation and fractional crystallization (EC-AFC) formulation. Journal of Petrology 42, 999-1018.

Stanley, W.D., Benz, H.M., Walters, M.A., Villaseñor, A. and Rodriguez, B.D. (1998) Tectonic controls on magmatism in The Geysers–Clear Lake region: Evidence from new geophysical models. Geological Society of America Bulletin 110, 1193-1207.

Stanley, W.D. and Blakely, R.J. (1995) The Geysers-Clear Lake geothermal area, California—An updated geophysical perspective of heat sources. Geothermics 24, 187-221.

Stimac, J. (1993) The origin and significance of high-grade metamorphic xenoliths, Clear Lake volcanics, California.

Stimac, J.A., Goff, F. and Wohletz, K. (2001) Thermal modeling of the Clear Lake magmatic-hydrothermal system, California, USA. Geothermics 30, 349-390.

Stimac, J.A. and Pearce, T.H. (1992) Textural evidence of mafic-felsic magma interaction in dacite lavas, Clear Lake, California. American Mineralogist 77, 795-809.

Sweetkind, D.S., Rytuba, J.J., Langenheim, V.E. and Fleck, R.J. (2011) Geology and geochemistry of volcanic centers within the eastern half of the Sonoma volcanic field, northern San Francisco Bay region, California. Geosphere 7, 629-657.

Tierney, C.R., Schmitt, A.K., Lovera, O.M. and de Silva, S.L. (2016) Voluminous plutonism during volcanic quiescence revealed by thermochemical modeling of zircon. Geology 44, 683-686.

Trail, D., Mojzsis, S.J., Harrison, T.M., Schmitt, A.K., Watson, E.B. and Young, E.D. (2007) Constraints on Hadean zircon protoliths from oxygen isotopes, Ti-thermometry, and rare earth elements. Geochemistry, Geophysics, Geosystems, 8(6), https://doi.org/10.1029/2006GC001449.

Trail, D., Bindeman, I.N., Watson, E.B. and Schmitt, A.K. (2009) Experimental calibration of oxygen isotope fractionation between quartz and zircon. Geochimica et Cosmochimica Acta 73, 7110-7126.

U.S. Geological Survey, 2017, 1/3rd arc-second Digital Elevation Models (DEMs) - USGS National Map 3DEP Downloadable Data Collection: U.S. Geological Survey. Accessed 2022-11-26

Valley, J.W., Kinny, P.D., Schulze, D.J. and Spicuzza, M.J. (1998) Zircon megacrysts from kimberlite: oxygen isotope variability among mantle melts. Contributions to Mineralogy and Petrology 133, 1-11.

Vervoort, J.D., Plank, T., and Prytulak, J. (2011) The Hf–Nd isotopic composition of marine sediments. Geochimica et Cosmochimica Acta, 75(20), 5903-5926.

Wagner, D.L., Saucedo, G.J., Clahan, K.B., Fleck, R.J., Langenheim, V.E., McLaughlin, R.J., Sarna-Wojcicki, A.M., Allen, J.R. and Deino, A.L. (2011) Geology, geochronology, and paleogeography of the southern Sonoma volcanic field and adjacent areas, northern San Francisco Bay region, California. Geosphere, 7(3), 658-683.

Wakabayashi, J. (2015) Anatomy of a subduction complex: Architecture of the Franciscan Complex, California, at multiple length and time scales. International Geology Review 57, 669-746.

Walters, M.A. and Combs, J. (1992) Heat flow in The Geysers-Clear Lake geothermal area of northern California, USA, Monograph on the Geysers Geothermal Field. Geothermal Resources Council, pp. 43-53.

Weber, G., Caricchi, L., Arce, J.L. and Schmitt, A.K. (2020) Determining the current size and state of subvolcanic magma reservoirs. Nature communications 11, 1-14.

Wiedenbeck, M., Hanchar, J.M., Peck, W.H., Sylvester, P., Valley, J., Whitehouse, M., Kronz, A., Morishita, Y., Nasdala, L. and Fiebig, J. (2004) Further characterisation of the 91500 zircon crystal. Geostandards and Geoanalytical Research 28, 9-39.

Wilson, C.J.N., Charlier, B.L.A., Fagan, C.J., Spinks, K.D., Gravley, D.M., Simmons, S.F. and Browne, P.R.L. (2008) U–Pb dating of zircon in hydrothermally altered rocks as a correlation tool: application to the Mangakino geothermal field, New Zealand. Journal of Volcanology and Geothermal Research, 176(2), 191-198.

Formblatt Kumulative Dissertation Stand 14.02.2023

1. **Publikation/*Publication*:**
   Vollständige bibliographische Referenz/*Complete bibliographic reference:*
   Angeles-De La Torre, C. A., Schmitt, A. K., Danisík, M., Gerdes, A., Hertwig, A., & McCurry, M. (2025). Linking Zircon Crystallization to Magmatic Processes in Basalt Dominated Lava Fields: the Eastern Snake River Plain-Craters of the Moon Testbed. Journal of Petrology, egaf040.
2. Erst- oder gleichberechtigte Autorenschaft/*First or equal authorship:* Ja/*Yes* ☑ Nein/*No* ☐
3. Veröffentlicht/*Published* ☑ Zur Veröffentlichung akzeptiert/*Accepted* ☐

   Q1/Q2:* Ja/*Yes* ☑ Nein/*No* ☐
   **SCImago Journal Rank (SJR) indicator*
   Im Erscheinungsjahr oder im letzten verfügbaren Vorjahr/*In the year of publication or the last prior year available:* 2025

   Eingereicht/*Submitted* ☐ Noch nicht eingereicht/*Not yet submitted* ☐
4. **Beteiligungen/*Contributions*****

Contributor Role	Doktorand/in/ *Doctoral student*	Co-Autor/in 1/ *Co-author 1*	Co-Autor/in 2/ *Co-author 2*
Name, first name	Angeles De La Torre Carlos A.	Schmitt Axel K.	Danisík Martin
Methodology	☑	☐	☐
Software	☐	☐	☑
Validation	☑	☑	☑
Formal analysis	☑	☑	☑
Investigation	☑	☐	☑
Resources	☑	☐	☐
Data Curation	☑	☑	☐
Writing-Original Draft	☑	☐	☐
Writing-Review&Editing	☑	☑	☑
Visualization	☑	☐	☐
Supervision	☐	☑	☐
Project administration	☐	☑	☐
Funding acquisition	☐	☑	☐

***Kategorien des CRediT (Contributor Roles Taxonomy, https://credit.niso.org/)*

Hiermit bestätige ich, dass alle obigen Angaben korrekt sind/*I confirm that all declarations made above are correct.*

Unterschrift/*Signature* ____________ A. K.

Doktorand/in/Doctoral student | Co-Autor/in 1/Co-author 1 | Co-Autor/in 2/Co-author 2

Betreuungsperson/*Supervisor:*

Hiermit bestätige ich, dass alle obigen Angaben korrekt sind und dass die selbstständigen Arbeitsanteile des/der Doktoranden/in an der aufgeführten Publikation hinreichend und signifikant sind/*I confirm that all declarations made above are correct and that the doctoral student's independent contribution to this publication is significant and sufficient to be considered for the cumulative dissertation.*

Prof. Dr. Axel K. Schmitt | A. K. | 29/05/2025

Name/*Name* | Unterschrift/*Signature* | Datum/*Date*

Appendix II

Linking zircon crystallization to magmatic processes in basalt dominated lava fields: The Eastern Snake River Plain – Craters of the Moon testbed

Authors

Carlos A. Angeles-De La Torre, Axel K. Schmitt, Martin Danisík, Axel Gerdes, Andreas Hertwig, & Michael McCurry

ABSTRACT

Throughout the Quaternary, the Eastern Snake River Plain (ESRP) has been the focal zone of bimodal volcanism which filled an elongated downwarp within the northwestern North American continental lithosphere. In the wake of the southwest–northeast trending Yellowstone hotspot track and its silicic caldera volcanism, massive outpourings of olivine tholeiite lava occurred within the ESRP, but several prominent rhyolite domes and intermediate lava flows also erupted in its center. Along its northern margin, the Craters of the Moon volcanic field (COM) is also dominated by Middle Pleistocene–Holocene mafic lavas, but they comprise comparatively Fe-rich and Mg-poor trachybasalts and three evolved basaltic trachyandesite to trachydacite flows emplaced during its youngest eruptive episode. The occurrence of zircon crystals in these young lavas and rhyolite domes provides a unique opportunity to evaluate zircon crystallization in well-preserved and accessible basalt-dominated lava fields as analogs to large igneous provinces in the geologic past. Zircon crystallization ages determined by U-Pb and U-Th dating methods were paired with crystal-scale trace element and isotopic ($\delta^{18}O$, εHf) data. Additionally, the eruption age of the evolved COM Highway flow was determined by combined (U-Th)/He and U-Th dating. U-Pb data indicate crystallization ages between 1,540 ±10 ka in the oldest and 335 ± 3 ka (2se) in the youngest ESRP rhyolite domes which are consistent with reported K-Ar and $^{40}Ar/^{39}Ar$ eruption ages (1,400 ± 28 – 327 ± 3.2 ka). Similarly, U-Th ages averaging $6.2\,^{+2.6}_{-2.5}$ ka compared to (U-Th)/He ages of 2.05 ± 0.56 ka (2se) for evolved COM lava also indicate crystallization with preeruptive residence over several millennia. Values for $\delta^{18}O$ (ESRP: +1.89 to +4.32; COM: +5.13 to +6.03) and εHf (ESRP: -6.4 to -1.6; COM: -11.9 to -8.9) suggest that ESRP and COM magmas originated form a similar mantle source, but evolved via divergent assimilation and fractional crystallization paths. These paths for ESRP and COM magmas depend on the abundance of hydrothermally altered felsic rocks in the crust, which strongly influence ESRP magmas on the axis, but less so the COM magmas at the margins of the downwarp. Zircon crystallization postdates assimilation and is facilitated by progressive Zr enrichment due to extensive fractional crystallization. Parallel whole rock and zircon trace element (e.g., Zr/Hf, Eu/Eu*) fractional crystallization trends at nearly identical degrees of remaining liquid support autocrystic zircon crystallization and argue against crystal recycling from largely solidified crystal mushes. In a global comparison to volcanic rocks from large igneous provinces, such high-Zr mafic-intermediate lavas are scarce. Thus, autocrystic zircon in mafic lavas are clearly exceptional and should be scrutinized against potential contamination

using trace element or isotopic data. Unless Zr abundances are exceptionally high, zircon saturation in mafic magmas only appears achievable in interstitial melt pockets in slowly crystallizing sills or intrusions.

INTRODUCTION

Zircon has become an indispensable tool to reconstruct thermochemical conditions of magmas, providing unique insights into the processes of magma origins, storage, and solidification, especially for felsic magmas prone to zircon saturation. Even in basalt-dominated environments such as mid-ocean ridges and oceanic islands zircon is present either in gabbroic to plagiogranitic rocks or rare evolved lavas (Carley *et al*., 2014; Grimes *et al*., 2007; 2011; Schmitt *et al*., 2011). However, the occasional presence of zircon in rapidly cooled basaltic lavas, remains enigmatic, especially as such lavas are widespread surface constituents of Earth, Moon, and the terrestrial planets. Explanations range from in-situ crystallization to extraneous origins through natural or laboratory contamination (e.g., Bjerga *et al.*, 2022; Bea *et al.*, 2022; Rojas-Agramonte et al., 2022). The search for datable zircon in mafic rocks is relevant for oceanic magmatism, continental rifts, but in particular for large igneous provinces (LIPs), which are characterized by the emplacement of large volumes of predominantly mafic magma over short durations in either continental or oceanic settings with pervasive and large-scale impacts on regional to global environments (e.g., Ernst, 2014). Reconstructing these impacts from LIP events throughout geological time requires reliable geochronological constraints. In some cases, this has been successfully achieved by dating zircon crystals in intercalated evolved rocks (e.g., O'Connor *et al.*, 2022; Schoene *et al.*, 2015), or in slowly cooled sills or dikes (e.g., Gaynor *et al.*, 2022), although these are typically rare or poorly exposed. Where zircon has been reported from LIP mafic volcanic rocks and their metamorphic equivalents, its provenance often remains controversial. Besides crystallization in evolved melts, either in isolated pockets or in larger reservoirs, other interpretations include autocrystic crystallization (Hartmann *et al.*, 2019; Schulz *et al.*, 2006; Zhu *et al.*, 2016), sediment contamination in the crust (e.g., Shumlyanskyy *et al.*, 2016) or the mantle source (Xu *et al.*, 2018), or local contamination followed by zircon resorption and re-growth (Gaynor *et al.*, 2022, 2023; Davies *et al.*, 2021). Baddeleyite, which can crystallize in silica-undersaturated melts typical for LIPs, has been harnessed as a viable dating alternative (Davies *et al.*, 2017), but often baddeleyite crystals are small, its age accuracy can be compromised by Pb loss and, in comparison to zircon, its petrochronological significance is much less established (Schaltegger & Davies, 2017).

Zircon saturation experiments (e.g., Borisov & Aranovich, 2019, Crisp & Berry, 2022, Gervasoni *et al.*, 2016, Shao *et al.*, 2019, Watson, 1996, Watson & Harrison, 1983, Zhang & Xu, 2016) predict crystallization in evolved melts under conditions met in slowly crystallizing basaltic magmas forming intrusive rocks (e.g., Bea *et al.*, 2006, Grimes *et al.*, 2011, Hodych *et al.*, 2004, Shumlyanskyy *et al.*, 2016, Zheng *et al.*, 2011). These studies also invoke rapid dissolution of xenocrystic zircon in contact with hot, mafic melts (within <1 day; Borisova et al., 2022; cf. Xu *et al.*, 2018). Some studies emphasized local saturation in restricted highly evolved melt pockets where zircon precipitation is feasible (e.g., Bea *et al.*, 2022). Yet, reliable criteria for distinguishing between xenocrystic and autocrystic zircon in mafic hosts are lacking, which limits the petrochronological potential of zircon in such rocks.

To investigate zircon crystallization in the context of mafic magmatism, we turned to the Eastern Snake River Plain (ESRP) as a young analog for ancient LIPs (Fig. 1). Because of its Quaternary age, the ESRP allows reconstruction of zircon crystallization at high temporal fidelity. Although not a LIP per se, the ESRP is in direct lineage with the Columbia River flood basalt event. In the ESRP, southwest–northeast migration of the Yellowstone hotspot track has triggered massive outpourings of basaltic lavas that erupted from large shield volcanoes in the wake of preceding silicic caldera volcanism (Pierce & Morgan, 1992, Smith & Braile, 1994). Basaltic volcanism is predominant in the ESRP, which during the Holocene alone witnessed formation of at least eight lava fields that cover ~13% of its surface area. Among these volcanic fields, Craters of the Moon (COM) is the largest, which, in conjunction with the Kings Bowl and Wapi, has produced more than 60 eruptions over the past 15,000 years (Kuntz, 1992, Kuntz *et al.*, 1986, Kuntz *et al.*, 2007). Additionally, in the middle ESRP, the basaltic strata were penetrated and intruded by several Pleistocene evolved lavas and domes. Although some of these domes form prominent landmarks in the ESRP, their collective volume is only a small fraction of the total mafic output (McCurry et al., 2008).

To cover the full spectrum of zircon in intermediate–silicic rocks in a predominantly mafic volcanic field, this study reports U-Th-Pb ages, O and Hf isotopes, and trace element compositions for zircon from all exposed ESRP domes. Similarly, zircon was investigated from three of the most recent COM trachyandesite lavas flows, and from a xenolith collected in the area as a potential crustal contaminant. Zircon crystallization ages in combination with new (U-Th)/He as well as published K-Ar and ^{40}Ar/^{39}Ar eruption ages underscore autocrystic zircon formation shortly before the eruption, whereas isotopic and trace element petrochronology links the zircon cargo in the ESRP and COM lavas to a liquid line of descent controlled by extensive fractional crystallization which postdates crustal assimilation.

Initiation and evolution of ESRP-COM magmatism

The ESRP is a topographic depression of 400-km length and 50–100-km width located in southern Idaho, USA (Fig. 1). In conjunction with the Columbia River Basalt province and caldera-related deposits of the Yellowstone hotspot track, this system represents one of the world's premiere examples of a large-volume continental igneous province (e.g., Christiansen, 2001, Coble & Mahood, 2012, Colón *et al.*, 2018, Hildreth *et al.*, 1991, Nash *et al.*, 2006, Pierce & Morgan, 2009). Volcanism in the area is extensive in both space and time (Fig. 1a): it started with the Miocene McDermitt caldera overlapping northern Nevada and southeastern Oregon (c. 16.4 Ma) and then progressively moved eastward forming in sequence the volcanic fields of Juniper Mountain/Owyhee Humboldt (c. 14–13 Ma), Bruneau-Jarbidge (c. 12.7–10.5 Ma), and Twin Falls (c. 11–6 Ma), followed by composite calderas of Picabo (c. 10–6 Ma), Heise (c. 8–4 Ma), and ultimately Yellowstone as the current volcanic focus (Anders *et al.*, 2019, Colón *et al.*, 2018, Henry *et al.,* 2017*;* Kuntz, 1992, Morgan & McIntosh, 2005, Shervais *et al.*, 2006, Shervais & Hanan, 2008, Stout *et al.*, 1994, Watts *et al.*, 2011). Subsequently and overlying the older Yellowstone-type rhyolitic ignimbrites and lava flows, the Pliocene–Quaternary ESRP (Fig. 1b) is the site of extensive, predominantly olivine tholeiitic volcanism covering a large swath of southern Idaho (e.g., Geist *et al.*, 2002, Hanan *et al.*, 1997, Hughes *et al.*, 2002a, Hughes *et al.*, 2002b, Kuntz, 1992, Leeman, 1982a, Reid, 1995, Shervais *et al.*, 2006). The youngest center in the ESRP is the Craters of the Moon volcanic field (COM) with morphologically extremely well-preserved volcanic shields, cinder and spatter cones. COM lavas were emplaced at the northern end of the Great Rift (Fig. 1c), a 2–8 km wide and up to 85 km long belt of dike-fed extensional fissures that follow the same NW-SE orientation as regional normal faults of the Basin and Range Province (Chadwick *et al.*, 2007, Kuntz, 1992, Kuntz *et al.*, 1986, Leeman *et al.*, 1976). The COM covers ~1,600 km^2, has a total volume of about 30 km^3, and is considered the largest Holocene lava field in the USA (Kuntz, 1992, Stout *et al.*, 1994).

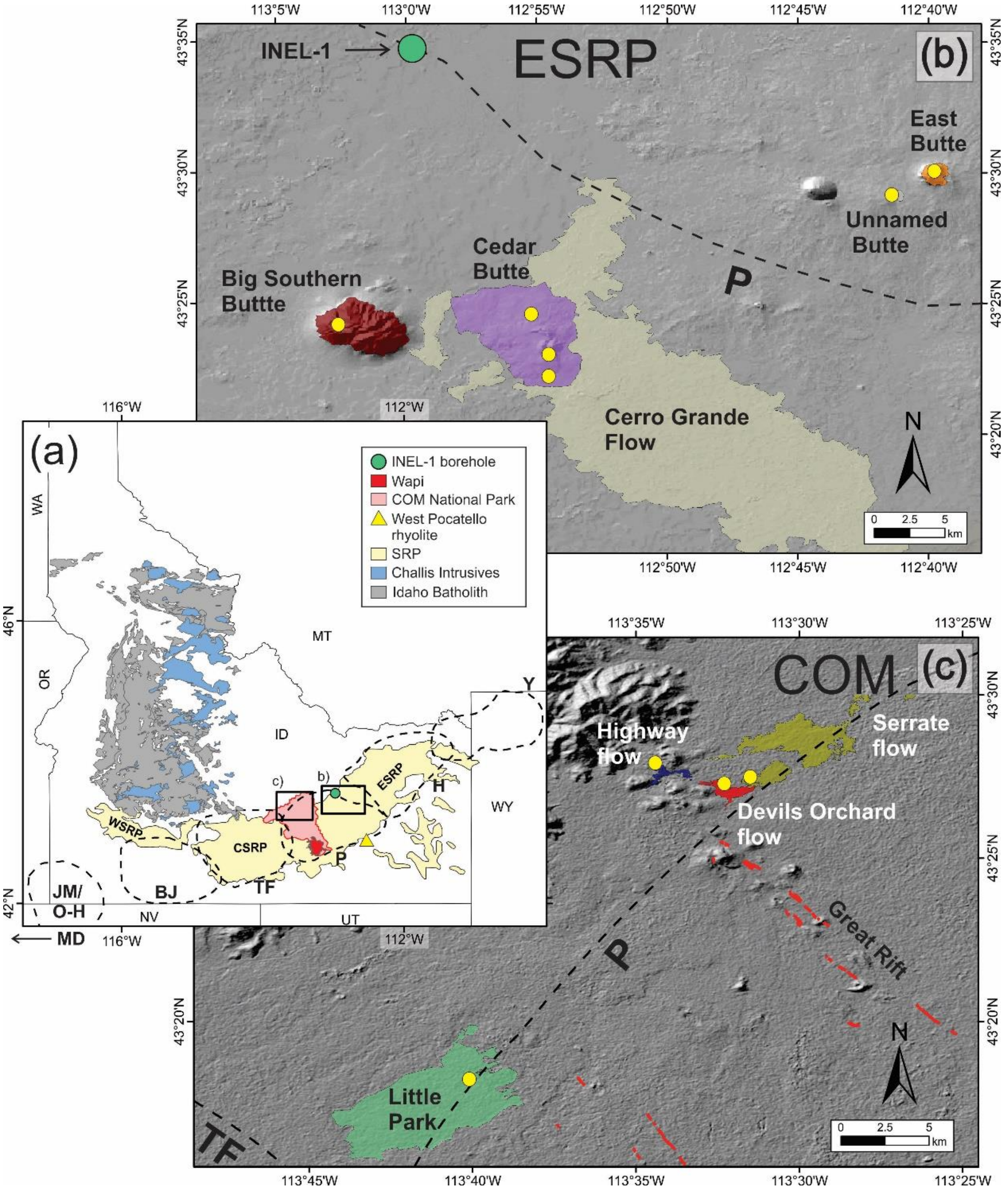

Fig. 1. *Snake River Plain overview map with subdivisions of western, central, and eastern domains (WSRP, CSRP, and ESRP, respectively) as well as the Craters of the Moon (COM) volcanic field (delineated by the national monument boundaries) and additional geological features mentioned in the text (a). Dashed lines encompass time transgressive caldera fields of the Mid-Miocene to Quaternary Yellowstone hotspot track (MD = McDermitt, JM/O-H = Juniper Mountain/Owyhee Humboldt, BJ = Bruneau-Jarbidge, TW = Twin Falls, P = Picabo, H = Heise, and Y = Yellowstone) after McCurry and Rodgers (2009). Extent of Idaho Batholith and Challis Intrusives*

shown after Gaschnig et al. (2010). Sample locations for (b) ESRP Quaternary rhyolite domes and (c) COM basaltic trachyandesite intermediate flows. The Pleistocene-Holocene Cerro Grande basalt flow is plotted for comparison, and the basaltic Little Park lava field indicates sampling location for a COM xenolith. Caldera boundaries are shown as dashed lines (see panel a) along with other geological features mentioned in the text. Digital elevation model uses ASTER GDEM data (https://gdemdl.aster.jspacesystems.or.jp) and the geological units are based on Kuntz et al. (1994; 2007).

The crustal underpinnings of Yellowstone hotspot and subsequent ESRP volcanism (Fig. 1) include Archean rocks that belong to the western margin of the Wyoming Province (e.g., Chamberlain *et al.*, 2003) as demonstrated by crustal xenolith populations and chemical contamination signatures in the volcanic rocks (Kuntz, 1992, Leeman, 1982b, Menzies *et al.*, 1984). The Cretaceous Idaho Batholith underlies the westernmost parts of the Snake River Plain (e.g., Gaschnig *et al.*, 2011, Hyndman, 1983). In addition, the regional upper crust comprises Paleozoic–Mesozoic sedimentary strata, as well as shallow intrusions and volcanic deposits of Eocene age that are subsumed under the Challis magmatic episode (Fisher & Johnson, 1995a, Fisher & Johnson, 1995b). Eocene–Miocene to recent Basin and Range block faulting subsequently extended and dissected the crust, although faults are largely buried by younger volcanic rocks in the ESRP (e.g., Faulds *et al.*, 1998). Drill cores in the center of the ESRP (e.g., INEL-1; Fig. 1) and O-isotopic compositions of caldera and post-caldera units also indicate pervasive hydrothermal alteration of intra-caldera fill for the Miocene–Pleistocene volcanism (Boroughs *et al.*, 2012, Drew *et al.*, 2013, Ellis *et al.*, 2013). Remelting and/or assimilation of such rocks produces a characteristic low-δ^{18}O magma signature for many of the rhyolites (e.g., Bindeman & Simakin, 2014, Colón *et al.*, 2018, Drew *et al.*, 2013).

ESRP-COM magma evolution and the presence of zircon

Pliocene–Holocene post-hotspot volcanism in the ESRP is dominantly mafic, with lava flow outpourings that formed large shield volcanoes collectively reaching thicknesses of 1.7–3.1 km (Anders & Sleep, 1992, Chadwick *et al.*, 2023, Rodgers *et al.*, 2002, Whitehead, 1992). Near the axis of the ESRP, evolved volcanism produced several endogenous domes (Unnamed Butte, East Butte, Cedar Butte, Big Southern Butte; Fig 1a) and cryptodomes that created surface uplift but remained concealed in the subsurface (e.g., Middle Butte, Buckskin Dome, and Ferry Butte) between c. 1.4 and 0.3 Ma without any apparent time-transgressive relation (Kuntz & Dalrymple, 1979, McCurry *et al.*, 1999, McCurry *et al.*, 2008, Spear, 1979, Spear & King, 1982). Rhyolite predominates in these domes, except for Cedar Butte flows, drilled samples from Unnamed Butte, and enclaves from East Butte which are intermediate in composition (McCurry *et al.*, 2008). Although individual domes stand out prominently by up to ~700 m from the ESRP lava plains and reach impressive volumes of ~10 km^3 in the case of Big Southern Butte, the collective volume of evolved lavas and domes of ~105 km^3 is subordinate to the estimated 12,300 km^3 of mafic lava flows (McCurry *et al.*, 2008). Zircon in ESRP rhyolites has been petrographically identified as an accessory mineral (e.g., McCurry et al., 1999; Ganske, 2006); its presence in ESRP intermediate rocks, however, has been elusive. No detailed petrochronological characterization of ESRP zircon existed prior to this study. Whole rock Zr abundances record a shift from initially increasing towards decreasing abundances with increasing SiO_2, and thus zircon saturation has been indirectly inferred to begin at 58–61 wt.% SiO_2 (McCurry *et al.,* 2008; Fig. 2a). The exception are some intermediate compositions from a drillhole underneath Unnamed Butte in the ESRP, where a direct mixing trend between basaltic and rhyolitic endmembers without Zr-enrichment is evident (Fig. 2a).

COM eruptive periods are classified according to their stratigraphic age ranging from "H" at c. 15 ka to "A" at c. 2.5 ka (Kuntz *et al.*, 2007). During the most recent period A, eight lava flows erupted from vents on the northern end of the Great Rift (Fig. 1b) mapped as the Broken Top, Blue Dragon, Trench Mortar Flat, North Crater, Big Craters, Serrate, Devils Orchard, and Highway flows (Kuntz *et al.*, 1986, Kuntz *et al.*, 2007, Stearns, 1928). Among these, Serrate, Devils Orchard, and Highway flows share the same appearance as jagged blocky and aa flows of evolved, trachyandesitic composition. In contrast to the ESRP mafic lavas, which contain only rarely xenoliths, these are comparatively abundant in COM lavas. Xenoliths comprise two major types, felsic granulites and vesicular rhyolites (e.g., Leeman *et al.*, 1976, Stout *et al.*, 1994). The granulitic type is sourced in Archean basement (e.g., Leeman *et al.*, 1985, Menzies *et al.*, 1984), whereas the rhyolitic type has been assigned to Tertiary volcanic rocks present in the upper crust (Putirka *et al.*, 2009). Evolved COM lavas of period A also contain accessory zircon, which is absent in the more primitive basaltic lavas that erupted during the earlier periods (Kuntz *et al.*, 1986, Stout *et al.*, 1994). On one hand, zircon in COM lavas hosted in glomerocrysts has been interpreted as indicative for a xenocrstic origin (Stout *et al.*, 1994), but on the other, autocrystic zircon has been predicted from decreasing Zr abundances with increasing SiO_2 at ~59 wt.% (Leeman *et al.,* 1976; Fig. 2a).

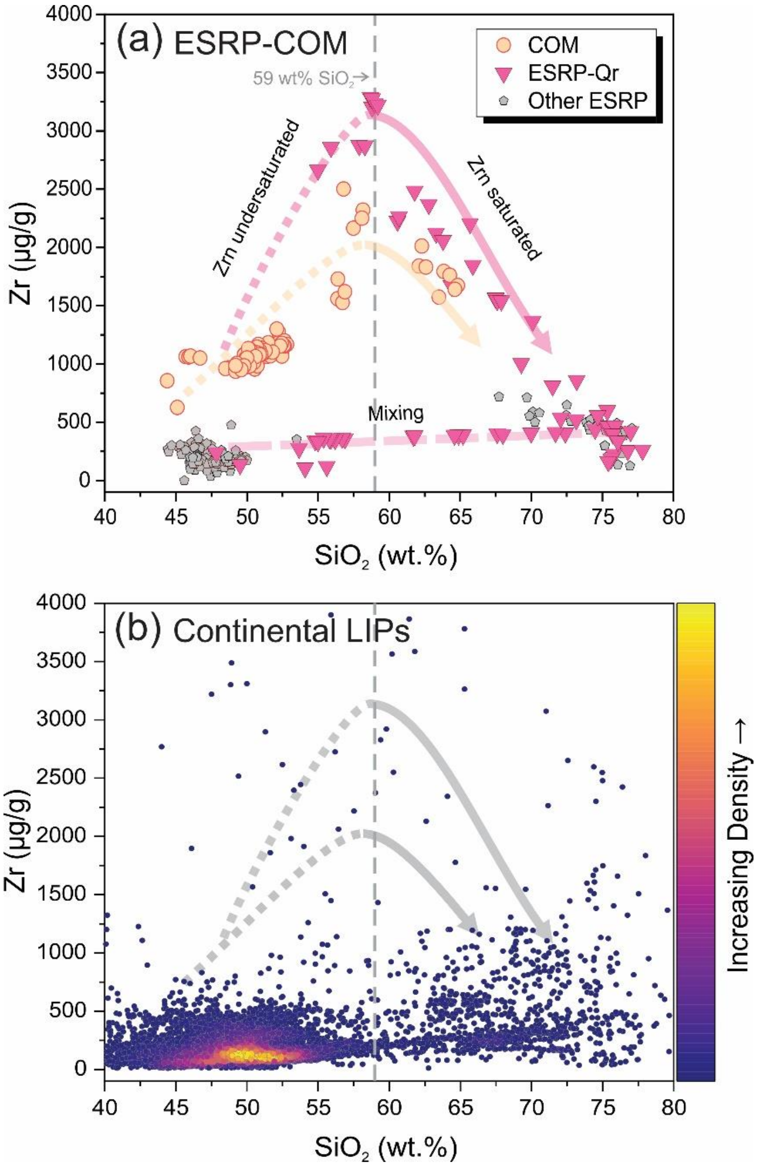

Fig. 2. *Whole rock trace element Zr abundances against SiO_2 for Quaternary (Qr) volcanic rocks of the ESRP and COM systems (a). Short-dashed lines indicate magmatic Zr enrichment due to the incompatible behavior of Zr, whereas solid lines designate Zr depletion after the melt reaches zircon saturation at ~59 SiO_2 wt% (McCurry et al., 2008; Chadwick et al., 2023). Long-dashed line represents magma mixing inferred from drill samples of Unnamed Butte (McCurry et al., 2008). To compare whole rock compositions for EPSR and COM with volcanic rocks from large igneous provinces (LIPs), data for continental flood basalt provinces are plotted (b) from pre-compiled data for North American Igneous Province, Siberian Traps, Deccan, Central Atlantic Magmatic Province, Emeishan, Karoo and Ferrar, Paraná, and Etendeka (DIGIS Team, 2023). Gray arrows representing schematic Zr-evolution trends as in panel (a).*

MATERIAL AND METHODS

For the ESRP evolved centers, three samples from Cedar Butte, and one sample each from Unnamed Butte, East Butte, and Big Southern Butte were collected for this study (Table1; Fig. 1b). For COM evolved lavas, one sample each from Devils Orchard and Highway flows, as well as two samples from Serrate flow were acquired within the Craters of the Moon National Monument (Fig. 1c; Table 1). Several cm-sized granulitic xenoliths were sampled from Serrate flow, but because of their small size, these were only used for petrographic inspection. A large (~12 cm in diameter) xenolith fragment from the Idaho State University collection was therefore included, which was derived from Little Park hawaiite flow on the south-southeast side of the COM (Fig. 1c).

Samples were crushed using a hammer or a hydraulic press, and the fine fraction was sieved to <250 µm. All powders were passed through hydrodynamic density separation yielding heavy minerals concentrates. For COM, the ilmenite-rich concentrates were further processed in a Frantz magnetic separator to enrich the non-magnetic minerals including zircon. Zircon crystals were then hand-picked under a binocular microscope and mounted in epoxy together with zircon reference materials AS3 (Paces & Miller, 1993), 91500 (Wiedenbeck *et al.*, 2004) and Temora 2 (Black *et al.*, 2004). Epoxy mounts were ground with silicon carbide abrasives to expose grain interiors and then polished using diamond paste (1 µm).

For scanning electron microscope (SEM) analysis using the Heidelberg University LEO 440, epoxy mounts were coated with a 20 nm Au layer. Images were generated using a backscattered electron (BSE) detector and a Gatan Mini-CL detector at beam conditions of 20 keV and 2.0–4.0 nA, and 10 keV and 15 nA, respectively, to visualize internal zircon textures. After that, the Au coat was gently removed, and mounts were ultrasonically cleaned with aqueous decontaminants and rinsed multiple times with deionized water and methanol. They were then coated with a ~50 nm Au layer prior to secondary ionization mass spectrometry (SIMS) analysis.

U-Th-Pb geochronology and trace elements

For disequilibrium dating, zircon interiors were analyzed using the CAMECA ims 1300-HR^3 SIMS at the John de Laeter Centre at Curtin University, Australia. A $^{16}O^-$ primary beam of ~40 nA in Gaussian mode was focused to an ~25 µm diameter spot, and secondary ions were extracted at 10 kV and steered through a 400 µm contrast aperture, a 4000 µm field aperture, and a 50 eV bandpass energy slit in circular mode. The secondary column was tuned to a mass resolution m/Δm ~5000

(250 μm multi-collector slit width). Secondary ion intensities of 244.03, $^{230}Th^{16}O$, $^{232}Th^{16}O$, and $^{238}U^{16}O$ were collected simultaneously in L2 and L1 electron multipliers (EMs) for the 244.03 background and $^{230}Th^{16}O$ peak, whereas Faraday cups with 10^{12} Ω resistors were used in C and FC2 positions for the high-abundance peaks $^{232}Th^{16}O$ and $^{238}U^{16}O$ for 10 s per cycle. The static magnetic field was maintained using a nuclear magnetic resonance probe. $^{90}Zr^{90}Zr^{16}O_4$ and $^{90}Zr^{92}Zr^{16}O_4$ were measured by electrostatic peak switching using the dsp2-x deflector for 1 s per cycle, followed by another dsp2-x switch to measure off-peak intensities as background/baseline on 244.3, 246.3, 248.3, and 254.3 for 5 s per cycle. Each analysis started with a 30 s pre-sputtering during which the beam was rastered over a 10 × 10 μm area to remove surface contaminants, followed by automatic centering of the transfer deflectors. Secondary ion intensities were integrated over 20 cycles and corrected for dead-time and FC baseline using the in-house ZIPSv. 3.1.1. data reduction software. Backgrounds measured on 244.03 and 246.3 were averaged and subtracted from the $^{230}Th^{16}O$ peak. The U-Th relative sensitivity factor (RSF) was calibrated from linear regression in $^{208}Pb/^{206}Pb$ vs. $^{232}ThO/^{238}UO$ space (Reid *et al.*, 1997), and the accuracy of measured (^{230}Th)/(^{238}U) (activities indicated by parentheses) was confirmed by repeatedly analyzing secular equilibrium zircon reference AS3 (1099.1 Ma; Paces & Miller Jr, 1993), which yielded a weighted average (^{230}Th)/(^{238}U) = 1.008 ± 0.016 (2se uncertainties throughout, unless otherwise indicated; mean square of weighted deviates MSWD = 1.09; n = 11). 91500 reference zircon (81.2 μg/g U; Wiedenbeck *et al.*, 1995) was used to calibrate $^{238}UO/^{90}Zr^{90}Zr^{16}O_4$ to infer U abundances. All analyses on unknowns where the signal of 246.03 was not at least 10% higher than the 244.03 background where omitted.

For U-Pb geochronology, crystals were analyzed using a 12–18 nA $^{16}O^-$ primary beam with a spot diameter of ~20 μm, with secondary ions being transmitted through contrast and field apertures of 400 and 3000 μm, respectively, and an energy bandpass of 50 eV in rectangular mode. For ^{232}Th and ^{238}U, a -20 eV offset was applied, but not for the other species ($^{94}Zr_2O$, ^{204}Pb, ^{206}Pb, ^{207}Pb, ^{208}Pb, ^{238}UO, and $^{238}UO_2$). Secondary ions were detected using the axial electron multiplier in peak hopping mode for 10 cycles after 20 s of pre-sputtering with a 10 × 10 μm raster. Replicate analyses of AS3 (COM), Temora2 (ESRP) and 91500 (COM and ESRP) zircon references were used to establish U-Pb, U-Th, and U-Zr RSFs. For the U-Pb RSF, this was achieved by applying a linear regression in $^{238}UO_2/^{238}U$ vs. $^{206}Pb/^{238}U$ space; U-Th RSF values were determined from regression in $^{208}Pb/^{206}Pb$ vs. $^{232}Th/^{238}U$, and for the U-Zr RSF values an 81.2 μg/g U abundance of 91500 zircon along with stoichiometric Zr was used (Wiedenbeck *et al.*, 1995). Zircon reference 91500 analyzed as a control yielded a ^{206}Pb/^{238}U age of 1066 ± 13 Ma (MSWD = 0.17, n = 21) relative to the reported age of 1065 Ma (Wiedenbeck *et al.*, 1995). Common Pb was corrected using ^{207}Pb, and all ^{206}Pb/^{238}U ages were adjusted for initial disequilibrium in ^{230}Th, which was estimated using measured Th/U in zircon divided by whole-rock Th/U for the corresponding sample from Ford (2005) and Ganske (2006) as stated in Table S1. All radiometric ages are calculated as weighted averages and uncertainties are reported at 95% confidence, accounting for excess scatter by multiplying with the square root of the MSWD if >1, and the corresponding percentile of the Student t distribution for the appropriate degree of freedom (Mahon, 1996). Systematic uncertainties (*e.g.,* from decay constants) for such young zircons are negligible at the stated error levels; practically, this means that multiple levels of age error (i.e., without and with decay constant uncertainty; e.g., Condon *et al.*, 2024) result in the same numerical value, and hence only one error level is stated for simplicity. Similarly, the comparison between different age methods (*e.g.,* U-Pb and K-Ar) theoretically should account for systematic uncertainties resulting from the respective decay constants or references used, but in practice our calculations show that these effects are smaller than the rounded uncertainties stated. For the same reason, we also cite published values as given in the literature.

Trace elements were obtained following methods described in Schmitt *et al.* (2017), applying a ~15 nA ^{16}O$^-$ primary beam in Gaussian mode that targeted the same craters previously analysed for U-Th-Pb geochronology; no extra coating was needed for this step. Energy filtered (-100 eV) secondary ions were detected at low (m/Δm = 2000) mass resolution. Molecular interferences of light rare earth element (LREE) oxides on atomic ion species of the middle and heavy rare earth elements (MREE, HREE) were subtracted for ^{156}Gd$^+$ (^{140}CeO$^+$), ^{158}Gd$^+$ (^{142}CeO$^+$, ^{142}NdO$^+$), ^{159}Tb$^+$ (^{143}NdO$^+$), ^{165}Ho$^+$ (^{149}SmO$^+$), ^{169}Tm$^+$ (^{153}EuO$^+$), ^{172}Yb$^+$ (^{156}GdO$^+$), and ^{175}Lu$^+$ (^{159}TbO$^+$) using correction factors for oxide and hydride species determined on doped glasses. Trace element RSFs were calibrated on NIST SRM 610 (Pearce *et al.*, 1997), and accuracy was monitored by analyzing 91500 reference zircons (Wiedenbeck *et al.*, 2004). All data on unknowns were screened for anomalies in the light rare earth element index (LREE-I = Dy/Nd + Dy/Sm), discarding all values <30 (Bell *et al.*, 2016; 2019), which are interpreted to indicate overlap onto non-zircon phases (e.g. apatite, glass, or oxide inclusions). Titanium abundances in zircon were translated into Ti-in-zircon crystallization temperatures (TiZr) based on the equation in Ferry and Watson (2007). For ESRP, a value of $\alpha TiO_2 = 0.57$ was calculated from magnetite-ilmenite equilibrium exchange (Ghiorso & Evans, 2008) from Unnamed Butte using compositions reported in McCurry *et al.* (2008). Because most ESRP lavas contain quartz, $\alpha SiO_2 = 1$ is applied, acknowledging that for Cedar Butte intermediate lavas this is likely an overestimate (e.g., by ~35°C for $\alpha SiO_2 = 0.72$). For COM evolved flows, magnetite-ilmenite compositions form Stout *et al.* (1994) yielded $\alpha TiO_2 = 0.55$, and $\alpha SiO_2 = 0.72$ assuming melt equilibrium with orthopyroxene (Beattie, 1993). For completeness, COM xenolith zircon temperatures were also calculated assuming unity values of $aTiO_2$ and $aSiO_2$ in the absence of other constraints (Fig. S3). Analytical uncertainties translate into temperature uncertainties of <10 °C based on the external reproducibility of Ti analysis of 91500 zircon reference (4.7 ± 0.3 µg/g; 1s; n = 11). Melt oxygen fugacity (fO_2) is expressed relative to the fayalite-magnetite-quartz buffer (ΔFMQ) after Loucks *et al.* (2020). The full SIMS petrochronological data set, including values for the secondary zircon references, is presented in the Supplement (Tables S1–S3).

(U-Th)/He zircon dating

After the U–Th disequilibrium dating, zircon from Highway flow were dated by (U–Th)/He methods in the Western Australia ThermoChronology Hub (WATCH) Facility at the John de Laeter Centre (Curtin University), following the methods described in (Danišík *et al.*, 2012, Danišík *et al.*, 2017, Danišík *et al.*, 2020). This sample was selected as it yielded comparatively abundant zircon in heavy mineral separates. Representative zircon crystals were individually photographed and measured for physical dimensions with the purpose of calculating their dimensions to further correct the ages for alpha ejection (Ft-correction; Farley *et al.*, 1996). Our initial experiments on He extraction in the investigated zircon revealed extremely low He contents in single zircon crystals stemming from their young eruption age. Therefore, composite samples with multiple zircon grains were analyzed to increase the He signal. Accordingly, multi-grain aliquots (n = 33, 50, and 44) were prepared by selecting zircon grains of similar size and shape to minimize variation in Ft correction factors. The selected grains were then transferred and packed into niobium (Nb) microtubes and loaded into an Alphachron II instrument for He extraction. ^4He together with other gases were extracted at ~1250 °C under ultra-high vacuum using a diode laser, cleaned on Ti-Zr getters, and spiked with 99.9% pure ^3He gas. The volume of ^4He was measured by isotope dilution on a QMG 220 M1 Pfeiffer Prisma Plus mass spectrometer. A “re-extract” was run after each analysis to verify complete outgassing of the crystal. Helium gas signals were corrected for blank, determined by analysing empty Nb microtubes interspersed between the unknowns using the same gas extraction procedure. After the He measurements, Nb microtubes containing the crystals were retrieved from the Alphachron, spiked with ^{235}U and ^{230}Th, and dissolved in Parr acid digestions vessels in two cycles of HF, HNO_3 (cycle 1), and HCl acids (cycle 2), following the procedures described in Evans *et al.* (2005). Sample, blank, and spiked standard solutions were then diluted with Milli-Q water and analysed by isotope dilution for ^{238}U and ^{232}Th, and by external calibration for ^{147}Sm on an Agilent 7700 ICP-MS. The total analytical uncertainty (TAU) was calculated as a square root of sum of squares of uncertainty on He and weighted uncertainties on U, Th, and Sm measurements. The zircon (U-Th)/He ages were corrected for alpha ejection (Ft-correction) after Farley *et al.* (1996), whereby homogenous distributions of U, Th, and Sm were assumed for the crystals, and average Ft correction factor was calculated from Ft factors of individual grains in each aliquot. Fish Canyon Tuff zircon with a (U–Th)/He age of 28.3 ± 1.3 Ma (Reiners, 2005) was used as reference standard yielding a mean (U–Th)/He age of 28.5 ± 1.8 Ma (n = 3). The Ft-corrected (U–Th)/He ages were corrected for disequilibrium using the MCHeCalc software (Schmitt *et al.*, 2010) where the D_{230} parameter was calculated after dividing the Th/U ratios from the composite samples by the Highway flow whole-rock value (Chadwick *et al.*, 2023), whereas D_{231} was assumed as 3.0 based on Pa/U zircon–rhyolite melt partitioning ratio (Schmitt, 2007). The full data set, including values for the secondary zircon reference, is presented in the supplement (Table S4).

Oxygen and Hafnium isotopes

Oxygen isotope (^{16}O and ^{18}O) analysis of zircon was performed in two sessions using the CAMECA ims 1280-HR at the Heidelberg Ion Probe (HIP) laboratory. Primary beam intensities were 1.0–1.6 nA (Cs^+, critically illuminated, 10 μm raster) and negative secondary ions of ^{16}O and ^{18}O were simultaneously detected using two FCs in the multi-collection array with electrometers equipped with a 10^{10} Ω resistor for ^{16}O and a 10^{12} Ω resistor for ^{18}O measurements. Each analysis comprised 20 s of pre-sputtering (12 μm raster), automatic centering routines for the secondary beam, and 75 s of data collection (15 cycles of 5 s integration time). The FC baselines were recorded during the pre-sputtering. For ^{16}O, the corresponding baseline was subtracted from raw counts, whereas for ^{18}O a model was fitted to all individual FC baseline measurements per day, and interpolated values were used for correction. Zircon reference materials 91500 (δ^{18}O = +9.86 ‰; Wiedenbeck *et al.*, 2004) and AS3 (secondary standard, δ^{18}O = +5.34 ‰; Trail *et al.*, 2007) were intermittently analyzed to determine instrumental mass fractionation factors and to monitor and correct instrumental drift. For drift correction, 10–15 unknowns were bracketed by eight analyses of 91500 or AS3 as primary references; the average repeatability (1s) for them was 0.17, (n = 48) and 0.16 (n = 75) for the two sessions (Table S5). Analytical uncertainties were calculated by propagating the internal error of each analysis and the standard error of the corresponding bracket in quadrature. Accuracy was monitored from replicate analyses of secondary reference zircons, and results were always within <0.4 ‰ of the reported values. All $\delta^{18}O$ values are relative to VSMOW (Baertschi, 1976).

For Hf isotope measurements, a ThermoScientific NEPTUNE Plus multicollector (MC)-ICP-MS system at FIERCE, Goethe University Frankfurt coupled to a RESOlution 193nm ArF Excimer (Resonetics) laser system with a S155 two volume ablation cell was used. The analytical method including data processing was as described in Gerdes and Zeh (2006), (2009). Laser spots with lateral dimension of ~33 µm in diameter were set on top of SIMS analysis pits. Each grain was ablated for 38 s using a fluence of 3.5 J cm^{-2} and a frequency of 5.2 Hz, which resulted in an ablation rate of 0.6 µm s^{-1}, or ~23 µm total depth. An exponential law with $^{179}Hf/^{177}Hf$ value of 0.7325 was used for instrumental mass bias corrections. For Yb isotopes, instrumental mass bias was corrected using the Hf mass bias of the individual integration step multiplied by a daily βHf/βYb offset factor (see Gerdes & Zeh, 2009). This correction factor is very reproducible for over 20 years with a value of 1.080. All data were adjusted relative to the JMC475 $^{176}Hf/^{177}Hf$ ratio = 0.282160 and quoted uncertainties are quadratic additions of the within-run precision of each analysis and the reproducibility of JMC475 (0.0028% 2se, n = 8). Initial $^{176}Hf/^{177}Hf$ and εHf were calculated using the U-Th-Pb and U-Pb ages determined by SIMS, and the following CHUR parameters: $^{176}Lu/^{177}Hf = 0.0336$, and $^{176}Hf/^{177}Hf = 0.282785$ (Bouvier et al., 2008). Secondary zircon reference GJ-1 ($^{176}Yb/^{177}Hf$ of < 0.008) and Temora ($^{176}Yb/^{177}Hf$ of 0.02-0.07) analysed in the same analytical session show a repeatability of 0.6 and 0.8 εHf units (2s) and agree well with published values (Table S6).

Table 1. Summary table of average U-Th and U-Pb ages and isotopic compositions of the zircons from ESRP and COM in this study. Map unit designations are stated in parentheses. For comparison, eruptions ages and whole rock compositional data were compiled from the literature. Uncertainties for age data are stated at 95% confidence; isotopic ratios are stated with 2se uncertainties (see supplementary tables S1–S6 for individual zircon data).

Unit	Eruption age (ka)	SiO_2 (wt%)	Zr (µg/g)	Sample name	Coordinates (WGS 84)		Zircon crystallization age		$\delta^{18}O$	εHf^{g}
					Latitude °N	Longitude °W	(ka or *Ma*)	MSWD		
ESRP										
Big Southern Butte	327 ± 3.2^{a}	76.4^{d}	309^{d}	BSB	43.40311	−113.04247	335 ± 5	0.56	+3.67 ± 0.37	-4.7 ± 0.9
Cedar Butte (Qpc)		67.5^{d}	1,563^{d}	CBD	43.38417	−112.90831	426 ± 8	1.14	+3.60 ± 0.48	-4.4 ± 1.5
Cedar Butte (Qr1 flow)	400 ± 28^{a}	67.6^{d}	1,551^{d}	CBF	43.37106	−112.90831	434 ±15	1.73	+3.78 ± 0.45	-3.4 ± 2.0
Cedar Butte (Qb5 flow)		61.8^{d}	2,483^{d}	CBF	43.40978	−112.91944	459 ± 37	0.94	+4.01 ± 0.28	-3.9 ± 1.8
East Butte	580 ± 90^{b}	75.4^{d}	465^{d}	EB	43.50100	−112.66256	697 ± 10	0.71	+2.68 ± 0.41	-4.8 ± 1.6
Unnamed Butte	1,400 ± 28^{b}	62.7^{d}	580^{d}	UNB	43.48661	−112.68986	1,534 ± 22	0.81	+2.21 ± 0.24	-5.0 ± 1.2
COM										
Serrate flow (A)		58.7^{e}	1,677^{e}	SF	43.45798	−113.52443			+5.41 ± 0.48	-10.5 ± 1.4
Devils Orchard flow (A)	2.4 ± 0.3^{c}	58.1^{e}	1,850^{e}	DOF	43.45492	−113.53540	$6.24^{+2.61}_{-2.55}$	1.32	+5.68 ± 0.35	-10.6 ± 1.5.
Highway flow (A)		60.6^{e}	1,600^{e}	HF	43.46518	−113.57297			+5.54 ± 0.31	-10.3 ± 1.6
Little Park (D)	-	-	-	Xenolith	43.30207	−113.66669	*3,239 ± 15*^{f}	4.8	+5.82 ± 0.47	-75.8 ± 2.0

[a] ^{40}Ar/^{39}Ar age from Turrin et al. (2023)

[b] K-Ar age from Kuntz et al. (1994)

[c] ^{14}C age from Big Craters cogenetic flow from Kuntz et al. (2007)

[d] Average from McCurry et al. (2008)

[e] Average from Chadwick et al. (2023)

[f] U-Pb age in Ma in italics

[g] initial value for average zircon crystallization age, except for xenolith which is stated for a Holocene age

RESULTS

Zircon crystallization and eruption ages

Most of the zircon crystals from ESRP rhyolite domes and flows have typical dimensions of >100 µm in length (up to 320 µm) and occur as individual crystals in the matrix (Fig. 3a). By contrast, COM lava flow zircon crystals are generally smaller and between 60 and 250 µm in length and they are also frequently ingrown with other mineral phases, especially with olivine and ilmenite (Fig. 3b-d). Zircon crystal morphology in both sample suites is mostly euhedral and dominated by prismatic forms. Internal structures include glass and apatite inclusions, with CL imaging frequently showing coarse oscillatory and minor sector zonation, as well as dark interiors for ESRP and COM (Fig. 4a-b). COM xenolith zircons are up to ~250 µm long and have rounded edges. Internally, they display fine oscillatory zonation with truncated inner domains (Fig. 4c).

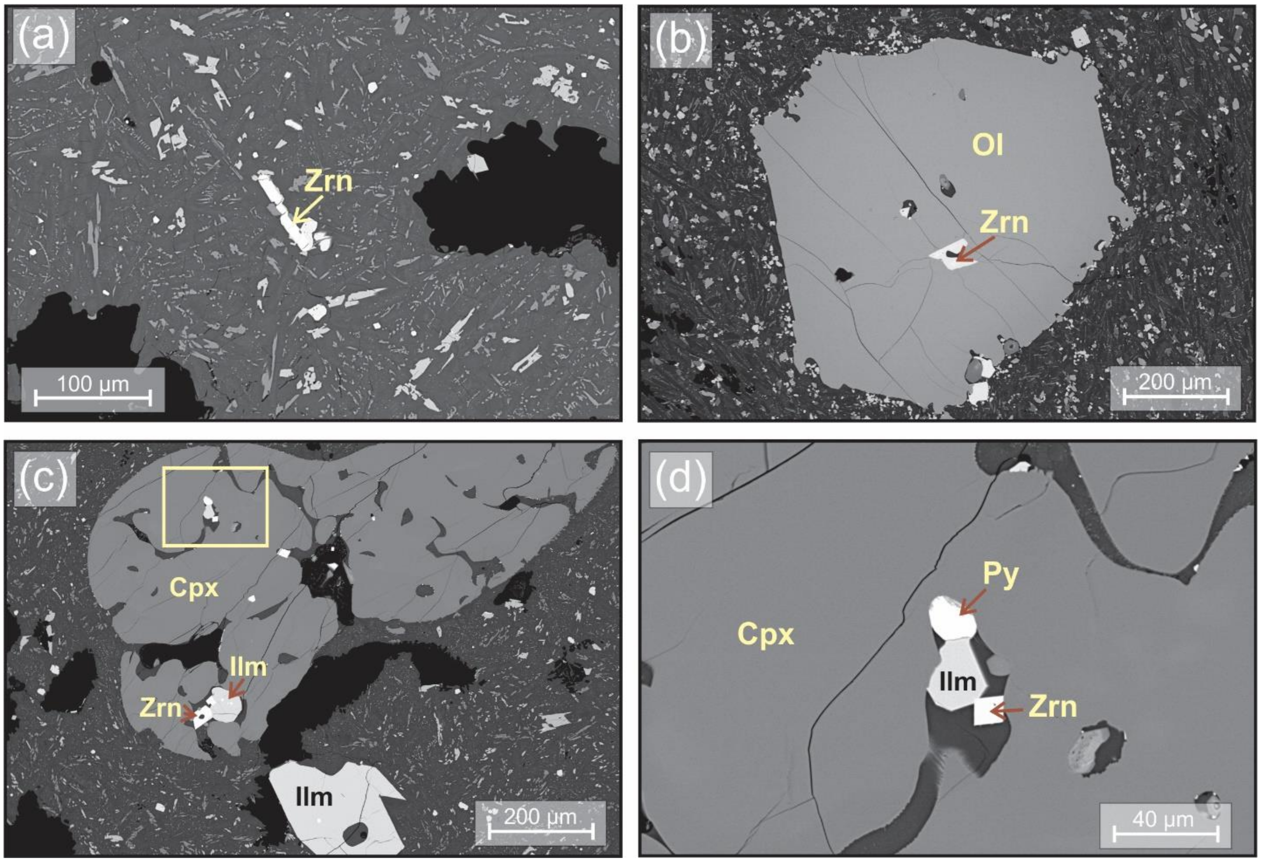

Fig. 3. *Backscattered electron images for COM thin sections: (a) zircon crystal in matrix; (b) zircon crystal included in olivine; (c) two zircon crystals associated with ilmenite and pyrite partially included in clinopyroxene; (d) enlarged image of zircon included in clinopyroxene*

ESRP zircon crystallization ages typically predate the corresponding eruption ages based on published K-Ar and ^{40}Ar/^{39}Ar results (Table 1 and Fig. 5a-f; Kuntz *et al.*, 1994; Turrin et al., 2023). The oldest dome, Unnamed Butte, yielded a ^{206}Pb/^{238}U age of 1,534 ± 22 ka (MSWD = 0.81, n = 38) while the published K-Ar age is 1,400 ± 28 ka (Kuntz *et al.*, 1994). After a c. 800 ka hiatus, the next youngest zircon crystallization episode occurred underneath East Butte at 697 ± 10 ka (MSWD = 0.71, n = 22) with a K-Ar date of 580 ± 90 ka recording the eruption. Following another hiatus of c. 250 ka, the Cedar Butte dome and one of its stratigraphically lowest flows (silicic trachyte Qr1; McCurry *et al.*, 2008) record the same zircon crystallization episode at 426 ± 8 (MSWD = 1.14, n = 21) and 434 ± 15 ka (MSWD = 1.73, n = 22), respectively. A second flow from Cedar Butte (mafic trachyte Qb5) yielded similar zircon crystallization ages averaging 459 ± 37 ka (MSWD = 0.94, n = 13), but uncertainties are elevated because of comparatively low U concentrations in these zircons (see next section). Collectively, Cedar Butte zircon crystallization ages are close to the K-Ar and ^{40}Ar/^{39}Ar ages of 400 ± 19 ka and 400 ± 28 ka, respectively (Kuntz *et al.*, 1994; Turrin et al., 2023). The youngest zircon crystallization ages were determined for Big Southern Butte dome at 335 ± 5 ka (MSWD = 0.56, n = 37), whereas the inferred eruption age based on K-Ar and ^{40}Ar/^{39}Ar geochronology is only slightly younger at 309 ± 10 ka and 327 ± 3.2 ka, respectively (Kuntz *et al.*, 1994; Turrin et al., 2023). The differences between U-Pb zircon crystallization ages and eruption ages (Δt) translate into zircon residence times that are generally brief (between 8 ± 5 ka for Big Southern Butte and 134 ± 47 ka for Unnamed Butte). Even when considering decay constant uncertainties for the different dating methods, these values only change insignificantly (i.e. when using Renne et al., 2010, vs. the original Steiger and Jäger, 1977, values, zircon residence times are between 23 ± 13 ka for Big Southern Butte and 121 ± 46 ka for Unnamed Butte).

Zircon crystals extracted from Craters of the Moon evolved lavas (Highway, Devils Orchard, and Serrate flows) fall on the same near-horizontal trend in the (^{230}Th)/(^{232}Th) vs. (^{238}U)/(^{232}Th) diagram (Fig. 6a), signifying very recent zircon crystallization. By fixing an isochron through a melt composition as represented by whole-rock data for Highway flow (Reid, 1995) which we used also for (U-Th)/He dating, a model age of $6.2^{+2.6}_{-2.5}\ ka$ (MSWD = 1.30; n = 23) is obtained. Only four crystals (two from Devils Orchard flow and two from Highway flow) lie on the equiline, in agreement with five reconnaissance rim analyses on xenolith zircons, thus indicating zircon crystallization ages >375 ka. For zircon in secular equilibrium from the Devils Orchard flow, we subsequently determined concordant $^{206}Pb/^{238}U$ ages of 23.2 ± 2.0 Ma and 1390 ±132 Ma, respectively. In order to quantify the difference between zircon crystallization and eruption ages for COM, (U-Th)/He zircon dating was performed on three composite zircon samples from previously undated Highway flow. The resulting (U-Th)/He age of 2.05 ± 0.56 ka (n = 3; Goodness of fit = 0.48) agrees with the inferred eruption age for Highway flow based on stratigraphic correlation with the most recent flows from period A for which ^{14}C ages indicate emplacement at c. 2.4 ka (e.g., Kuntz *et al.*, 2007). This translates into a nominal Δt = 4.1 ± 2.7 ka, implying that zircon residence for the evolved COM lavas was on the millennial scale. Zircon from COM xenolith MHK-01 is mostly discordant (Fig. 6b), with discordia pointing to, with one exception, an Archean crystallization age that is defined by a 3,239 ± 15 Ma upper concordia intercept of an errorchron defined by the data (MSWD = 4.8; n = 18). The lower intercept at 155 ± 117 Ma indicates Cenozoic Pb-loss.

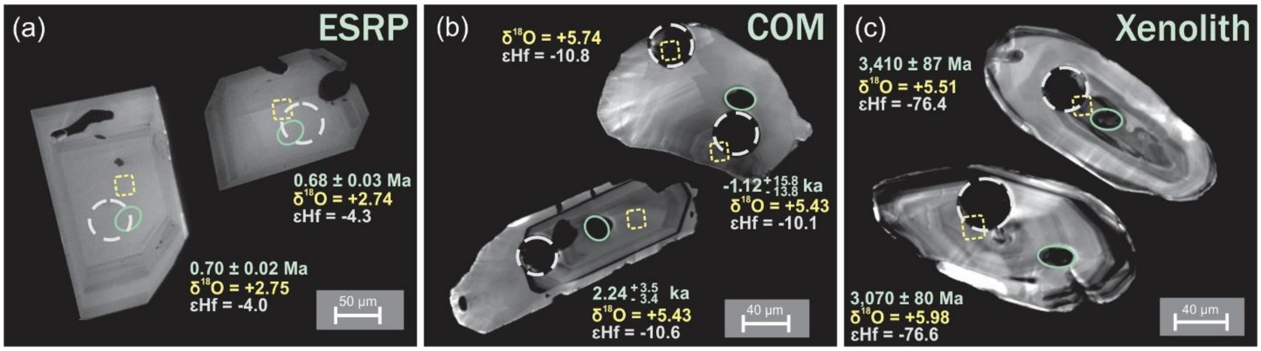

Fig. 4. *Cathodoluminscence images of zircon from ESRP and COM samples: (a) East Butte zircons SRP_EB_113 (left) and SRP_EB_111 (right), (b) Devils Orchard flow zircon COM_DOF_49 (upper) and Highway flow zircon COM_HF_14 (lower), and (c) xenolith zircon from Little Park flow COM_MHK_01_61 (upper) and COM_MHK_01_100 (lower). Note oscillatory and minor sector zonation in a and b, as well as rounded crystal boundaries in c. Analytical spots and corresponding zircon ages and isotopic values are matched by color; trace elements (not shown) were analysed in the same spot as for dating.*

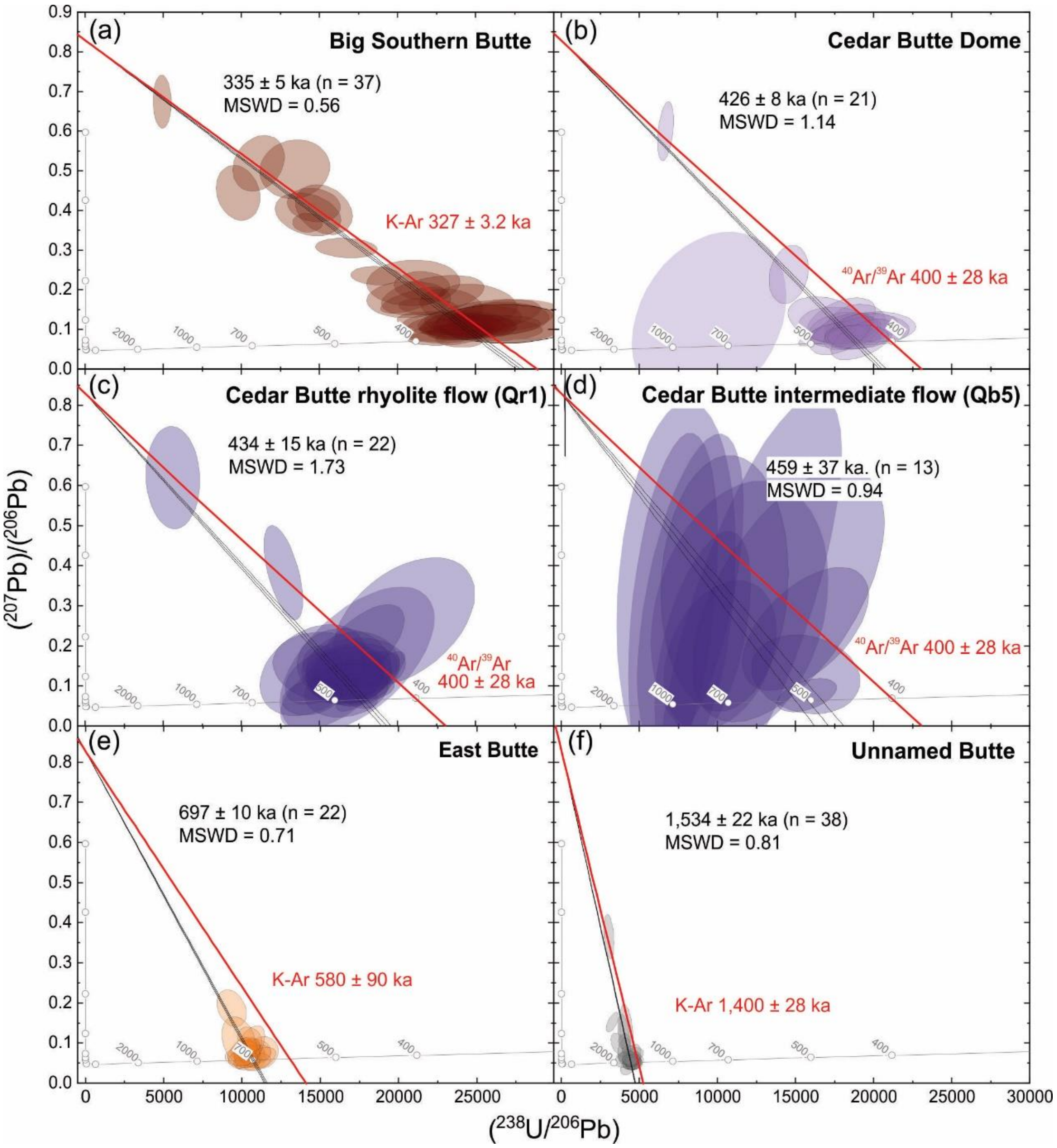

Fig. 5. *Zircon ^{207}Pb/^{206}Pb vs. ^{238}U/^{206}Pb data (2se) for ESRP rhyolite domes and intermediate flows plotted uncorrected for common Pb. Individual samples are plotted for Big Southern Butte (a), Cedar Butte Dome (b), Cedar Butte rhyolite flow (c), Cedar Butte intermediate flow (d), East Butte (e), and Unnamed Butte (f). Data define linear arrays between common Pb (y-axis intercept) and radiogenic Pb. Sample ages were calculated as weighted averages of ^{206}Pb/^{238}U ages which were individually adjusted for initial disequilibrium of ^{230}Th (see text). Concordia is plotted for disequilibrium of ^{230}Th and ^{231}Pa at the time of crystallization using initial activity ratios for the intermediate daughter and parent isotopes of 0.2 and 2.2, respectively. Red line shows model isochrons for eruption ages (Table 1).*

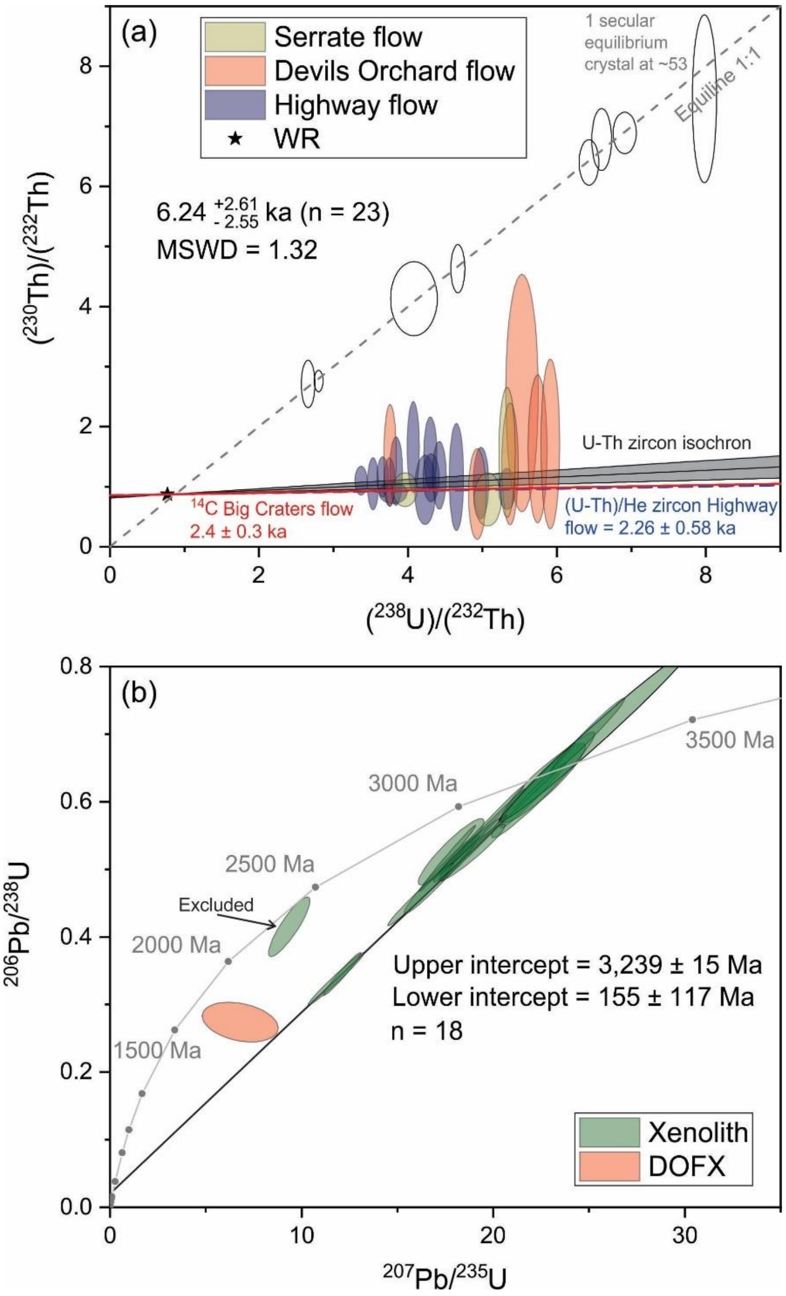

Fig. 6. *(a) Zircon (^{230}Th)/(^{232}Th) vs. (^{238}U)/(^{232}Th) isochron diagram for COM intermediate lavas. Whole rock composition of Highway flow (Reid, 1995) is used to anchor the isochron. Model isochron based on the average (U-Th)/He zircon age is plotted for comparison. Open ellipses overlapping with the equiline are interpreted as secular equilibrium xenocrysts, in part confirmed by U-Pb analysis. (b) Zircon ^{206}Pb/^{238}U vs. ^{207}Pb/^{235}U data from the xenolith and two secular equilibrium crystals from the Devils Orchard flow. Data is corrected for common Pb using measured ^{204}Pb. Lower and upper concordia intercept ages are determined using Isoplot R (Vermeesch, 2018); error ellipses and ages at 2se.*

Zircon trace elements

Uranium concentrations in the ESRP zircon crystals range from 15 µg/g (Qb5 flow from Cedar Butte) to 2,970 µg/g (Big Southern Butte). As typical for igneous zircon (e.g., Grimes *et al.*, 2007), they also correlate with Y, HREE (e.g., Yb), Hf, and Th concentrations, with a large compositional range covered by Cedar Butte intermediate lava flows, whereas concentrations for individual domes are higher and largely homogeneous (e.g., Fig. S1). Uranium concentrations in COM zircon start at a similarly low limit of 11 µg/g, but only reach a maximum value of 512 µg/g; other trace elements including Y, Yb, Hf, and Th track this enrichment trend (Fig. S1). Xenolith zircon U concentrations range from 225 to 1,450 µg/g, with typical correlations between U and these trace elements (Fig. S1). U/Yb ratios are used to discriminate petrogenetic origins of zircon, especially between continental and oceanic crustal sources with U/Yb > 0.1 and < 0.1, respectively (Grimes *et al.*, 2007). Zircon from the ESRP domes plots near U/Yb = 1, whereas the least enriched zircon from the Cedar Butte and COM intermediate flows are close to the U/Yb = 0.1 line (Fig. S2). Xenolith and xenocrystic zircons, by contrast, typically display U/Yb >1 (Fig. S2).

All ESRP and COM zircon REE patterns are enriched in HREE relative to MREE and LREE (Fig. 7a-h) with typical magmatic slopes as expressed by Gd/Yb being on average between 0.07 and 0.1, respectively. They also display negative Eu and positive Ce anomalies which primarily reflect plagioclase fractionation and preferential incorporation of Ce^{4+} into zircon controlled by fO_2, respectively (Loucks *et al.*, 2020, Trail *et al.*, 2024, Trail *et al.*, 2012). Cedar Butte intermediate lavas display a wide range of Eu/Eu* from 0.03 to 0.74, again similar to COM zircon with a range of 0.14–0.63. Zircon from the rhyolitic ESRP domes are individually homogeneous, with Eu/Eu* decreasing in the order (average ± 1s): East Butte (0.079 ± 0.010), Unnamed Butte (0.052 ± 0.011), Big Southern Butte (0.037 ± 0.003), and Cedar Butte dome (0.058 ± 0.088). Xenolith zircon REE patterns are comparatively steep (average Gd/Yb = 0.05), and Eu/Eu* ranges between 0.06 and 0.58.

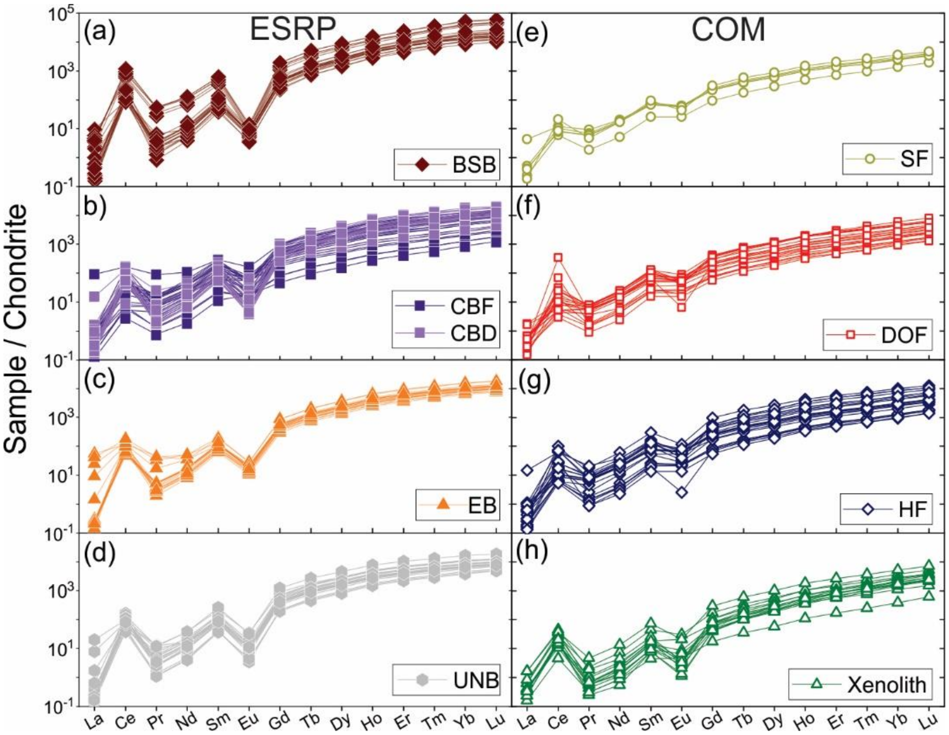

Fig. 7. *Chondrite normalized REE abundances for ESRP (a-d), COM (e-g) and xenolith (h) zircon crystals. All data were screened for contamination by non-zircon phases using the LREE-I > 30 filter (see text). Unit abbreviations from Table 1. Chondrite values from Anders and Grevesse (1989).*

Translating Ti concentrations into TiZr values indicates average temperatures for zircon crystallization from 733 °C (Unnamed Butte) to 683 °C (Big Southern Butte). In comparison, higher, but variable TiZr values are determined for ESRP Cedar Butte (695–928 °C; Fig. 8a) and COM lava flows (710–919 °C; Fig. 8c). TiZr values positively correlate with Eu/Eu* and Zr/Hf (Fig. 8b and d), indicating that variable Ti concentrations in zircon primarily record magmatic temperature variations rather than variable $aTiO_2$. Changes in temperature correlate with oxidation state (ΔFMQ) only in the intermediate lavas of ESRP and COM. They start out at high temperature below FMQ, consistent with low-fO_2 inferred for ESRP magma differentiation (Whitaker *et al.*, 2008), and reach high (ΔFMQ = +2–3), but constant values for rhyolitic zircon (Fig. 9a-b). By contrast, the prominent decrease in Th/U and Gd/Yb for the rhyolitic ESRP lavas suggests co-precipitation of apatite preferentially incorporating Th and MREE (Fig. 9c and e) while is neglected for the COM zircon (Fig. 9d and f). Xenolith TiZr values are nominally between 710 and 838 °C (Fig S3).

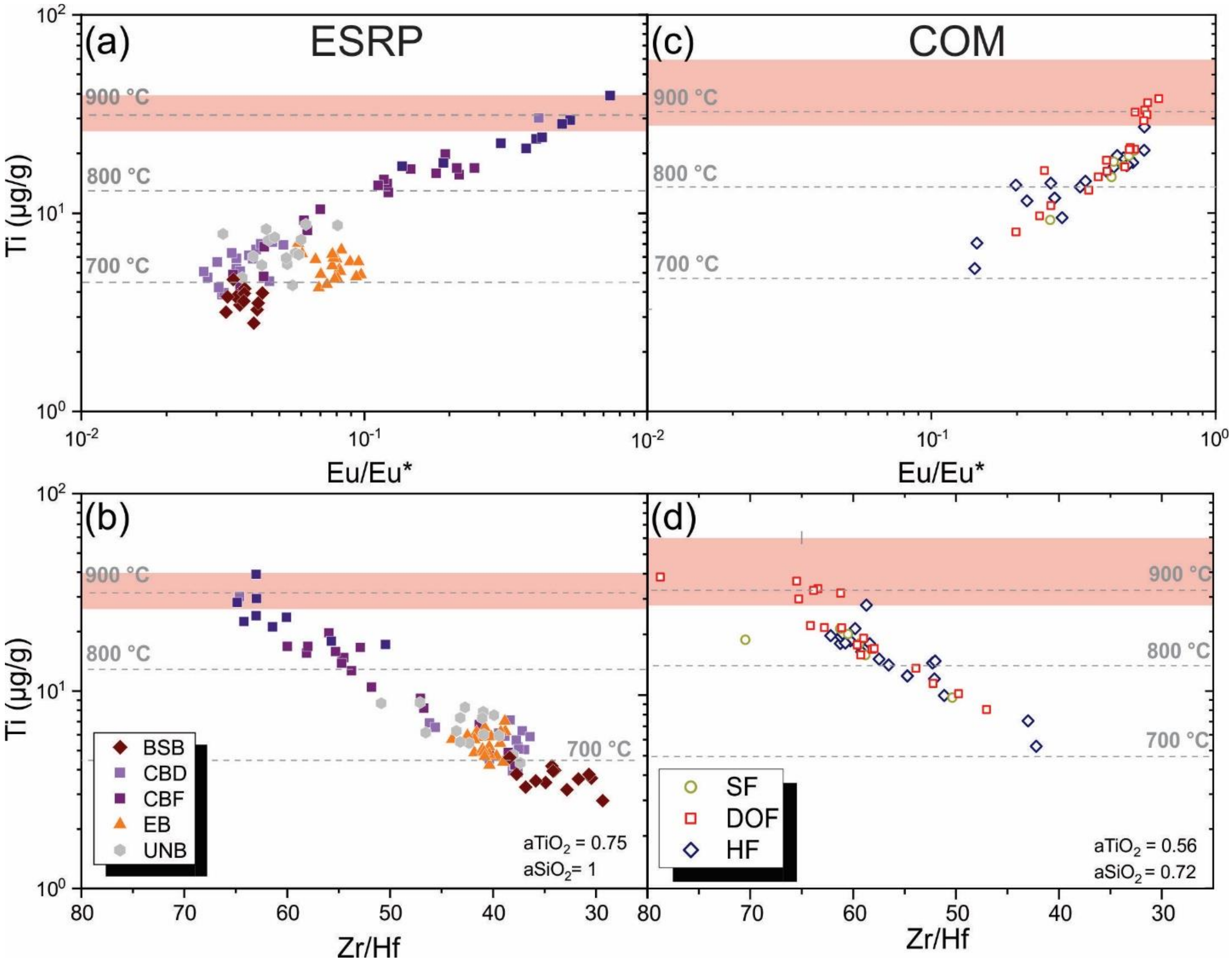

Fig. 8. *Zircon Ti abundances with corresponding Ti-in-zircon temperatures (dash-dot lines) calculated for ESRP (a-b) and COM (c-d) samples against Eu/Eu* and Zr/Hf. Average zircon saturation temperatures for corresponding whole rock compositions (red fields) were calculated after Crisp and Berry et al. (2022). Unit abbreviations from Table 1.*

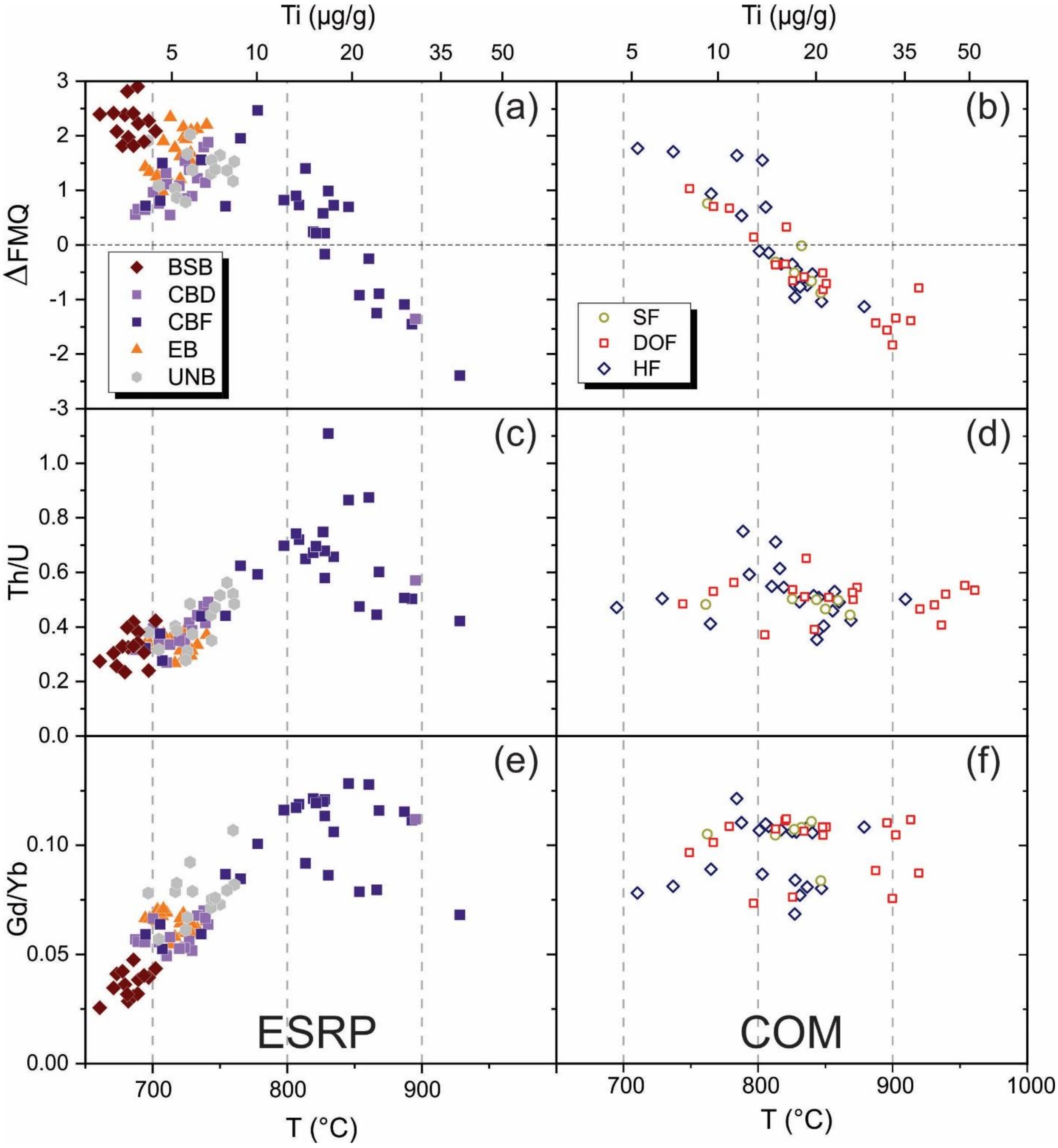

Fig. 9. *Zircon Ti abundances and Ti-in-zircon temperatures calculated for ESRP and COM zircon crystals against (a-b) ΔFMQ calculated after Loucks et al. (2020), Th/U (c-d), and Gd/Yb (e-f). Unit abbreviations from Table 1.*

Zircon O- and Hf-isotopes

ESRP zircon $\delta^{18}O$ values overall vary between +1.99 and +4.32 (Table S5; Fig. 10a), significantly below typical mantle zircon values (+5.3 ± 0.3; Valley *et al.*, 2005). Although zircon $\delta^{18}O$ averages for individual ESRP domes and lavas are distinct, individual units display homogeneous $\delta^{18}O$ within analytical uncertainty (Table 1; Fig. 10a). The lowest average values are present in Unnamed Butte (+2.21 ± 0.24; 2s), followed by East Butte (+2.68 ± 0.41). In comparison, Big Southern Butte with an average of +3.67 ± 0.37 and Cedar Butte flows and dome (+3.85 ± 0.45 and +3.67 ± 0.37, respectively) are isotopically slightly heavier. By contrast, COM zircon $\delta^{18}O$ values are +5.54 ± 0.31 (Highway flow), +5.68 ± 0.65 (Devils Orchard flow), and +5.41 ± 0.48 (Serrate flow), all closely overlapping mantle zircon compositions, without any significant difference between units. Zircon crystals from the COM granulite xenolith have an average $\delta^{18}O$ value of +5.82 ± 0.47, which is slightly elevated relative to mantle values (Fig. 10b).

Zircon εHf values for ESRP vary between -6.4 and -1.3 (Table S6; Fig. 10c). Whereas $\delta^{18}O$ values between different ESRP domes and flows are variable, their Hf-isotopic composition is remarkably homogeneous (Table 1; Fig. 10c). In stark contrast, COM lava flow zircon εHf values are more negative (-12.0 to -8.9; Table S6; Fig. 10d). Precambrian zircons from the xenolith display the lowest εHf values between -77.1 and -73.2 for present day. Initial values calculated back to the concordia upper intercept age are between -4.1 and 0.3, near or slightly below the chondritic value. In all cases, zircon εHf values are lower than regional mafic rocks representing potential parental magmas with average εHf = +0.6 (Stefano *et al.*, 2019).

DISCUSSION

Autocrystic and xenocrystic provenance of ESRP and COM zircons

ESRP and COM are volcanic fields dominated by mafic lava flows which based on their high temperatures and low Zr abundances were far from zircon saturation. One key difference between the ESRP with its prominent—albeit volumetrically subordinate—rhyolite domes is the complete lack of such highly evolved magma compositions in the erupted COM lavas. Cedar Buttes lavas together with enclaves in East Butte and some Unnamed Butte borehole samples in the ESRP are intermediate in composition with similar SiO_2 as evolved COM lavas (Fig. 2a). With differentiation, Zr increases during the zircon undersaturated path; at SiO_2 concentrations of ~59 wt.% Zr depletion kicks in, which is indicative of zircon saturation (Fig. 2). Hence, autocrystic zircon is expected for ESRP rhyolites, and our geochronological data confirm this, as no xenocrysts were detected among 140 zircon crystals dated, and all U-Pb crystallization ages are close to the Middle–Late Pleistocene eruption ages inferred from K-Ar and $^{40}Ar/^{39}Ar$ dating. For the COM intermediate lavas with SiO_2 between 52.3 and 64.6 wt.% (Chadwick *et al.*, 2023), the presence of autocrystic zircon is less clear cut in the Zr vs. SiO_2 diagram because averages across the ~59 wt.% SiO_2 boundary are subequal (Fig. 2). Kuntz (1992) reported zircon in granulitic xenoliths within COM lavas, whereas Stout *et al.* (1994) were first to note the presence of accessory zircon in COM lava flows. They described it as inclusions in plagioclase megacrysts and glomerocrysts comprising olivine, clinopyroxene, magnetite, and apatite. Based on textural considerations, Stout *et al.* (1994) concluded that the presence of zircon points to crustal contamination, and/or crystallization from melts unusually enriched in Zr, but neither the xenolith nor melt sources for these zircon crystals were identified.

Based on U-Th zircon crystallization ages, we classify most COM zircon crystals as Holocene. U-Th disequilibrium dating of magmatic accessory minerals is based on the decay of ^{230}Th with a shorter half-life compared with its indirect long-lived parent ^{238}U, and it is applicable to the time until the system reaches secular equilibrium (i.e. <375 ka; Cheng *et al.*, 2000). Diffusion experiments for the relevant parent-daughter elements U and Th (Cherniak & Watson, 2003) indicate negligible mobility even at the magmatic conditions (i.e. ~930 °C; Putirka *et al.*, 2009), and U-Th zircon ages therefore reliably date crystallization in the magma. By contrast, He diffusion in zircon is fast (e.g*.,* Reiners *et al.*, 2004; Cherniak *et al.,* 2009; Gautheron *et al.,* 2020), and although zircon crystallization predates the eruption, the (U-Th)/He zircon ages record eruptive cooling at 2.26 ±0.29 ka. The overlapping uncertainties between U-Th and (U-Th)/He imply zircon crystallization immediately prior to eruption. Moreover, the (U-Th)/He zircon eruption age overlaps within uncertainty with ^{14}C ages for mafic lavas of period A (Kuntz *et al.*, 2007), confirming that the evolved COM flows are part of the youngest eruptive episode of the field.

Only four zircons in secular equilibrium were found in Highway and Devils Orchard flows. For two of these, U-Pb ages indicate Oligocene–Miocene and Proterozoic ages. Trace elements and isotopic compositions ($\delta^{18}O$, εHf) for one of the undated zircons resembles the Archean xenolith population. Although xenocrysts are rare in COM lavas, these data confirm that Archean country rock contaminated COM lavas, but also that other lithologies are present at depth, including hotspot-related felsic rocks (e.g., Putirka *et al.*, 2009).

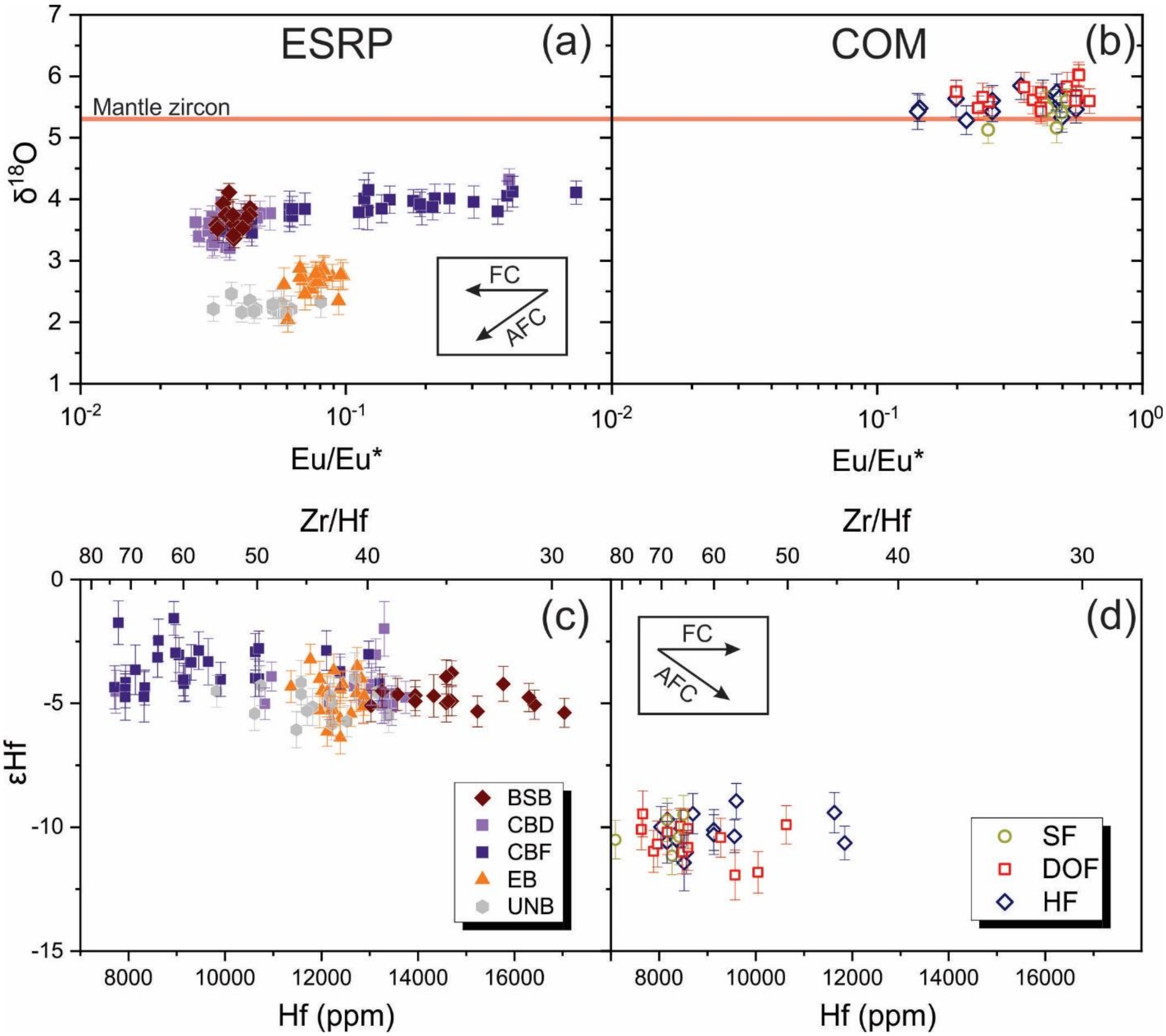

Fig. 10. *Zircon O isotopes vs. Eu/Eu* (a-b), and zircon Hf isotopes vs. Hf (c-d) for ESRP and COM systems (2se). Arrows indicate schematic trends for fractional crystallization (FC) and assimilation coupled with fractional crystallization (AFC). Unit abbreviations from Table 1.*

Boundary constraints for magma evolution from previous whole-rock based models

Before evaluating new zircon petrochronological data, we briefly review existing models for magma evolution in the ESRP-COM systems. Mafic endmembers in the ESRP comprise primitive olivine tholeiite magmas which generally experienced only minor fractional crystallization and negligible assimilation of Archean basement (e.g., Leeman, 1982a). COM lavas are generally more evolved than the ESRP olivine tholeiites and the most mafic endmembers differ compositionally from the bulk of the ESRP olivine tholeiites (Christiansen & McCurry, 2008). Nonetheless, intermediate to evolved magmas in the ESRP and the COM follow a common evolutionary trend (Christiansen & McCurry, 2008). Starting from the most primitive intermediate composition of Cedar Butte, a low-Si rhyolite is reached after 77 % fractional crystallization (McCurry *et al.*, 2008). For COM, the compositional range of the youngest eruptive period A, which includes the most evolved lavas erupted from this field, indicates fractional crystallization of 50% between less and more evolved lavas flows as represented by Big Craters (51.5 wt.% SiO_2) and Highway Flow (63.5 wt.% SiO_2) (Leeman *et al.*, 1976). Minor co-variation between isotopic ratios (e.g., $^{87}Sr/^{86}Sr$; $^{143}Nd/^{144}Nd$) and fractionation indices (e.g., SiO_2) for this suite of lavas also requires crustal assimilation concomitant with fractional crystallization (AFC; Chadwick *et al.*, 2023, Putirka *et al.*, 2009). COM parental liquids can be linked to ESRP parent magmas with small addition (~1–2%) of Archean crust during a first assimilation stage (Chadwick *et al.*, 2023, Kuntz, 1992, Leeman *et al.*, 1976, Putirka *et al.*, 2009). A second stage of assimilation involved addition of 15–20% felsic wallrocks that are the mid-crustal equivalents to upper-crust derived rhyolitic xenoliths in some COM lavas (Putirka *et al.*, 2009). Even higher degrees of assimilation at 31% were modelled for a rhyolite crustal endmember equivalent to rocks from the Miocene Picabo volcanic field that erupted as a precursor to modern Yellowstone (Chadwick *et al.*, 2023). The evolved COM lavas are inferred to reflect protracted magma storage and differentiation in middle crustal reservoirs at 14–17 km (Putirka *et al.*, 2009).

High and low temperature zircon in basalt dominated systems

Having established the predominantly autocrystic origins of zircon in ESRP and COM rocks, it is possible to compare the thermochemical conditions at which they crystallized with constraints from whole rock data. The isotopic invariance of zircon in individual units indicates that assimilation was negligible during zircon crystallization, and we therefore interpret zircon trace elements as primarily controlled by fractional crystallization of the host magma. For ESRP, the average of the Cedar Buttes lavas (Table 2) was selected as a zircon-undersaturated parental magma (McCurry *et al.*, 2008), and for COM, the starting composition was the most mafic rock sample of the three investigated lava flows (Devils Orchard flow, SiO_2 = ~52 wt.%; Table 2; Chadwick *et al.*, 2023). As differentiation indicators, we modelled trace element ratios (Eu/Eu*, Zr/Hf) because absolute abundances in zircon are often highly variable at the sub-µm-scale (e.g., Hofmann *et al.*, 2009). By varying F (fraction of remaining liquid), Eu/Eu* in the remaining melt was obtained using bulk distribution coefficients for Sm, Eu, and Gd calculated based on the mineral assembly required to reach evolved compositions from the respective parental magmas (Table 2). Literature partition coefficients (Table 2) were compiled matching the trachyandesite and basaltic trachyandesite starting compositions for ESRP and COM, respectively.

Modelled melt Eu/Eu* was transformed into zircon Eu/Eu* using the partition coefficient $(\mathrm{Eu/Eu^*})_D$ derived from Trail *et al.* (2024):

$$\left(\frac{Eu}{Eu*}\right)_D = \frac{1}{1+10^{0.30\pm0.04-(0.27\pm0.03)\times\Delta\mathrm{FMQ}}} \quad (1)$$

where the parameter ΔFMQ as the logarithmic difference in fO_2 to the FMQ buffer was derived from the zircon oxygeobarometer of Loucks *et al.* (2020) (Fig. 10). Zr/Hf in zircon was calculated based on the Zr-Hf geothermometer of Aranovich and Bortnikov (2018):

$$T = \frac{1531}{lnK_d+0.883} \quad (2)$$

where the parameter K_d is a ratio of the respective partition coefficients between melt (M) and zircon (S) as:

$$K_d = (X_{Zr}^S \times X_{Hf}^M)/(X_{Zr}^M \times X_{Hf}^S) \quad (3)$$

(X representing concentrations of Zr and Hf in µg/g). Following Aranovich and Bortnikov (2018), T is calculated as a function of fractional crystallization via:

$$f = 1 + k(T - T_0) \quad (4)$$

where *k* refers to the inverse of the difference between the initial temperature of zircon saturation (Fig.8; T_0, which was varied between 900 and 1150 °C) and the end of zircon crystallization (here: 650 °C). The *f* value in Equation 4 strictly represents the remaining melt fraction after zircon crystallization. Because our model is intended to only capture the melt evolution during zircon saturation, we can equate *f* with F, and use the *f*-dependent model temperature in Equation 4 to calculate ΔFMQ in Equation 1.

Curves for zircon Eu/Eu* and Zr/Hf in ESRP and COM from the respective fractional crystallization scenarios parallel the principal trends displayed by the data. For ESRP, zircon trace elements are matched by F values ranging from just under 1 to ~0.25 (Fig. 11a), whereas a narrower range between F = ~0.95 and ~0.40 covers the data for COM (Fig. 11b). The bulk (~77%) of ESRP zircon plots near the lower end of the modelled trend, consistent with the rhyolitic host rock. Only Cedar Butte intermediate flow zircon records crystallization at F > 0.5. The bulk (~87%) of COM zircon is consistent with near-saturation crystallization at F > 0.5, whereas only ~13% indicate crystallization from residual melts at F < 0.5. Although not directly indicating temperature, the modelled temperatures also agree with the observed TiZr distribution for ESRP and COM, where most ESRP zircon crystals indicate low temperature crystallization, whereas TiZr for intermediate Cedar Butte and COM lavas are closer to the respective zircon saturation temperatures derived from their whole-rock compositions (Fig. 8).

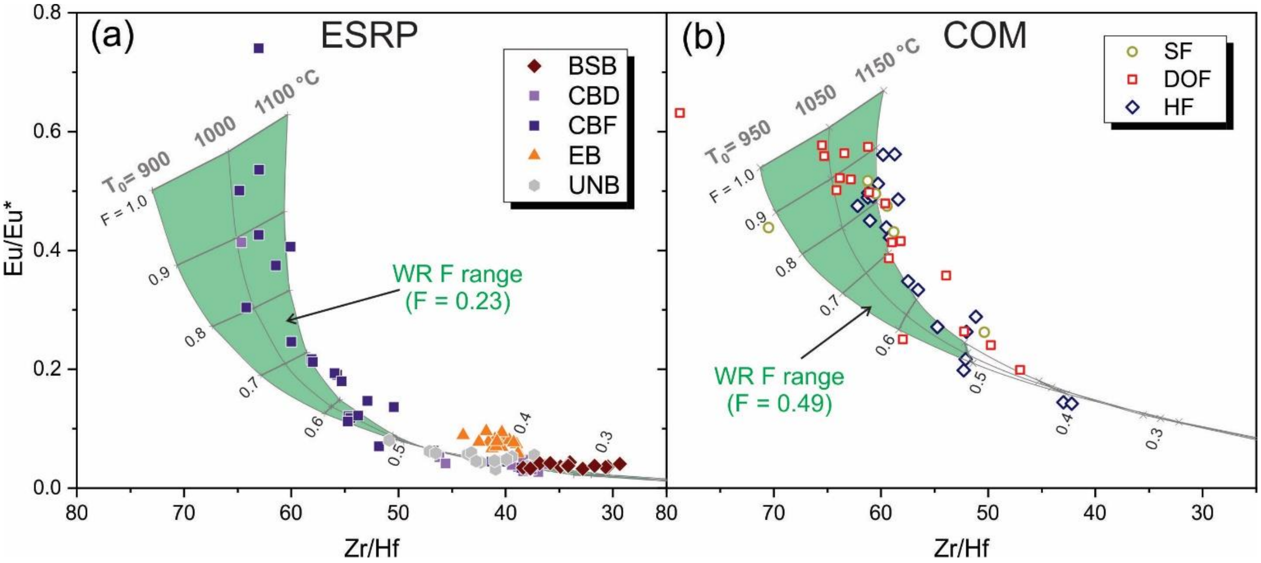

Fig. 11. *Fractional crystallization models for zircon Eu/Eu* vs. Zr/Hf compositions for ESRP (a) and COM lavas (b; see text). Green fields represent the range of F values (fraction of remaining liquid) of the whole rock-based models from the literature (F = 0.23 for ESRP; McCurry et al., 2008; F = 0.49 for COM; Leeman et al., 1996). Unit abbreviations from Table 1.*

For ESRP, zircon trace elements and TiZr values faithfully record melt evolution by fractional crystallization as previously modelled based on whole rock compositions. These models indicate that ESRP rhyolites are residual melts after significant crystallization (F = 0.23; McCurry *et al.*, 2008), remarkably close to the value obtained from modelling zircon trace elements (F = 0.25; Fig. 11a). For COM, whole rock fractional crystallization was previously modelled for the compositional range displayed by evolved COM period A magmas at F = 0.49; notably, this is only a fraction of the total compositional range at COM that requires F = ~0.3 to cover the entire range between SiO_2 = ~44 and ~64 wt.% (Leeman *et al.*, 1976). The value of F = 0.49 closely corresponds to the modelled compositional range for the majority of COM zircons that crystallized at F > 0.5, and only a small portion of zircon also records a crystal content of up to 60% (F = 0.4) that is not captured by bulk lava compositions (Fig. 11).

Table 2. Summary of modelling parameters for fractional crystallization (FC).

Mineral phase	ESRP						COM					
	Abundance (%)	Partition coeficients			Concentration (µg/g)		Abundance (%)	Partition coeficient			Concentration (µg/g)	
		Sm	Eu	Gd	Zr	Hf		Sm	Eu	Gd	Zr	Hf
Ol	9.8	0.028[a]	0.017[a]	0.016[a]			16.7	0.028[a]	0.017[a]	0.016[a]		
Pl	48.1	0.168[b]	4.2[b]	0.24[b]			66.7	0.146[c]	2.35[c]	0.044[c]		
Cpx	17.5	1.890[c]	1.69[c]	0.78[d]								
Mt	20.2	0.024[e]	2.52[e]	0.018[e]			11.9	0.08[g]	0.07[g]	0.3[g]		
Ap	4.4	31.4[f]	25.2[f]	21.7[f]			4.8	14.6[h]	9.6[h]	15.8[h]		
Total	100						100					
D*		**1.80**	**3.94**	**1.21**				**1.80**	**3.94**	**1.21**		
Parental magma		29.2	8.80	26.6	2373	49.6		26.01	7.65	24.04	1153	23.4

[a] Dunn & Sen (1994)

[b] Dudas et al. (1971)

[c] Nagasawa (1973)

[d] Larsen (1979)

[e] Lemarchand et al. (1987)

[f] Luhr et al. (1984)

[g] Mahood & Stimac (1990)

[h] Paster et al. (1974)

Zircon as a recorder of crustal assimilation in ESRP and COM parental magmas

Different AFC models have been explored to explain the isotopic (e.g., Sr, Nd, Pb, Th) and compositional covariation of igneous rocks in the ESRP (e.g., Chadwick *et al.*, 2023, Leeman & Manton, 1971, Leeman *et al.*, 1976, McCurry *et al.*, 2008, Putirka *et al.*, 2009, Reid, 1995, Stout *et al.*, 1994). As an outcome of these models, a similar primitive magmatic parent has been invoked for ESRP and COM (Putirka *et al.*, 2009), whereas crustal assimilation produced different isotopic evolutionary trends. The abundance of Archean xenoliths in COM basaltic–intermediate lavas also implies a strong role for assimilation of such a crustal component for COM magmas, and likely less so for ESRP.

Zircon isotopic ratios ($\delta^{18}O$ and εHf) are invariant with indicators for temperature and/or differentiation (e.g., TiZr, Eu/Eu*, and Zr/Hf) (Fig. 8). This implies that crustal assimilation, which clearly shifted host magma compositions relative to uncontaminated mantle values, predates zircon crystallization. Furthermore, trace element as well as O and Hf isotopic differences also exist between ESRP and COM zircon (Figs. 9 and 10), and we therefore explore AFC models independently for both magma systems (Table 3). For our AFC modelling (Table 3), we use equations from DePaolo (1981) to reproduce the Hf and O isotopic trends in zircon, acknowledging that this approach ignores energy conservation constraints as well as recharge, and may only incompletely capture complex multi-stage wallrock assimilation upon magma ascent (e.g., Huppert *et al.,* 1985; Bohrson & Spera, 2001, Spera & Bohrson, 2001). Nonetheless, this approach has reasonably reproduced the observed whole rock data trends for COM, thus facilitating a direct comparison between published whole rock and new zircon-based AFC models. For the same reason, we also adopted AFC parameters (e.g., rate of assimilation over rate of crystallization r = 0.8) from previous models (Putirka *et al.*, 2009). We acknowledge that zircon only covers the last stages of a protracted differentiation path, and hence only retroactively records the previous isotopic evolution of the mafic parent magma.

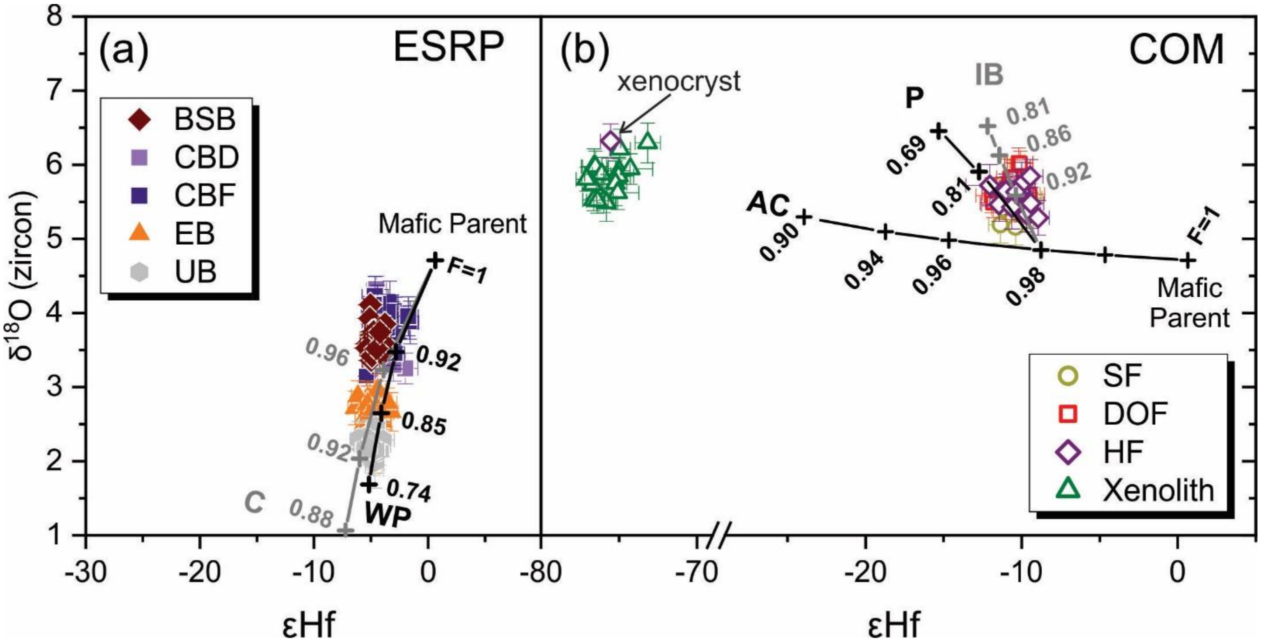

Fig. 12. *Covariation diagram of O vs. Hf isotopes with AFC trends modelled for a common parental magma ($\delta^{18}O = +5.71$, εHf = +0.6) and different crustal endmembers. Numbers indicate the fraction of remaining melt (F). Crustal endmembers for ESRP (a) are Challis group (C) and hydrothermally altered West Pocatello rhyolite (PR). For COM (b), two-stage AFC initially uses an Archean crust (AC) endmember, and subsequently unaltered Picabo caldera rhyolite (P) and Idaho Batholith (IB) granite as endmembers. For both systems, an r = 0.8 value (ratio of assimilation to fractionation; Table 2) was used based on Putrika et al. (2009). Unit abbreviations from Table 1.*

For the ESRP, assimilation of rocks with sub-mantle $\delta^{18}O$ is evident (Table 3; Fig. 12a). Suitable low-$\delta^{18}O$ rocks are present within the Yellowstone hotspot track (e.g., in the Picabo volcanic field; Drew *et al.*, 2013), and as regional Eocene volcanic rocks and their subvolcanic intrusive equivalents of the Challis group (Criss *et al.*, 1991, Kuntz *et al.*, 1986). Assimilation of Archean crust has been suggested to play a minimal role (<7%) for ESRP rhyolite magmas (McCurry *et al.*, 2008), which is supported by Hf-isotopes in ESRP zircon, which would allow only for assimilation of 0.3% of Archean rocks with εHf = -44 (Vervoort & Patchett, 1996). Assimilation of plutonic equivalents of altered Picabo ignimbrites (e.g., West Pocatello rhyolite) and Challis altered rocks would match the observed $\delta^{18}O$ and εHf values in ESRP zircon after ~26% and ~8% of fractional crystallization with concomitant assimilation (Fig. 12a). These comparatively low values of F (i.e. 0.74 and 0.92) require that the EPSR magmas continued to fractionate significantly after their isotopic composition was fixed during earlier AFC stages (Fig. 12a). This agrees with invariant zircon $\delta^{18}O$ and εHf within each of the ESRP units, independent of the apparent amount of assimilation experienced by their assumed parental magmas.

In contrast to ESRP zircon with sub-mantle $\delta^{18}O$ compositions, COM evolved lavas contain zircon with $\delta^{18}O$ slightly above mantle values (Fig. 10b). The lower εHf coupled with higher $\delta^{18}O$ in COM zircon relative to ESRP requires a two-stage AFC evolution (Putirka *et al.*, 2009): the first stage involves assimilation of ~1% of Archean crust, which is followed by a second stage which mainly increases $\delta^{18}O$ while maintaining nearly constant εHf (Fig. 12b). Possible candidates for the second stage of assimilation include unaltered intracaldera wallrocks from the Tertiary hotspot (e.g., similar to Tuff of Arbon Valley from the Picabo volcanic field; Drew *et al.*, 2013) and late Cenozoic felsic plutons from the Idaho Batholith (Gaschnig *et al.*, 2011, King *et al.*, 2007). Corresponding F values of 0.81 and 0.86 are again larger than the overall range in F recorded in primitive to intermediate COM lava compositions (0.3; e.g., Leeman *et al.*, 1976) (Fig. 12). Moreover, as with ESRP lavas, zircon $\delta^{18}O$ and εHf values are homogeneous in the COM lavas, indicating that AFC must predate the magmatic differentiation recorded by zircon (Fig.10). Comparatively high degrees of oxidation that are recorded in low-T zircon (Fig. 9), however, indicate that oxidized fluids of surface origin may have influenced the wallrocks of the shallow magma reservoirs where differentiation occurred (e.g., Colon et al., 2018).

Magma evolution in the ESRP and COM volcanic fields from the zircon perspective

Magmatic evolution in the ESRP is the product of a complex differentiation history that ultimately started with an inferred picrite parent (MgO >10%; McCurry *et al.*, 2008, Putirka *et al.*, 2009). Ascending from the mantle, these parental magmas ponded in the lower crust (> 20 km) until fractional crystallization to MgO concentrations of <10 wt. % caused their density to decrease, facilitating further ascent within the crust (Putirka *et al.*, 2009). In addition to effusive eruption of the resulting olivine-tholeiites in discrete rift zones, these magmas also formed an extensive sill complex (e.g., Peng & Humphreys, 1998, Sparlin *et al.*, 1982) aided by low density silicic intrusions and their Yellowstone-type eruptive equivalents that predominate along the axis of the ESRP (Fig. 13). At the ESRP margins, pre-existing Archean crust is preferentially preserved and therefore exerts a stronger influence on COM magmas relative to those erupted along the axis of the downwarp, where the crust was strongly reworked during passing of the Yellowstone hotspot (McCurry *et al.*, 2008, Putirka *et al.*, 2009). While these magmas ponded in the middle to upper crust, strong Fe-enrichment and a concomitant increase in density hindered eruption until they became sufficiently evolved (Christiansen & McCurry, 2008), possibly further aided by assimilation of mid-crustal felsic rocks (e.g., Chadwick *et al.*, 2023, Putirka *et al.*, 2009). Ultimately, evolved magmas comprising basaltic trachyandesite–rhyolite formed as the end products of differentiation in shallow reservoirs where assimilation was largely inhibited (McCurry *et al.*, 2008).

Zircon δ^{18}O and εHf isotopes are consistent with two independent branches of differentiation from a similar mantle source, where assimilation of Archean crust is negligible for the ESRP, but required to explain COM isotopic compositions (Fig. 12). Distinct δ^{18}O trends also point to differential assimilation of mid–upper crustal rocks: ESRP parental magmas assimilated hydrothermally altered low-δ^{18}O rocks prevailing along the axis of the Yellowstone track (Fig. 12a), whereas for COM only high-δ^{18}O crustal mid-crustal endmembers are detected. These could either represent unaltered intrusions at the margins of the Yellowstone hotspot track, or pre-existing early Cenozoic plutons (Fig. 12). Isotopic clustering of zircon from individual domes and lava flows without correlation between isotopic values and host magma composition indicates that zircon crystallization postdates these different histories of crustal assimilation (Fig. 13). Assimilation and fractional crystallization of the ESRP and COM parental magmas led to progressive enrichment of Zr (Fig. 2), but at the stage of reaching zircon saturation, assimilation within the upper crust had largely ceased.

Table 3. Summary of modelling parameters for assimilation coupled with fractional crystallization (AFC).

D	1		0.1	
r	0.8[a]		0.8[a]	
	$\delta^{18}O$	**O (wt.%)**	**εHf**	**Hf (µg/g)**
Mafic Parent (MP)	+5.71[b]	50	+0.6[c]	3[b]
Crustal endmembers				
Archean Crust (AC)	+7.4[d]	50	-44[e]	9[e]
Challis volcanics (C)	-3.6[f]	50	-12.5[g]	9[g]
West Pocatello Rhyolite (WP)	+1.41[h]	50	-7.5[h]	6.5[i]
Tuff of Arbon Valley (P)	+7.9[h]	50	-28[h]	1.4[h]
Idaho Batholith (IB)	+9.06[j]	50	-18.6[k]	2.9[k]

[a] Putirka et al. (2009)

[b] Hart et al. (1999)

[c] average Stefano et al. (2019)

[d] Watts et al. (2010)

[e] Vervoort and Patchett (1996)

[f] Criss et al. (1991)

[g] Gaschnig et al. (2011)

[h] Drew et al. (2013)

[i] for felsic volcanics from Condie (1993)

[j] Atlanta lobe average from King et al. (2007)

[k] Atlanta lobe average from Gaschnig et al. (2011)

For the ESRP domes, we observe a systematic relationship between the zircon $\delta^{18}O$ isotopic composition and geographical location, as well as their age: the eastern domes (East Butte; Unnamed Butte) are older and have lower $\delta^{18}O$, whereas the western domes (Big Southern Butte; Cedar Butte) are younger and have higher $\delta^{18}O$ (Table 1). Although the eastern domes overlie the inferred Arbon Valley Tuff caldera margin (e.g., Anders *et al.*, 2019), where hydrothermal alteration is reasonably expected to be intense, their zircon cargo displays comparatively high $\delta^{18}O$. Magma residence durations as derived from the difference between crystallization and eruption ages (Δt) are more protracted for the eastern domes, and briefer for the western domes. This may indicate that the magma system producing the eastern domes was potentially larger and longer-lived, resulting in more efficient crustal assimilation compared to the source magma for the western domes. The most evolved lava flows at COM erupted after a hiatus of c. 1 ka at the beginning of eruptive period A (Kuntz *et al.*, 1986). Period A magmas formed in two stratified but physically interconnected bodies where the younger and more mafic magmas from below triggered evacuation of the shallower, more evolved body (Chadwick *et al.*, 2023). The brief zircon residence time of c. 4.3 ka is consistent with the evolved period A magmas being leftovers from earlier eruptive periods, indicating magma differentiation within several millennia at most.

Zircon in basalt-dominated magma systems

High-temperature zircon crystallization for COM and ESRP basaltic trachyandesite and trachyandesite magmas near their respective zircon saturation temperatures of ~900 °C was facilitated by the high Zr contents of their host melts (Figs. 2b and 8). The strong enrichment of Zr in these magmas was the consequence of multiple fractional crystallization episodes that for the ESRP and COM systems reached extreme levels (857 µg/g at 44.4 wt. % SiO_2) compared to a global compilation of LIP volcanic rocks (DIGIS Team, 2021; median 148 µg/g at 50.0 wt.%; Fig. 2b). Even the most primitive COM lavas have comparatively low MgO contents (4.9 wt. %; Leeman et al., 1976), which requires prior magmatic differentiation. The high Zr melt abundances that trigger zircon saturation are then produced by further fractional crystallization, which in the case of COM are estimated at F = 0.3 (e.g., Leeman *et al.*, 1976). Furthermore, zircon crystallization at high temperatures can be caused by local saturation in crystal boundary layers (Bacon, 1989) or confined pores after extensive solidification and fractionation of initially low-Zr mafic magmas (Bea *et al.*, 2022). Local saturation in COM magmas is texturally evident by zircon being commonly associated with olivine, clinopyroxene, ilmenite, and pyrite, sometimes in confined melt pockets (Fig. 3). However, zircon is also present in the matrix (Fig. 3a), and its composition is consistent with crystallization of an evolving, high-temperature melt as indicated by the fractional crystallization model involving the same mineral phases (olivine, plagioclase, clinopyroxene, magnetite, and apatite) as observed in the COM lavas. Typical magmatic oscillatory CL zonation and absence of inherited cores further support this interpretation (Fig. 4). The consistent range of F values recorded by zircon and whole-rock compositions argues against zircon recycling from a crystal-rich mush, although a small proportion of zircon in COM lavas indicates slightly more differentiated and cooler source melts than represented by the bulk rock (Fig. 11). This is consistent with a layered architecture proposed for the COM magma system, where shallow, evolved melt strata were flushed by the arrival of more mafic magma from below (Chadwick *et al.*, 2023).

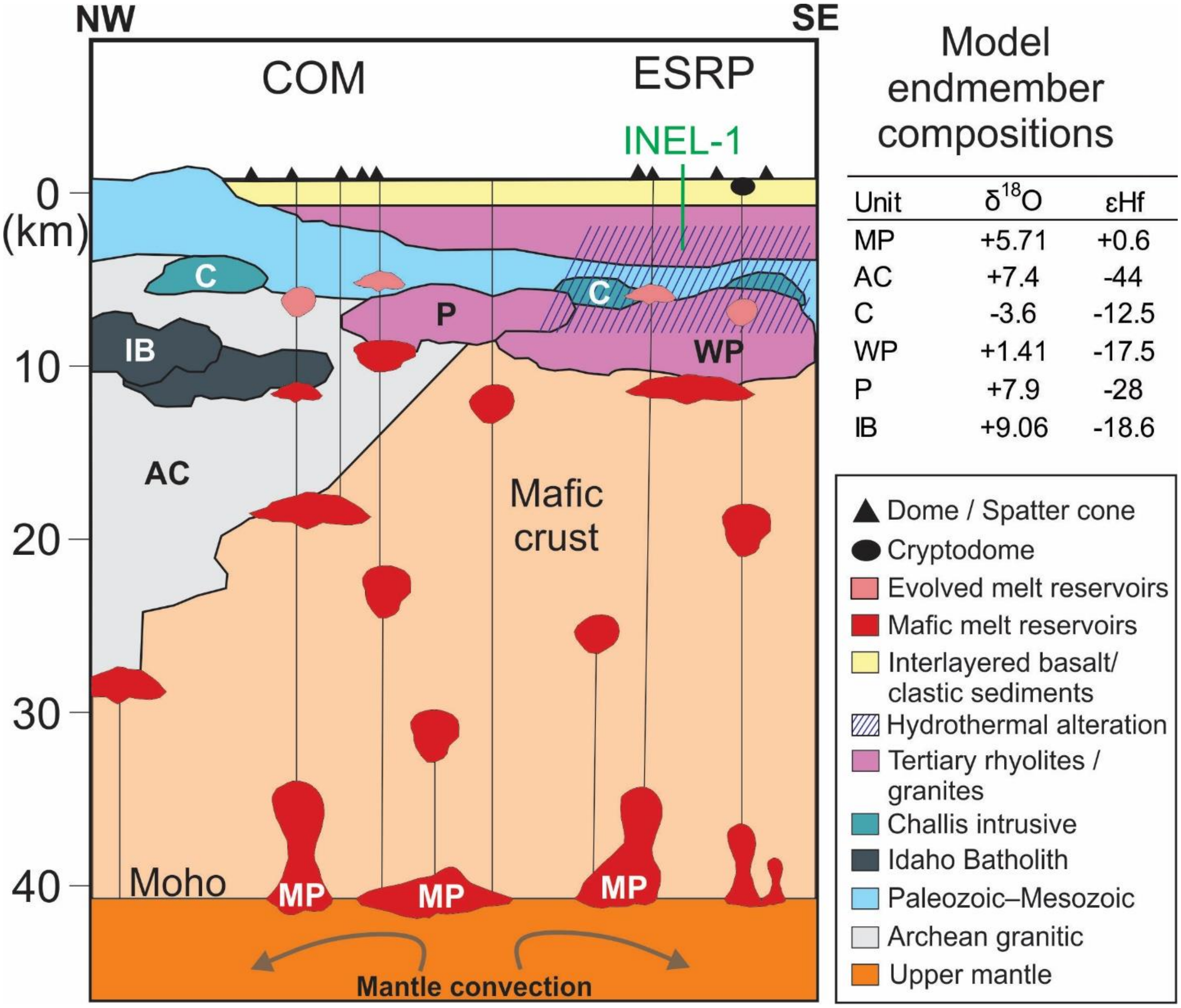

Model endmember compositions

Unit	$\delta^{18}O$	εHf
MP	+5.71	+0.6
AC	+7.4	-44
C	-3.6	-12.5
WP	+1.41	-17.5
P	+7.9	-28
IB	+9.06	-18.6

Fig.13. *Simplified conceptual model for COM and ESRP Quaternary magma genesis, modified after McCurry et al. (2008). Picrite or high-Mg olivine tholeiite magmas generated at the Moho (MP) experienced extensive fractional crystallization during ascent through the crust. For COM magmas, this ascent was accompanied by mid-crustal assimilation of an Archean component (AC), followed by additional minor assimilation of rocks from either the Idaho Batholith (IB) or unaltered Tertiary intracaldera rocks (P) at the margins of the hot spot track. In contrast, ESRP magmas assimilated significant amounts of altered Challis volcanic (C) rocks, Tertiary intracaldera rocks, or their plutonic equivalents at mid to upper crustal levels (WP). Zircon crystallized during*

subsequent magma residence which lasted for few 1,000 years in the case of the COM evolved lavas, and not more than c. 100 kyrs for ESRP rhyolites.

Despite the unequivocal autocrystic nature of most ESRP and COM zircons, and the clear correlation between zircon presence in lavas and the compositional turnover from Zr enrichment to depletion in the whole rock data, the comparison between Figs. 2a and b implies that this is a globally rare phenomenon because high-Zr intermediate and rhyolitic magmas are exceedingly scarce in LIPs. Nonetheless, the ESRP-COM systems serve as valuable testbeds for constraining the conditions under which zircon saturation can occur in mafic magmas typical for LIPs. The scarcity of low-MgO, high-FeO, and high-Zr magmas in the terrestrial volcanic record could imply that they often remained unerupted and solidified at depth. This notion is supported by frequent cryptodome formation in the ESRP (McCurry *et al.*, 2008) as well as evidence for eruptions of evolved magmas requiring external triggering such as mobilization due to mafic recharge (Chadwick *et al.*, 2023). Another important observation is that trace elements and isotopic compositions of ESRP and COM zircons indicate a lack of contamination during zircon crystallization, albeit their host magmas experienced significant crustal contamination during their earlier stages of differentiation. This contrasts with localized contamination of mafic sills intruded into basin sediments, which formed zircon that is isotopically heterogeneous (Davies *et al.*, 2021; Gaynor *et al.*, 2022; Gaynor *et al.*, 2023), whereas ESRP and COM zircons are homogeneous within each unit. This comparison underscores that a petrochronological approach integrating age information with trace element and isotopic constraints is essential for resolving autocrystic vs. xenocrystic zircon origins in LIP environments.

CONCLUSIONS

The study of intermediate–silicic lavas from the ESRP and COM volcanic fields unravels how magmatic processes imprint on zircon, and how zircon compositions reflect magma evolution in basalt-dominated systems. Autocrystic zircon crystallization is indicated by U-Pb and U-Th dating that closely aligns with the Middle–Late Pleistocene and Holocene eruption ages for ESRP and COM lavas, respectively, with only rare xenocrystic zircon detected. The progressive enrichment in melt Zr due to extensive fractional crystallization is a prerequisite for zircon formation in these systems. Once zircon saturation is achieved in both ESRP and COM melts, their trace element composition parallels magmatic differentiation via fractional crystallization where ~40% and ~25% residual melts represent the most evolved lavas in the respective fields. ESRP and COM zircons also record different pathways of crustal interaction of a common mantle-derived parental magma. For the ESRP, assimilation of Archean crust is negligible, but low-δ^{18}O rocks generated by hydrothermal alteration of felsic volcanics of Yellowstone-type calderas were likely assimilated to a significant degree. By contrast, COM parental magmas clearly interacted with Archean crust, and in a second stage with unaltered felsic crustal components at the margins of the Yellowstone hotspot track.

The ESRP-COM systems serve as a unique analogue for zircon behavior in LIP settings where basaltic magmas predominate. The results for the ESRP-COM zircons indicate that Zr enrichment sufficient to saturate zircon at high temperatures requires extensive fractional crystallization of mantle-derived magmas in a multi-level lithosphere-scale architecture. While magma conditions amenable to crystallize high-T zircon might be reached in other LIPs, the overall scarcity of mafic–intermediate high-Zr volcanic rock compositions in the global data base (comprising data from the North American Igneous Province, Siberian Traps, Deccan, Central Atlantic Magmatic Province, Emeishan, Karoo and Ferrar, Paraná, and Etendeka LIPs; DIGIS Team, 2023). suggests special circumstances for the formation or eruption of such melts. Zircon in mafic volcanic rocks from ancient LIPs thus should be carefully vetted against potential xenocrystic or contamination origins.

ACKNOWLEDGEMENTS

The authors would like to thank Mary Hodges (USGS), Alexander Varychev, Ilona Fin, and Oliver Wienand for assistance in sample preparation, as well as Ana Karen Gonzales Ambrocio for digitizing and drafting the map. Additionally, we acknowledge support from the administration of Craters of the Moon National Monument for collecting lava samples. Journal editor Mary Reid and three reviewers, including Sean P. Gaynor and two anonymous reviewers, are thanked for their insightful and diligent comments.

This is FIERCE contribution No. 197.

DATA AVAILABILITY STATEMENT

Analytical data for this study is available in the online supplementary material, and in EarthChem Library, at https://doi.org/10.60520/IEDA/113491.

REFERENCES

Anders, M. H., DiVenere, V. J., Hemming, S. R. & Gombiner, J. (2019). ^{40}Ar/^{39}Ar and paleomagnetic constraints on the age and areal extent of the Picabo volcanic field: Implications for the Yellowstone hotspot. *Geosphere* **15**, 716-735.

Anders, E., & Grevesse, N. (1989). Abundances of the elements: Meteoritic and solar. *Geochimica et Cosmochimica Acta* **53(1)**, 197-214.

Anders, M. H. & Sleep, N. H. (1992). Magmatism and extension: The thermal and mechanical effects of the Yellowstone hotspot. *Journal of Geophysical Research: Solid Earth* **97**, 15379-15393.

Aranovich, L. Y. & Bortnikov, N. (2018). New Zr–Hf geothermometer for magmatic zircons. *Petrology* **26**, 115-120.

Bacon, C. R. (1989). Crystallization of accessory phases in magmas by local saturation adjacent to phenocrysts. *Geochimica et Cosmochimica Acta* **53**, 1055-1066.

Baertschi, P. (1976). Absolute ^{18}O content of standard mean ocean water. *Earth and Planetary Science Letters* **31**(3), 341-344.

Bea, F., Bortnikov, N., Cambeses, A., Chakraborty, S., Molina, J., Montero, P., Morales, I., Silantiev, S. & Zinger, T. (2022). Zircon crystallization in low-Zr mafic magmas: Possible or impossible? *Chemical Geology* **602**, 120898.

Bea, F., Montero, P., González-Lodeiro, F., Talavera, C., Molina, J., Scarrow, J., Whitehouse, M. & Zinger, T. (2006). Zircon thermometry and U–Pb ion-microprobe dating of the gabbros and associated migmatites of the Variscan Toledo Anatectic Complex, Central Iberia. *Journal of the Geological Society* **163**, 847-855.

Beattie, P. (1993). Olivine-melt and orthopyroxene-melt equilibria. *Contributions to Mineralogy and Petrology* **115**, 103-111.

Bell, E. A., Boehnke, P., & Harrison, T. M. (2016). Recovering the primary geochemistry of Jack Hills zircons through quantitative estimates of chemical alteration. *Geochimica et Cosmochimica Acta*, **191**, 187-202.

Bell, E. A., Boehnke, P., Barboni, M. & Harrison, T. M. (2019). Tracking chemical alteration in magmatic zircon using rare earth element abundances. *Chemical Geology* **510**, 56-71.

Bindeman, I. & Simakin, A. (2014). Rhyolites—Hard to produce, but easy to recycle and sequester: Integrating microgeochemical observations and numerical models. *Geosphere* **10**, 930-957.

Bjerga, A., Stubseid, H. H., Pedersen, L. E. R., & Pedersen, R. B. (2022). Radiation damage allows identification of truly inherited zircon. *Communications Earth & Environment* **3**, 37.

Black, L. P., Kamo, S. L., Allen, C. M., Davis, D. W., Aleinikoff, J. N., Valley, J. W., Mundil, R., Campbell, I. H., Korsch, R. J. & Williams, I. S. (2004). Improved ^{206}Pb/^{238}U microprobe geochronology by the monitoring of a trace-element-related matrix effect; SHRIMP, ID–TIMS, ELA–ICP–MS and oxygen isotope documentation for a series of zircon standards. *Chemical Geology* **205**, 115-140.

Bohrson, W. A. & Spera, F. J. (2001). Energy-constrained open-system magmatic processes II: application of energy-constrained assimilation–fractional crystallization (EC-AFC) model to magmatic systems. *Journal of Petrology* **42**, 1019-1041.

Borisov, A. & Aranovich, L. (2019). Zircon solubility in silicate melts: New experiments and probability of zircon crystallization in deeply evolved basic melts. *Chemical Geology* **510**, 103-112.

Borisova, A. Y., Bindeman, I. N., Toplis, M. J., Zagrtdenov, N. R., Guignard, J., Safonov, O. G., Bychkov, A. Y., Shcheka, S., Melnik, O. E., Marchelli, M., & Fehrenbach, J. (2020). Zircon survival in shallow asthenosphere and deep lithosphere. *American Mineralogist* **105**, 1662-1671.

Boroughs, S., Wolff, J. A., Ellis, B. S., Bonnichsen, B. & Larson, P. B. (2012). Evaluation of models for the origin of Miocene low-δ18O rhyolites of the Yellowstone/Columbia River Large Igneous Province. *Earth and Planetary Science Letters* **313**, 45-55.

Carley, T. L., Miller, C. F., Wooden, J. L., Padilla, A. J., Schmitt, A. K., Economos, R. C., Bindeman, I. N. & Jordan, B. T. (2014). Iceland is not a magmatic analog for the Hadean: Evidence from the zircon record. *Earth and Planetary Science Letters*, **405**, 85-97.

Chadwick, D., Payne, S., Van Hove, T. & Rodgers, D. (2007). Contemporary tectonic motion of the eastern Snake River Plain: A campaign global positioning system study. *Tectonics* **26**.

Chadwick, J., Chadwick, C. & Kamenov, G. (2023). Compositional evolution of polygenetic fissure volcanic systems: Insights from the latest eruptions at Craters of the Moon Volcanic Field. *Geochemistry, Geophysics, Geosystems* **24**, e2022GC010740.

Chamberlain, K. R., Frost, C. D. & Frost, B. R. (2003). Early Archean to Mesoproterozoic evolution of the Wyoming Province: Archean origins to modern lithospheric architecture. *Canadian Journal of Earth Sciences* **40**, 1357-1374.

Cheng, H., Edwards, R. L., Hoff, J., Gallup, C. D., Richards, D. & Asmerom, Y. (2000). The half-lives of uranium-234 and thorium-230. *Chemical Geology* **169**, 17-33.

Cherniak, D. J. & Watson, E. B. (2003). Diffusion in zircon. *Reviews in Mineralogy and Geochemistry* **53**, 113-143.

Cherniak, D.J., Watson, E.B., Thomas, J.B., 2009, Diffusion of helium in zircon and apatite: *Chemical Geology* **268**, 155-166.

Christiansen, E. H. & McCurry, M. (2008). Contrasting origins of Cenozoic silicic volcanic rocks from the western Cordillera of the United States. *Bulletin of Volcanology* **70**, 251-267.

Christiansen, R. L. (2001). The Quaternary and Pliocene Yellowstone Plateau volcanic field of Wyoming, Idaho, and Montana. *U.S. Geological Survey Professional Paper* **729-G**, 1-120.

Coble, M. A. & Mahood, G. A. (2012). Initial impingement of the Yellowstone plume located by widespread silicic volcanism contemporaneous with Columbia River flood basalts. *Geology* **40**, 655-658.

Colón, D. P., Bindeman, I. N., Wotzlaw, J.-F., Christiansen, E. H. & Stern, R. A. (2018). Origins and evolution of rhyolitic magmas in the central Snake River Plain: insights from coupled high-precision geochronology, oxygen isotope, and hafnium isotope analyses of zircon. *Contributions to Mineralogy and Petrology* **173**, 1-18.

Condie, K.C. (1993). Chemical composition and evolution of the upper continental crust: contrasting results from surface samples and shales. *Chemical Geology* **104**: 1-37. doi: 10.1016/0009-2541(93)90140-E.

Condon, D., Schoene, B., Schmitz, M., Schaltegger, U., Ickert, R. B., Amelin, Y., Augland, L. E., Chamberlain, K. R., Coleman, D. S., Connelly, J. N., Corfu, F., Crowley, J. L., Davies, J. H. F. L., Denyszyn, S. W., Eddy, M. P., Gaynor, S. P., Heaman, L. M., Huyskens, M. H., Kamo, S., Kasbohm, J., Keller, C. B., MacLennan, S. A., McLean, N. M., Noble, S., Ovtcharova, M., Paul, A., Ramezani, J., Rioux, M., Sahy, D., Scoates, J. S., Szymanowski, D., Tapster, S., Tichomirowa, M., Wall, C. J., Wotzlaw, J.-F., Yang, C., & Yin, Q.-Z. (2024). Recommendations for the reporting and interpretation of isotope dilution U-Pb geochronological information. *Geological Society of America Bulletin* **136**, 4233–4251.

Crisp, L. J. & Berry, A. J. (2022). A new model for zircon saturation in silicate melts. *Contributions to Mineralogy and Petrology* **177**, 71, https://doi.org/10.1007/s00410-022-01925-6.

Criss, R. E., Fleck, R. J. & Taylor Jr, H. P. (1991). Tertiary meteoric hydrothermal systems and their relation to ore deposition, northwestern United States and southern British Columbia. *Journal of Geophysical Research: Solid Earth* **96**, 13335-13356.

Danišík, M., Lowe, D. J., Schmitt, A. K., Friedrichs, B., Hogg, A. G. & Evans, N. J. (2020). Sub-millennial eruptive recurrence in the silicic Mangaone Subgroup tephra sequence, New Zealand, from Bayesian modelling of zircon double-dating and radiocarbon ages. *Quaternary Science Reviews* **246**, 106517.

Danišík, M., Schmitt, A. K., Stockli, D. F., Lovera, O. M., Dunkl, I. & Evans, N. J. (2017). Application of combined U-Th-disequilibrium/U-Pb and (U-Th)/He zircon dating to tephrochronology. *Quaternary Geochronology* **40**, 23-32.

Danišík, M., Shane, P., Schmitt, A. K., Hogg, A., Santos, G. M., Storm, S., Evans, N. J., Fifield, L. K. & Lindsay, J. M. (2012). Re-anchoring the late Pleistocene tephrochronology of New Zealand based on concordant radiocarbon ages and combined ^{238}U/^{230}Th disequilibrium and (U–Th)/He zircon ages. *Earth and Planetary Science Letters* **349**, 240-250.

Davies, J., Marzoli, A., Bertrand, H., Youbi, N., Ernesto, M., Greber, N., Ackerson, M., Simpson, G., Bouvier, A.-S. & Baumgartner, L. (2021). Zircon petrochronology in large igneous provinces reveals upper crustal contamination processes: new U–Pb ages, Hf and O isotopes, and trace elements from the Central Atlantic magmatic province (CAMP). *Contributions to Mineralogy and Petrology* **176**, 1-24.

Davies, J. H. F. L., Marzoli, A., Bertrand, H., Youbi, N., Ernesto, M. & Schaltegger, U. (2017). End-Triassic mass extinction started by intrusive CAMP activity. *Nature communications* **8**, 1-8.

Davies, J. H. F. L., Marzoli, A., Bertrand, H., Youbi, N., Ernesto, M., Greber, N. D., Ackerson, M., Simpson, G., Bouvier, A.-S., Baumgartner, L., Pettke, T., Farina, F., Ahrenstedt, H. V., & Schaltegger, U. (2021). Zircon petrochronology in large igneous provinces reveals upper crustal contamination processes: new U–Pb ages, Hf and O isotopes, and trace elements from the Central Atlantic magmatic province (CAMP). *Contributions to Mineralogy and Petrology* **176**(6), 1–24.

DePaolo, D. J. (1981). Trace element and isotopic effects of combined wallrock assimilation and fractional crystallization. *Earth and Planetary Science Letters* **53**, 189-202.

DIGIS Team, 2021, "GEOROC Compilation: Geochemical and isotopic rock compositions from continental flood basalts held in the GEOROC database", https://doi.org/10.25625/WSTPOX, Goettingen Research Online / Data, V1

Drew, D. L., Bindeman, I. N., Watts, K. E., Schmitt, A. K., Fu, B. & McCurry, M. (2013). Crustal-scale recycling in caldera complexes and rift zones along the Yellowstone hotspot track: O and Hf isotopic evidence in diverse zircons from voluminous rhyolites of the Picabo volcanic field, Idaho. *Earth and Planetary Science Letters* **381**, 63-77.

Dudas, M.J., Schmitt, R.A. and Harward, M.E. (1971). Trace element partitioning between volcanic plagioclase and dacitic pyroclastic matrix. *Earth and Planetary Science Letters* **11**(5): 440-446. doi: 10.1016/0012-821X(71)90206-8

Dunn, T. and Sen, C. (1994). Mineral/Matrix Partition-Coefficients for Ortho-Pyroxene, Plagioclase, and Olivine in Basaltic to Andesitic Systems - a Combined Analytical and Experimental-Study. *Geochimica et Cosmochimica Acta* **58**(2): 717-733. doi: 10.1016/0016-7037(94)90501-0.

Ellis, B., Wolff, J., Boroughs, S., Mark, D., Starkel, W. & Bonnichsen, B. (2013). Rhyolitic volcanism of the central Snake River Plain: a review. *Bulletin of Volcanology* **75**, 1-19.

Ernst, R. E. (2014). *Large igneous provinces*: Cambridge University Press.

Evans, N., Byrne, J., Keegan, J. & Dotter, L. (2005). Determination of uranium and thorium in zircon, apatite, and fluorite: Application to laser (U-Th)/He thermochronology. *Journal of Analytical Chemistry* **60**, 1159-1165.

Farley, K., Wolf, R. & Silver, L. (1996). The effects of long alpha-stopping distances on (U-Th)/He ages. *Geochimica et Cosmochimica Acta* **60**, 4223-4229.

Faulds, J. E., Varga, R. J. & Stewart, J. (1998). The role of accommodation zones and transfer zones in the regional segmentation of extended terranes. *Special Papers-Geological Society of America* **323**, 1-46.

Fisher, F. & Johnson, K. (1995a). Challis volcanic terrane. *Geology and mineral resource assessment of the Challis* **1**, 41-43.

Fisher, F. S. & Johnson, K. M. (1995b). Geology and mineral resource assessment of the Challis 1 x 2 quadrangle, Idaho. *U.S. Geological Survey Professional Paper* **1525**, 1-204.

Ford, M. T. (2005). The petrogenesis of quaternary rhyolite domes in the bimodal Blackfoot volcanic field, Southeastern Idaho. MSc thesis Idaho State University.

Ganske, R. R. (2006). The geology and petrology of the East Butte area, Bingham County, Idaho. MSc thesis Idaho State University.

Gaschnig, R. M., Vervoort, J. D., Lewis, R. S. & Tikoff, B. (2011). Isotopic evolution of the Idaho batholith and Challis intrusive province, northern US Cordillera. *Journal of Petrology* **52**, 2397-2429.

Gautheron, C., Djimbi, D.M., Roques, J., Balout, H., Ketcham, R.A., Simoni, E., Pik, R., Seydoux-Guillaume, A.M., Tassan-Got, L., 2020, A multi-method, multi-scale theoretical study of He and Ne diffusion in zircon: *Geochimica et Cosmochimica Acta* **268**, 348-367.

Gaynor, S. P., Svensen, H. H., Polteau, S., & Schaltegger, U. (2022). Local melt contamination and global climate impact: Dating the emplacement of Karoo LIP sills into organic-rich shale. *Earth and Planetary Science Letters* **579**, 117371.

Gaynor, S. P., Davies, J. H., & Schaltegger, U. (2023). High-precision geochronology of LIP intrusions: records of magma–sediment interaction. *Elements* **19**(5), 302-308.

Geist, D. J., Sims, E. N., Hughes, S. S., McCurry, M., Link, P. & Mink, L. (2002). Open-system evolution of a single episode of Snake River Plain magmatism. *Special Papers-Geological Society of America* **353**, 193-204.

Gerdes, A. & Zeh, A. (2006). Combined U–Pb and Hf isotope LA-(MC-) ICP-MS analyses of detrital zircons: comparison with SHRIMP and new constraints for the provenance and age of an Armorican metasediment in Central Germany. *Earth and Planetary Science Letters* **249**, 47-61.

Gerdes, A. & Zeh, A. (2009). Zircon formation versus zircon alteration—new insights from combined U–Pb and Lu–Hf in-situ LA-ICP-MS analyses, and consequences for the interpretation of Archean zircon from the Central Zone of the Limpopo Belt. *Chemical Geology* **261**, 230-243.

Gervasoni, F., Klemme, S., Rocha-Júnior, E. R. & Berndt, J. (2016). Zircon saturation in silicate melts: a new and improved model for aluminous and alkaline melts. *Contributions to Mineralogy and Petrology* **171**, 1-12.

Ghiorso, M. S. & Evans, B. W. (2008). Thermodynamics of rhombohedral oxide solid solutions and a revision of the Fe-Ti two-oxide geothermometer and oxygen-barometer. *American Journal of Science* **308**, 957-1039.

Greber, N. D., Davies, J. H., Gaynor, S. P., Jourdan, F., Bertrand, H. & Schaltegger, U. (2020). New high precision U-Pb ages and Hf isotope data from the Karoo large igneous province;

implications for pulsed magmatism and early Toarcian environmental perturbations. *Results in Geochemistry* **1**, 100005.

Grimes, C. B., John, B. E., Kelemen, P., Mazdab, F., Wooden, J., Cheadle, M. J., Hanghøj, K. & Schwartz, J. (2007). Trace element chemistry of zircons from oceanic crust: A method for distinguishing detrital zircon provenance. *Geology* **35**, 643-646.

Grimes, C. B., Ushikubo, T., John, B. E. & Valley, J. W. (2011). Uniformly mantle-like δ 18 O in zircons from oceanic plagiogranites and gabbros. *Contributions to Mineralogy and Petrology* **161**, 13-33.

Hanan, B., Vetter, S. & Shervais, J. (1997). Basaltic volcanism in the eastern Snake River Plain: lead, neodymium, strontium isotope constraints from the Idaho INEL WO-2 core site basalts. *Geol Soc Am Abs* **29**, A298.

Hart, S.R., Blusztajn, J., Dick, H.J.B., Meyer, P.S. and Muehlenbachs, K. (1999). The fingerprint of seawater circulation in a 500-meter section of ocean crust gabbros. *Geochimica et Cosmochimica Acta* **63**: 4,059-4,080. doi: 10.1016/S0016-7037(99)00309-9.

Hartmann, L. A., Baggio, S. B., Brückmann, M. P., Knijnik, D. B., Lana, C., Massonne, H. J., ... & Arena, K. R. (2019). U-Pb geochronology of Paraná volcanics combined with trace element geochemistry of the zircon crystals and zircon Hf isotope data. *Journal of South American Earth Sciences* **89**, 219-226.

Henry, C. D., Castor, S. B., Starkel, W. A., Ellis, B. S., Wolff, J. A., Laravie, J. A., McIntosh, W. C., & Heizler, M. T. (2017). Geology and evolution of the McDermitt caldera, northern Nevada and southeastern Oregon, western USA. *Geosphere* **13**(4), 1066-1112.

Hildreth, W., Halliday, A. N. & Christiansen, R. L. (1991). Isotopic and chemical evidence concerning the genesis and contamination of basaltic and rhyolitic magma beneath the Yellowstone Plateau volcanic field. *Journal of Petrology* **32**, 63-138.

Hodych, J. P., Cox, R. A. & Košler, J. (2004). An equatorial Laurentia at 550 Ma confirmed by Grenvillian inherited zircons dated by LAM ICP-MS in the Skinner Cove volcanics of western Newfoundland: implications for inertial interchange true polar wander. *Precambrian Research* **129**, 93-113.

Hofmann, A. E., Valley, J. W., Watson, E. B., Cavosie, A. J. & Eiler, J. M. (2009). Sub-micron scale distributions of trace elements in zircon. *Contributions to Mineralogy and Petrology* **158**, 317-335.

Hughes, S. S., McCurry, M. & Geist, D. J. (2002a). Geochemical correlations and implications for the magmatic evolution of basalt flow groups at the Idaho National Engineering and Environmental Laboratory. *Special Papers-Geological Society of America* **353**, 151–173.

Hughes, S. S., Wetmore, P. H., Casper, J. L. & Bonnichsen, B. (2002b). Evolution of Quaternary tholeiitic basalt eruptive centers on the eastern Snake River Plain, Idaho. *Tectonic and Magmatic Evolution of the Snake River Plain Volcanic Province: Idaho Geological Survey Bulletin* **30**, 363-385.

Huppert, H. E., Stephen, R., & Sparks, J. (1985). Cooling and contamination of mafic and ultramafic magmas during ascent through continental crust. *Earth and Planetary Science Letters* **74**(4), 371-386.

Hyndman, D. W. (1983). The Idaho batholith and associated plutons, Idaho and western Montana. In: Roddick, J.A. (ed.) *Circum-Pacific Plutonic Terranes*, Geological Society of America Memoir, 213-240.

King, E. M., Beard, B. L. & Valley, J. W. (2007). Strontium and oxygen isotopic evidence for strike/slip movement of accreted terranes in the Idaho batholith. *Lithos* **96**, 387-401.

Kuntz, M. A. (1992). A model-based perspective of basaltic volcanism, eastern Snake River Plain, Idaho. *Geological Society of America Memoirs* **179**, 289-304.

Kuntz, M. A., Champion, D. E., Spiker, E. C. & Lefebvre, R. H. (1986). Contrasting magma types and steady-state, volume-predictable, basaltic volcanism along the Great Rift, Idaho. *Geological Society of America Bulletin* **97**, 579-594.

Kuntz, M. A. & Dalrymple, G. B. (1979). Geology, geochronology, and potential volcanic hazards in the Lava Ridge-Hells Half Acre area, eastern Snake River Plain, Idaho. *U.S. Geological Survey Open-File Report* **79-1657**, 1-81.

Kuntz, M. A., Skipp, B., Champion, D. E., Gans, P. B., VanSistine, D. P. & Snyders, S. R. (2007). Geologic map of the Craters of the Moon 30' x 60'quadrangle, Idaho. *U.S. Geological Survey Scientific Investigations Map* **2969**, 1-64.

Kuntz, M. A., Skipp, B. A., Lanphere, M. A., Scott, W. E., Pierce, K. L., Dalrymple, G. B., Champion, D. E., Embree, G. F., Page, W. R., Morgan, L. A., Smith, R. P., Hackett, W. R., & Rodgers, D. W. (1994). Geologic map of the Idaho National Engineering Laboratory and adjoining areas, eastern Idaho (IMAP 2330). U.S. *Geological Survey*. https://doi.org/10.3133/i2330

Larsen, L.M. (1979). Distribution of Ree and Other Trace-Elements between Phenocrysts and Peralkaline Undersaturated Magmas, Exemplified by Rocks from the Gardar Igneous Province, South Greenland. *Lithos* **12**(4): 303-315. doi: 10.1016/0024-4937(79)90022-7.

Leeman, W. P. (1982a). Olivine tholeiitic basalts of the Snake River Plain, Idaho. In: Bonnichsen, B. & Breckenridge, R.M. (eds.) *Cenozoic Geology of Idaho*. Idaho Bureau of Mines and Geology Moscow, 181-191.

Leeman, W. P. (1982b). Rhyolites of the Snake River plain-Yellowstone Plateau Province, Idaho and Wyoming; a summary of petrogenetic models. In: Bonnichsen, B. & Breckenridge, R.M. (eds.) *Cenozoic Geology of Idaho*. Idaho Bureau of Mines and Geology Moscow, 193-202.

Leeman, W. P. & Manton, W. (1971). Strontium isotopic composition of basaltic lavas from the Snake River Plain, southern Idaho. *Earth and Planetary Science Letters* **11**, 420-434.

Leeman, W. P., Menzies, M. A., Matty, D. J. & Embree, G. F. (1985). Strontium, neodymium and lead isotopic compositions of deep crustal xenoliths from the Snake River Plain: evidence for Archean basement. *Earth and Planetary Science Letters* **75**, 354-368.

Leeman, W. P., Vitaliano, C. J. & Prinz, M. (1976). Evolved lavas from the snake river plain: craters of the moon national monument, Idaho. *Contributions to Mineralogy and Petrology* **56**, 35-60.

Lemarchand, F., Benoit, V. and Calais, G. (1987). Trace element distribution coefficients in alkaline series. *Geochimica et Cosmochimica Acta* **51**: 1,071-1,081. doi: 10.1016/0016-7037(87)90201-8.

Loucks, R. R., Fiorentini, M. L. & Henríquez, G. J. (2020). New magmatic oxybarometer using trace elements in zircon. *Journal of Petrology* **61**, egaa034, doi: 10.1093/petrology/egaa034.

Luhr, J.F., Carmichael, I.S.E. and Varekamp, J.C. (1984). The 1982 eruptions of El Chichon volcano, Chiapas, Mexico: mineralogy and petrology of the anhydrite-bearing pumices. Journal of Volcanology and Geothermal Research 23: 69-108. doi: 10.1016/0377-0273(84)90057-X.

Mahon, K. I. (1996). The New "York" regression: Application of an improved statistical method to geochemistry. *International Geology Review* **38**(4), 293-303.

Mahood, G.A. and Stimac, J.A. (1990). Trace-element partitioning in pantellerites and trachytes. Geochimica et Cosmochimica Acta 54: 2,257-2,276. doi: 10.1016/0016-7037(90)90050-U.

McCurry, M., Hackett, W. R. & Hayden, K. (1999). Cedar Butte and cogenetic Quaternary rhyolite domes of the eastern Snake River Plain. In: Hughes, S.S. & Thackray G.D. (eds.), *Guidebook to the Geology of Eastern Idaho.* Idaho Museum of Natural History, 169-179.

McCurry, M., Hayden, K. P., Morse, L. H. & Mertzman, S. (2008). Genesis of post-hotspot, A-type rhyolite of the Eastern Snake River Plain volcanic field by extreme fractional crystallization of olivine tholeiite. *Bulletin of Volcanology* **70**, 361-383.

Menzies, M., Leeman, W. & Hawkesworth, C. J. (1984). Geochemical and isotopic evidence for the origin of continental flood basalts with particular reference to the Snake River Plain Idaho, US A. *Philosophical Transactions of the Royal Society of London. Series A, Mathematical and Physical Sciences* **310**, 643-660.

Morgan, L. A. & McIntosh, W. C. (2005). Timing and development of the Heise volcanic field, Snake River Plain, Idaho, western USA. *Geological Society of America Bulletin* **117**, 288-306.

Nash, B. P., Perkins, M. E., Christensen, J. N., Lee, D.-C. & Halliday, A. (2006). The Yellowstone hotspot in space and time: Nd and Hf isotopes in silicic magmas. *Earth and Planetary Science Letters* **247**, 143-156.

Nagasawa, H. (1973). Rare-Earth distribution in alkali rocks from Oki-Dogo Island, Japan. *Contributions to Mineralogy and Petrology* **39**: 301-308.

O'Connor, L., Szymanowski, D., Eddy, M. P., Samperton, K. M. & Schoene, B. (2022). A red bole zircon record of cryptic silicic volcanism in the Deccan Traps, India. *Geology* **50**, 460-464.

Paces, J. B. & Miller Jr, J. D. (1993). Precise U-Pb ages of Duluth complex and related mafic intrusions, northeastern Minnesota: Geochronological insights to physical, petrogenetic, paleomagnetic, and tectonomagmatic processes associated with the 1.1 Ga midcontinent rift system. *Journal of Geophysical Research: Solid Earth* **98**, 13997-14013.

Paster, T.P., Schauwecker, D.S. and Haskin, L.A. (1974). The behavior of some trace elements during solidification of the Skaergaard layered series. *Geochimica et Cosmochimica Acta* **38**(10): 1,549-1,577. doi: 10.1016/0016-7037(74)90174-4.

Pearce, N. J., Perkins, W. T., Westgate, J. A., Gorton, M. P., Jackson, S. E., Neal, C. R. & Chenery, S. P. (1997). A compilation of new and published major and trace element data for NIST SRM 610 and NIST SRM 612 glass reference materials. *Geostandards Newsletter* **21**, 115-144.

Peng, X. & Humphreys, E. D. (1998). Crustal velocity structure across the eastern Snake River Plain and the Yellowstone swell. *Journal of Geophysical Research: Solid Earth* **103**, 7171-7186.

Pierce, K. L. & Morgan, L. A. (1992). The track of the Yellowstone hot spot: Volcanism, faulting, and uplift. In: Link, P.K., Kuntz, M.A. & Platt, L. (eds.) Regional Geology of Eastern Idaho and Western Wyoming, *Geological Society of America Memoir* **179**, 1-53.

Pierce, K. L. & Morgan, L. A. (2009). Is the track of the Yellowstone hotspot driven by a deep mantle plume?—Review of volcanism, faulting, and uplift in light of new data. *Journal of Volcanology and Geothermal Research* **188**, 1-25.

Putirka, K. D., Kuntz, M. A., Unruh, D. M. & Vaid, N. (2009). Magma evolution and ascent at the Craters of the Moon and neighboring volcanic fields, southern Idaho, USA: Implications for the evolution of polygenetic and monogenetic volcanic fields. *Journal of Petrology* **50**, 1639-1665.

Reid, M. R. (1995). Processes of mantle enrichment and magmatic differentiation in the eastern Snake River Plain: Th isotope evidence. *Earth and Planetary Science Letters* **131**, 239-254.

Reid, M. R., Coath, C. D., Harrison, T. M. & McKeegan, K. D. (1997). Prolonged residence times for the youngest rhyolites associated with Long Valley Caldera: ^{230}Th—^{238}U ion microprobe dating of young zircons. *Earth and Planetary Science Letters* **150**, 27-39.

Reiners, P. W. (2005). Zircon (U-Th)/he thermochronometry. *Reviews in Mineralogy and Geochemistry* **58**, 151-179.

Reiners, P. W., Spell, T. L., Nicolescu, S. & Zanetti, K. A. (2004). Zircon (U-Th)/He thermochronometry: He diffusion and comparisons with ^{40}Ar/^{39}Ar dating. *Geochimica et Cosmochimica Acta* **68**, 1857-1887.

Rodgers, D. W., Ore, H. T., Bobo, R. T., McQuarrie, N., Zentner, N., Bonnichsen, B., White, C. & McCurry, M. (2002). Extension and subsidence of the eastern Snake River Plain, Idaho. *Tectonic and Magmatic Evolution of the Snake River Plain Volcanic Province: Idaho Geological Survey Bulletin* **30**, 121-155.

Rojas-Agramonte, Y., Kaus, B. J., Piccolo, A., Williams, I. S., Gerdes, A., Wong, J., Xie, H., Buhre, S., Toukkeridis, T., Montero, P. & Garcia-Casco, A. (2022). Zircon dates long-lived plume dynamics in oceanic islands. *Geochemistry, Geophysics, Geosystems*, **23(11)**, e2022GC010485.

Schaltegger, U. & Davies, J. H. (2017). Petrochronology of zircon and baddeleyite in igneous rocks: Reconstructing magmatic processes at high temporal resolution. *Reviews in Mineralogy and Geochemistry* **83**, 297-328.

Schmitt, A. K. (2007). Ion microprobe analysis of (^{231}Pa)/(^{235}U) and an appraisal of protactinium partitioning in igneous zircon. *American Mineralogist* **92**, 691-694.

Schmitt, A. K., Klitzke, M., Gerdes, A. & Schäfer, C. (2017). Zircon hafnium–oxygen isotope and trace element petrochronology of intraplate volcanic rocks from the Eifel (Germany) and implications for mantle versus crustal origins of zircon megacrysts. *Journal of Petrology* **58**, 1841-1870.

Schmitt, A. K., Perfit, M. R., Rubin, K. H., Stockli, D. F., Smith, M. C., Cotsonika, L. A., Zellmer, G. F., Ridley, W. I. & Lovera, O. M. (2011). Rapid cooling rates at an active mid-ocean ridge from zircon thermochronology. *Earth and Planetary Science Letters*, **302(3-4)**, 349-358.

Schmitt, A. K., Stockli, D. F., Lindsay, J. M., Robertson, R., Lovera, O. M. & Kislitsyn, R. (2010). Episodic growth and homogenization of plutonic roots in arc volcanoes from combined U–Th and (U–Th)/He zircon dating. *Earth and Planetary Science Letters* **295**, 91-103.

Schoene, B., Samperton, K. M., Eddy, M. P., Keller, G., Adatte, T., Bowring, S. A., Khadri, S. F. & Gertsch, B. (2015). U-Pb geochronology of the Deccan Traps and relation to the end-Cretaceous mass extinction. *Science* **347**, 182-184.

Schulz, B., Klemd, R. & Brätz, H. (2006). Host rock compositional controls on zircon trace element signatures in metabasites from the Austroalpine basement. *Geochimica et Cosmochimica Acta* **70**, 697-710.

Shao, T., Xia, Y., Ding, X., Cai, Y. & Song, M. (2019). Zircon saturation in terrestrial basaltic melts and its geological implications. *Solid Earth Sciences* **4**, 27-42.

Shervais, J. W., Branney, M. J., Geist, D. J., Hanan, B. B., Hughes, S., Prokopenko, A. A. & Williams, D. F. (2006). HOTSPOT: the Snake River scientific drilling project–Tracking the Yellowstone Hotspot through space and time. *Scientific Drilling* **3**, 56-57.

Shervais, J. W. & Hanan, B. B. (2008). Lithospheric topography, tilted plumes, and the track of the Snake River–Yellowstone hot spot. *Tectonics* **27**, TC5004, doi:10.1029/2007TC002181

Shumlyanskyy, L., Nosova, A., Billström, K., Söderlund, U., Andréasson, P.-G. & Kuzmenkova, O. (2016). The U–Pb zircon and baddeleyite ages of the Neoproterozoic Volyn Large Igneous Province: implication for the age of the magmatism and the nature of a crustal contaminant. *GFF* **138**, 17-30.

Smith, R. B. & Braile, L. W. (1994). The yellowstone hotspot. *Journal of Volcanology and Geothermal Research* **61**, 121-187.

Sparlin, M. A., Braile, L. & Smith, R. B. (1982). Crustal structure of the eastern Snake River Plain determined from ray trace modeling of seismic refraction data. *Journal of Geophysical Research: Solid Earth* **87**, 2619-2633.

Spear, D. B. (1979). *The geology and volcanic history of the Big Southern Butte-East Butte area, eastern Snake River plain, Idaho*: State University of New York at Buffalo.

Spear, D. B. & King, J. S. (1982). The geology of Big Southern Butte, Idaho. *Cenozoic geology of Idaho: Idaho Bureau of Mines and Geology Bulletin* **26**, 395-403.

Spera, F. J. & Bohrson, W. A. (2001). Energy-constrained open-system magmatic processes I: General model and energy-constrained assimilation and fractional crystallization (EC-AFC) formulation. *Journal of Petrology* **42**, 999-1018.

Stearns, H. T. (1928). The" Craters of the Moon" in Idaho. *The Geographical Journal* **71**, 43-49.

Stefano, C. J., Mukasa, S. B. & Cabato, J. A. (2019). Elemental abundance patterns and Sr-, Nd- and Hf-isotope systematics for the Yellowstone hotspot and Columbia River flood basalts: Bearing on petrogenesis. *Chemical Geology* **513**, 44-53.

Stout, M., Nicholls, J. & Kuntz, M. (1994). Petrological and mineralogical variations in 2500–2000 yr BP lava flows, Craters of the Moon lava field, Idaho. *Journal of Petrology* **35**, 1681-1715.

Trail, D., Chowdhury, W., Tailby, N. D. & Ackerson, M. R. (2024). Ce and Eu anomalies in zircon as indicators of oxygen fugacity in subsolidus systems. *Geochimica et Cosmochimica Acta* **369**, 93-110.

Trail, D., Mojzsis, S. J., Harrison, T. M., Schmitt, A. K., Watson, E. B. & Young, E. D. (2007). Constraints on Hadean zircon protoliths from oxygen isotopes, Ti-thermometry, and rare earth elements. *Geochemistry, Geophysics, Geosystems* **8**.

Trail, D., Watson, E. B. & Tailby, N. D. (2012). Ce and Eu anomalies in zircon as proxies for the oxidation state of magmas. *Geochimica et Cosmochimica Acta* **97**, 70-87.

Turrin, B., Champion, D., Hackett, W.R., and Payne, S.J., 2023, Argon-isotopic age dating analyses for Eastern Snake River Plain volcanic rock samples: Battelle Energy Alliance Report, INL/RPT-23-74811, November, 113 p.

Valley, J., Lackey, J., Cavosie, A., Clechenko, C., Spicuzza, M., Basei, M. A. S., Bindeman, I., Ferreira, V., Sial, A. N. & King, E. (2005). 4.4 billion years of crustal maturation: oxygen isotope ratios of magmatic zircon. *Contributions to Mineralogy and Petrology* **150**, 561-580.

Vermeesch, P. (2018). IsoplotR: A free and open toolbox for geochronology. *Geoscience Frontiers*, **9(5)**, 1479-1493.

Vervoort, J. D. & Patchett, P. J. (1996). Behavior of hafnium and neodymium isotopes in the crust: constraints from Precambrian crustally derived granites. *Geochimica et Cosmochimica Acta* **60**, 3717-3733.

Watson, E. B. (1996). Dissolution, growth and survival of zircons during crustal fusion: kinetic principals, geological models and implications for isotopic inheritance. *Earth and Environmental Science Transactions of the Royal Society of Edinburgh* **87**, 43-56.

Watson, E. B. & Harrison, T. M. (1983). Zircon saturation revisited: temperature and composition effects in a variety of crustal magma types. *Earth and Planetary Science Letters* **64**, 295-304.

Watts, K. E., Bindeman, I. N. & Schmitt, A. K. (2011). Large-volume rhyolite genesis in caldera complexes of the Snake River Plain: insights from the Kilgore Tuff of the Heise Volcanic Field, Idaho, with comparison to Yellowstone and Bruneau–Jarbidge rhyolites. *Journal of Petrology* **52**, 857-890.

Whitaker, M. L., Nekvasil, H., Lindsley, D. H. & McCurry, M. (2008). Can crystallization of olivine tholeiite give rise to potassic rhyolites?—an experimental investigation. *Bulletin of Volcanology* **70**, 417-434.

Whitehead, R. (1992). Geohydrologic framework of the Snake River Plain regional aquifer system, Idaho and eastern Oregon. *U.S. Geological Survey Professional Paper* **1408-B**, 1-32.

Wiedenbeck, M., Alle, P., Corfu, F., Griffin, W. L., Meier, M., Oberli, F. v., Quadt, A. v., Roddick, J. & Spiegel, W. (1995). Three natural zircon standards for U-Th-Pb, Lu-Hf, trace element and REE analyses. *Geostandards Newsletter* **19**, 1-23.

Wiedenbeck, M., Hanchar, J. M., Peck, W. H., Sylvester, P., Valley, J., Whitehouse, M., Kronz, A., Morishita, Y., Nasdala, L. & Fiebig, J. (2004). Further characterisation of the 91500 zircon crystal. *Geostandards and Geoanalytical Research* **28**, 9-39.

Xu, Z., Zheng, Y. F., & Zhao, Z. F. (2018). Zircon evidence for incorporation of terrigenous sediments into the magma source of continental basalts. *Scientific Reports* **8**(1), 178.

Zhang, Y. & Xu, Z. (2016). Zircon saturation and Zr diffusion in rhyolitic melts, and zircon growth geospeedometer. *American Mineralogist* **101**, 1252-1267.

Zheng, J., Griffin, W., Li, L., O'Reilly, S. Y., Pearson, N., Tang, H., Liu, G., Zhao, J., Yu, C. & Su, Y. (2011). Highly evolved Archean basement beneath the western Cathaysia block, South China. *Geochimica et Cosmochimica Acta* **75**, 242-255.

Zhu, W.-G., Zhong, H., Li, Z.-X., Bai, Z.-J. & Yang, Y.-J. (2016). SIMS zircon U–Pb ages, geochemistry and Nd–Hf isotopes of ca. 1.0 Ga mafic dykes and volcanic rocks in the Huili area, SW China: Origin and tectonic significance. *Precambrian Research* **273**, 67-89.

Formblatt Kumulative Dissertation Stand 14.02.2023

1. **Publikation/*Publication*:**
   Vollständige bibliographische Referenz/*Complete bibliographic reference:*
   `Angeles-De La Torre, C. A., Schmitt, A. K.,Gerdes, A., Hertwig, A., McCurry, M. & Lovera, O. M. Provenance and thermal evolution of rhyolite magma in the Blackfoot volcanic field`

2. Erst- oder gleichberechtigte Autorenschaft/*First or equal authorship:* Ja/*Yes* ☑ Nein/*No* ☐

3. Veröffentlicht/*Published* ☐ Zur Veröffentlichung akzeptiert/*Accepted* ☐

   Q1/Q2:* Ja/*Yes* ☐ Nein/*No* ☐
   **SCImago Journal Rank (SJR) indicator*
   Im Erscheinungsjahr oder im letzten verfügbaren Vorjahr/*In the year of publication or the last prior year available:* _________

   Eingereicht/*Submitted* ☑ Noch nicht eingereicht/*Not yet submitted* ☐

4. **Beteiligungen/*Contributions*****

Contributor Role	Doktorand/in/ *Doctoral student*	Co-Autor/in 1/ *Co-author 1*	Co-Autor/in 2/ *Co-author 2*
Name, first name	Angeles De La Torre Carlos A.	Schmitt Axel K.	Hertwig Andreas
Methodology	☑	☐	☐
Software	☐	☐	☑
Validation	☑	☑	☑
Formal analysis	☑	☑	☑
Investigation	☑	☐	☑
Resources	☑	☐	☐
Data Curation	☑	☑	☐
Writing-Original Draft	☑	☐	☐
Writing-Review&Editing	☑	☑	☑
Visualization	☑	☐	☐
Supervision	☐	☑	☐
Project administration	☐	☑	☐
Funding acquisition	☐	☑	☐

***Kategorien des CRediT (Contributor Roles Taxonomy, https://credit.niso.org/)*

Hiermit bestätige ich, dass alle obigen Angaben korrekt sind/*I confirm that all declarations made above are correct.*

Unterschrift/*Signature* ________________ Doktorand/in/*Doctoral student* ________________ Co-Autor/in 1/*Co-author 1* A. Hertwig Co-Autor/in 2/*Co-author 2*

Betreuungsperson/*Supervisor:*
Hiermit bestätige ich, dass alle obigen Angaben korrekt sind und dass die selbstständigen Arbeitsanteile des/der Doktoranden/in an der aufgeführten Publikation hinreichend und signifikant sind/*I confirm that all declarations made above are correct and that the doctoral student's independent contribution to this publication is significant and sufficient to be considered for the cumulative dissertation.*

Prof. Dr. Axel Schmitt — Name/*Name*
Unterschrift/*Signature*
29/05/2025 — Datum/*Date*

Appendix III

Provenance and thermal evolution of rhyolite magma in the Blackfoot volcanic field

Authors

Carlos A. Angeles-De La Torre, Axel K. Schmitt, Axel Gerdes, Andreas Hertwig, Michael McCurry, & Oscar M. Lovera

Abstract

The bimodal Blackfoot Volcanic Field (BVF) in eastern Idaho hosts Middle–Late Pleistocene rhyolite domes that are among the youngest topaz rhyolites worldwide. Despite young volcanism in the BVF, its geothermal potential has remained elusive. To evaluate the magmatic and thermal evolution of the BVF, we investigated zircon crystals from seven domes by U-Pb and U-Th geochronology as well as correlative trace element and isotopic ($\delta^{18}O$, εHf) analysis. For the three northern domes and the central Sheep Island dome, zircon crystallization occurred between 1,006 and 785 ka, indicating younger eruption ages than previously reported. Zircon populations from the three southern domes are on average distinctly younger (mostly 63.4–55.2 ka) and overlap literature $^{40}Ar/^{39}Ar$ ages. For the northern domes, Sheep Island, and the southern domes, zircon $\delta^{18}O$ averages are similar (+4.54, +3.86, and +4.45, respectively), whereas the corresponding εHf averages are more variable and strongly negative at -13.4, -15.3, and -10.1, indicating higher contributions of Archean crust compared to coeval rhyolites from the Eastern Snake River Plain. Cooling and fractionation of a 120 km³ magma reservoir emplaced at 95 ka and 6 km depth successfully reproduces zircon ages, magma temperatures, and combined volumes for the southern domes and a geophysically inferred silicic intrusion. This indicates that temperatures at ~4 km depth could still exceed 300 °C today, although the absence of geothermal surface manifestations and low temperatures encountered in a nearby exploration well suggests that thermal waters above this deep geothermal resource are diluted and diverted in a structurally controlled hydrological system.

1 Introduction

Regions characterized by a high density of young volcanic vents often indicate underlying magma chambers or recent sill intrusions, making them prime indicators of magmatic heat centers within the crust (e.g., Shervais *et al.*, 2024). These areas are particularly attractive for geothermal exploration due to their potential for elevated subsurface temperatures. One such region of interest is the Snake River Plain-Yellowstone magmatic province, United States, which stands out due to its high heat flow as a consequence of extensive volcanic activity associated with the apparent southwest-to-northeast migration of the Yellowstone hotspot (Armstrong *et al.*, 1975; Ellis *et al.*, 2013; Pierce and Morgan, 1992; Smith and Braile, 1994). With temperatures exceeding 200°C at depths of ~4 km, this region is recognized as one of North America's geothermally most promising provinces (e.g. Blackwell *et al.*, 1992; Tester *et al.*, 2006). However, its geothermal potential remains largely untapped, as demonstrated by the U.S. Geological Survey's estimate of up to 4,937 MWe of undiscovered geothermal resources in Idaho alone (Williams *et al.*, 2008), which if developed could increase current geothermal energy production in the United States by more than ~250% (as of 2023; U.S. Energy Information Administration, 2025).

The Snake River Plain-Yellowstone system is a classic example of bimodal (basalt–rhyolite) volcanism, which is predominantly attributed to mantle-derived magmatism (e.g., Anders *et al.*, 2014; Bonnichsen *et al.*, 2008; Christiansen and McCurry, 2008; Hildreth *et al.*, 1991; Leeman, 2007; McCurry *et al.*, 2008; McCurry and Rodgers, 2009; Morgan, 1971; Nash *et al.*, 2006; Pierce and Morgan, 2009; Stachnik *et al.*, 2008; Wright *et al.*, 2002). The silicic volcanism, spanning from the Miocene to Pliocene, comprises formation of large caldera complexes along the hotspot track, progressing from northern Nevada through southern Idaho and culminating in present-day Yellowstone, Wyoming (e.g., Anders *et al.*, 2019; Colón *et al.*, 2018; Henry *et al.*, 2017; Kuntz, 1992; Morgan and McIntosh, 2005; Shervais *et al.*, 2006; Stout *et al.*, 1994; Watts *et al.*, 2011). In the wake of the hotspot track, extensive olivine tholeiitic basalt flows have largely covered the earlier silicic deposits (e.g., Geist *et al.*, 2002; Hanan *et al.*, 1997; Hughes *et al.*, 2002a, b; Kuntz, 1992; Leeman, 1982; Reid, 1995; Shervais *et al.*, 2006). Coeval Quaternary rhyolitic volcanism is restricted to the eastern Snake River Plain (ESRP) and peripheral areas where it is manifested as cryptodomes and endogenous lava domes (Kuntz and Dalrymple, 1979; McCurry *et al.*, 1999; McCurry *et al.*, 2008; Spear, 1979; Spear and King, 1982). This includes the Blackfoot Volcanic Field (BVF), once considered "one of the most favorable geothermal prospects in Idaho" (Welhan *et al.*, 2013). Located ~60 km southeast of the ESRP, the BVF is the region's youngest bimodal volcanic field, featuring widespread basaltic volcanism interspersed with rhyolite lava domes (Fiesinger *et al.*, 1982; McCurry *et al.*, 2014).

The BVF is a promising geothermal target because of its Quaternary age and potential for large subsurface intrusions. Since 1.6 Ma, approximately 1.2 km^3 of rhyolite has erupted in the BVF (Ford, 2005) with three topaz-bearing rhyolite domes in the center of the BVF erupted as recently as 57 ± 8 ka ($^{40}Ar/^{39}Ar$; Heumann, 1999). Gravity anomalies suggest that in addition to the extrusive rhyolites, two silicic intrusions of 40 and 60 km^3 each were emplaced as shallow as <1 km deep in the central BVF (Hastings *et al.*, 2021). Regional spring waters display He and $\delta^{13}C$ isotope gas compositions and emission rates similar to those observed at quiescent volcanic systems (Lewicki *et al.*, 2013). Moreover, regional thermal springs have temperatures reaching up to 33°C, but these are distal and concentrated along basin-bounding faults (Autenrieth *et al.*, 2011). The absence of surface geothermal manifestations and the lack of high-temperature resources at drillable depths directly associated with the volcanoes also casts doubts on the geothermal potential of the BVF (Autenrieth *et al.*, 2011; Welhan *et al.*, 2013; 2014). Several hypotheses have been proposed to explain this apparent conundrum. These include the possibility that associated magmatic intrusions were either too small or too deeply emplaced to sustain geothermal activity, or that the presence of a cold aquifer masks deeper thermal anomalies (Neupane *et al.*, 2014; Welhan *et al.*, 2014).

Zircon petrochronology has been instrumental in advancing the understanding of rhyolite genesis within the ESRP and elsewhere (e.g. Colón *et al.*, 2018; Drew, 2013; Ellis *et al.*, 2013, 2019; McCurry and Rodgers, 2009). Since zircon saturation in magma is temperature-dependent (Watson and Harrison, 1983), zircon geochemistry and isotopic signatures provide direct insights into magma thermal histories and compositional evolution. Furthermore, zircon age spectra have proven valuable for reconstructing long-term magmatic fluxes, offering critical constraints on the volumes and rates of magma generation (Angeles-De La Torre *et al.*, 2023; Caricchi *et al.*, 2014, 2016; Friedrichs *et al.*, 2021; Liu *et al.*, 2021; Lukács *et al.*, 2018; Melnik *et al.*, 2021; Ratschbacher *et al.*, 2018; Schmitt *et al.*, 2023; Tierney *et al.*, 2016; Weber *et al.*, 2020). This study presents U-Th-Pb zircon ages, O and Hf isotope compositions, and trace element geochemistry of zircon from the BVF rhyolites. Collectively, these data were used to constrain a thermal model for the underlying magma system which suggest the presence of a shallow magma reservoir that retains geothermal potential in the shallow crust

2 Geological Background

2.1 Evolution of the Blackfoot Volcanic Field (BVF)

The bimodal BVF (Fig. 1) consists of Quaternary scoria cones, tuff rings, basalt flows, rhyolitic domes and maar complexes located at the northeastern border of the Basin and Range extensional province, where several graben structures are superimposed on a thick package of overthrust Archean basement to Mesozoic deposits and became infilled by collectively ~100 km^3 of lava that ponded to a maximum depth of ~230 m (McCurry *et al.,* 2015). The majority of the basalts in this field are interpreted to have erupted both before and after the emplacement of the rhyolite domes with ages reported between c. 1,040 and 27.5 ka (Luedke and Smith, 1983; Pickett, 2004). The volumetrically subordinate rhyolite domes in the BVF have an estimated total volume of ~1.2 km^3 (Ford, 2005) and follow a linear distribution along a primary NNW-NNE-trending fault system (Hastings *et al.*, 2021; Polun, 2011). The northern subfield of the BVF comprises three rhyolite domes—Northern Dome West, Middle, and East—which represent the oldest rhyolitic units in the BVF with reported K-Ar ages of 1,590 ± 60 ka for Northern Dome West and 1,410 ± 150 ka for Northern Dome East (Luedke and Smith, 1983). Two rhyolitic islands within the Blackfoot Reservoir, Sheep Island and Gull Island, are located ~17 km SSW of the northern dome field with Sheep Island being dated at 1,400 ± 200 ka using K-Ar methods (Luedke and Smith, 1983).

Approximately 10 km to the south three prominent rhyolite domes named China Hat, China Cap, and North Cone domes form a NE-SW trending array at the southern end of the Blackfoot reservoir (Fig. 1). This southern dome subfield was emplaced following phreatomagmatic explosive activity, which is evident by basal pyroclastic deposits and by lava partially infilling maar-like depressions (McCurry *et al.,* 2015). One NW-elongated negative gravity anomaly directly underlies these rhyolites domes, whereas a second anomaly with a similar elongation is present adjacent to the NE of them (Hastings *et al.*, 2021). These anomalies have been interpreted as two separate silicic bodies in the upper crust (<1 km), with estimated volumes of ~40 km^3 and ~60 km^3, respectively (Hastings *et al.*, 2021). Quaternary ENE-trending normal faults overlying these bodies are distinct from the regional extensional faults (Polun, 2011) and are possibly linked to emplacement or eruptive venting from subsurface magma intrusions (e.g., Hastings *et al.*, 2021).

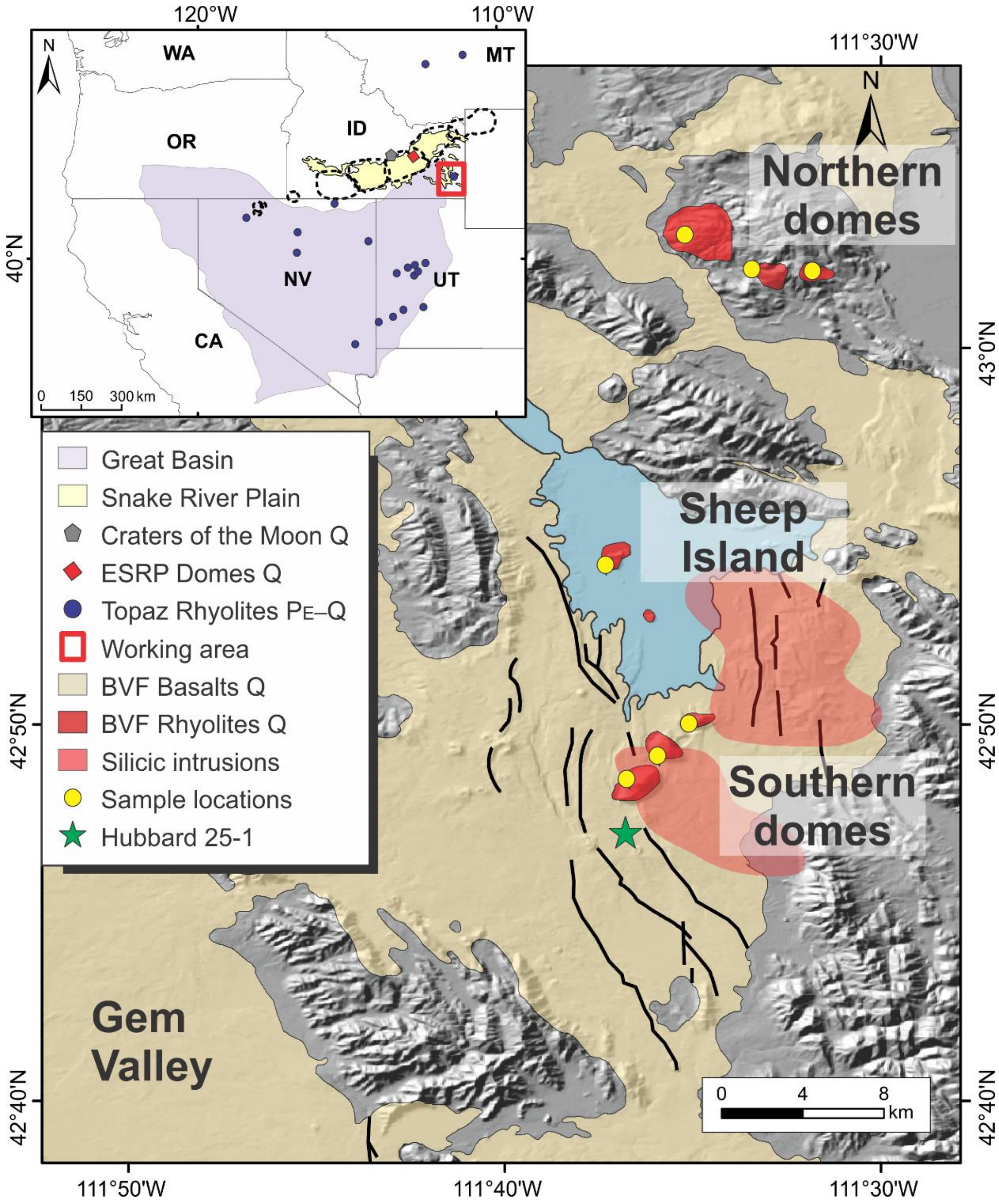

Fig. 1. *Blackfoot Volcanic Field (BVF) overview map with sample locations marked (exact coordinates in Table 1). Possibly cogenetic shallow (<1 km deep) silicic intrusions are outlined based on 600 m thickness contours (Hastings et al., 2021). Hubbard-25 is a well with temperature data (see text). Inset map shows the transgressive calderas associated with the Yellowstone hotspot track (dashed lines) after McCurry and Rodgers (2009). Topaz rhyolite locations are from Christiansen et al. (2007). Digital elevation model was generated from GeoMapApp (www.geomapapp.org) CC BY (Ryan et al., 2009).*

China Hat, China Cap, and North Cone yielded ^{40}Ar/^{39}Ar sanidine ages of 52 ± 14 ka, 75 ± 6 ka, and 57 ± 6 ka, respectively, but the preferred eruption age for all three domes was stated as 57 ± 8 ka (Heumann, 1999). Whole rock U-series data defining an isochron age of 49 ± 11 ka for the same domes support a young eruption age (Heumann, 1999). Reconnaissance zircon U-series data for China Hat define an isochron of 66 ± 14 ka (Schmitt, 2011), whereas two populations distinguished in their uranium concentrations and cathodoluminescence brightness were reported in (Bernal *et al.*, 2014) with crystallization ages of $57.4^{+2.2}_{-2.2}$ and $56^{+8.0}_{-7.2}\ ka$ for the high U/low luminescence crystals, and $267^{+42}_{-33}\ ka$ for the low U/high luminescence populations.

Primitive olivine tholeiite lava flows, which are mineralogically and geochemically equivalent to those of the ESRP (Fiesinger *et al.*, 1982, Pickett, 2004; McCurry *et al.,* 2015), are attributed to partial melting of pyroxenite-veined, spinel-lherzolite mantle rocks (McCurry *et al.,* 2015), with up to 60% fractional crystallization leading to rare trachybasalt compositions (Fiesinger *et al.*, 1982). The bimodal nature of the BVF is underscored by the presence of enclaves that compositionally define a magmatic mixing trend between mafic and felsic endmembers (Goldsby, 2017; Lochridge, 2016). For BVF rhyolites, assimilation-fractional crystallization (AFC) models suggest that the BFV olivine tholeiite parent only experienced limited upper crustal assimilation of <20% Archean crust (Ford, 2005; Lochridge, 2016). The highly differentiated and sparsely porphyritic BVF rhyolites contain phenocrysts of quartz, sanidine, plagioclase, and minor biotite, hornblende, orthopyroxene, magnetite, and ilmenite with accessory allanite, apatite, thorite, and zircon (Ford, 2005; Heumann, 1999; Dayvault *et al.,* 1984). Topaz crystals have also been identified in the three southern domes, but its occurrence is rare and associated with fractures and vesicles suggesting a non-magmatic high-T vapor phase (Dayvault *et al.,* 1984). In addition, pre-eruptive mafic magma recharge is evident from intermingled mafic enclaves (McCurry *et al.,* 2015). Amphibole and Fe-Ti oxide thermobarometry suggested rhyolite storage at ~12–14 km at ~760°C (Ford, 2005; McCurry *et al.,* 2015); storage pressures are re-evaluated in Section 5.3.

2.2 Rhyolite origins in adjacent geodynamic settings: Eastern Snake River Plain and Great Basin

Because of the proximity of the BVF to the ESRP and the chemical similarity between their olivine tholeiite endmembers (Fiesinger *et al.*, 1982), it is also instructive to consider rhyolite genesis in the ESRP as a potential analog. The early stages of rhyolitic volcanism associated with the

Yellowstone hotspot are marked by the formation of multiple calderas along the Snake River Plain over the past c. 16.4 Ma and progression to its present-day focal point at Yellowstone (e.g., Armstrong *et al.*, 1975; Henry *et al.*, 2017; Pierce and Morgan, 2009). The sequential development of these calderas implies intense reworking of the Archean basement by up to 340,000 km^3 of gabbroic intrusions (McCurry and Rodgers, 2009; Peng and Humphreys, 1998; Sparlin *et al.*, 1982). Individual calderas evolved cyclically over a c. 2–4 Ma lifecycle million-year gap, with large-volume caldera forming eruptions in successive centers being separated by c. 2 Ma (Bindeman and Simakin, 2014). A defining feature of Yellowstone hotspot volcanism is the widespread occurrence of low-δ^{18}O rhyolites with some of the most extreme ^{18}O depletions known in terrestrial magmas that are attributed to remelting of hydrothermally altered intracaldera rocks (e.g., Bindeman and Simakin, 2014; Bonnichsen *et al.*, 2008; Colón *et al.*, 2018; Drew, 2013; Ellis *et al.*, 2013).

In the wake of silicic caldera volcanism, outpourings of olivine tholeiitic lava accumulated over the last c. 4 Ma in the ESRP to a thickness of 1–2 km, including the Holocene Craters of the Moon basaltic volcanic field (Kuntz et al., 1992). This was associated with a late stage of Quaternary rhyolite volcanism, which is spatially separated from the activity at Yellowstone caldera, and which produced endogenic domes, flows, and cryptodomes either simultaneously with, or slightly before or after effusion of the olivine tholeiite flows (McCurry *et al.*, 2008). Although the ESRP is dominantly bimodal, rare intermediate compositions have been identified as lava flows and enclaves within rhyolite domes in outcrop and drill cores (McCurry *et al.*, 2008). Notably, three Holocene trachyandesitic lava flows at Craters of the Moon share geochemical affinities with the less evolved compositions observed in the Late Pleistocene Cedar Butte dome (Christiansen and McCurry, 2008; McCurry *et al.*, 2008).

Proposed models for ESRP rhyolite genesis include extensive fractional crystallization of mantle-derived basalt (e.g., Leeman *et al.*, 1976; McCurry *et al.*, 2008; McCurry and Rodgers, 2009) or partial melting of lower crustal rocks triggered by sustained basaltic intrusion (e.g., Bonnichsen *et al.*, 2008; Christiansen and McCurry, 2008; Leeman *et al.*, 1976). In contrast to the caldera-related rhyolites of the ESPR, the small-volume Quaternary rhyolites and their intermediate precursors in the ESRP exhibit only minor assimilation of Archean crust (McCurry *et al.*, 2008; Putirka *et al.*, 2009; Angeles-De La Torre *et al.,* 2025). However, at Craters of the Moon located along the margins of the ESRP where Archean basement remained relatively undisturbed during the passage of the Yellowstone hot spot, the influence of Archean basement on the Holocene basaltic magmas and their differentiates is detectable (e.g., Putirka *et al.*, 2009). Moreover, assimilation of hydrothermally altered volcanic rocks is indicated by low-δ^{18}O zircon in Quaternary rhyolites from the axial ESPR, whereas no such influence is detected for zircon in evolved Craters of the Moon lavas (Angeles-De La Torre *et al.,* 2025).

While Quaternary ESRP rhyolites in their bimodal association are broadly similar to those of the BVF, the BVF rhyolites also exhibit distinct geochemical signatures, which are characterized by high fluorine abundances reflected by the presence of F-rich topaz as an accessory mineral, high enrichments in certain high field strength trace elements such as Y, Nb, and Ta, as well as extreme depletions in feldspar-compatible trace elements including Sr, Ba, and Eu (Heumann, 1999; Ford, 2005; McCurry et al., 2015). These are also the defining features for topaz rhyolites, a group of ~30 volcanic centers scattered throughout the extensional provinces of the western United States, which erupted over the past c. 50 Ma (Christiansen *et al.*, 2007). Several of these are also associated with economically important mineral deposits (e.g. Spor Mountain, Utah, for Be ores; Ayuso *et al.*, 2020). Because of this similarity, the southern domes of the BVF has been identified the youngest known topaz rhyolite complex (Christiansen *et al.*, 1986). Topaz rhyolites younger than c. 15 Ma are generally volumetrically subordinate to coeval basaltic volcanism in bimodal associations within the Great Basin, where extended Precambrian basement is a common denominator in their distribution (Best *et al.*, 1980; Christiansen *et al.*, 1983). Pure anatexis of felsic continental crustal rocks is largely dismissed as a potential origin of topaz rhyolites. Instead, their formation is attributed to extensive fractional crystallization from mantle-derived basalts, or to lower crustal partial melting of juvenile mafic intrusions that may have interacted to a minor degree with pre-existing felsic continental crust (Christiansen *et al.*, 2007).

3 Sampling and methods

Approximately 1 kg of rock material was collected from each of the three northern subfield domes (Northern Dome West, Middle, and East), Sheep Island, and the three southern domes (China Hat, China Cap, and North Cone) for this study (Fig. 1; Table 1). Samples were initially crushed with a hammer and dry-sieved to isolate the <250 µm fraction. Heavy mineral concentrates, including zircon, were then separated using hydrodynamic density enrichment techniques. Individual crystals were hand-picked under a binocular microscope and mounted in epoxy, along with zircon reference materials AS3 (Paces and Miller, 1993), 91500 (Wiedenbeck *et al.*, 1995; Wiedenbeck *et al.*, 2004), and Temora 2 (Black *et al.*, 2004). Epoxy mounts were ground with silicon carbide abrasives to expose grain interiors and subsequently polished using 1 µm diamond paste.

To assess internal textures and potential zonation of crystals from the dense fraction, mounts were coated with a 20 nm Au layer and imaged using a Zeiss EVO MA 15 scanning electron microscope (SEM) at Heidelberg University. Backscattered electron (BSE) images were acquired using a high-definition backscatter detector at high voltage beam conditions of 18 keV and 0.5–4.0 nA. Cathodoluminescence (CL) images were acquired using a variable pressure secondary electron detector in low vacuum mode at 10 keV and 10 nA. Additionally, energy dispersive X ray spectroscopy (EDS) and Raman microscopy was performed for the identification of mineral phases using an Oxford Instruments AZtec detector and a WITec alpha300 R spectrometer, respectively. Prior to secondary ion mass spectrometry (SIMS) analysis, the Au coating was gently removed by wiping the surface with tissue and ethanol, followed by ultrasonic cleaning in aqueous decontaminants. Samples were then rinsed multiple times with deionized water and methanol before being recoated with an ~50 nm Au layer to ensure optimal surface conductivity for SIMS analysis.

3.1 U-Th-Pb geochronology and trace elements

Zircon U-Th-Pb geochronology was conducted using the CAMECA ims 1300-HR3 SIMS at the John de Laeter Centre, Curtin University, following the analytical procedures detailed in Angeles-De La Torre *et al.* (2025). For disequilibrium dating, a $^{16}O^-$ primary beam (~40 nA) in Gaussian mode was focused to a ~25 µm spot, with secondary ions extracted at 10 kV and analyzed at a mass resolution m/Δm of ~5000. Secondary ion intensities of 244.03 (background) and $^{230}Th^{16}O$ were collected by electron multipliers, whereas the intense $^{232}Th^{16}O$ and $^{238}U^{16}O$ beams were detected in Faraday cups (FCs); all four masses were measured simultaneously. Data were acquired over 20 cycles and corrected for dead-time and FC baseline using the in-house ZIPSv. 3.1.1. data reduction software. the accuracy of measured (^{230}Th)/(^{238}U) was monitored using secular equilibrium reference zircon AS3 which yielded a weighted average (^{230}Th)/(^{238}U) = 1.016 ± 0.020 (2se uncertainties; mean square of weighted deviates MSWD = 3.64; n = 11).

For U-Pb geochronology, a 12–18 nA $^{16}O^-$ primary beam was focused to ~20 µm, with secondary ions transmitted through 400 µm and 3000 µm contrast and field apertures, respectively, and an energy bandpass of 50 eV in rectangular mode. Secondary ions, including Pb, U, Th, and Zr species, were measured in peak-hopping mode over 10 cycles following a 20 s pre-sputtering. Calibration of relative sensitivity factors (RSFs) for U-Pb, U-Th, and U-Zr was performed using AS3 and 91500 zircon references, applying established regression methods. Zircon reference 91500 analyzed as a control yielded a $^{206}Pb/^{238}U$ age of 1071 ± 27 Ma (2se; MSWD = 0.37, n = 5) relative to the reported age of 1065 Ma (Wiedenbeck *et al.*, 1995). Common Pb corrections were conducted using measured ^{207}Pb, and $^{206}Pb/^{238}U$ ages were corrected for initial ^{230}Th disequilibrium using Th/U ratios from whole-rock data (Ford, 2005). Age uncertainties are reported at 95% confidence, incorporating excess scatter where necessary (Mahon, 1996). Systematic uncertainties related to decay constants are negligible at the stated precision, and comparisons between dating methods follow standard approaches (Condon *et al.*, 2024).

During U-Th and U-Pb analyses, only Th and U abundances were estimated from comparison of $^{238}UO/^{90}Zr_2{}^{16}O_4$ and $^{238}U/^{94}Zr_2O$ with 91500 reference zircon (81.2 µg/g U; Wiedenbeck *et al.*, 1995), respectively, and the Th/U RSF determined from $^{208}Pb/^{206}Pb$. A complete set of trace elements was obtained following methods described in Schmitt *et al.* (2017), utilizing a ~15 nA $^{16}O^-$ primary beam in Gaussian mode to target the same craters previously examined for U-Th-Pb geochronology, without requiring additional coating. Trace element relative sensitivity factors (RSFs) were calibrated against NIST SRM 610 (Pearce *et al.*, 1997), with accuracy assessed through analyses of 91500 reference zircons (Wiedenbeck *et al.*, 2004). All data on unknowns with Mg >2.5 µg/g, $^{57}Fe/^{30}Si$ >0.00082 and LREE-I <30 (LREE-I = Dy/Nd + Dy/Sm; (Bell *et al.*, 2016, 2019) were rejected because they are likely compromised by overlap onto non-zircon phases (e.g. apatite, glass, or oxide inclusions). Titanium abundances in zircon (TiZr) were used as a proxy to estimate the crystallization temperatures following the equations in Ferry and Watson (2007). A value of $\alpha TiO_2 = 0.52$ was calculated from the magnetite-ilmenite exchange equilibrium (Ghiorso and Evans, 2008) using the compositions reported for the southern domes (Ford, 2005). Quartz is an abundant mineral phase within the rhyolite domes meaning that the system is effectively saturated in silica and therefore value of $\alpha SiO_2 = 1$ was used. Analytical uncertainties translate into temperature uncertainties of <10 °C based on the external reproducibility of Ti analysis of 91500 zircon reference (4.6 ± 0.3 µg/g; 1s; n = 12). Zircon trace elements were also used to estimate melt oxygen fugacity relative to the fayalite-magnetite-quartz buffer (ΔFMQ; Loucks *et al.*, 2020).

Table 1. Summary of zircon U–Pb and U-Th average ages and isotopic compositions for the Blackfoot Volcanic Field (BVF) rhyolite domes. Reported eruption ages are included for context and comparison with new zircon data. Age uncertainties are given at the 95% confidence level, while isotopic compositions are reported with 2 standard deviations. Full individual zircon data are provided in Supplementary Tables S1–S5.

Unit	Eruption age (ka)	Sample name	Coordinates (WGS 84)		Zircon crystallization age		$\delta^{18}O$	εHf
			Latitude	Longitude	(ka)	MSWD		
BVF northern Domes								
Northern Dome West	1590 ± 60[a]	NDW	43.05081667	-111.5856667	957 ± 24	0.94	+4.68 ± 0.35	-13.3 ± 1.1
Northern Dome Middle	1410 ± 150[a]	NDM	43.03546667	-111.5558	984 ± 26	1.17	+4.51 ± 0.36	-13.6 ± 1.1
Northern Dome East	—	NDE	43.03473333	-111.52915	1,006 ± 28	0.86	+4.45 ± 0.36	-13.3 ± 1.1
Sheep Island	1400 ± 200[a]	SI	42.90360238	-111.6209037	825 ± 11	2.82	+3.86 ± 0.55	-15.3 ± 1.2
BVF southern domes								
China Hat	52 ± 14[b]	CHD	42.80895	-111.61065	$63.1^{+0.6}_{-0.5}$ $58.3^{+1.2}_{-1.4}$	0.72 1.16	+4.51 ± 0.56	-10.1 ± 1.9
China Cap	75 ± 6[b]	CCD	42.81921667	-111.59735	$63.4^{+0.6}_{-0.6}$ $56.4^{+1.2}_{-1.2}$	2.24 0.74	+4.40 ± 0.47	-10.2 ± 1.6
North Cone	57 ± 6[b]	NCD	42.83405	-111.58345	$63.2^{+0.6}_{-0.6}$ $55.2^{+1.2}_{-1.1}$	1.25 1.73	+4.42 ± 0.45	-10.2 ± 1.7

[a] K/Ar age from Luedke and Smith, 1983

[b] Eruption $^{40}Ar/^{39}Ar$ age from Heumann, 1999

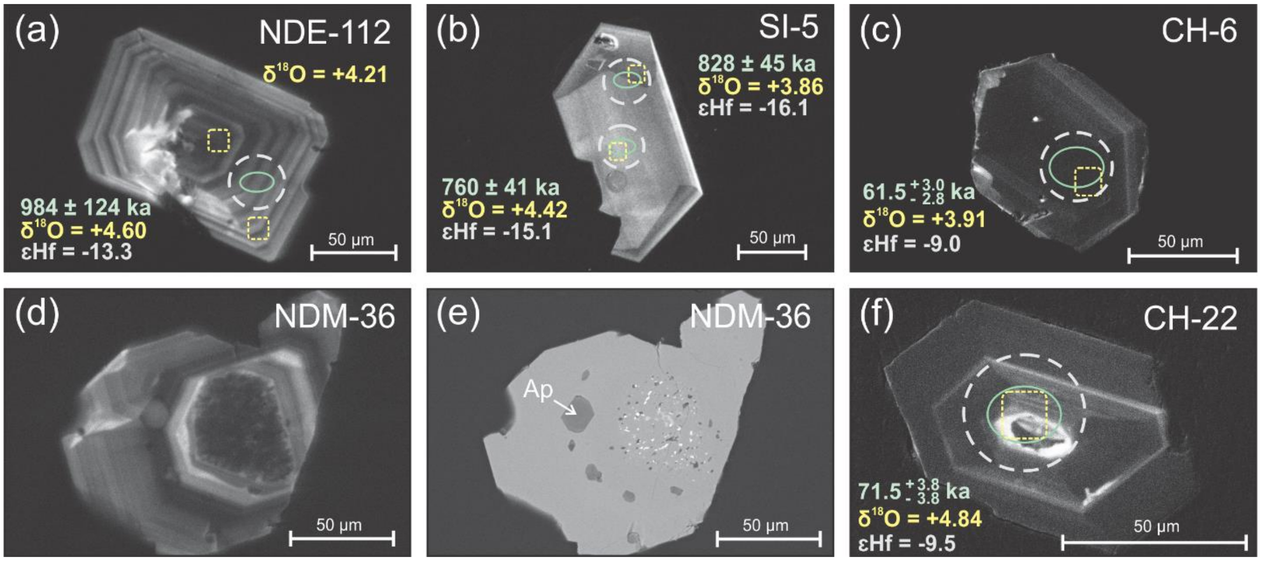

Fig. 2. *Cathodoluminescence images of selected zircon crystals from BVF northern domes (a), Sheep Island (b) and southern domes (c). Paired cathodoluminescence and backscattered electron images of inclusion rich interiors in zircon from the middle northern dome (d, e). Low-U, bright interior overgrown with dark zircon (cathodoluminescence) from China Hat dome (f). Note the characteristic dark domains in crystals form the southern domes (c, f) compared to the older rhyolites. Analytical spot locations and corresponding ages and isotopic values are displayed matched by color.*

3.2 Oxygen and hafnium isotopes

Oxygen isotope ($^{18}O/^{16}O$ as $\delta^{18}O$ relative to V-SMOW; Baertschi, 1976) analyses of zircon followed the methodology described in Angeles-De La Torre *et al.* (2025) and were conducted using the CAMECA ims 1280-HR at the Heidelberg Ion Probe laboratory. Analyses were performed in three sessions, using a Cs^+ primary beam (0.8–1.6 nA, 10 μm raster) to generate negative secondary ions of ^{16}O and ^{18}O, which were simultaneously detected in multi-collection mode. Zircon reference material AS3 ($\delta^{18}O$ = +5.34 ‰; Trail *et al.*, 2007) was used for instrumental mass fractionation and drift corrections, with 10–15 unknowns bracketed by reference material analyses yielding an average repeatability (2 standard deviations) of 0.28 (n = 46), 0.26 (n = 42), and 0.32 (n = 20) across the three sessions. Analytical uncertainties were propagated by combining internal errors with bracket reference zircon errors in quadrature. Data quality was monitored through replicate measurements of secondary reference zircon 91500 ($\delta^{18}O$ = +9.86 ‰;

Wiedenbeck *et al.*, 2004), for which an average $\delta^{18}O$ value of +9.81 ± 0.32 and +10.00 ± 0.28 (2 standard deviations) were obtained.

Hafnium isotope ($^{176}Hf/^{177}Hf$) analyses for BVF zircon were conducted in the same session as in Angeles-De La Torre *et al.* (2025), with analytical procedures based on Gerdes and Zeh (2006, 2009). A ThermoScientific NEPTUNE Plus MC-ICP-MS coupled to a RESOlution 193 nm ArF Excimer (Resonetics) laser system with an S155 two-volume ablation cell was used at FIERCE, Goethe University Frankfurt. Laser ablation was conducted with a 33 µm spot size, a fluence of 3.5 J cm^{-2}, a repetition rate of 5.2 Hz, and a total ablation depth of ~23 µm. Instrumental mass bias was corrected using an exponential law with $^{179}Hf/^{177}Hf = 0.7325$, while Yb mass bias corrections applied a daily βHf/βYb offset factor of 1.080 (Gerdes and Zeh, 2009), which has remained consistent for over 20 years. Data were normalized to the JMC475 standard ($^{176}Hf/^{177}Hf = 0.282160$), with quoted uncertainties incorporating within-run precision and JMC475 reproducibility (0.0028% 2s, n = 8). Initial $^{176}Hf/^{177}Hf$ and εHf values were calculated using SIMS-derived U-Th-Pb and U-Pb ages, assuming CHUR parameters of $^{176}Lu/^{177}Hf = 0.0336$ and $^{176}Hf/^{177}Hf = 0.282785$ (Bouvier *et al.*, 2008). Secondary zircon standards GJ-1 ($^{176}Yb/^{177}Hf < 0.008$) and Temora ($^{176}Yb/^{177}Hf = 0.02–0.07$) analyzed in the same session yielded repeatabilities of 0.6 and 0.8 εHf units (2s), in good agreement with published values.

4. Results

4.1 Zircon crystallization and eruption ages

Zircon crystals in the BVF are predominantly euhedral and prismatic, with an average length of ~100 µm (Fig. 2a-f). Crystals commonly contain individual inclusions of apatite, melt, and thorite with characteristic dimensions of few to tens of micrometers (Figs. 2e and 3c). In addition, some crystals interiors are riddled with sub-micrometre inclusions representing at least three different phases plus voids (Fig. 2d-e). These domains are also dark in CL and texturally identical to inclusion-rich interiors described for Yellowstone zircon in Troch *et al.* (2018). Zircon from the northern domes commonly displays oscillatory zoning, some with dark-CL interiors, whereas crystals from Sheep Island and the southern domes are primarily dark in CL with coarse oscillatory zoning and sector zoning (Fig. 2b-c). Additionally, CL-bright cores are present in some zircon crystals from BVF domes (Fig. 2f). Thorite in the northern domes is exclusively present as inclusions in zircon, whereas in the southern domes it exists as individual crystals of similar size as zircon, as well as contiguously intergrown with zircon (Fig. 3a-b). Topaz crystals were also identified in heavy mineral separates; their CL activity in fact outshines that of cogenetic zircon in BVF rhyolites (Fig. 3c). Zircon intergrown with topaz suggests that topaz is also a liquidus phase (Webster et al., 1987). EDS and Raman microscopy also identified clinofergusonite-(Y) intergrown with thorite and zircon (Fig. 4), which have been previously described for topaz rhyolites (Congdon and Nash, 1988).

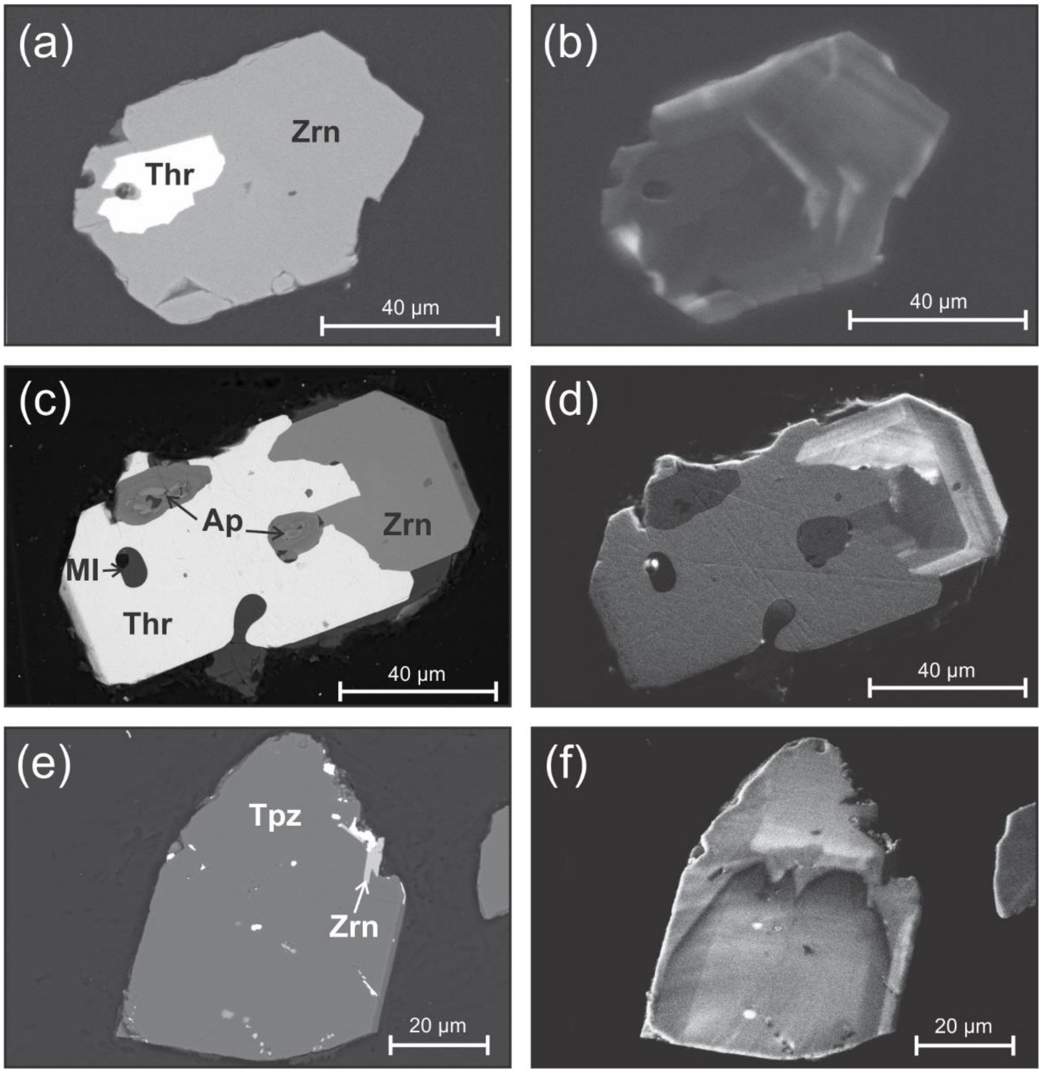

Fig. 3. *Paired backscattered electron and cathodoluminescence images of thorite and zircon crystals from Northern dome West, (a–b) and China Cap (c–d). Corresponding images for a topaz crystal intergrown with a small zircon from China Hat are shown in e–f; spots with high backscattered electron image brightness are caused by residual gold. Note that whereas thorite only appears as inclusions in zircon from the northern domes, it is often present intergrown with zircon in the southern domes; apatite inclusions are common in zircon from all BVF rhyolite domes.*

Zircon crystallization ages from Northern Dome East, Middle and West yielded average $^{206}Pb/^{238}U$ ages of 1,006 ± 28 ka (MSWD = 0.86; n = 30), 984 ± 26 ka (MSWD = 1.17; n = 32) and 957 ± 24 ka (MSWD = 0.94; n = 29), respectively, which overlap within uncertainty (Fig. 5a-c). Sheep Island average $^{206}Pb/^{238}U$ zircon crystallization ages are generally younger than those from the northern domes, with individual zircon ages ranging from c. 740 to 980 ka (Fig.- 5d). Even excluding the three oldest (c. 960 ka) zircon ages in the population as potential carryover from the northern dome system, the MSWD for the remaining crystallization ages is still elevated (average 825 ± 11 ka; MSWD = 2.82; n = 52), indicating a heterogeneous population. To obtain a near-eruption age for Sheep Island, a minimum zircon crystallization age of 785 ± 23 ka was extracted from this population by finite mixture modelling using IsoplotR (Vermeesch, 2018). Similarly, for the southern domes, multiple crystallization age populations are resolved in the U-Th disequilibrium ages. Populations in the finite mixture modelling were considered distinct only if their 2σ errors did not overlap; this approach resulted in separating two discrete age populations for the majority of zircon ages in all domes (Fig. 6a-c). For China Hat, these crystallization age groups average $63.1\,^{+0.6}_{-0.5}\;ka\;(MSWD = 0.72, n = 24)$ and $58.3\,^{+1.2}_{-1.4}\;ka\;(MSWD = 1.16, n = 6)$. Similarly, China Cap zircon crystallization ages are separated as $63.4\,^{+0.6}_{-0.6}\;ka\;(MSWD = 2.24, n = 24)$ and $56.4\,^{+1.2}_{-1.2}\;ka\;(MSWD = 0.74, n = 5)$, and finally, for North Cone as $63.2\,^{+0.6}_{-0.6}\;ka\;(MSWD = 1.25, n = 29)$ and $55.2\,^{+1.2}_{-1.1}\;ka\;(MSWD = 1.73, n = 4)$. Occasional older crystals are present, which are also distinct from the younger groups due to lower U abundances of <10,000 µg/g. These were excluded from the average age calculations, and their crystallization model ages based on zircon-whole rock pairs are stated individually (Fig. 6). A heterogeneous younger zircon age population with high U abundances was also detected for China Hat using LA-ICP-MS analysis with ages in good agreement to those presented here (Bernal *et al.*, 2014). A second, low-U zircon crystal population was also detected in China Hat dome, which averages $267^{+42}_{-33}\;ka$ (Bernal *et al.*, 2014). However, the older zircon crystals detected on our study are much fewer compared to Bernal *et al.* (2014), and are at most 81 ka and 101 ka for China Hat and China Cap domes, respectively (Fig. 6). The only zircon xenocryst among all BVF analyses was identified in China Cap, and it yielded an age of 38.4 ± 3.9 Ma.

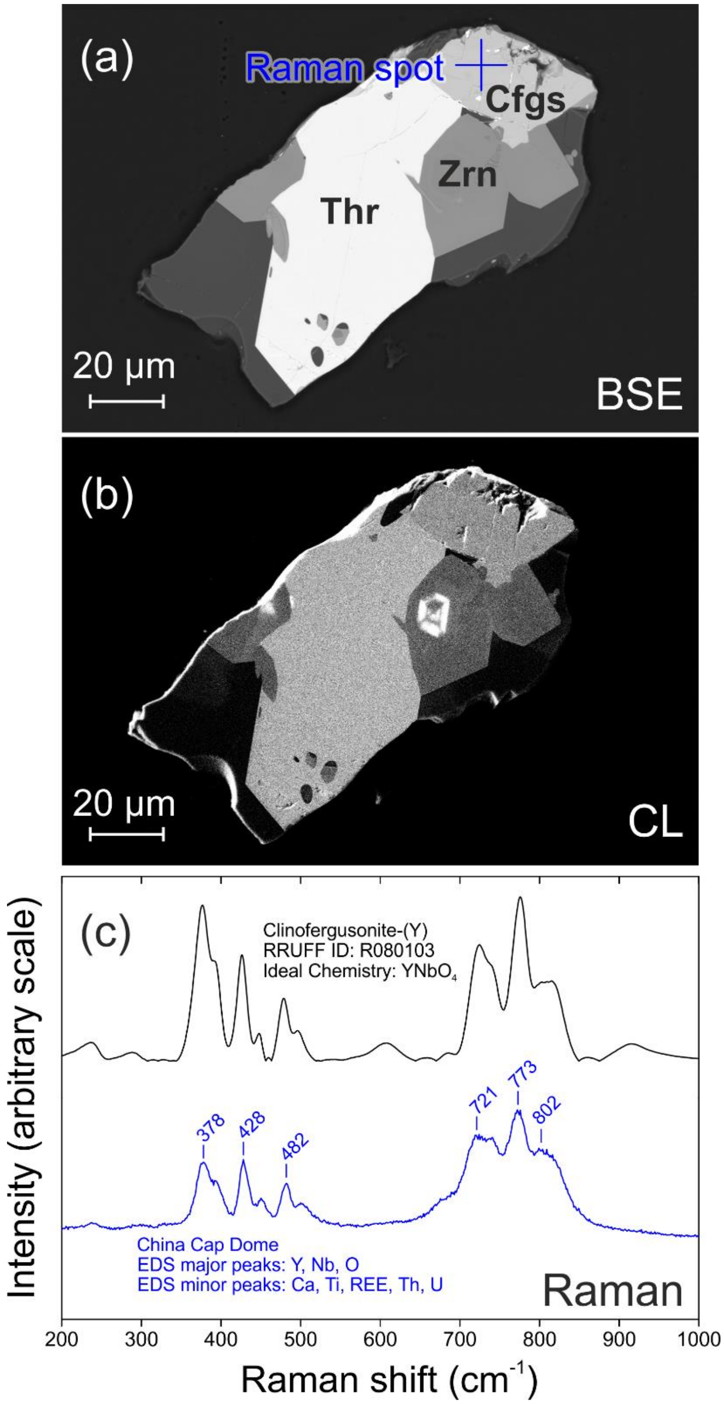

Fig. 4. Paired backscattered electron and cathodoluminescence images of clinofergusonite-(Y) intergrown with thorite and zircon (a-b). Raman spectra as shift relative to a laser wavelength of 532 nm (c) for clinofergusonite-(Y) from China Cap dome (spot location in a) and the reference from the RRUFF data base (Lafuente et al., 2015).

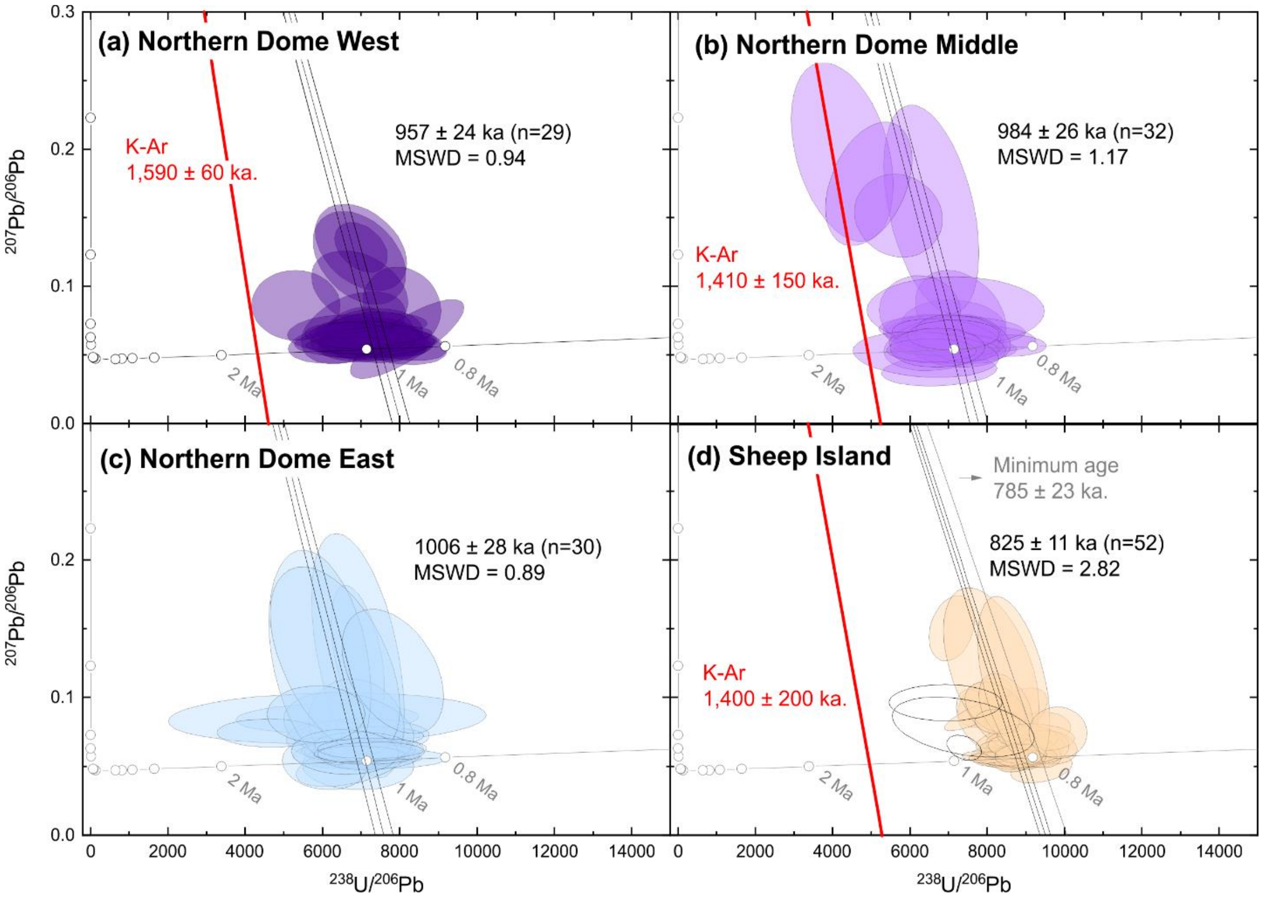

Fig. 5. *Zircon $^{207}Pb/^{206}Pb$ vs. $^{238}U/^{206}Pb$ data (error ellipses: 2se; ages: 95% confidence intervals) of BVF northern domes (a-c) and Sheep Island (d) plotted uncorrected for common Pb with concordia plotted adjusted for disequilibrium of ^{230}Th and ^{231}Pa at the time of crystallization using initial activity ratios for the intermediate daughter and parent isotopes of 0.2 and 2.2, respectively. Mixing lines between a fixed common Pb composition (y-axis intercept) and a radiogenic $^{206}Pb/^{238}U$ corresponding to the weighted average $^{206}Pb/^{238}U$ ages adjusted individually for initial disequilibrium of ^{230}Th (see text) are shown in black. Red lines show corresponding trend lines for K-Ar ages from the literature, which are always unreasonably old compared to the zircon crystallization ages, which define a maximum eruption age (Table 1).*

Overall, zircon crystallization ages for the northern domes and Sheep Island are significantly younger than published eruption ages based on K-Ar geochronology (Luedke and Smith, 1983). Specifically, the K-Ar ages predate the zircon crystallization ages by 425 ± 152 ka (Northern Dome Middle), 633 ± 65 ka (Northern Dome West), and 575 ± 200 ka (Sheep Island). Decay constant uncertainties are negligible compared to these differences, but unfortunately no analytical details are available for the vintage K-Ar ages in Luedke and Smith (1983). However, the presence of crystal age heterogeneity, either caused by antecrysts or xenocrysts, is suspected to have affected the K-Ar decay system for the southern BVF domes based on unreasonably old ^{40}Ar/^{39}Ar ages in relation to the whole-rock U-Th isochron age (Heumann, 1999). Only the ^{40}Ar/^{39}Ar eruption age of 57 ± 8 ka was deemed reliable by Heumann (1999), which agrees well with the youngest zircon age population in the southern domes (Fig. 6). This underscores that the zircon crystallization ages for the northern domes and Sheep Island may more reliably represent the eruption ages than the reported K-Ar dates.

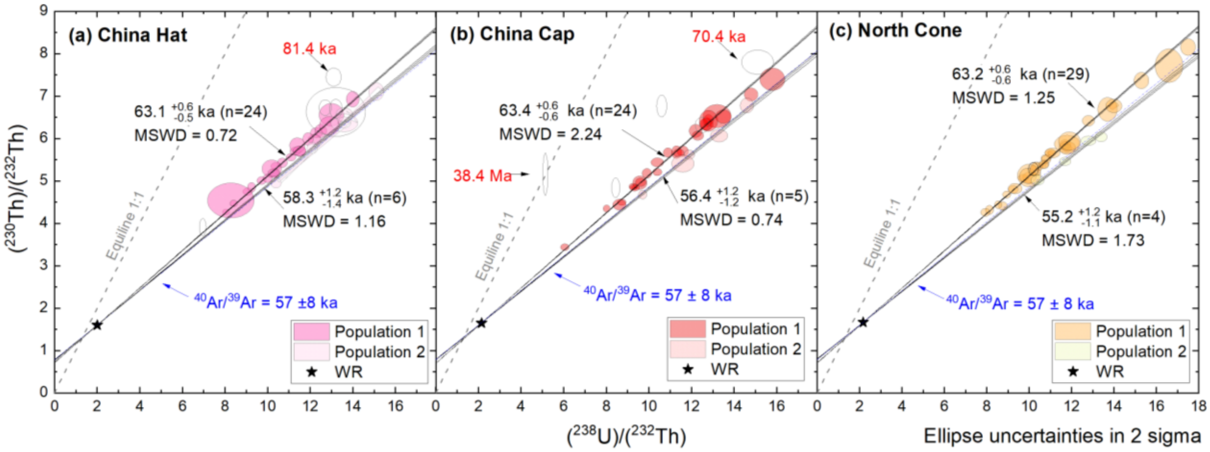

Fig. 6. *Zircon (^{230}Th)/(^{232}Th) vs. (^{238}U)/(^{232}Th) isochron diagram (error ellipses: 2se; ages: 95% confidence intervals) for BVF China Hat (a), China Cap (b) and North Cone (c), southern domes. Whole rock compositions (Heuman, 1999) are used to anchor isochrons. Blue lines show model isochrons for the ^{40}Ar/^{39}Ar-based eruption age estimate (Heuman, 1999). Open ellipses display analyses with U concentrations <10,000 µg/g which are interpreted as antecrysts (Bernal et al., 2014) and omitted in the average age calculation. Only one crystal plots on the equiline and is interpreted as a secular equilibrium xenocryst as confirmed by a 38.4 Ma ^{206}Pb/^{238}U age.*

4.2 Zircon trace elements

Zircon uranium concentrations within the BVF vary significantly across different domes and through time. The northern domes exhibit an average U content of ~5,046 µg/g, while zircons from Sheep Island show a marked increase to ~18,578 µg/g. The southern domes record the highest average concentration, reaching ~26,481 µg/g. These uranium abundances correlate well with other trace elements like Th, Hf, Y, and HREE, reflecting geochemical trends within the magmatic system. U/Yb ratios, which serve as an indicator of the zircon source (Grimes *et al.*, 2007), suggest a continental crustal origin, with progressively increasing values from ~2.55 in the northern domes to ~4.10 at Sheep Island and ~6.01 in the southern domes (Fig. 7c).

All BVF zircons display REE patterns characterized by enrichment in HREE relative to MREE and LREE (Fig. 8a-h), along with pronounced negative Eu and positive Ce anomalies. The gradient of the zircon REE patterns expressed as Gd/Yb (with low values indicating steeper slopes from MREE towards HREE) shows overall little variation, except for few high-Eu/Eu* and low-U crystals which have slightly higher Gd/Yb (Fig. 7a). The Eu depletion is primarily attributed to plagioclase fractionation, whereas the Ce anomaly reflects the preferential incorporation of Ce^{4+} into zircon, controlled by magmatic oxidation state (Loucks *et al.*, 2020; Trail *et al.*, 2012, 2024). Estimates of magma oxidation state, based on Ce, U, and Ti in zircon (Loucks *et al.*, 2020), suggest an average ΔFMQ of ~0.3 for both the northern and southern domes, consistent with typical topaz rhyolite values (Christiansen *et al.*, 1983). However, Sheep Island zircons yield a lower ΔFMQ of −1.1, indicating a slightly more reduced magmatic environment. In addition to oxidation state, Eu anomalies further reinforce the classification of BVF magmas as highly fractionated evolved topaz rhyolites. The northern domes exhibit a broad range of Eu/Eu* values from 0.011 to 0.234, whereas Sheep Island zircons have a more uniform average of ~0.013. The southern domes show the most extreme fractionation, with Eu/Eu* averaging ~0.008.

Zircon saturation in silicate melts is primarily governed by temperature and the concentration of Zr in the melt (Boehnke *et al.*, 2013; Watson and Harrison, 1983). For BVF rhyolite magmas, zircon saturation occurred at 710 ± 36 °C (based on the calibration and the 5% uncertainty envelope in Boehnke *et al.*, 2013) and whole-rock compositions from the literature (Ford, 2005; Heuman, 1999). The titanium content in zircon (TiZr) also serves as a proxy for crystallization temperature (Fig. 9), and estimated temperatures range from 645 °C to 833 °C in the northern domes. Comparatively lower values are displayed for Sheep Island ranging from 596 °C to 723 °C, but apparent temperatures increase again in the southern domes, spanning from ~678 °C to 836 °C. Although all BVF zircons are highly fractionated, some crystals in the northerns domes preserve comparatively less evolved compositions, as indicated by low U (253 µg/g) and high Eu/Eu* (0.203), Zr/Hf (52), and TiZr (827 °C). These slightly more primitive zircons follow expected magmatic trends, where TiZr vs. Eu/Eu*, TiZr vs. Zr/Hf and TiZr vs. U (Fig. 9a-c) are correlated.

The deviations from, and in part reversals in this trend along with the remarkably low TiZr values are similar to observations in Matthews *et al.* (2015) and Troch *et al.* (2018), who suggested a change in Ti partitioning behavior when non-stochiometric components reach a certain level in highly evolved zircon. This is discussed further in Section 5.2.

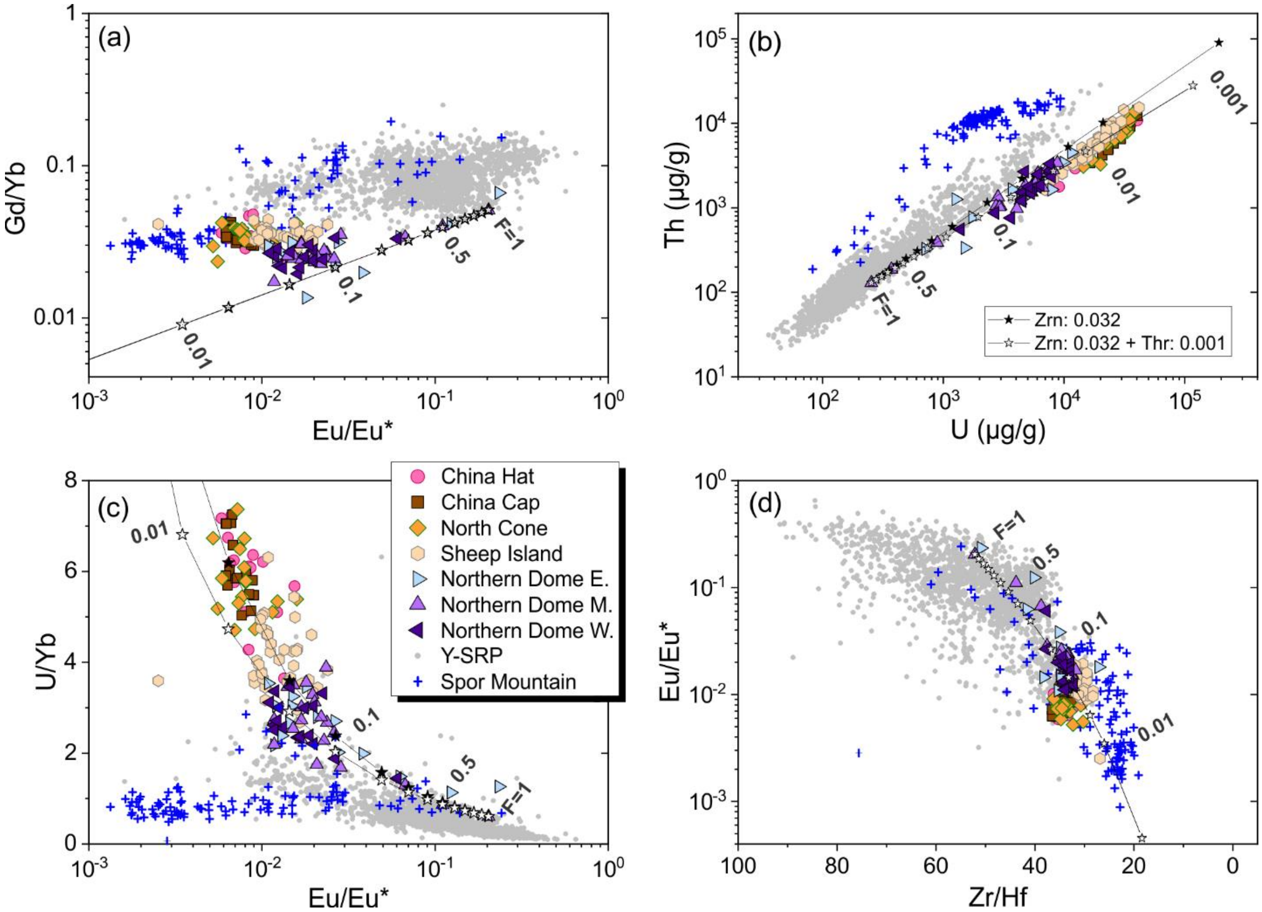

Fig. 7. *Fractional crystallization models and trace element concentrations for zircon from the BVF, Yellowstone-Snake River Plain (Y-SRP) and Spor Mountain topaz rhyolites. a) Gd/Yb vs. Eu/Eu*; b) Th vs. U; c) U/Yb vs. Eu/Eu*; and d) Eu/Eu* vs. Zr/Hf. Models account for crystallization of zircon alone and zircon plus thorite as accessory phases (see text). Numbers along model curves indicate the remaining melt fraction (F). All unknowns were screened for contamination by non-zircon phases and are omitted from the plot (for complete data see Supplementary Table 3).*

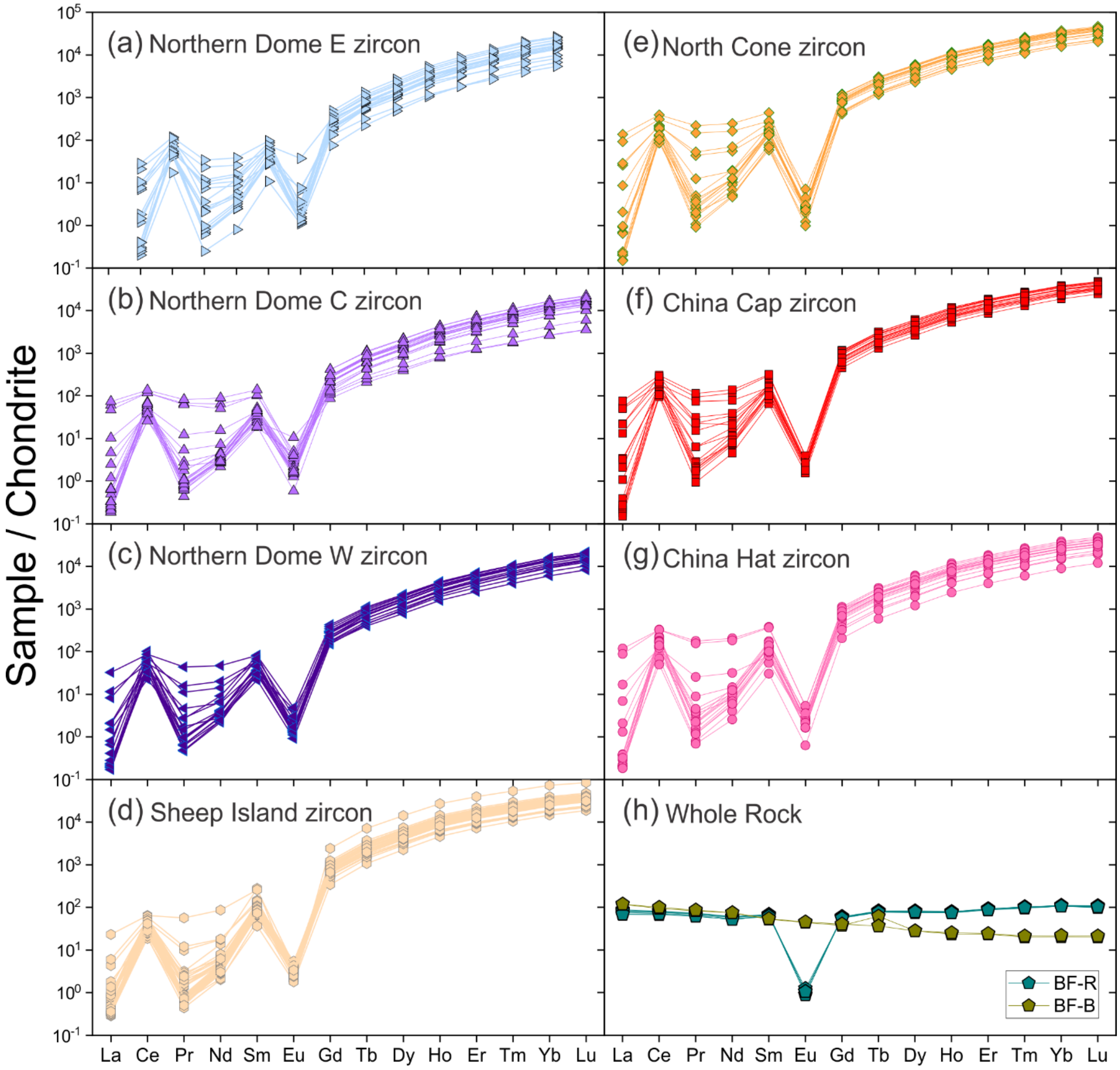

Fig. 8. *Chondrite normalized zircon REE abundances for the northern domes (a-c), Sheep Island (d) and southern domes (e-f). Whole rock REE abundances for BVF basalts and rhyolites from the southern domes (Heumann, 1999) are show for comparison (h). Chondrite CI values are from McDonough & Sun (1995). Data were screened as in Fig. 7.*

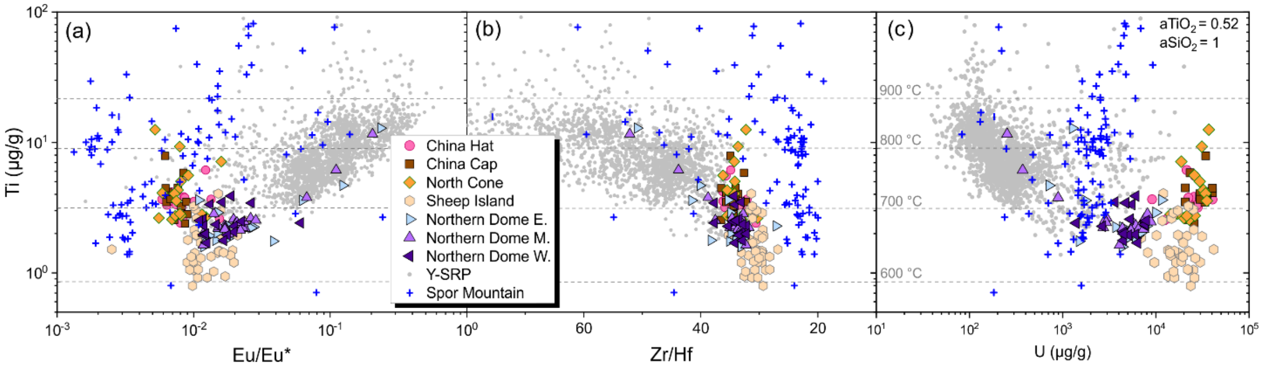

Fig. 9. Zircon Ti concentrations and equivalent Ti-in-zircon temperatures (dash-dot lines) for the BVF rhyolite domes, Yellowstone-Snake River Plain (Y-SRP) and Spor Mountain topaz rhyolites, against Eu/Eu (a), Zr/Hf (b) and U (c). Note that Ti concentrations in zircon systematically decrease with increasing differentiation as indicated by lower Eu/Eu* and Zr/Hf, and higher U for Y-SRP as well as BVF northern dome and Sheep Island rhyolites. Zircon compositions for the BVF southern domes and Spor Mountain deviate from this trend (see text). Data were screened as in Fig. 7.*

4.3 Zircon O- and Hf-isotopes

Zircon $\delta^{18}O$ values within the northern and southern domes of the BVF are homogeneous within analytical uncertainty (Fig. 10a) and are slightly below values for typical mantle-derived zircon (+5.3; Valley *et al.*, 1998). For the northern domes, zircon crystals display an average value of +4.54 ± 0.40, with the only exceptions being three crystals, two from the East dome and one from Middle dome with values of +6.94, +7.41 and +8.22, respectively, which are being excluded in the average calculation. This is indistinguishable from the values for the southern domes averaging $\delta^{18}O$ = +4.45 ± 0.51. Sheep Island is the only BVF location with a lower average zircon $\delta^{18}O$ = +3.86 ± 0.55 compared to the rest of the field. The isolated zircon xenocryst has a significantly higher $\delta^{18}O$ = +6.79 ± 0.17, which is typical for continental crustal zircon.

Zircon εHf values for the BVF vary between -16.3 and -7.1 (Fig. 10b). Unlike the $\delta^{18}O$ values, zircon Hf isotopic composition within the domes are variable according to the age and location of the domes (Fig. 11). Collectively, the northern domes are distinctly more negative compared to the southern domes (average εHf values are -13.4 ± 1.1 and -10.1 ± 1.7, respectively), whereas Sheep Island displays the lowest zircon values of the topaz rhyolite domes in the BVF with an average εHf = -15.3 ± 1.2. When plotting isotopic compositions against zircon fractionation indices (e.g., Eu/Eu*, Zr/Hf), trends are generally horizonal (Fig. 10), which is consistent with fractionation where the melt remains isolated from isotopically distinct reservoirs during zircon crystallization. In contrast, AFC involving regional continental crustal rocks would produce inclined trends, depending on the composition of the contaminant (Section 5.1).

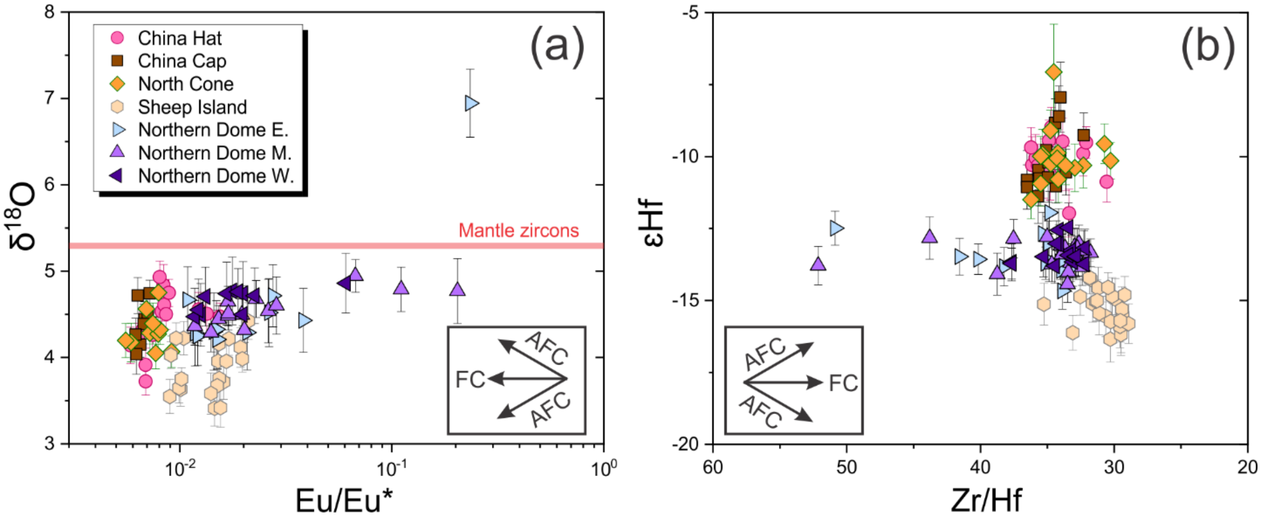

Fig. 10. *Isotope compositions for BVF zircon against trance element indices of differentiation: a)* $\delta^{18}O$ *vs. Eu/Eu* and b) εHf vs. Hf. Inset figures indicate trends for fractional crystallization (FC) and assimilation coupled with fractional crystallization (AFC). Pure FC produces horizontal trends from right to left, whereas AFC of a primitive mantle-derived magma would show stronger crustal contribution with differentiation. In the case of* $\delta^{18}O$*, crustal contaminants could have lower or higher values compared to mantle, whereas for εHf the Archean basement has strongly negative values (see text). Red line stands for the mantle zircon* $\delta^{18}O$ *value of +5.3 (Valley et al. 1998). Data were screened as in Fig. 7.*

5. Discussion

5.1 Parental magmas for topaz rhyolites (AFC)

Zircon isotopic homogeneity within each of the BVF rhyolite domes suggests that their isotopic composition was inherited from a parental magma, and zircon only recorded this isotopic signature retroactively. Although there is minor variability between the different age groups (Fig. 11a-b), O isotopic differences clearly separate the BVF zircons from the higher crustal $\delta^{18}O$ values that range between +6.26 and +9.35 for a suite of Archean xenoliths from the ESPR (Watts *et al.*, 2010). This is even more pronounced for the Hf isotopic compositions of BVF zircon, which despite their strongly negative values are much higher than εHf expected for melts solely derived from Archean rocks (Vervoort and Patchett, 1996). Average zircon εHf = -75 has been reported for Archean granitic xenoliths from the COM volcanic field (DuFrane *et al.*, 2007; Angeles-De La Torre *et al.*, 2025), supporting a strongly negative crustal εHf, although partial melting along with incomplete zircon resorption can cause decoupling between zircon and whole rock isotopic compositions (e.g., Wang *et al.*, 2018). Regardless, the clear differences in $\delta^{18}O$ and εHf preclude pure anatexis of Archean crust as the source for the BVF rhyolite magmas, in line with previous petrogenetic models for BVF rhyolites. These models argued based on whole rock $^{87}Sr/^{86}Sr$ and εNd isotope data that rhyolite magmas are extreme differentiates of mantle-derived basalt which experienced assimilation of Archean crust upon polybaric storage in the crust (Ford 2005; McCurry et al., 2015; Lochridge, 2016). Initial $^{230}Th/^{232}Th$ ratios determined by whole-rock analyses for BVF southern domes (Heumann, 1999) and those indicated by zircon isochrons are higher than expected for Archean basement, but they closely overlap with $^{230}Th/^{232}Th$ for ESPR mafic rocks (Reid, 1995). This further supports derivation of the BVF rhyolites from a mafic parent with a depleted mantle signature (Heumann, 1999; Reid, 1995).

Mafic endmembers associated with volcanism in the ESPR and adjacent regions such as the central Snake River Plain and the BVF have radiogenic isotopic compositions ($^{87}Sr/^{86}Sr$, $^{143}Nd/^{144}Nd$, $^{176}Hf/^{177}Hf$) that plot along an extension of the mantle array beyond bulk silicate earth, implying that they experienced minor degrees of assimilation of Archean crust (e.g., (Hughes *et al.*, 2002a; Pickett, 2004; Putirka *et al.*, 2009; Rivera *et al.*, 2021; Stefano *et al.*, 2019; McCurry *et al.,* 2015). In the ESPR, Quaternary basalts and rhyolites isotopically overlap, especially for robust indicators such as $^{143}Nd/^{144}Nd$ (e.g., McCurry *et al.*, 2008), whereas $^{87}Sr/^{86}Sr$ in Sr-poor rhyolites may be easily affected by alteration or lithic contaminants. By contrast, BVF primitive basalts are distinct from the progressively crustally influenced evolved basalts and rhyolites (e.g., McCurry *et al.,* 2015). This has been attributed to increasing degrees of Archean crustal assimilation during the evolution from basalt to rhyolite (Ford, 2005). Although only indirect indicators for the isotopic composition of the parental magma, the O and Hf isotopes in zircon from BVF rhyolites are robust, and can supplement existing assimilation models, thus providing further constrains on the contribution of Archean crust to a basalt-dominated magmatic system.

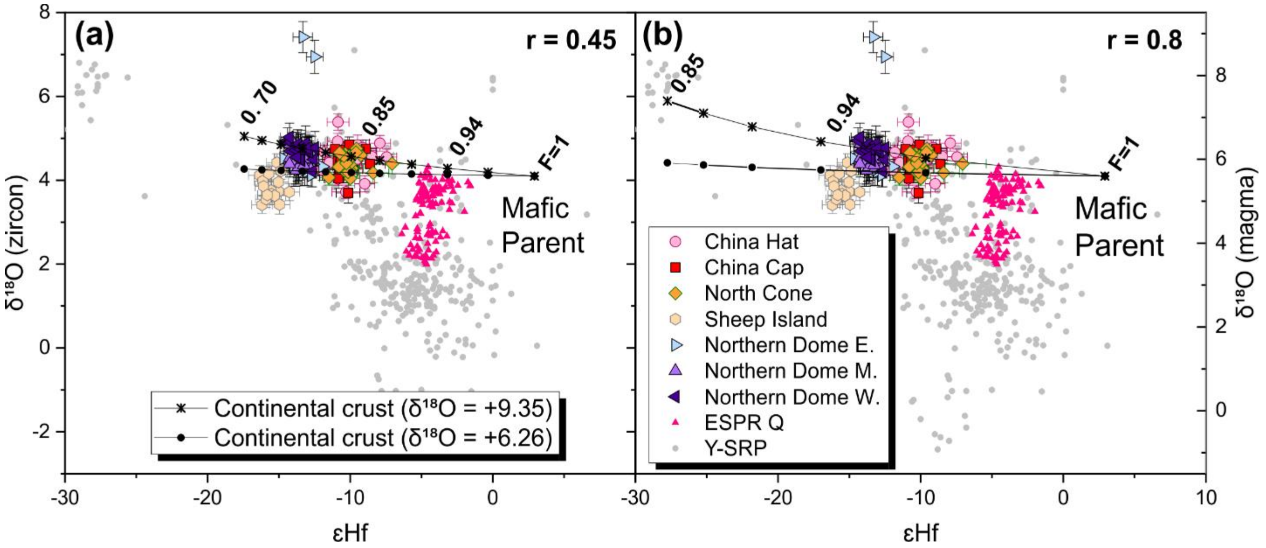

Fig. 11. *Zircon covariation diagram for $\delta^{18}O$ and εHf isotopic compositions for BVF in comparison to Yellowstone-Snake River Plain caldera-related rhyolites (Y-SRP) and Quaternary domes from the Eastern Sanke River Plain (ESRP Q). Solid lines represent AFC trends modelled from a common mafic parent ($\delta^{18}O$ = +5.6, εHf = +2.9) and two different endmembers with the same εHf = -44.0 and different $\delta^{18}O$= +9.35 and + 6.26 values, respectively (see text). The model also explores different assimilation over fractionation rates (r) of r = 0.45 (a) and r = 0.8 (b). Data were screened as in Fig. 7.*

The current genetic model for the mafic parents in the BVF magma system proposes subcrustal upper mantle melting due to heating above a vertically ascending stream of mantle material centered on the axis of the ESRP (McCurry *et al.,* 2015). A melt layer near the Moho (e.g., Peng and Humphreys, 1998) is feeding a polybaric intracrustal magma system, promoting fractional crystallization and crustal assimilation, although the main magma volumes erupted as relatively unmodified olivine-tholeiite lava flows (McCurry *et al.,* 2015). While in this scenario the primitive magmas are similar for the BVF and ESPR, different pathways of crustal interaction are likely, depending on the proximity to the Yellowstone hotspot track. Along its axis, Archean basement was overprinted into a diorite-like average crustal composition, whereas at its edges the Archean crust remained comparatively unaffected, which includes the crust underneath the BVF (e.g. Christiansen and McCurry, 2008; McCurry and Rodgers, 2009; Putirka *et al.*, 2009). Another difference between the ESRP and BVF magma evolution pathways is the likely absence of hydrothermally altered crust, which is linked to intense meteoric fluid percolation along caldera-related faults that abound on the axis of the hotspot track (Colón *et al.*, 2018). Both hypotheses regarding the crustal structure underneath the BVF can be tested by AFC modelling of the zircon isotopic indicators for the rhyolite parental magmas.

To reproduce O and Hf isotopic compositions in BVF zircon, we applied the AFC model of DePaolo (1981) and used Gem Valley basalt with $\delta^{18}O$ = +5.6 as the composition of the mafic parent (Watts *et al.*, 2010). In the absence of published Hf isotopic data for BVF basalts, we leverage the established petrological and geochemical similarity between BVF and ESRP basalts (Fiesinger *et al.*, 1982; Pickett, 2004; McCurry et al., 2015) and adopted εHf = +2.9 for the mantle-derived parent, which is the most primitive value determined for Yellowstone hotspot basalts (Stefano *et al.*, 2019). This εHf approximation is also equivalent to a maximum εNd = +1 determined for a large regional data set (e.g., Leeman *et al.*, 1982; McCurry *et al.*, 2008; Nash *et al.*, 2006; Putirka *et al.*, 2009; Rivera *et al.*, 2021). Although isotopic heterogeneity in the mantle (e.g. Manea *et al.*, 2009) and unaccounted crustal assimilation limits the uniqueness of this endmember choice, it is consistent with previous models and thus ensures comparability. For the crustal assimilant, $\delta^{18}O$ was varied between +6.26 and +9.35, covering the range of ESRP xenolith whole-rock values (Watts *et al.*, 2010). To further align our AFC model with those in the literature, εHf = -44 and Hf = 9 µg/g were selected as representative of the assimilated Archean crust (e.g., Drew, 2013). Additionally, bulk magma and crustal rock oxygen abundances were set at 50 wt.%, while an Hf concentration of 3 µg/g for the mafic parent, was chosen as typical for depleted mantle (Hofmann, 1988). Crustal assimilation-to-fractional crystallization curves are shown for ratios of r = 0.45 and 0.8 (Fig. 11a-b), which are between values from previous models using energy conservation constraints (Ford, 2005; Lochride, 2016) and those explaining differentiated magma genesis for COM (Putirka *et al.*, 2009).

Zircon $\delta^{18}O$ and εHf values in the BVF align with AFC model curves for r = 0.45 and 0.8 at degrees of fractional crystallization expressed as F = fraction of remaining melt of 0.73–0.89 and 0.94–0.98, respectively (Fig. 11a-b). Although the exact quantities of crustal contamination of the parent are strongly model dependent (cf. Drew *et al.*, 2013), we can conclude that assimilation of Archean crust plays a more significant role in shaping the isotopic composition of BVF zircon compared to those from Quaternary ESRP rhyolites. Moreover, the AFC trends defined by Archean xenoliths are unsupportive of assimilation of a low-$\delta^{18}O$ crustal component, which instead is prominent in

Quaternary and older rhyolite zircon from the axial ESRP except for zircon from the Tuff of Arbon Valley (Drew *et al.*, 2013). The minor variations in the BVF zircon compositions, provided that their evolution path shares the same endmembers, imply lower degrees of assimilation for the younger southern domes compared to the northern domes and Sheep Island. Higher degrees of assimilation may be favored by elevated crustal temperatures and/or more protracted magma residence times. This is consistent with Sheep Island rhyolite originating from the most contaminated parent in the BVF system, which may represent residual magma from the earlier northern dome phase, as indicated by zircon antecrysts being carried over into the Sheep Island magma. By contrast, the lesser degrees of crustal assimilation in the southern domes may indicate the (re-)location of the magma system to a relatively cold crustal environment following a magmatic hiatus of c. 800 ka. In the absence of published O-Hf zircon data for Paleogene–Quaternary topaz rhyolites from the western USA, the BVF data are thus far the only constraints on these isotopic systems for their respective parental magmas.

5.2 Near eutectic rhyolite magma storage recorded by zircon

Although zircon crystals have inherent limitations in recording the evolution of the magma from which their evolved host melt originated, they effectively capture the magmatic history once zircon saturation is reached. The isotopic invariability observed in BVF zircon further supports the idea that their trace element composition was primarily controlled by closed-system fractional crystallization. Indeed, the BVF zircon trace element compositions exhibit a broad, but continuous spectrum. They generally indicate more fractionated melt compositions (e.g., lower Eu/Eu*, lower Zr/Hf, higher U and Th abundances) compared to zircon from Snake River Plain-Yellowstone rhyolites (Fig.7). Nonetheless, the most primitive BVF zircon crystals compositionally overlap with the bulk of the Snake River Plain-Yellowstone rhyolite zircon population, albeit towards the lower and upper ends of the Gd/Yb and U/Yb distributions, respectively (Fig. 7a). The same trace element characteristics as for BVF zircon (low Eu/Eu*, low Zr/Hf, high U and Th) are also found for zircon from the Spor Mountain topaz rhyolite (Fig. 7; Ayuso *et al.*, 2020). Primitive Spor Mountain zircon also shares affinities to the bulk of Snake River Plain-Yellowstone zircon compositions, although Th abundances are generally elevated (Fig. 7b). Unlike BVF zircon which evolves towards high U/Yb with decreasing Eu/Eu*, Spor Mountain zircon U/Yb remains constant at comparatively low U/Yb, similar to the Snake River Plain-Yellowstone zircon population (Fig. 7c). To further elucidate the underlying causes for these similarities, but also the divergent behavior of zircon in highly evolved rhyolites, fractional crystallization models were evaluated to constrain the compositional changes of the BVF magma as recorded by zircon.

For our model, we invoked a near-eutectic mineral assemblage consisting of 35% quartz, 28% K-feldspar, and 27% plagioclase, which closely resembles previous models developed for Yellowstone zircon (Troch *et al.*, 2018), only adding 10% amphibole as a component present in BVF rhyolites (Ford, 2005). Additionally, we included apatite (0.1%) as an accessory phase, consistent with petrographic observations showing apatite as a common inclusion mineral (Fig. 2e, 3c). We also explored the roles of zircon and thorite as additional, and frequently observed accessory phases in some BVF rocks, presenting model calculations that incorporate only zircon (0.032%) and combined zircon-thorite fractionation at 0.032% and 0.001%, respectively (Fig. 7). Partition coefficients for most elements were obtained from literature sources (Table 2), with the exception of thorite, where values for Eu and Gd were interpolated from reported values (Congdon and Nash, 1991) using best-fit curves for the elastic strain equation of Blundy and Wood (1994). The starting composition was based on the zircon analysis with the lowest U concentration from the Middle Northern Dome, (BF_NDM_Zr6; Supplementary Table 3).

For the northern subfield, the fractional crystallization model aligns with the zircon trace element trend requiring F values as low as ~0.02, implying extensive fractional crystallization within these units (Fig. 7). Zircon from Sheep Island continues the same trends at even higher degrees of fractionation (F = 0.01), supporting a potential genetic link that is also indicated by antecryst recycling from the northern domes (Fig. 7). Zircon from the southern dome subfield, although probably not directly consanguineous with the northern dome magmas, also requires extreme fractionation, in some cases (e.g., U/Yb) even exceeding those recorded by Sheep Island zircon (Fig. 7). Incorporating thorite slightly improves the fit for Th/U primarily for zircon from Sheep Island and the southern dome subfield, but the comparatively high U partitioning value of thorite relative to Yb also shifts the model curve away from the data (Fig. 7c). Another mismatch is observed in Gd/Yb, particularly for Sheep Island and the southern domes, where the model predicts decreasing Gd/Yb, whereas zircon from these samples remain constant in Gd/Yb. We attribute this deviation to the model disregarding additional accessory phases that could exert a strong influence on the REE budget such as allanite (Ford, 2005) and clinofergusonite-(Y) (this study; Fig. 4) at F values <0.3 (Fig. 7a and c). Regardless of these simplifications, the model indicates extremely low abundances of residual melt, which are maximum estimates because the parental magma already differentiated already prior to zircon saturation.

Titanium partitioning in BVF zircon also appears to deviate from the expected decrease with progressive fractionation as indicated by increasing U and decreasing Eu/Eu* (Fig. 9c). A reversal occurs at very high U (~10,000 µg/g) and low Eu/Eu* (~0.01) where Ti concentrations start to increase (Fig. 9c). This corresponds to a model F value of ~0.03 (Fig. 7), and would lead to an overestimation of temperature. A similar effect has been reported for Yellowstone zircons at U concentrations >1,000 µg/g (Matthews *et al.*, 2015; Troch *et al.*, 2018), where excessive incorporation of trace elements increases lattice strain and enhances Ti uptake in zircon (Troch *et al.*, 2018). The most evolved zircon crystals from the Spor Mountain topaz rhyolite (Fig. 9c), display a similar, and even more extreme trend, which was explained by the presence of inclusions and cracks in zircon (Ayuso *et al.*, 2020). However, this is clearly not the case for the generally intact and very young zircon crystals from BVF rhyolites. Furthermore, because BVF zircon with U >1000 µg/g still show reasonably low Ti concentrations corresponding to temperatures of ~700–600°C, we offer the alternative explanation that besides lattice strain in zircon, Ti partitioning may also be enhanced by the high fluorine content of topaz-bearing BVF melts. Because fluorine increases rutile solubility in melts (Keppler, 1993), we expect higher Ti abundances in fluorine-rich melts, which may also boost Ti partitioning into zircon at a given temperature. At the same time, the presence of volatiles including fluorine may depress the solidus temperatures to the range observed in the lowest TiZr data. Equally low solidus temperatures have been experimentally determined for fluorine-rich melts (Webster *et al.*, 1987), and even lower TiZr temperatures are reported for Spor Mountain topaz rhyolites (as low as 520°C; Ayuso et al., 2020).

Extreme fractional crystallization has also been documented for Yellowstone zircon, where trace element patterns indicate up to 99.9% crystallization (e.g., Troch et al., 2018). BVF zircon textures further support crystallization in an extremely fractionated melt, as indicated by CL-dark domains, which for the northern domes and Sheep Island predominantly extend only to the rims, but to the entire crystal for the southern domes (Fig. 2c and f). Such CL-dark zircon domains are commonly associated with plutonic environments (e.g., Corfu *et al.*, 2003; Hoskin, 2000) and to near-solidus pockets in highly evolved rhyolites (Troch *et al.*, 2018). According to our model, <1% residual melt from which the most evolved zircon crystallized represents only a tiny fraction of the total intruded magma volume, which must have been solidified to >99%. This seemingly contradicts the crystal-poor nature of the erupted BVF rhyolites. We therefore invoke preeruptive mobilization of a nearly completely solidified intrusive body by magmatic reheating, as supported by the presence of mafic enclaves within the domes (McCurry *et al.,* 2015; Goldsby, 2017).

Although our AFC model successfully predicts the BVF isotopic compositions being derived from an ESPR-like mafic parent, the divergent trace element trends between Snake River Plain-Yellowstone and BVF zircon require additional factors to influence magmatic differentiation. The isotopic composition of BVF zircon records higher contributions of Archean crust compared to Snake River Plain-Yellowstone zircon (Fig. 11). Because of this, the trace element inventory of the parental magmas also differed, and these differences were subsequently intensified through fractional crystallization (McCurry *et al.,* 2015). Even the most primitive BVF zircon crystals generally have higher U/Yb than Snake River Plain-Yellowstone zircon at similar Eu/Eu* (Fig. 7c), with increasing U/Yb being a hallmark of continental crustal influence (Grimes *et al.*, 2007). The divergent zircon evolutionary trends between BVF and Spor Mountain are also intriguing, but difficult to interpret because of potential metamictization and intense hydrothermal alteration involving F-rich fluids of Spor Mountain zircon (Ayuso *et al.*, 2020).

Although our fractional crystallization model allows for a compositional continuum from the most primitive zircon in the northern subfield to the more evolved ones in the southern subfield, the c. 800 ka zircon crystallization age hiatus suggests these systems evolved independently in both time and space. Notably, the southern domes lack primitive zircon compositions (Fig. 7). One possible explanation is that the eruption preferentially remobilized the residual melt fraction in an intrusive body, thereby incorporating mostly evolved zircon crystals into the erupting magma, whereas earlier formed zircon would be locked up in a solid residue. This extraction of evolved melt could have occurred over multiple differentiation stages, but also due to a mafic injection which reactivated a largely crystalline system and scavenged zircon from the interstitial melt prior to eruption.

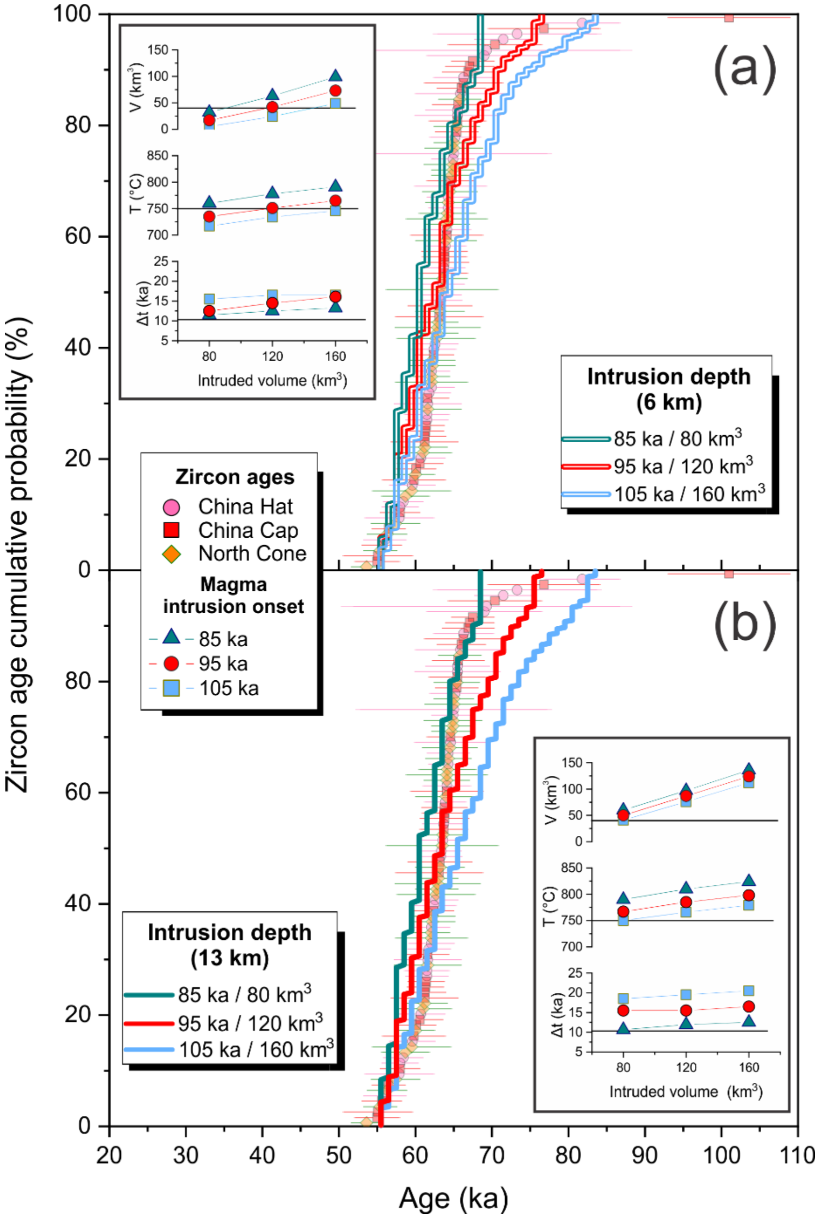

Fig. 12. *Thermal model outputs for zircon crystallization ages shown as a cumulative probability density function in comparison to the ranked order ages for BVF southern domes (Fig. 6). In all models, zircon crystallization ended with the eruption at 55 ka, whereas the initial filling of the magma reservoir (T = 1100 °C) was varied between 105 and 85 ka. The models tested two different magma reservoir depths at 6 km (a) and 13 km (b) respectively. Inset figures summarize model zircon age offsets (Δt), magma volumes (V) and magma temperatures (T) for different total magma reservoir volumes and different filling ages (see text). Individual results for each run are listed in Supplementary Table S6.*

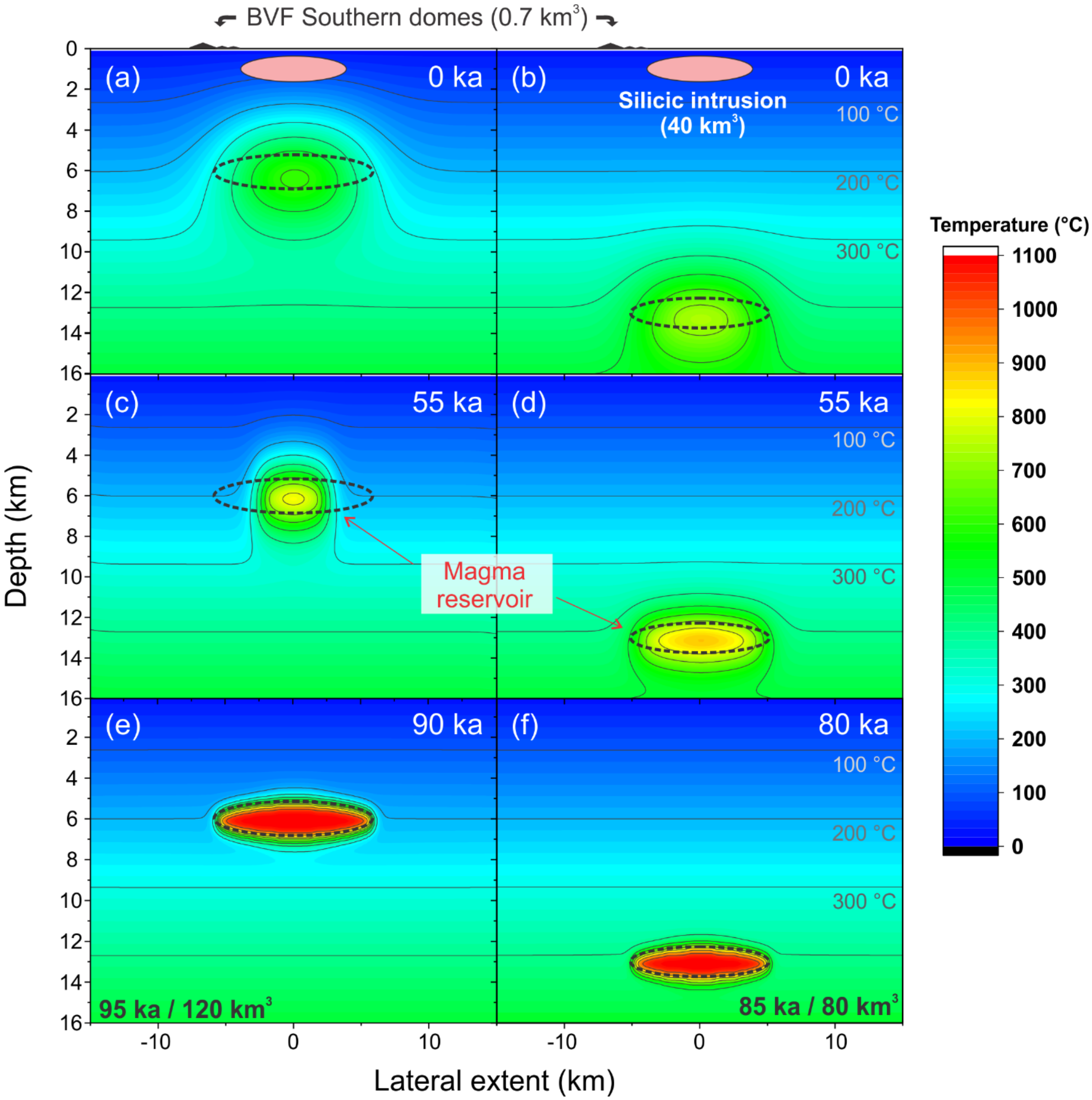

Fig. 13. *Thermal evolution of the crust for a cooling magma reservoir at 6 and 13 km depth (Fig. 11). Panels display the thermal history of a magma reservoir and the surrounding country rocks with the present-day condition on top (a-b), at 55 ka prior to eruption in the middle (c-d), and immediately after magma reservoir filling at the bottom (e-f). Black dashed line represents the total magma reservoir volume with a height to width aspect ratio of 1:7 (note 1.5-fold vertical exaggeration). Southern domes and an inferred 40 km*^{3} *silicic intrusion at <1 km (Hastings et al., 2021) are plotted for comparison.*

5.3 Constraints on the heat source for a hidden geothermal system

The relative youth of the BVF magma system as documented by the agreement between zircon crystallization and $^{40}Ar/^{39}Ar$ eruption ages for the southern domes supports previous notions of the BVF representing a promising geothermal target (Shervais *et al.*, 2024). However, while surface expressions of Late Pleistocene volcanism are an important indicator for identifying hidden geothermal reservoirs, young eruption ages alone are insufficient because magmatic sources can be either too small or too deep to effectively raise the geothermal gradient at depths that can be reached by drilling. Estimating magma volumes is thus critical, and zircon crystallization timescales are a first-order observable which can be translated into quantitative constraints on the longevity and size of a magmatic system where zircon crystallized through thermochemical modelling (e.g., Caricchi *et al.*, 2014; Schmitt *et al.*, 2023; Tierney *et al.*, 2016; Weber *et al.*, 2020). Zircon data thus can provide a unique perspective on the thermal structure of the reservoir from where the extrusive and shallow intrusive (Hastings *et al.*, 2021) BVF rhyolite magmas were extracted, which can then be extrapolated to the present day.

The thermochemical modeling presented here is based on the approach of (Tierney *et al.*, 2016), which varies magma input rates with a prescribed recharge interval and duration to simulate zircon age distributions observed in volcanic and plutonic rocks. This model follows the recharge–assimilation–fractional crystallization framework of Spera and Bohrson (2001) and simulates magma evolution within a 20 × 60 km (depth × width) section of the upper to middle crust, using a grid resolution of 0.1 × 0.1 km. A constant heat flux is maintained at both the surface and the base of the model domain. Magma is injected into the center of an ellipsoidal intrusion according to a defined recharge rate, maintaining a fixed aspect ratio (height to width). With each new pulse, the model tracks the temperature evolution in both magma and surrounding rock, specifically identifying cells within the zircon crystallization window where magma is above the solidus and melts are likely to achieve zircon saturation. Zircon production is calculated for these cells and integrated over time until magma extraction; as we are concerned with modelling the zircon record in volcanic rocks, only cells with melt present at the time of eruption (>700 °C) are counted. Initial conditions such as intrusion depth, recharge magma temperature, recharge rate, and run duration are predefined for each simulation (Table S6). Model outputs are assessed using cumulative probability density functions and the age offset (Δt), calculated as the difference between the 84th percentile zircon age and the youngest zircon crystallization age population.

We applied this model to the youngest BVF rhyolite episode as represented by the southern domes. Guided by textural and geochemical zircon evidence indicating that the rhyolite magma evolved in a dominantly closed system, we simulate a single pulse of magma injection and monitored its cooling until the time of eruption. A trachybasaltic magma composition with an initial temperature of 1100 °C was used (Whitaker *et al.*, 2008) under the assumption that earlier AFC processes already evolved the parental mantle-derived magma towards the BVF rhyolite isotopic composition. Filling of the reservoir starts at ~5 km^3 and reaches the prescribed intrusion volume within 5000 years. Hornblende barometry applied to the southern domes has suggested magma storage depths at ~13 km (Ford, 2005), whereas a machine learning-based thermobarometer applied to whole-rock compositions of BVF rhyolites yields shallower depths between 5.5 and 9 km (Weber and Blundy, 2024) with a pressure-depth conversion assuming an average crustal density of 2,830 kg/m^3. Limiting depths of 6 and 13 km were thus explored in the model (Fig. 12a-b). The ambient geothermal gradient was set to ~30 °C/km (e.g., Welhan *et al.*, 2014), and the reservoir is sill-shaped (aspect ratio = 0.14). More spherical geometries would result in more protracted cooling durations, which would increase Δt.

To constrain plausible solutions that reproduce the zircon crystallization age offset ($\Delta t = 10.7$ ka), two additional criteria were applied: firstly, by the time of eruption (rounded to 55 ka), the system must retain at least 40 km^3 of magma (V) at a temperature >700 °C, corresponding to the combined volumes of the shallow silicic intrusion (Hastings *et al.*, 2021) and the erupted domes (Ford, 2005); this approach is based on the assumption that the intrusion and domes are contemporaneous as implied by Hastings *et al.* (2021). Secondly, the eruptible magma must match the estimated eruption temperature ($T \leq 750$ °C), based on ilmenite-magnetite geothermometry (Ford, 2005). Models for zircon crystallization in magma reservoirs with total intrusive volumes of 80, 120, and 160 km^3 emplaced at 85, 95, and 105 ka were explored, and the outcomes compared to the observed zircon age distribution (Fig. 12a-b).

Models emplaced at 6 km and 13 km depth generally produce narrow zircon age ranges ($\Delta t = 10.7$–20.5 ka). Solutions that approximate the observed $\Delta t = 10.7$ ka are preferentially found for a shallow reservoir (Fig. 12a). This is due to more rapid cooling at shallow crustal levels, whereas deeper intrusions cool more gradually. In parallel, early-crystallized zircon at shallow levels is locked within the solidified regions of the reservoir, limiting the range of Δt in the melt-present regions. By contrast, extended zircon crystallization with somewhat broader age spectra are favored when a larger fraction of eruptible melt is maintained at elevated temperatures between an early onset of intrusion (105 ka) until the eruption due to higher ambient temperature at depth (Fig. 12b). In addition to Δt, we also evaluate volume and temperature criteria, where the 13 km magma reservoir readily produces the required V > 40 km^3, but at the same time the average magma temperature remains exceedingly high (T >>750 °C). The only exception is the early intrusion (at 105 ka/80 km^3), which becomes sufficiently cool, but also results in comparatively large Δt = 18.5 ka, nearly twice as much as the observed value (Fig. 12b). The overall best-fit scenario is thus for a 95 ka/120 km^3 intrusion emplaced at 6 km depth, where after 40 ka of cooling ~42 km^3 of magma at ~751 °C is retained—satisfying all V, T, and Δt criteria.

Figure 12 presents the modelled crustal geothermal gradients for the best-fit 95 ka/120 km^3 model at 6 km and the less favorable 85 ka/80 km^3 model at 13 km, which predicts an acceptable Δt but overshoots on magma T. These are evaluated at three distinct time steps: after the total magma volume has been emplaced (Fig. 13e–f), immediately before eruption (Fig. 13c–d), and at present-day (Fig. 13a–b). In the 13 km magma reservoir scenario (Fig. 13, right panels), some residual melt is predicted even at present day, whereas the 6 km scenario indicates a completely solidified, but still warm body. Both models also provide insights into the expected modern thermal condition at a depth of 0–4 km, which is considered accessible by geothermal drilling based on global compilations (e.g., Lukawski *et al.*, 2014). For the 13 km magma reservoir, the crust at 0–4 km remains thermally undisturbed (Fig. 13b). In contrast, the 6 km reservoir model produces significantly higher thermal anomalies in this depth range, with modelled present-day temperatures exceeding 300 °C at ~4 km depth directly above the magma reservoir (Fig. 13a).

The thermal models conservatively target only the magma volume of the silicic intrusion and the erupted domes, neglecting any magma or cumulates left behind at the depth of the magma reservoir. Moreover, the model excludes any late-stage mafic recharge that would have thermally rejuvenated the system. The presence of mafic intrusions in the southern dome lavas indicates that such a recharge event happened shortly before eruption, and therefore our model may have underestimated the volume and temperature of the reservoir at c. 55 ka. Additionally, the model ignores any shallow thermal disturbances related to the silicic intrusion. In the absence of direct sampling of the silicic intrusion, we cannot be sure whether it is indeed cogenetic and coeval with the southern domes (Hastings et al., 2021). Lastly, heat transport in our model is purely conductive, which is a reasonable assumption for the environment surrounding the magma reservoir, but convection involving groundwater is likely within shallow rocks.

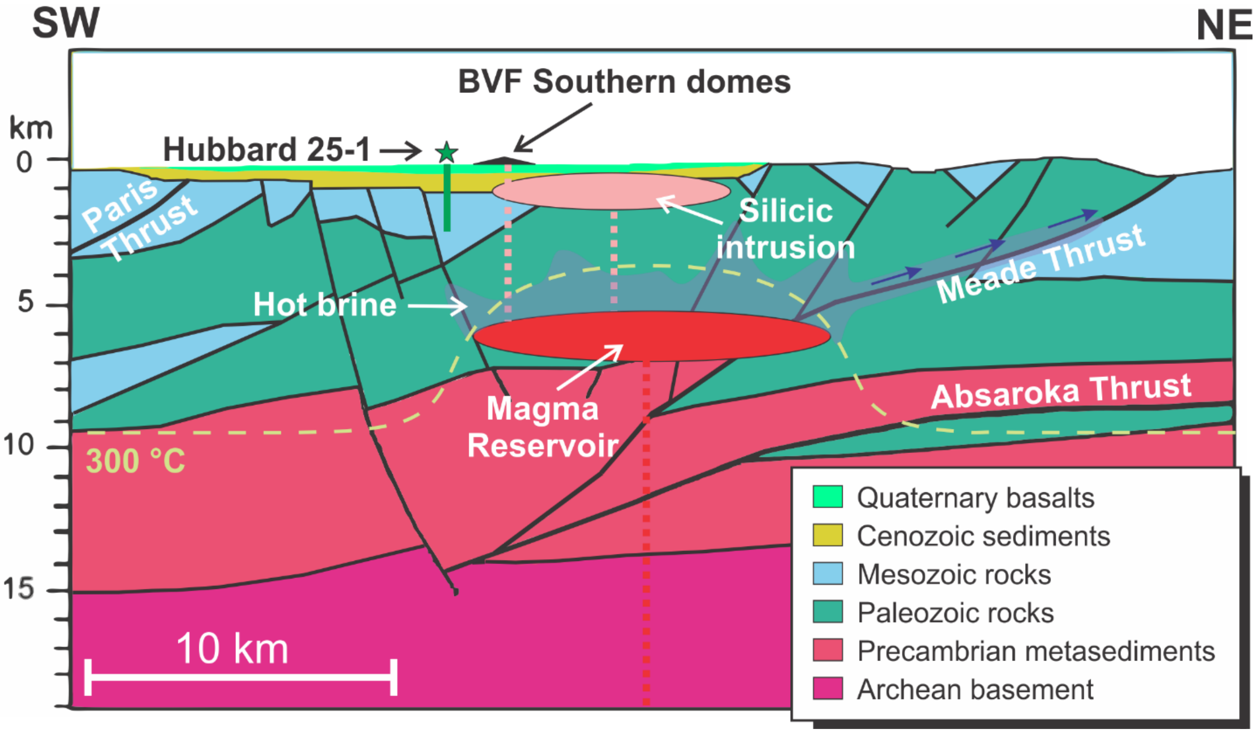

Fig. 14. *Conceptual model for the BVF modern geothermal system and its underlying magma reservoir after Welhan et al. (2014) superimposed with the conductive heat transport model from Fig. 12a. This model only accounts for the final magma emplacement where rhyolite is produced by extensive fractional crystallization after the isotopic composition of a trachybasaltic parent has already been established. The isotopic composition of the trachybasalt was controlled by AFC involving mantle-derived olivine tholeiite interacting with Archean basement at a deeper level (not shown). The ~120 km*^{3} *upper crustal magma reservoir at 6 km depth has fed a ~40 km*^{3} *silicic intrusion and surface rhyolite domes presumably at c. 55 ka (Hastings et al., 2021). It also produced a halo of elevated temperature, presently predicted to reach 300 °C at 4 km depth. The low temperatures in exploratory well Hubbard 25-1 therefore suggest dilution and diversion of hot brines above the cooling magma reservoir, which are likely migrating towards the northeast along permeable structures in the overthrust basement rocks.*

If our preferred model of a 6 km magma reservoir originally comprising 120 km^3 intruded at 95 ka is applicable, then explanations are required for the absence of geothermal manifestations within this part of the BVF and the comparatively low temperatures in the Hubbard-25-1 exploration well (maximum 96 °C; McCurry *et al.*, 2011; Fig. 14). Based on previous studies (e.g., Autenrieth *et al.*, 2011; Goldsby, 2017; Goldsby *et al.*, 2017; Shervais *et al.*, 2024; Welhan *et al.*, 2013, 2014), the geothermal signal associated with a silicic magma reservoir underneath the southern domes may be obscured by the regional hydrogeological setting, including an extensive aquifer, the insulating effect of a thick basalt cover, or complex regional thrust fault systems, including the Paris and Meade thrusts to the SE and NW of the sediment- and basalt-filled graben structure (Fig. 14). Under these conditions, magmatic heat may have become diluted in meteoric waters or redirected along deep-reaching faults towards a region of high heat flow NE of the BVF (Fig. 14).

6. Conclusions

Zircon petrochronology provides new insights into origins, crystallization and eruption history, and current thermal state of topaz rhyolite magmas within the Blackfoot volcanic field. U-Pb zircon crystallization ages for the northern dome complex and Sheep Island (on average between 1,006 and 785 ka) are significantly younger than previously published K-Ar ages, requiring a revision of the eruptive activity in this part of the field. In contrast, U-Th disequilibrium dating of the southern domes yielded an overall zircon age range of 63.4–55.2 ka, with the youngest zircon ages aligning closely with the reported ^{40}Ar/^{39}Ar eruption age (Heumann, 1999) and indicating zircon crystallization until immediately before eruption.

Zircon O- and Hf-isotopic compositions reinforce that BVF topaz rhyolites are derived from a mantle-sourced olivine tholeiite involving assimilation and extensive fractional crystallization. The contribution from Archean crust in BVF topaz rhyolites was more intense compared to Quaternary ESPR rhyolites, although the exact amounts of crustal assimilation are difficult to quantify. The almost universal absence of xenocrystic zircon also supports a hot, mafic parent which rapidly resorbed any crustal zircon. Moreover, the lack of zircon carryover from the Mid Pleistocene rhyolite episode of the northern and central parts of the BVF to the southern domes indicates independent magmatic systems that were individually short-lived relative to the overall c. 1 Ma eruptive history of the BVF. Uncorrelated isotopes and trace element indices of fractionation in zircon demonstrate that extensive fractional crystallization took place after the isotopic composition of the parent was established. Zircon textural features such as CL-dark and sometimes inclusion-rich domains, elevated trace element abundances, and co-crystallization with thorite support protracted, near-solidus crystallization. A final mafic injection into an already highly crystalline reservoir appears to have rejuvenated the magma system.

Thermochemical modeling supports the filling of a magma reservoir located at ~6 km depth with a volume of ~120 km³ starting at c. 95 ka, which upon cooling and differentiation supplied magma for both, eruption of the southern domes and emplacement of a shallow (<1 km deep) silicic body inferred from gravimetry data (Hastings *et al.*, 2021). Model results also imply that the former magma reservoir is now subsolidus, but still supports an elevated geothermal gradient with >300 °C at ~4 km depth (Fig. 13a). Although this implies that the BVF retains magmatic heat at depths accessible for drilling, its shallow thermal structure is likely modulated by regional aquifers, insulating basalt cover, complex fault networks and/or hydrothermal convection. Further exploration including geochemical tracing of magmatic components in regional geothermal fluids (Goldsby *et al.,* 2017; Lewicki *et al*., 2013) and elucidating the potential role of a cryptic silicic intrusion (Hastings *et al.*, 2021) are important to refine quantitative geothermal assessments for the BVF.

7. Acknowledgements

The authors would like to thank, Alexander Varychev, Ilona Fin, and Oliver Wienand for assistance in sample preparation, as well as Ana Karen Gonzales Ambrocio for digitizing and drafting the map.

8. Declaration of generative AI and AI-assisted technologies in the writing process.

During the preparation of this work, the authors used ChatGPT (by OpenAI) to improve readability and check for grammar and language issues in the manuscript. All content generated with the assistance of this tool was carefully reviewed and edited by the authors, who take full responsibility for the final version of the manuscript.

8. References

Anders, M. H., DiVenere, V. J., Hemming, S. R. & Gombiner, J. (2019). 40Ar/39Ar and paleomagnetic constraints on the age and areal extent of the Picabo volcanic field: Implications for the Yellowstone hotspot. *Geosphere* **15**, 716-735.

Anders, M. H., Rodgers, D. W., Hemming, S. R., Saltzman, J., DiVenere, V. J., Hagstrum, J. T., Embree, G. F. & Walter, R. C. (2014). A fixed sublithospheric source for the late Neogene track of the Yellowstone hotspot: Implications of the Heise and Picabo volcanic fields. *Journal of Geophysical Research: Solid Earth* **119**, 2871-2906.

Angeles-De La Torre, C. A., Schmitt, A. K., Lovera, O. M., Gassert, H., Gerdes, A. & Harvey, J. C. (2023). A common magma source for plutonic and volcanic rocks of the Geysers geothermal field, California: Volume and intrusive history derived from zircon. *Chemical Geology* **624**, 121414.

Angeles-De La Torre, C. A., Schmitt, A. K., Danisík, M., Gerdes, A., Hertwig, A., & McCurry, M. (2025). Linking Zircon Crystallization to Magmatic Processes in Basalt Dominated Lava Fields: the Eastern Snake River Plain–Craters of the Moon Testbed. *Journal of Petrology*, egaf040.

Armstrong, R. L., Leeman, W. P. & Malde, H. E. (1975). K--Ar dating quaternary and Neogene volcanic rocks of the Snake River Plain, Idaho. *Am. J. Sci.;(United States)* **275**.

Autenrieth, K., McCurry, M., Welhan, J. & Polun, S. (2011). Conceptual Subsurface Model of the Blackfoot Volcanic Field. *Southeast Idaho: A Potential Hidden Geothermal Resource: GRC Transactions* **35**, 695-698.

Ayuso, R., Foley, N., Vazquez, J. & Jackson, J. (2020). SHRIMP U-Pb zircon geochronology of volcanic rocks hosting world class Be-U mineralization at Spor Mountain, Utah, USA. *Journal of Geochemical Exploration* **209**, 106401.

Baertschi, P. (1976). Absolute 18O content of standard mean ocean water. *Earth and Planetary Science Letters* **31(3)**, 341-344.

Bell, E. A., Boehnke, P., Barboni, M. & Harrison, T. M. (2019). Tracking chemical alteration in magmatic zircon using rare earth element abundances. *Chemical Geology* **510**, 56-71.

Bell, E. A., Boehnke, P. & Harrison, T. M. (2016). Recovering the primary geochemistry of Jack Hills zircons through quantitative estimates of chemical alteration. *Geochimica et Cosmochimica Acta* **191**, 187-202.

Bernal, J., Solari, L., Gómez-Tuena, A., Ortega-Obregón, C., Mori, L., Vega-González, M. & Espinosa-Arbeláez, D. (2014). In-situ 230Th/U dating of Quaternary zircons using LA-MCICPMS. *Quaternary Geochronology* **23**, 46-55.

Best, M., McKee, E. & Damon, P. (1980). Space-time-composition patterns of late Cenozoic mafic volcanism, southwestern Utah and adjoining areas. *American Journal of science* **280**, 1035-1050.

Bindeman, I. & Simakin, A. (2014). Rhyolites—Hard to produce, but easy to recycle and sequester: Integrating microgeochemical observations and numerical models. *Geosphere* **10**, 930-957.

Black, L. P., Kamo, S. L., Allen, C. M., Davis, D. W., Aleinikoff, J. N., Valley, J. W., Mundil, R., Campbell, I. H., Korsch, R. J. & Williams, I. S. (2004). Improved 206Pb/238U microprobe geochronology by the monitoring of a trace-element-related matrix effect; SHRIMP, ID–TIMS, ELA–ICP–MS and oxygen isotope documentation for a series of zircon standards. *Chemical Geology* **205**, 115-140.

Blackwell, D. D., Kelley, S. & Steele, J. L. (1992). Heat flow modeling of the Snake River Plain, Idaho. *US Department of Energy Report for contract DE-AC07-761DO1570* **109**.

Blundy, J. & Wood, B. (1994). Prediction of crystal–melt partition coefficients from elastic moduli. *Nature* **372**, 452-454.

Boehnke, P., Watson, E. B., Trail, D., Harrison, T. M. & Schmitt, A. K. (2013). Zircon saturation re-revisited. *Chemical Geology* **351**, 324-334.

Bonnichsen, B., Leeman, W. P., Honjo, N., McIntosh, W. C. & Godchaux, M. M. (2008). Miocene silicic volcanism in southwestern Idaho: geochronology, geochemistry, and evolution of the central Snake River Plain. *Bulletin of Volcanology* **70**, 315-342.

Bouvier, A., Vervoort, J. D. & Patchett, P. J. (2008). The Lu–Hf and Sm–Nd isotopic composition of CHUR: constraints from unequilibrated chondrites and implications for the bulk composition of terrestrial planets. *Earth and Planetary Science Letters* **273**, 48-57.

Caricchi, L., Simpson, G. & Schaltegger, U. (2014). Zircons reveal magma fluxes in the Earth's crust. *Nature* **511**, 457-461.

Caricchi, L., Simpson, G. & Schaltegger, U. (2016). Estimates of volume and magma input in crustal magmatic systems from zircon geochronology: the effect of modeling assumptions and system variables. *Frontiers in Earth Science* **4**, 48.

Christiansen, E., Burt, D., Sheridan, M. & Wilson, R. (1983). The petrogenesis of topaz rhyolites from the western United States. *Contributions to Mineralogy and Petrology* **83**, 16-30.

Christiansen, E. H., Haapala, I. & Hart, G. L. (2007). Are Cenozoic topaz rhyolites the erupted equivalents of Proterozoic rapakivi granites? Examples from the western United States and Finland. *Lithos* **97**, 219-246.

Christiansen, E. H. & McCurry, M. (2008). Contrasting origins of Cenozoic silicic volcanic rocks from the western Cordillera of the United States. *Bulletin of Volcanology* **70**, 251-267.

Christiansen, E. H., Sheridan, M. F. & Burt, D. M. (1986). The geology and geochemistry of Cenozoic topaz rhyolites from the western United States. *Geological Society of America -Special Papers,* 74

Colón, D. P., Bindeman, I. N., Wotzlaw, J.-F., Christiansen, E. H. & Stern, R. A. (2018). Origins and evolution of rhyolitic magmas in the central Snake River Plain: insights from coupled high-precision geochronology, oxygen isotope, and hafnium isotope analyses of zircon. *Contributions to Mineralogy and Petrology* **173**, 1-18.

Condon, D., Schoene, B., Schmitz, M., Schaltegger, U., Ickert, R. B., Amelin, Y., Augland, L. E., Chamberlain, K. R., Coleman, D. S. & Connelly, J. N. (2024). Recommendations for the reporting and interpretation of isotope dilution U-Pb geochronological information. *Geological Society of America Bulletin* **136**, 4233-4251.

Congdon, R. D., & Nash, W. P. (1988). High-fluorine rhyolite: an eruptive pegmatite magma at the Honeycomb Hills, Utah. *Geology*, **16(11)**, 1018-1021.

Congdon, R. D. & Nash, W. (1991). Eruptive pegmatite magma: rhyolite of the Honeycomb Hills, Utah. *American Mineralogist* **76**, 1261-1278.

Corfu, F., Hanchar, J. M., Hoskin, P. W. & Kinny, P. (2003). Atlas of zircon textures. *Reviews in Mineralogy and Geochemistry* **53**, 469-500.

DePaolo, D. J. (1981). Trace element and isotopic effects of combined wallrock assimilation and fractional crystallization. *Earth and Planetary Science Letters* **53**, 189-202.

Drew, D. L. (2013). An isotopic, trace element, and volatile investigation of large-volume rhyolite generation at the Picabo volcanic field of the Yellowstone hotspot track. University of Oregon.

Drew, D. L., Bindeman, I. N., Watts, K. E., Schmitt, A. K., Fu, B. & McCurry, M. (2013). Crustal-scale recycling in caldera complexes and rift zones along the Yellowstone hotspot track: O and Hf isotopic evidence in diverse zircons from voluminous rhyolites of the Picabo volcanic field, Idaho. *Earth and Planetary Science Letters* **381**, 63-77.

DuFrane, S., Vervoort, J., Leeman, W. & Wolf, D. (2007). Hafnium isotope composition of Archean zircons from xenoliths of the Snake River Plain, Idaho. *AGU Fall Meeting Abstracts*, V43B-1375.

Ellis, B., Wolff, J., Boroughs, S., Mark, D., Starkel, W. & Bonnichsen, B. (2013). Rhyolitic volcanism of the central Snake River Plain: a review. *Bulletin of Volcanology* **75**, 1-19.

Ellis, B. S., Schmitz, M. D. & Hill, M. (2019). Reconstructing a Snake River Plain 'super-eruption' via compositional fingerprinting and high-precision U/Pb zircon geochronology. *Contributions to Mineralogy and Petrology* **174**, 1-16.

Ferry, J. & Watson, E. (2007). New thermodynamic models and revised calibrations for the Ti-in-zircon and Zr-in-rutile thermometers. *Contributions to Mineralogy and Petrology* **154**, 429-437.

Fiesinger, D., Perkins, W. D. & Puchy, B. J. (1982). Mineralogy and petrology of Tertiary-Quaternary volcanic rocks in Caribou County, Idaho. *Cenozoic geology of Idaho: Idaho Bureau of Mines and Geology Bulletin* **16**, 465-488.

Ford, M. T. (2005). The petrogenesis of quaternary rhyolite domes in the bimodal Blackfoot volcanic field, Southeastern Idaho. MSc thesis Idaho State University. 133 p.

Friedrichs, B., Schmitt, A. K., Lovera, O. M. & Atıcı, G. (2021). Zircon as a recorder of contrasting magma recharge and eruptive recurrence patterns. *Earth and Planetary Science Letters* **571**, 117104.

Geist, D. J., Sims, E. N., Hughes, S. S., McCurry, M., Link, P. & Mink, L. (2002). Open-system evolution of a single episode of Snake River Plain magmatism. *Geological Society of America - Special Papers*, 193-204.

Gerdes, A. & Zeh, A. (2009). Zircon formation versus zircon alteration—new insights from combined U–Pb and Lu–Hf in-situ LA-ICP-MS analyses, and consequences for the interpretation of Archean zircon from the Central Zone of the Limpopo Belt. *Chemical Geology* **261**, 230-243.

Ghiorso, M. S. & Evans, B. W. (2008). Thermodynamics of rhombohedral oxide solid solutions and a revision of the Fe-Ti two-oxide geothermometer and oxygen-barometer. *American Journal of science* **308**, 957-1039.

Goldsby, R. (2017). Insights Into Topaz Rhyolite Magma Evolution From Mafic Enclaves and Melt Inclusion Volatile SIMS Analyses, China Hat, SE Idaho. MSc thesis Idaho State University. 76 p.

Goldsby, R., McCurry, M., Schmitt, A. K. & Welhan, J. (2017) Dynamic Open-System Volatile Evolution of a Shallow Magmatic System, China Hat, SE Idaho: Implications for Magmatic Associated Blind Geothermal Systems. *GRC Transactions* **41**, 10

Grimes, C. B., John, B. E., Kelemen, P., Mazdab, F., Wooden, J., Cheadle, M. J., Hanghøj, K. & Schwartz, J. (2007). Trace element chemistry of zircons from oceanic crust: A method for distinguishing detrital zircon provenance. *Geology* **35**, 643-646.

Hanan, B., Vetter, S. & Shervais, J. (1997). Basaltic volcanism in the eastern Snake River Plain: lead, neodymium, strontium isotope constraints from the Idaho INEL WO-2 core site basalts. *Geol Soc Am Abs* **29**, A298.

Hastings, M. S., Connor, C., Wetmore, P., Malservisi, R., Connor, L., Rodgers, M. & La Femina, P. C. (2021). Large-Volume and Shallow Magma Intrusions in the Blackfoot Reservoir Volcanic Field (Idaho, USA). *Journal of Geophysical Research: Solid Earth* **126**, e2021JB022507.

Henry, C. D., Castor, S. B., Starkel, W. A., Ellis, B. S., Wolff, J. A., Laravie, J. A., McIntosh, W. C. & Heizler, M. T. (2017). Geology and evolution of the McDermitt caldera, northern Nevada and southeastern Oregon, western USA. *Geosphere* **13**, 1066-1112.

Heumann, A. (1999). Timescales of Processes within Silicic Magma Chambers. PhD Dissertation, University Amsterdam, 200 p.

Hildreth, W., Halliday, A. N. & Christiansen, R. L. (1991). Isotopic and chemical evidence concerning the genesis and contamination of basaltic and rhyolitic magma beneath the Yellowstone Plateau volcanic field. *Journal of Petrology* **32**, 63-138.

Hofmann, A. W. (1988). Chemical differentiation of the Earth: the relationship between mantle, continental crust, and oceanic crust. *Earth and Planetary Science Letters* **90**, 297-314.

Hoskin, P. W. (2000). Patterns of chaos: fractal statistics and the oscillatory chemistry of zircon. *Geochimica et Cosmochimica Acta* **64**, 1905-1923.

Hughes, S. S., McCurry, M. & Geist, D. J. (2002a). Geochemical correlations and implications for the magmatic evolution of basalt flow groups at the Idaho National Engineering and Environmental Laboratory. In: Link, P.K., Mink, L.L. (Eds.), Geology, Hydrogeology, and Environmental Remediation: Idaho National Engineering and Environmental Laboratory, Eastern Snake River Plain, Idaho, 353. *Geological Society of America*, pp. 151–173. Special Paper.

Hughes, S. S., Wetmore, P. H., Casper, J. L. & Bonnichsen, B. (2002b). Evolution of Quaternary tholeiitic basalt eruptive centers on the eastern Snake River Plain, Idaho. *Tectonic and Magmatic Evolution of the Snake River Plain Volcanic Province: Idaho Geological Survey Bulletin* **30**, 363-385.

Keppler, H. (1993). Influence of fluorine on the enrichment of high field strength trace elements in granitic rocks. *Contributions to Mineralogy and Petrology* **114**, 479-488.

Kuntz, M. A. (1992). A model-based perspective of basaltic volcanism, eastern Snake River Plain, Idaho. *Geological Society of America Memoirs* **179**, 289-304.

Kuntz, M. A. & Dalrymple, G. B. (1979). Geology, geochronology, and potential volcanic hazards in the Lava Ridge-Hells Half Acre area, eastern Snake River Plain, Idaho. *U.S. Geological Survey Open-File Report* **79-1657**, 66 p.

Leeman, W. (2007). Scope of Silicic Magmatism Associated With the Snake River Plain-Yellowstone (SRPY)" Hotspot" Track. *AGU Fall Meeting Abstracts*, V41F-07.

Leeman, W. P. (1982). Olivine tholeiitic basalts of the Snake River Plain, Idaho. *Cenozoic geology of Idaho*: Idaho Bureau of Mines and Geology Moscow, 181-191.

Leeman, W. P., Bonnichsen, B. & Breckenridge, R. (1982). Development of the Snake River Plain-Yellowstone Plateu Province, Idaho and Wyoming: An Overview and Petrologic Model. *Cenozoic Geology of Idaho*. Idaho Bureau of Mines and Geology Moscow, 155-177.

Leeman, W. P., Vitaliano, C. J. & Prinz, M. (1976). Evolved lavas from the snake river plain: craters of the moon national monument, Idaho. *Contributions to Mineralogy and Petrology* **56**, 35-60.

Lewicki, J. L., Hilley, G. E., Dobeck, L., McLing, T. L., Kennedy, B. M., Bill, M., & Marino, B. D. V. (2013). Geologic CO2 input into groundwater and the atmosphere, Soda Springs, ID, USA. *Chemical Geology*, **339**, 61-70.

Liu, P.-P., Caricchi, L., Chung, S.-L., Li, X.-H., Li, Q.-L., Zhou, M.-F., Lai, Y.-M., Ghani, A. A., Sihotang, T. & Sheldrake, T. E. (2021). Growth and thermal maturation of the Toba magma reservoir. *Proceedings of the National Academy of Sciences* **118**, e2101695118.

Lochridge, W. K. (2016). Constraining the Petrogenesis of the Quaternary Topaz Rhyolite Lava Domes in the Bimodal Blackfoot Volcanic Field, Southeastern Idaho. MSc thesis Idaho State University. 102 p.

Loucks, R. R., Fiorentini, M. L. & Henríquez, G. J. (2020). New magmatic oxybarometer using trace elements in zircon. *Journal of Petrology* **61**, egaa034.

Luedke, R. G. & Smith, R. L. (1983). Map showing distribution, composition, and age of late Cenozoic volcanic centers in Idaho, western Montana, west-central South Dakota, and northwestern Wyoming. *U.S. Geological Survey Misc.* Inv. Series Map I-1091-E.

Lukács, R., Harangi, S., Guillong, M., Bachmann, O., Fodor, L., Buret, Y., Dunkl, I., Sliwinski, J., von Quadt, A. & Peytcheva, I. (2018). Early to Mid-Miocene syn-extensional massive silicic volcanism in the Pannonian Basin (East-Central Europe): Eruption chronology, correlation potential and geodynamic implications. *Earth-science reviews* **179**, 1-19.

Lukawski, M. Z., Anderson, B. J., Augustine, C., Capuano Jr, L. E., Beckers, K. F., Livesay, B. & Tester, J. W. (2014). Cost analysis of oil, gas, and geothermal well drilling. *Journal of Petroleum Science and Engineering* **118**, 1-14.

Mahon, K. I. (1996). The New "York" regression: Application of an improved statistical method to geochemistry. *International Geology Review* **38**, 293-303.

Manea, V., Manea, M., Leeman, W. P. & Schutt, D. L. (2009). The influence of plume head–lithosphere interaction on magmatism associated with the Yellowstone hotspot track. *Journal of Volcanology and Geothermal Research* **188**, 68-85.

Matthews, N. E., Vazquez, J. A. & Calvert, A. T. (2015). Age of the L ava C reek supereruption and magma chamber assembly at Yellowstone based on 40 A r/39 A r and U-P b dating of sanidine and zircon crystals. *Geochemistry, Geophysics, Geosystems* **16**, 2508-2528.

McCurry, M., Hackett, W. R. & Hayden, K. (1999). Cedar Butte and cogenetic Quaternary rhyolite domes of the eastern Snake River Plain. *Guidebook to the Geology of Eastern Idaho: Idaho Museum of Natural History*. p. 169-179

McCurry, M., Hayden, K. P., Morse, L. H. & Mertzman, S. (2008). Genesis of post-hotspot, A-type rhyolite of the Eastern Snake River Plain volcanic field by extreme fractional crystallization of olivine tholeiite. *Bulletin of Volcanology* **70**, 361-383.

McCurry, M. & Rodgers, D. W. (2009). Mass transfer along the Yellowstone hotspot track I: Petrologic constraints on the volume of mantle-derived magma. *Journal of Volcanology and Geothermal Research* **188**, 86-98.

McCurry, M., Welhan, J., Polun, S., Autenrieth, K. & Rodgers, D. (2011). Geothermal potential of the Blackfoot Reservoir-Soda Springs Volcanic Field: A hidden geothermal resource and natural laboratory in SE Idaho. *University of Idaho Geology and Hydrogeology* **35**, 917-924.

McCurry, M. O., Pearson, D. M., Welhan, J. A., Kobs-Nawotniak, S. E. & Fisher, M. A. (2014). Origin and potential geothermal significance of China Hat and other late Pleistocene topaz rhyolite lava domes of the Blackfoot Volcanic Field, SE Idaho. *AGU Fall Meeting Abstracts*, V33A-4830.

McCurry, M., Pearson, D., Welhan, J., Natwotniak, S.K., and Fisher, M., 2015, Origin and potential geothermal significance of China Hat and other late Pleistocene topaz rhyolite lava domes of the Blackfoot volcanic field, SE Idaho*: GRC Transactions*, v. **39**, p. 35–48.

McDonough, W. F., & Sun, S. S. (1995). The composition of the Earth. *Chemical Geology*, **120(3-4)**, 223-253.

Melnik, O. E., Utkin, I. S. & Bindeman, I. N. (2021). Magma chamber formation by dike accretion and crustal melting: 2D thermo-compositional model with emphasis on eruptions and implication for zircon records. *Journal of Geophysical Research: Solid Earth* **126**, e2021JB023008.

Morgan, L. A. & McIntosh, W. C. (2005). Timing and development of the Heise volcanic field, Snake River Plain, Idaho, western USA. *Geological Society of America Bulletin* **117**, 288-306.

Morgan, W. J. (1971). Convection plumes in the lower mantle. *Nature* **230**, 42-43.

Nash, B. P., Perkins, M. E., Christensen, J. N., Lee, D.-C. & Halliday, A. (2006). The Yellowstone hotspot in space and time: Nd and Hf isotopes in silicic magmas. *Earth and Planetary Science Letters* **247**, 143-156.

Neupane, G., Mattson, E. D., McLing, T. L., Palmer, C. D., Smith, R. W. & Wood, T. R. (2014). Deep geothermal reservoir temperatures in the Eastern Snake River Plain, Idaho using multicomponent geothermometry. Idaho National Lab.(INL), Idaho Falls, ID (United States). Report number: INL/CON-13-30541

Paces, J. B. & Miller Jr, J. D. (1993). Precise U-Pb ages of Duluth complex and related mafic intrusions, northeastern Minnesota: Geochronological insights to physical, petrogenetic, paleomagnetic, and tectonomagmatic processes associated with the 1.1 Ga midcontinent rift system. *Journal of Geophysical Research: Solid Earth* **98**, 13997-14013.

Pearce, N. J., Perkins, W. T., Westgate, J. A., Gorton, M. P., Jackson, S. E., Neal, C. R. & Chenery, S. P. (1997). A compilation of new and published major and trace element data for NIST SRM 610 and NIST SRM 612 glass reference materials. *Geostandards newsletter* **21**, 115-144.

Peng, X. & Humphreys, E. D. (1998). Crustal velocity structure across the eastern Snake River Plain and the Yellowstone swell. *Journal of Geophysical Research: Solid Earth* **103**, 7171-7186.

Pickett, K. E. (2004). Physical volcanology, petrography, and geochemistry of basalts in the bimodal Blackfoot volcanic field, southeastern Idaho. MSc thesis Idaho State University. 92 p.

Pierce, K. L. & Morgan, L. A. (1992). The track of the Yellowstone hot spot: Volcanism, faulting, and uplift. In: Link, P.K., Kuntz, M.A. & Platt, L. (eds.) Regional Geology of Eastern Idaho and Western Wyoming, *Geological Society of America Memoir* **179**, 1-53.

Pierce, K. L. & Morgan, L. A. (2009). Is the track of the Yellowstone hotspot driven by a deep mantle plume?—Review of volcanism, faulting, and uplift in light of new data. *Journal of Volcanology and Geothermal Research* **188**, 1-25.

Polun, S. G. (2011). Kinematic analysis of Late Pleistocene faulting in the Blackfoot lava field, Caribou County, Idaho. MSc thesis Idaho State University. 86 p.

Putirka, K. D., Kuntz, M. A., Unruh, D. M. & Vaid, N. (2009). Magma evolution and ascent at the Craters of the Moon and neighboring volcanic fields, southern Idaho, USA: Implications for the evolution of polygenetic and monogenetic volcanic fields. *Journal of Petrology* **50**, 1639-1665.

Ratschbacher, B. C., Keller, C. B., Schoene, B., Paterson, S. R., Anderson, J. L., Okaya, D., Putirka, K. & Lippoldt, R. (2018). A new workflow to assess emplacement duration and melt residence time of compositionally diverse magmas emplaced in a sub-volcanic reservoir. *Journal of Petrology* **59**, 1787-1809.

Reid, M. R. (1995). Processes of mantle enrichment and magmatic differentiation in the eastern Snake River Plain: Th isotope evidence. *Earth and Planetary Science Letters* **131**, 239-254.

Rivera, T. A., White, C. M., Schmitz, M. D. & Jicha, B. R. (2021). Petrogenesis of pleistocene basalts from the Western snake river plain, Idaho. *Journal of Petrology* **62**, egaa108.

Schmitt, A. K. (2011). Uranium series accessory crystal dating of magmatic processes. *Annual Review of Earth and Planetary Sciences* **39**, 321-349.

Ryan, W. B. F., S.M. Carbotte, J. Coplan, S. O'Hara, A. Melkonian, R. Arko, R.A. Weissel, V. Ferrini, A. Goodwillie, F. Nitsche, J. Bonczkowski, and R. Zemsky (2009), Global Multi-Resolution Topography (GMRT) synthesis data set, *Geochem. Geophys. Geosyst.,* **10**, Q03014, doi:10.1029/2008GC002332.

Schmitt, A. K., Klitzke, M., Gerdes, A. & Schäfer, C. (2017). Zircon hafnium–oxygen isotope and trace element petrochronology of intraplate volcanic rocks from the Eifel (Germany) and implications for mantle versus crustal origins of zircon megacrysts. *Journal of Petrology* **58**, 1841-1870.

Schmitt, A. K., Sliwinski, J., Caricchi, L., Bachmann, O., Riel, N., Kaus, B. J. P., Cisneros de Léon, A., Cornet, J., Friedrichs, B. & Lovera, O. (2023). Zircon age spectra to quantify magma evolution. *Geosphere* **19**, 1006-1031.

Shervais, J. W., Branney, M. J., Geist, D. J., Hanan, B. B., Hughes, S., Prokopenko, A. A. & Williams, D. F. (2006). HOTSPOT: the Snake River scientific drilling project–Tracking the Yellowstone Hotspot through space and time. *Scientific Drilling* **3**, 56-57.

Shervais, J. W., DeAngelo, J., Glen, J. M., Nielson, D. L., Garg, S., Dobson, P., Gasperikova, E., Sonnenthal, E., Liberty, L. M. & Newell, D. L. (2024). Geothermal play fairway analysis, part 1: Example from the Snake River Plain, Idaho. *Geothermics* **117**, 102865.

Smith, R. B. & Braile, L. W. (1994). The yellowstone hotspot. *Journal of Volcanology and Geothermal Research* **61**, 121-187.

Sparlin, M. A., Braile, L. & Smith, R. B. (1982). Crustal structure of the eastern Snake River Plain determined from ray trace modeling of seismic refraction data. *Journal of Geophysical Research: Solid Earth* **87**, 2619-2633.

Spear, D. B. (1979). *The geology and volcanic history of the Big Southern Butte-East Butte area, eastern Snake River plain, Idaho*: PhD Dissertation State University of New York at Buffalo. 106 p.

Spear, D. B. & King, J. S. (1982). The geology of Big Southern Butte, Idaho. *Cenozoic geology of Idaho: Idaho Bureau of Mines and Geology Bulletin* **26**, 395-403.

Spera, F. J. & Bohrson, W. A. (2001). Energy-constrained open-system magmatic processes I: General model and energy-constrained assimilation and fractional crystallization (EC-AFC) formulation. *Journal of Petrology* **42**, 999-1018.

Stachnik, J., Dueker, K., Schutt, D. L. & Yuan, H. (2008). Imaging Yellowstone plume-lithosphere interactions from inversion of ballistic and diffusive Rayleigh wave dispersion and crustal thickness data. *Geochemistry, Geophysics, Geosystems* **9**. 1-21

Stefano, C. J., Mukasa, S. B. & Cabato, J. A. (2019). Elemental abundance patterns and Sr-, Nd-and Hf-isotope systematics for the Yellowstone hotspot and Columbia River flood basalts: Bearing on petrogenesis. *Chemical Geology* **513**, 44-53.

Stout, M., Nicholls, J. & Kuntz, M. (1994). Petrological and mineralogical variations in 2500–2000 yr BP lava flows, Craters of the Moon lava field, Idaho. *Journal of Petrology* **35**, 1681-1715.

Tester, J. W., Anderson, B. J., Batchelor, A. S., Blackwell, D. D., DiPippo, R., Drake, E. M., Garnish, J., Livesay, B., Moore, M. & Nichols, K. (2006). The future of geothermal energy. *Massachusetts Institute of Technology* **358**, 1-3.

Tierney, C. R., Schmitt, A. K., Lovera, O. M. & de Silva, S. L. (2016). Voluminous plutonism during volcanic quiescence revealed by thermochemical modeling of zircon. *Geology* **44**, 683-686.

Trail, D., Chowdhury, W., Tailby, N. D. & Ackerson, M. R. (2024). Ce and Eu anomalies in zircon as indicators of oxygen fugacity in subsolidus systems. *Geochimica et Cosmochimica Acta* **369**, 93-110.

Trail, D., Mojzsis, S. J., Harrison, T. M., Schmitt, A. K., Watson, E. B. & Young, E. D. (2007). Constraints on Hadean zircon protoliths from oxygen isotopes, Ti-thermometry, and rare earth elements. *Geochemistry, Geophysics, Geosystems* **8**.

Trail, D., Watson, E. B. & Tailby, N. D. (2012). Ce and Eu anomalies in zircon as proxies for the oxidation state of magmas. *Geochimica et Cosmochimica Acta* **97**, 70-87.

Troch, J., Ellis, B. S., Schmitt, A. K., Bouvier, A.-S. & Bachmann, O. (2018). The dark side of zircon: textural, age, oxygen isotopic and trace element evidence of fluid saturation in the subvolcanic reservoir of the Island Park-Mount Jackson Rhyolite, Yellowstone (USA). *Contributions to Mineralogy and Petrology* **173**, 1-17.

U.S. Energy Information Administration. (2025, January). Electric power monthly: January 2025. U.S. Department of Energy. https://www.eia.gov/electricity/annual/

Valley, J. W., Kinny, P. D., Schulze, D. J. & Spicuzza, M. J. (1998). Zircon megacrysts from kimberlite: oxygen isotope variability among mantle melts. *Contributions to Mineralogy and Petrology* **133**, 1-11.

Vermeesch, P. (2018). IsoplotR: A free and open toolbox for geochronology. *Geoscience Frontiers* **9**, 1479-1493.

Vervoort, J. D. & Patchett, P. J. (1996). Behavior of hafnium and neodymium isotopes in the crust: constraints from Precambrian crustally derived granites. *Geochimica et Cosmochimica Acta* **60**, 3717-3733.

Wang, D., Wang, X.-L., Cai, Y., Goldstein, S. L. & Yang, T. (2018). Do Hf isotopes in magmatic zircons represent those of their host rocks? *Journal of Asian Earth Sciences* **154**, 202-212.

Watson, E. B. & Harrison, T. M. (1983). Zircon saturation revisited: temperature and composition effects in a variety of crustal magma types. *Earth and Planetary Science Letters* **64**, 295-304.

Watts, K. E., Bindeman, I. N. & Schmitt, A. K. (2011). Large-volume rhyolite genesis in caldera complexes of the Snake River Plain: insights from the Kilgore Tuff of the Heise Volcanic Field, Idaho, with comparison to Yellowstone and Bruneau–Jarbidge rhyolites. *Journal of Petrology* **52**, 857-890.

Watts, K. E., Leeman, W. P., Bindeman, I. N. & Larson, P. B. (2010). Supereruptions of the Snake River Plain: Two-stage derivation of low-δ18O rhyolites from normal-δ18O crust as constrained by Archean xenoliths. *Geology* **38**, 503-506.

Weber, G. & Blundy, J. (2024). A machine learning-based thermobarometer for magmatic liquids. *Journal of Petrology* **65**, egae020.

Weber, G., Caricchi, L., Arce, J. L. & Schmitt, A. K. (2020). Determining the current size and state of subvolcanic magma reservoirs. *Nature communications* **11**, 5477.

Webster, J. D., Holloway, J. R., & Hervig, R. L. (1987). Phase equilibria of a Be, U and F-enriched vitrophyre from Spor Mountain, Utah. *Geochimica et Cosmochimica Acta*, **51(3)**, 389-402.

Welhan, J., Garwood, D. & Feeney, D. (2013). The Blackfoot volcanic field, southeast Idaho: A hidden high-T geothermal resource revealed through data mining of the National Geothermal Data Repository. *GRC Trans* **37**, 365-374.

Welhan, J., Gwyunn, M., Payne, S., McCurry, M., Plummer, M. & Wood, T. (2014). The Blackfoot volcanic field, southeast Idaho: a hidden high-temperature geothermal resource in the Idaho thrust belt. *Proceedings of the 39th Workshop on Geothermal Reservoir Engineering Stanford University, Stanford, California*. February 24-26, 2014, v. SGP-TR-202, p. 1–13.

Whitaker, M. L., Nekvasil, H., Lindsley, D. H. & McCurry, M. (2008). Can crystallization of olivine tholeiite give rise to potassic rhyolites?—an experimental investigation. *Bulletin of Volcanology* **70**, 417-434.

Wiedenbeck, M., Alle, P., Corfu, F., Griffin, W. L., Meier, M., Oberli, F. v., Quadt, A. v., Roddick, J. & Spiegel, W. (1995). Three natural zircon standards for U-Th-Pb, Lu-Hf, trace element and REE analyses. *Geostandards newsletter* **19**, 1-23.

Wiedenbeck, M., Hanchar, J. M., Peck, W. H., Sylvester, P., Valley, J., Whitehouse, M., Kronz, A., Morishita, Y., Nasdala, L. & Fiebig, J. (2004). Further characterisation of the 91500 zircon crystal. *Geostandards and Geoanalytical Research* **28**, 9-39.

Williams, C. F., Reed, M. J., Mariner, R. H., DeAngelo, J. & Galanis, S. P. (2008). Assessment of moderate-and high-temperature geothermal resources of the United States. *U.S. Geological Survey*. **2008-3082** 4 p.

Wright, K. E., McCurry, M., Hughes, S. S. & Bonnichsen, B. (2002). Petrology and geochemistry of the Miocene tuff of McMullen Creek, central Snake River Plain. *Tectonic and magmatic evolution of the Snake River Plain volcanic province. Idaho Geol Surv Bull* **30**, 177-194.

Supplementary material

Article	Content	Description
I The Geysers	PDF paper	Original Paper
	Figure S1	La vs LREE-I
	Figure S2	U vs Yb
	Figure S3	U vs age
	Figure S4	Model runs continue recharge
	Figure S5	Model runs independent
	Figure S6	Model runs temperature and geothermal gradient
	Figure S7	Temperature vs Age
	Figure S8	Best fit model with CMVC
	Table S1	U-Pb zircon SIMS results
	Table S2	Summary Unknown (Trace elements, δ^{18}O and eHf)
II Craters of the Moon	PDF paper	Original Paper
	Fig S1	Trace elements correlation Matrix
	Fig S2	U vs Yb
	Fig S3	Ti abundances with corresponding Ti-in-zircon temperatures
	Table S1	U-Pb zircon SIMS results
	Table S2	Zircon U-Th SIMS results
	Table S3	Zircon trace element SIMS results
	Table S4	Composite zircon (U-Th)/He ages
	Table S5	Zircon SIMS O isotope data
	Table S6	Zircon LA-MC-ICPMS Lu-Hf isotope data
III Blackfoot	JVGR_BF_TS1	U-Pb zircon SIMS results
	JVGR_BF_TS2	U-Th zircon SIMS results
	JVGR_BF_TS3	Zircon trace element SIMS results
	JVGR_BF_TS4	Zircon SIMS O isotope data
	JVGR_BF_TS5	Zircon LA-MC-ICPMS Lu-Hf isotope data
	JVGR_BF_TS6	Thermal model set up and results

Table 1. **S***upplementary material from each scientific article listened in this cumulative dissertation.*

You will find the Supplementary material of each paper listened in the table in the following QR code:

To the supplementary material

Acknowledgements

First of all, I would like to express my deep gratitude to my supervisor, Axel Schmitt. I was incredibly fortunate to meet him and be accepted as his student. We shared many adventures during our field trips, and his energy and enthusiasm for spreading knowledge helped me grow tremendously. Above all, I want to thank him for his patience, not only when I demonstrated my "driving skills," but especially during the review of my scientific writing.

I would also like to thank the co-authors of the papers included in this dissertation: Andreas Hertwig, Michael McCurry, Martin Danisík, Janet Harvey, Oscar Lovera, and Axel Gerdes. I like to think that I formed friendships with many of them, and I will always remember their efforts in shaping this research project.

A special thanks to the members of my evaluation committee, Lucie Tajcmanova, Yamirka Rojas-Agramonte, and especially Mario Trieloff, for helping me during the final bureaucratical stages of my work. I also owe a special thanks to the entire team at the Heidelberg university institute who contributed to the development of this thesis: Alexander Varichev, Torsten Hoffmann, Ilona Fin, Oliver Wienand, Francisco Cueto, Dan Schuppenhauer, Katharina Cionoiu, and Winfred Schwarz.

Finally, I want to thank my colleagues with whom I shared many adventures during these three and a half years: Simon Hammerich, for always helping me battle the bureaucratic monster that is the German government; Anne Sturm, for teaching me through bouldering that there are muscles it's better not to feel; Andreas Hertwig again, for all his support, trips to the Mensa, and a couple of beers we still owe each other. I also want to thank my best friend and breakfast buddy, Rezvaneh Jamaliashtiani, who, along with my dear lunch club friends Maren Kahl, Shuang-Qing Li, and Cristian Bergemann, shared countless stories with me. Lastly, I'd like to thank Haoyu Hu, the last friend I made before submitting this thesis, and also Cara (hallo Cara!).

Agradecimientos (para hispanoparlantes)

Quiero agradecer a mi padre Marcelino Angeles López que pudo heredarme al menos un poco de su infinito interés por la vida, la ciencia, el mundo y el universo y que logró sacar al científico que hay en mí. Quiero Agradecer a mi madre Irma De La Torre Carlos por todo su amor incondicional y ser siempre mi red de seguridad emocional, no habría podido jamás desear una mejor madre. Agradezco a mi hermana Sibel y a mi sobrino Ian Gibran, ambos son mi motor para seguir siendo el mejor ejemplo y llevarlos siempre en mi corazón.

Agradezco sobre todo a Joel Ortiz García, mi roca y mi confidente, sin su apoyo no habría tenido el valor de ser quien soy, ni de estar donde estoy, además de ser mi compañero de aventuras y en quien confío incondicionalmente, *Kuta'avi ri nuu ro Mani ri, kuenda ro kuu ri, ¡Kuni Mani ri nuu ro!*

A la Doctora Julie Roberge, le agradezco haberme entrenado y enseñado tanto, siempre me he considerado una extensión de su conocimiento, y sé que nunca hubiera llegado tan lejos de no haberla conocido, siempre voy a considerarme con suerte de haber podido aprender de usted.

Agradezco también a mi mejor amiga en el mundo Ana, quien a la fecha también está agradecida en dos de mis artículos (y contando) ella y Mónica son las mejores amigas que siempre pude desear. De igual forma, me gustaría agradecer a Nancy Morgan, mi buscadora de artículos por toda su ayuda. También incluyo en esta lista a la familia que pude escoger estando en Alemania, quienes me hicieron sentir menos solo y mi red de apoyo en un país con comida extraña: Vivian, Graciela, Luisa, Houda, Lorena, Erick y mi último anexado amigo inducidor pasivo al alcoholismo y a los paseos en bicicleta, Lalo Piedras.